UNIVERSITY OF OKLAHOMA

GRADUATE COLLEGE

ASSESSING SCANNING STRATEGIES WITH ALL-DIGITAL PHASED ARRAY WEATHER RADARS FOR CHARACTERIZATION AND DETECTION OF MICROBURSTS

A THESIS

SUBMITTED TO THE GRADUATE FACULTY

in partial fulfillment of the requirements for the

Degree of

MASTER OF SCIENCE IN METEOROLOGY

By

CONNOR BROCK PEARSON
Norman, Oklahoma
2022

ASSESSING SCANNING STRATEGIES WITH ALL-DIGITAL PHASED ARRAY WEATHER RADARS FOR CHARACTERIZATION AND DETECTION OF MICROBURSTS

A THESIS APPROVED FOR THE
SCHOOL OF METEOROLOGY

BY THE COMMITTEE CONSISTING OF

Dr. Tian-You Yu, Chair

Dr. David Bodine

Dr. Sebastian Torres

Dr. Robert Palmer

Dr. Pierre Emmanuel Kirstetter

Dr. Xuguang Wang

Acknowledgments

I would like to start off by thanking God for His faithfulness and provision during this time. He has provided immense strength and perseverance to me throughout this project, and I could not have accomplished this without His help. I would also like to thank my parents, Tom and Cheryl Pearson, for their support and pushing me to be the best that I can be.

I also want to extend a huge thank you to Dr. Tian-You Yu, Dr. David Bodine, and Dr. Sebastian Torres for regularly meeting with me. Your helpful insights and guidance for the last couple of years has been extremely instrumental in this project. Your impact on this thesis was tremendous, and I am forever grateful. I also want to thank Dr. Robert Palmer, Dr. Pierre Emmanuel Kirstetter, and Dr. Xuguang Wang for serving on my committee.

I would like to also thank Dr. David Schvartzman for generating the transmit patterns used within this project. This research is much better because of this contribution. A special thanks to Sam Emmerson for help with many different requests throughout the project.

Some of the computing for this project was performed at the OU Supercomputing Center for Education and Research (OSCER) at the University of Oklahoma (OU). This computing was extremely beneficial when running the CM1 model located at `https://www2.mmm.ucar.edu/people/bryan/cm1/` as of 5/27/2021.

Table of Contents

Appendix A

Appendix B

List of Tables

List of Figures

Abstract

Microbursts are a rapidly evolving, vertically oriented meteorological phenomena that can be extremely hazardous to aviation, and other human activities, if left undetected. The temporal resolution and vertical sampling of the current operational weather radar network (NEXRAD) is too coarse to properly observe the evolution of microbursts and their precursor signatures. However, a potential polarimetric phased array weather radar (PAR) should be able to improve both temporal resolution and spatial sampling of the atmosphere to provide better observation of rapidly evolving hazards such as microbursts. All-digital PAR technology is extremely flexible as a wide array of scanning techniques are available to use; however, this flexibility is not without trade-offs, and these trade-offs are important for understanding how a potential PAR network would operate.

This thesis will lay out a framework and tool set for the study of microbursts and their precursor signatures with varying PAR scanning strategies. This project is the first of its kind to investigate the question of what trade-offs are associated with different scanning strategies when using a planar, mechanically rotating, all-digital PAR to observe and detect microbursts and their precursor signatures, including dual-polarization variables. The scanning strategies analyzed include a traditional volume coverage pattern (VCP) 212, a true range-height indicator (RHI) scan, and imaging at three different spoiled beamwidths in elevation. VCP 212 represents the current operational capacity for microburst observation and detection. True RHI scanning and imaging are more feasible on a PAR system, and they can provide faster temporal resolution and finer vertical sampling.

The framework and tools developed herein are tested in a proof-of-concept analysis by looking at a single wet microburst producing storm generated within a numerical weather prediction (NWP) simulation. Using this NWP simulation data, scanning strategies are implemented through the use of a radar emulator, RSim. These emulations are then analyzed both qualitatively and quantitatively to compare size, shape, and intensity observations of different microburst precursor signatures: descending reflectivity columns

(DRCs), specific differential phase (K_{DP}) cores, and mid-level convergence. Because of the use of NWP simulations, error analysis is also performed to characterize the impact of estimation errors. The results of this test case analysis of one wet microburst imply that, when utilizing imaging, there is a limit to the benefits provided by increased temporal resolution. This limit occurs at temporal resolutions equal to 30 s and an imaging spoil factor of 5°. When utilizing any spoil factor larger than 5°, the effects of data degradation become too great for the scanning strategy to overcome, and the representativeness of the model environment is degraded and estimation errors become large. However, these results can only be considered preliminary because the analysis only serves as a proof-of-concept.

Chapter 1

Introduction

1.1 Background and Motivation

One of the most extensive weather radar networks in existence is the Next Generation Weather Radar (NEXRAD) system located in the United States (US). The NEXRAD network was the result of a billion-dollar modernization effort in the late 1980s and early 1990s for the National Weather Service (NWS) (Bleistein, 2010). The NEXRAD network is comprised of Weather Surveillance Radar - 1988 Doppler (WSR-88D) radars that were installed from 1990 through 1997 (Crum and Alberty, 1993). NEXRAD is a joint effort between three different federal agencies that extensively use it to perform their duties outlined by the US government. These three agencies are the National Weather Service (NWS), Federal Aviation Administration (FAA), and the Department of Defense (DoD). Different WSR-88Ds are "owned" by the three different federal agencies, but the entire network is primarily used by each for weather monitoring. This shared use of the NEXRAD system has been a great cost-saver for everyone involved because new algorithms and any other improvements developed with funding from one agency are available to everyone (Bleistein, 2010). In 2013, the entire NEXRAD network was upgraded to be capable of utilizing dual-polarization technology which can dramatically improve the observations made by the radars (Smalley et al., 2015). Currently, there are 159 operational NEXRAD WSR-88D radars throughout the United States and its territories (Guam and Puerto Rico). Generally speaking, the coverage provided by these radars is very beneficial for looking at the lower atmosphere over the majority of the United States (Figure 1.1) (Radar Operations Center, 2021a).

The current NEXRAD system is nearing its operational lifetime, and the WSR-88Ds have almost gone through a full Service Life Extension Program (SLEP) which focused on

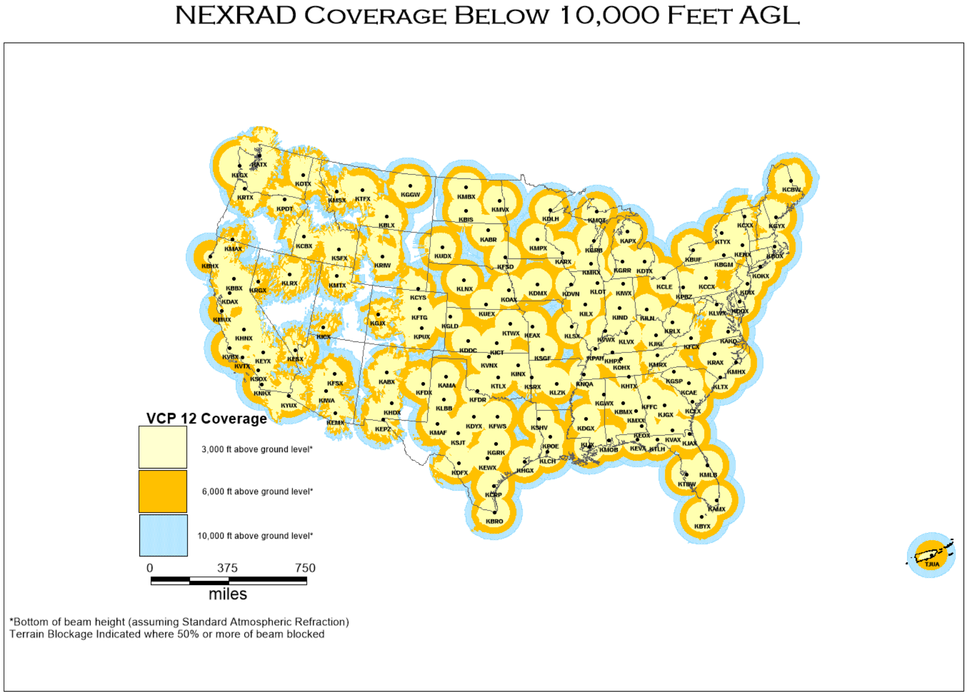

Figure 1.1: Map of the contiguous United States and Puerto Rico showing NEXRAD coverage below 10,000 feet above ground level (AGL) (Radar Operations Center, 2021a).

digital signal processor technology refreshment, transmitter refurbishment, pedestal refurbishment, and equipment shelter refurbishment (Radar Operations Center, 2021b). Because no current replacement has been determined for the WSR-88D NEXRAD network, there is preparation for a future SLEP to hopefully extend the WSR-88D network through 2040. However, it is not feasible to continually perform SLEPs on an aging weather radar network because the cost of continuing will ultimately become too burdensome. Thus, the need for a viable replacement of the NEXRAD network has become of great importance over recent years. However, in order to get everything in place to replace the NEXRAD network in the late 2030s, a decision will need to be made regarding the design of the network before 2030 (Weber et al., 2019).

The NWS has already stated that more rapid temporal resolution is vital moving forward (FAA, 2017). Any future operational weather radar network is required to perform at least as well as the current WSR-88D network in terms of spatial sampling (1° beamwidth and 0.5° sampling for super resolution with 250 meter range sampling). However, it is required that this new network also have a temporal resolution much finer than the current NEXRAD network. The current WSR-88Ds have volumetric update times anywhere between 4 and 7 min depending upon which volume coverage pattern (VCP) is used and what scanning techniques are chosen (Automated Volume Scan Evaluation and Termination (AVSET), Multiple Elevation Scan Option for Supplemental Adaptive Intra-Volume Low-Level Scan (MESO-SAILS), and Mid-Volume Rescan of Low-Level Elevations (MRLE)). These scanning techniques attempt to provide faster updates for the most important elevations to the operational meteorologist by rescanning the lowest elevation (SAILS), lowest group of elevations (MRLE). or by skipping the uppermost elevations if there are no significant echoes (AVSET). Although these scanning strategies generally help with providing faster updated information of important features (e.g., the 0.5° elevation for mesocyclone tracking and tornado vortex signature characterization), both SAILS and MRLE can lead to longer VCP update times resulting in delayed full-volume updates. These full-volume updates are vital to detect many radar signatures utilizing a full volume of data (e.g., hail size estimation), observe rapidly evolving meteorological phenomena, and for data assimilation (Wolfson and Meuse, 1993; Heinselman et al., 2012; Sun et al., 2014; Supinie et al., 2017). According to initial performance requirements, the required temporal resolution for a replacement system is 1 minute which is a large improvement upon the current NEXRAD VCP update times (FAA, 2017).

These faster update times have shown to be greatly beneficial in a number of areas of meteorological concern ranging from tornado observation and tracking, data assimilation, Quantitative Precipitation Estimates (QPE), and microburst detection (Wolfson and Meuse, 1993; Zrnic et al., 2007; Wang and Chandrasekar, 2010; Heinselman et al., 2012; Newman and Heinselman, 2012; Sun et al., 2014; Wilson et al., 2017; Supinie et al., 2017). While all of the above meteorological concerns are important, it is the purpose of this thesis to detail the framework that was developed to study the benefits and trade-offs of a potential future operational phased array radar (PAR) system in the detection and observation of wet microbursts and their precursor signatures.

One of the largest advantages of a PAR system is the scanning flexibility. A future PAR can utilize different scanning strategies such as beam-multiplexing (Yu et al., 2007), imaging (Isom et al., 2013), conventional VCPs, and adaptive scanning (Torres and Schvartzman, 2020) just to name a few. These different scanning strategies not only provide increased temporal resolution (to the NWS requirement of one minute for a NEXRAD replacement), but can also provide faster updates than the future 1-minute operational requirement. However, these faster updates have a few limitations such as the degradation of data quality. For example, imaging has been shown to provide updates over a $90^\circ \times 20^\circ$ sector in as little as six seconds (Kurdzo et al., 2017; Salazar et al., 2019); however, this quick update time requires using a 20° spoiled transmit beam, and the sidelobes associated with a 20° spoiled transmit beam are much higher than those associated with a pencil beam (1° beamwidth) which degrades the data quality. Furthermore, increased beam spoiling can degrade the sensitivity of the radar to negatively impacts its ability to detect weak echoes (especially at long ranges). Thus, the question becomes, with respect to microbursts and their precursor signatures, what is more important? Is it more important to have a fast temporal resolution to better observe the evolution of the signatures in question, to have good quality data to verify these signatures are accurately represented, or a combination of the two?

Previous research by Mahre et al. (2020) began to answer these questions by examining signatures associated with tornadoes such as tornado debris signatures (TDS) and mesocyclone strength (Mahre, 2020). However, these questions have never been answered in the context of microbursts. The overarching goal of this work is to develop a framework and tool set to study and quantify the trade-offs of using different scanning strategies to observe and detect microbursts and their associated precursor signatures.

1.2 Phased Array Radar

The leading candidate for a NEXRAD replacement appears to be a rotating PAR system, and a future PAR network has shown promise for meeting the National Oceanic and Atmospheric Administration's (NOAA) requirements including the temporal resolution of one minute. Much research has occurred over the past decade to study a future operational PAR network's feasibility. This research has focused on many different aspects of the necessary requirements for generating a future operational radar network such as data collection from prototype systems (Zrnic et al., 2007; Weber et al., 2020; Torres and Schvartzman, 2020), assessment of rapid-scan PAR benefits (Heinselman et al., 2008; Adachi et al., 2016; Kuster et al., 2016, 2021), potential signal processing techniques and benefits (Yu et al., 2007; Kurdzo et al., 2014; Zrnic et al., 2015; Melnikov et al., 2015), radar calibration (Fulton et al., 2016; Schuss et al., 2016; Fulton et al., 2018; Ivic et al., 2018), and adaptive scanning techniques (Heinselman and Torres, 2011; Torres et al., 2014; Torres and Schvartzman, 2020).

1.2.1 What is a PAR?

Before diving into the history of PARs, it is important to lay the groundwork and define what is meant by the term "Phased Array Radar." At its most fundamental level, a PAR consists of multiple radiating elements that can transmit and receive a signal (Skolnik, 1981; NSSL, 2022a; Mailloux, 2005). These radiating elements are arranged together to form a "phased array antenna" which is then used for transmitting and receiving electromagnetic (EM) engery. This antenna can be arranged in multiple different array patterns and can either be stationary or rotated mechanically depending on the radar architecture (Butler, 1998; Yu et al., 2007; Hondl and Emanuel, 2019; Schvartzman, 2020; NSSL, 2022b).

PARs differ significantly from their WSR-88D counterparts with mechanically rotating parabolic antenna. PARs operate on the premise of electronically generating the radar beam from an antenna of thousands of radiating elements, while WSR-88Ds use a single parabolic reflector to form the radar beam. Due to the antenna design of many transmit-receive elements, PARs can electronically shape and steer the beam almost instantaneously by controlling the phase and amplitude of each radiator's element; however, the WSR-88D radars require mechanical rotation of the parabolic dish in both azimuth and elevation to complete a volume scan (Skolnik, 1981; Zrnic et al., 2007). It should be noted that single-face PARs can be mechanically rotated in azimuth and elevation in order to scan a full 360° which serves as the baseline and leading architecture for a NEXRAD replacement network due to costs and dual-polarization data quality concerns (Schvartzman, 2020; Weber et al., 2021).

Until recently, all operational PARs had been single-polarization radars as there have been many different challenges with implementing dual-polarization on PARs (Zhang et al., 2008; Fulton and Chappell, 2010; Morin et al., 2019). These issues range from complications with weather radar calibration and measurements to maintaining gain and phase tolerances to poor cross-polar isolation associated with steering angles far off boresight (Fulton and Chappell, 2010; Morin et al., 2019). These issues are continually being addressed, and progress is being made through the development and operation of new dual-polarization PARs (Palmer et al., 2019; Salazar et al., 2019; Schvartzman, 2020; Schvartzman et al., 2022a,b; Torres and Wasielewski, 2022).

1.2.2 PAR History

The earliest operational use of PARs - defined as steered beam array antennas - can be traced back all the way to World War II by the British, Americans, and Germans (Skolnik, 1981). This technology made it possible to not only track objects in an easier manner, but it also allowed for the detecting and tracking of multiple objects (Visser, 2005). The phase shifts were accomplished using mechanical phase shifters; however, switching these to electronic phase shifters in the 1950s greatly increased the switching and steering speed of the beam allowing greater flexibility for detection and tracking objects of interest (Visser, 2005). In 1958, the US Navy attempted to develop a phased-array surface-to-air system called Typhon to offer more advanced multi-target abilities (Dranidis, 2003). By the 1960s, digital phase shifters were introduced allowing for even more flexibility and allowing for a computer to control the electronic steering of the beam (Visser, 2005). This lead to the development of the SPY-1/Aegis family of radars that were first demonstrated in 1977 and first used operationally in 1983 (Dranidis, 2003).

PARs up until this point required a feed network to operate and are known as “passive” radars. The feed network system would deliver the energy to be radiated from a single source to the individual radiators. This was not the best option because it was bulky, complicated, and subject to energy loss (Visser, 2005). However, in the 1980s, new PARs were designed to be “active” (Visser, 2005). The “active” terminology indicates that instead of relying on the feed network to supply the energy from a singular source (i.e., power amplifier), each individual radiator is equipped with its own transmitter, and this technology has been used ever since.

While PAR technology had been extensively used by the US Navy and DoD, it was not until the turn of the century when the meteorological community would begin to extensively investigate the benefits and limitations of PAR for weather observations. This occurred when collaborations between the US government, private sector companies, and the University of Oklahoma (OU) lead to the US Navy loaning a SPY-1A antenna to the National Severe Storms Laboratory (NSSL) (Forsyth et al., 2005). The antenna was installed at the National Weather Radar Testbed (NWRT) in Norman, Oklahoma about 20 km away from the Twin Lakes, Oklahoma (KTLX) WSR-88D radar (Heinselman et al., 2008; Bowden, 2014). Modifications were made so the 4352 element planar antenna was suitable for weather surveillance, but the radar began collecting data in May 2004 after some performance issues delayed the initial data collection (Forsyth et al., 2005; Bowden, 2014). The NWRT PAR was decommissioned in 2016 to make way for the Advanced Technology Demonstrator (ATD). This was a major upgrade in that the ATD uses modern technology, contains an overlapped sub-array architecture, and more importantly, is dual-polarization. The ATD became operational in the spring of 2021 and continues the legacy of the NWRT PAR by providing regular PAR data to the meteorological community to test the viability of polarimetric PARs as a potential replacement for the NEXRAD network.

Soon after the NWRT PAR started collecting data, other PARs began to be developed in the research community, but these radars were mobile. The use of mobile radars - not just mobile PARs - has been extensive and invaluable to our understandings of convective storms, supercells, and tornadoes (Wurman and Randall, 2001; Bluestein et al., 2010; Pazmany et al., 2013; Isom et al., 2013; Kurdzo et al., 2017). The first true mobile PAR that was developed for meteorological purposes was the Meteorological Weather Radar 2005 X-band Phased Array (MWR-05XP), and it was a modified Army tactical radar (Bluestein et al., 2010). The single-polarized MWR-05XP could be scanned electronically in elevation; however, it was limited in electronic azimuthal scanning (via frequency hopping), so it also employed rapid mechanical azimuth scanning to reach speeds of $180^{\circ} s^{-1}$ (Bluestein et al., 2010). The main downside of MWR-05XP to other conventional mobile radars was the fact that the half-power beamwidth was roughly 2° in both azimuth and elevation; however, it was able to provide an update time on the order of tens of seconds which was a great benefit for the observation of storm-scale features and studies of tornadogenesis (Bluestein et al., 2010; French et al., 2013).

A few years later, another mobile PAR was developed based on a new technique to observe storms: imaging (which is discussed more in Section 2.2.3.4). The Atmospheric Imaging Radar (AIR) was developed by the Advanced Radar Research Center (ARRC) at the OU, and its first field campaign occurred in the spring of 2012 (Isom et al., 2013; Kurdzo et al., 2017). After performing digital beamforming, the AIR was characterized by 1° beamwidth in azimuth and elevation and could complete a $90^{\circ} \times 20^{\circ}$ sector in under 6 s (Kurdzo et al., 2017). However, the AIR was a single-polarization radar, so no dual-polarization signatures were observed with it.

Two future mobile PAR radars include the Polarimetric Atmospheric Imaging Radar (PAIR) and an all-digital PAR (Horus). The PAIR will be a C-band mobile radar with 1.5° azimuthal and elevation resolution, 10-m range resolution, and should be able to scan a $360^\circ \times 20^\circ$ in about 6 s (Salazar et al., 2019). The PAIR will be made up of 76 subarray panels with 64 elements on each panel for a total of 4,864 elements (Salazar et al., 2019). One of the largest advantages of the PAIR over its predecessor is its dual-polarization design allows it to also measure dual-polarization variables such as differential phase (Φ_{dp}), differential reflectivity (Z_{DR}), and correlation coefficient (ρ_{hv}) along with the single polarization variables of reflectivity factor (Z_h), radial velocity (v_r), and spectrum width (σ_v).

Horus is another new mobile PAR being built by the ARRC at OU. Horus will be an all-digital, S-band polarimetric PAR (Palmer et al., 2019). Horus will ultimately be one of the most advanced radars in the nation (Kirker, 2018; Smith, 2018; Dynamic Sealing Technologies, Inc., 2020). At the current scale, the S-band Horus does not provide the ideal angular resolution expected with weather radars; however, the design of Horus is "extremely scalable", so future larger scale radars are not expected to have this problem (Palmer et al., 2019). This project exploits the all-digital system with a full-size antenna aperture. Thus, the system utilized herein can be considered a full-scale version of Horus.

1.2.3 PAR Applications

Since PARs started to be used by the meteorological community, there has been much research into how they could be applied to different meteorological phenomena. This ongoing research encompasses many different areas from which techniques are best for rapid scanning to producing observations of rapidly evolving meteorological processes to even gauging potential impacts and benefits to operational forecasters.

Figure 1.2: An example of the all-digital dual-polarization, mobile S-band radar (Horus).

1.2.3.1 Rapid Scanning Techniques

The beauty of all-digital PAR, like Horus, is that it provides so much flexibility that can be utilized to achieve many things dependent upon the desired need at any given time. This flexibility can be manipulated to provide faster update times, enhanced data quality, finer sampling, or a combination of the three. These techniques range from beam-multiplexing (Yu et al., 2007), multiple-beam technique (MBT) (Zrnic et al., 2015; Melnikov et al., 2015), and imaging (Isom et al., 2013; Mahre et al., 2020) just to name a few.

Each of these techniques has shown promise in allowing faster update times while generally preserving data quality. Beam-multiplexing (BMX) can improve data acquisition time by a factor of 2–4 while preserving data quality by exploiting the idea of independent-pair sampling (IPS) (Yu et al., 2007; Mahre, 2020; Mahre et al., 2020). The MBT transmits a certain number of beams, N_b, in N_b directions in rapid succession and then uses digital beamforming to separate the beams on receive; however, there are limitations to the multiple-beam technique, but the update times can be reduced by a factor equal to N_b (for $N_b > 1$) (Zrnic et al., 2015; Melnikov et al., 2015; Mahre et al., 2020). Now, while BMX and MBT do show promise in providing faster update times without loss of resolution or data quality, they are outside the scope of this study which looks to have applications not only to the Horus radar but also to the PAIR.

Imaging is another promising scanning technique that can drastically improve volumetric update time and will be analyzed within this study. At its core, imaging operates by transmitting a spoiled beam in azimuth and/or elevation to cover a large area with individual narrow receive beams formed through digital beamforming (Isom et al., 2013; Mahre, 2020). It has been shown that imaging can scan an entire 90° by 20° sector in as little as 6 seconds (Isom et al., 2013; Kurdzo et al., 2017). However, the trade-offs of utilizing this method include higher sidelobe levels, reduced sensitivity, and a broader mainlobe (Mahre et al., 2020).

One major benefit of imaging is the ability to spoil a transmit beam into different widths to quickly measure a larger volume - while balancing the aforementioned trade-offs. For example, the spoiled transmit beam can be spoiled to 2.5°, 5°, 10°, and even 20° beamwidths. Furthermore, due to the digital beamforming techniques employed to generate the receive beams, there is the possibility to oversample within the original transmitted beam. For example, in theory, within the 5° spoiled transmit beam, one could capture five receive beams spaced by 1.0°, nine spaced by 0.5°, or any number of arbitrary elevation angles.

1.2.3.2 PAR Observations of Meteorological Phenomena

PAR data have provided high temporal resolution observations of different convective-scale processes. These observations are vital as they provide the baseline for future PAR research and help researchers connect the engineering behind PAR technology to the actual meteorology occurring in the atmosphere.

The first major study to examine the observations associated with an S-band single polarization PAR data was Heinselman et al. (2008), and they examined how well the NWRT PAR observed different severe weather threats along with what benefits higher temporal resolution provided. In the study, the authors performed analysis of three separate cases involving rapidly evolving severe threats associated with deep convective storms (Heinselman et al., 2008). More specifically, they looked at a reintensifying supercell, microburst, and hailstorm with update times on the order of 1-min. In every situation, it was found that the high temporal resolution was advantageous compared to a traditional WSR-88D as storm-scale processes were observed, analyzed, and tracked with greater accuracy in both reflectivity and velocity, particularly in the vertical column (Heinselman et al., 2008).

Another analysis of NWRT PAR observations was performed by Newman and Heinselman (2012). This analysis focused on a quasi-linear convective system (QLCS) using a similar temporal resolution as Heinselman et al. (2008). Within the QLCS, different observations were made with the PAR and then compared to the nearby KTLX WSR-88D radar. These observations included a microburst, the midlevel jet, and the development and enhancement of a mesovortex circulation (Newman and Heinselman, 2012). Within this analysis, the pseudo-RHI PAR data was able to provide high vertical resolution with 22 elevation angles compared to the 14 elevation angles used by KTLX, and the temporal resolution was at worst 2 min for the NWRT PAR compared to the 4–6 min updates assocaited with KTLX (Newman and Heinselman, 2012). Within the comparisons between the NWRT PAR and KTLX, it was shown that these higher temporal resolution volumetric updates associated with PARs revealed potential precursors for damaging circulations in QLCSs such as a descending reflectivity column and the descent of high velocity from the midlevel jet toward the surface (Newman and Heinselman, 2012). It was also shown that the NWRT PAR data exhibited the descent of the microburst's reflectivity column in multiple volumetric updates compared to KTLX's one (Newman and Heinselman, 2012).

Kuster et al. (2015) put together an analysis of the May 31, 2013 El Reno, Oklahoma tornadoes to detail the advantages of PAR data from a forecaster's perspective. In the analysis, a forecaster who worked the event in real-time provided insights into the analysis between the 70-s NWRT PAR data and the 4.58 min KTLX data (Kuster et al., 2015). Within this analysis, the higher resolution PAR data was most advantageous when observing cycles of the low to midlevel mesocylones, changes in the extent and magnitude of storm inflow, rapid intensification of the two tornado vortex signatures, abrupt changes in the tornado circulation's motion, and more precision in the tornadic circulation's location (Kuster et al., 2015). This information can be vitally important for nowcasting and warning operations, as the forecaster can better communicate the location and magnitude of the threat to the public, first responders, and emergency managers (Kuster et al., 2015).

Adachi et al. (2016) utilized an X-band PAR to take rapid volumetric observations of a wet microburst in Japan. This analysis observed a DRC that developed around 3–5 km above ground level (AGL) and rapidly descended to the surface. Furthermore, a reflectivity notch was also observed that was believed to be associated with midlevel inflow. Adachi et al. (2016) eventually concluded that in addition to hydrometeor loading, the entrainment of midlevel dry air can play a role in driving a strong downdraft through evaporative cooling, and the precursors observed by the PAR were useful to provide a 5–10 min leadtime to the occurrence of low-level wind shear (downburst).

A paper detailing the analysis of observations from the X-band single-polarization AIR was published showcasing how atmospheric imaging performs in observing different severe storms (Kurdzo et al., 2017). Kurdzo et al. (2017) showcase the benefits of atmospheric imaging in being able to capture storm-scale features with a temporal resolution of 5–10 s. The observations presented showed changes in reflectivity structures that were likely associated with debris, the rapid intensification and dissipation of mesocyclones, and a transition of a large tornado into a rope stage tornado (Kurdzo et al., 2017). Griffen et al. (2019) also utilized AIR data to document the evolution of a dissipating tornado and were able to illustrate rapid changes in mesocyclone and tornado-scale processes over a few minutes.

A more recent paper by Kuster et al. (2021) used observations by KOUN for downburst precursor analysis. In this study, the authors detail the possibility and promise in using K_{DP} cores as a precursor signature to downbursts/microbursts at the surface (Kuster et al., 2021). Further research is ongoing to provide more observations of severe storms using PARs, and much focus has been to include dual-polarization observations from the ATD as well with the development and future deployment of the PAIR (Salazar et al., 2019) and Horus (Palmer et al., 2019).

1.2.3.3 Impact of PAR Data on Forecaster Decision Making

Finally, the impact and potential benefits to forecasters of rapid-scanning PAR data is an important research area if PARs are to be used operationally in the future. Much of the original concern was that the forecaster would become too inundated with information to effectively perform their duties with the use of rapid-scanning PAR technology. However, that is not necessarily the case. Four notable studies looked into this question deeply to see how forecasters performed using rapid-scanning PAR technology in an operational setting. These experiments operated under the name "Phased Array Radar Innovative Sensing Experiment (PARISE)," and they were held in 2010 (Heinselman et al., 2012), 2012 (Heinselman et al., 2015b), 2013 (Bowden, 2014; Bowden et al., 2015), and 2015 (Wilson et al., 2017).

The initial PARISE experiment in 2010 looked specifically at how well forecasters were able to warn on weak, short-lived tornadoes and involved comparing volumetric PAR data of 43 s to 4.5 min (Bowden, 2014; Heinselman et al., 2012; Bowden and Heinselman, 2016; Wilson et al., 2017). The forecasters that used the 43-s volume scans warned on an EF-1 tornado with a warning lead time of 11–18 min compared to the 0–6 min for the forecasters using the 4.5-min data (Bowden, 2014). Although the forecasters using rapid data did have longer warning lead times, they also had a higher false alarm ratio (FAR) which was of concern to the researchers (Heinselman et al., 2012; Wilson et al., 2017).

The concern about a higher FAR associated with the use of PAR data along with the small sample size lead to the 2012 PARISE which featured a new design of the experiment and increased number of cases for the participants (Heinselman et al., 2015b; Wilson et al., 2017). The main change was that forecasters worked individually on two weak tornadic and two non-tornadic cases using one minute PAR data (Bowden, 2014; Wilson et al., 2017). With the changes to the experiment, the median tornado warning lead time was 20 min, exceeding the EF0/EF1 warning lead time at the participants forecast offices (7 min) and NWS regions (8 min); furthermore, all but one participant had a FAR less than 0.5 indicating that the warning accuracy was better than random chance (Bowden, 2014; Heinselman et al., 2015b; Wilson et al., 2017).

The 2010 and 2012 PARISE experiments focused only on weak tornado events; thus, the 2013 PARISE experiment focused on warning decision processes during severe hail and wind events in order to understand how rapid updates impacted other severe warning decisions (Bowden, 2014; Bowden et al., 2015; Bowden and Heinselman, 2016). This experiment featured a control group (given 5-min updates) and an experimental group (given 1-min updates), and each group worked a simulated real-time event for a marginally severe hail event and a severe hail and wind event (Bowden, 2014; Bowden et al., 2015; Wilson et al., 2017). It was shown that the experimental group achieved a statistically significant increase in lead times with 21.5 min compared to the control group's 17.3 min (Bowden et al., 2015; Wilson et al., 2017).

The 2015 PARISE experiment looked to utilize information gathered in the previous three PARISE experiments and address limitations while also continuing to further researchers' understanding of forecasters' warning decision process (Wilson et al., 2017). The 2015 experiment had nine separate PAR cases observed by 30 participating forecasters with varying PAR update times ranging from 1 to 5 minutes (Heinselman et al., 2015a; Wilson et al., 2017). It was shown that the increasing temporal resolution showed the greatest benefit during the tornadic events; furthermore, there was a tendency for a longer initial warning lead times associated with severe wind and severe hail events (Wilson et al., 2017). The findings from these PARISE experiments show promise in forecasters' ability to leverage faster update times to provide longer warning lead times not only for tornadic events, but also severe hail/wind events, which is promising for warnings associated with rapidly evolving events such as microburst/downbursts (Bowden et al., 2015; Bowden and Heinselman, 2016; Wilson et al., 2017).

Over the course of all PARISE experiments, it was reported that forecasters were not cognitively overloaded; however, the was a slight increase in the cognitive workload due to temporal resolution (Heinselman et al., 2015a; Wilson et al., 2017). However, Wilson et al. (2017) further concluded that cognitive workload would rarely reach the excessive level for forecasters, and if the cognitive workload did reach the excessive level, it was not necessarily due to the influx of radar data with fast temporal resolution.

1.3 Microbursts

1.3.1 Microburst History

In the late 1970s and into the 1980s, Ted Fujita spent considerable time performing aerial surveys of the "effect of diverging winds" caused by thunderstorms (Fujita, 1981; Wakimoto, 2001). These winds were associated with strong, intense winds related to downdrafts as defined by Byers and Braham (1949). However, it was not until a couple decades later that the meteorology community and public would get a new term associated with downdrafts when Miller (1972) would define a "downrush" in his "Glossary of Selected Terms". Now, Ted Fujita argued that the term "downrush" implies that the winds are stronger than those associated with a "downdraft" defined in The Thunderstorm by Byers and Braham (1949) (Fujita, 1981). However, even after Miller (1972) coined the term "downrush", there was still not a term that was used to define an "extremely intense" downdraft similar to how an "extremely intense" or "damaging" tropical cyclone is termed a hurricane once a certain wind speed threshold is reached (Fujita and Caracena, 1977). Fujita (1976) and Fujita and Byers (1977) proposed the use of the term "downburst" when the "downdraft speed becomes comparable to or greater than the approximate rate of descent or climb of a jet aircraft [which is about 3.6 m s^{-1}] on the final approach or takeoff at 91 m (300 ft) above the surface" (Fujita, 1981; Fujita and Caracena, 1977). This definition would place a "downburst" into the uppermost category of "extremely intense" downdrafts, and this new term would carry the full weight of being associated with words like "strong", "intense", or "damaging" especially to aircraft operation near the surface.

One question that this raises is why was the term "downburst" dependent upon the rate of descent or climb of a jet aircraft? Well, the answer lies within the looking back into the 1970s and 1980s at a notable near miss and other airline accidents. On 1 August 1983, 2 years and 122 days after John Hinckley Jr. attempted to assassinate President Ronald Reagan, President Reagan was arriving at Andrews Air Force Base in Air Force One and landed at 1404 EDT on a dry runway (Samenow, 2013; Smith, 2014; van der Voort, 2021).

About five minutes later (1409:20 EDT), the winds began to increase from the northeast, and they reached a peak of greater than 61 m s^{-1} at 1410:45 EDT. As the eye of the microburst passed over the anemometer, wind speeds rapidly decreased to about 2 kts. Finally, as the back side of the microburst passed over the anemometer, the second wind peak occurred at 1413:40 EDT with winds from the southeast (Fujita, 1985; Wakimoto, 2001; Samenow, 2013; Smith, 2014). The President, passengers, and crew of Air Force One were extremely lucky that day for missing a microburst while trying to land at Andrews Air Force Base; however, others were not so lucky. Table 1.1 showcases 11 such airliner accidents from 1973 through 1994, with the majority happening prior to 1986. These 11 accidents were devastating because of the death toll and amount of lives changed through injuries or loss of loved ones. Sadly, it was not until the widely publicized crash of Delta Flight 191 in Dallas/Fort Worth on 2 August 1985 that the FAA began to quickly promote the generation of algorithms and trainings that could help pilots and air traffic controllers detect the threat of "wind shear", or "downbursts", in and around airports (Samenow, 2013; Smith, 2014).

Table 1.1: Details of 11 notable airline crashes that occurred between 1973 and 1994. *8 persons were killed on the ground when the airliner crashed making the death toll greater than the number of passengers and crew on board.

Date	Flight	Airport	Passengers	Injuries	Deaths
23 Jul. 1973	Ozark Airlines 809	St. Louis Lambert	44	6	38
30 Jan. 1974	Pan Am 806	Pago Pago	101	4	97
24 Jun. 1975	Eastern 66	JFK Airport	124	11	113
7 Aug. 1975	Continental 426	Denver-Stapleton	143	0	0
23 Jun. 1976	Allegheny 121	Philadelphia	106	86	0
3 Jun. 1977	Continental 63	Tuscon	91	0	0
9 Jul. 1982	Pan Am 759	New Orleans	145	-	153*
11 Jan. 1984	USAir 183	Detroit Metro.	56	10	0
31 May 1984	United 663	Denver-Stepleton	105	0	0
2 Aug. 1985	Delta 191	Dallas/Ft. Worth	152	25	136
2 Jul. 1994	USAir 1016	Charlotte-Douglas	57	20	37
		Total	1,124	162	564

With downbursts formally coming on the radar for many in the meteorology and aviation community, much more work was done to better understand and detect this phenomenon that can be so devastating to human activities - especially aviation. During this research period, the research of earlier scientists like Ted Fujita, John McCarthy, Roger Wakimoto, Fernando Caracena, and Horace Byers - just to name a few - was vital to further our understanding of downbursts because they had laid the ground work for newer research to flourish. These five scientists are responsible for some of the earliest avoidance procedures for dealing with downbursts and are responsible for much of our understanding and conceptual models.

1.3.2 Microburst Conceptual Models from Early Observations

Now, downbursts are a type of severe thunderstorm wind, and there are multiple different types of severe thunderstorm winds on varying different temporal and spatial scales. The downburst itself is within a broader scaling system of severe thunderstorm winds that Fujita observed during aerial surveys that were the foundation for some of his papers in the early 1980s (Fujita, 1981; Fujita and Wakimoto, 1981). In them, the downburst corresponds to a Meso-β feature, and it is at this point in history where the term "microburst" was coined as "a misoscale downburst with is horizontal dimension $<$ 4 km" (Fujita, 1981; Fujita and Wakimoto, 1981; Wakimoto, 1985) (Figure 1.3). A few years later, Wilson et al. (1984) added to this definition by also requiring radar measured differential velocity signatures across the divergent center to be greater than 10 m s^{-1}.

An important goal of the meteorological community is being able to conceptualize the complex nature of the atmosphere and its phenomena. This is no less true when it comes to microbursts. One of the earliest conceptual models was put together by Ted Fujita (1985) (Figure 1.4). In Figure 1.4, one can see the stages of the microbursts as it transitions from a "Midair Microburst" to a "Surface Microburst". A "midair microburst" is when a microburst has the characteristic winds located above anemometer heights, and it can

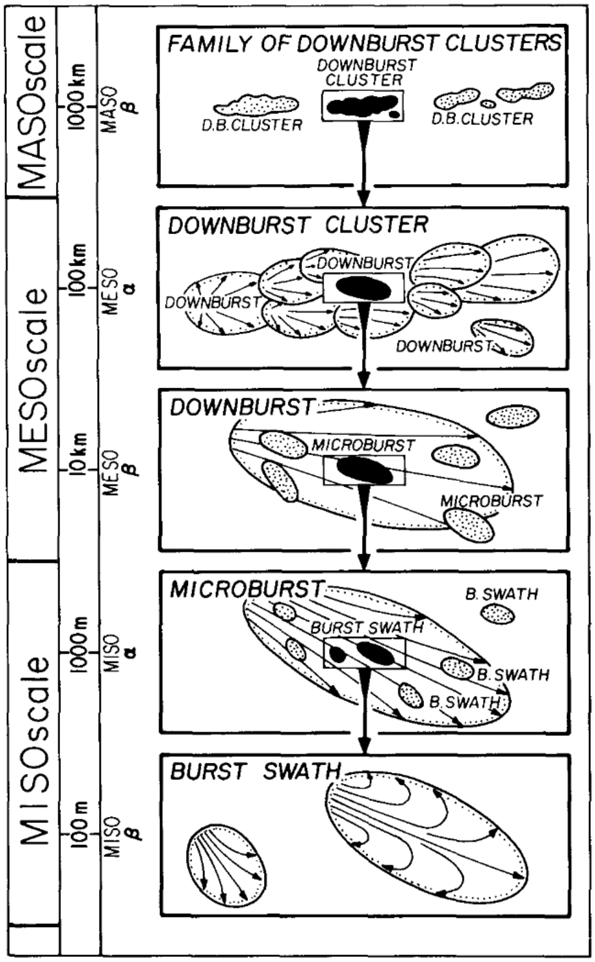

Figure 1.3: Figure 1 from Fujita (1981) classifying downburst damage patterns into 5 scales ranging from maso-β to miso-β. The microbursts are considered to be miso-α scale and often occur without a parent downburst.

dissipate while still aloft or continue its descent toward the surface (Fujita, 1985). Once the microburst reaches the surface, it is called a “surface microburst” and begins to spread out to maintain mass continuity and the conservation of momentum. Thus, this is a prime example of a conceptual model helping us observe pheonomena such as mass continuity and the conservation of momentum.

However, microbursts can be split into two different types depending upon the amount of rainfall and peak radar reflectivity factor value associated with the specified storm cell (Rodi et al., 1983; Wolfson, 1983; Caracena et al., 1983; Wilson et al., 1984; Wakimoto, 1985; Atkins and Wakimoto, 1991; Wakimoto, 2001). A dry, or low-reflectivity, microburst

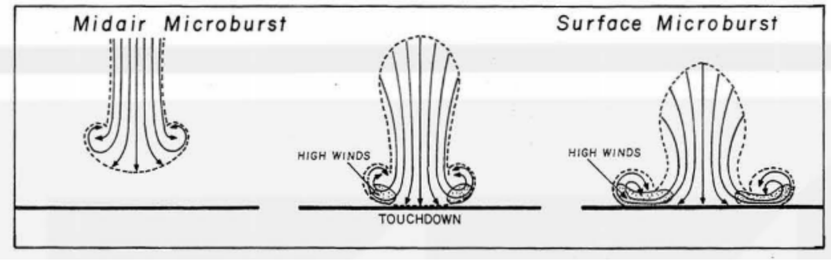

Figure 1.4: Figure 5.4 from Fujita (1985) showing a conceptual model for microburst structure irrespective of wet or dry classification.

is associated with little rainfall (less than 0.25 mm), have a peak radar reflectivity factor value of $<$ 35 dBZ, and are observed with virga shafts (Wakimoto, 1985; Atkins and Wakimoto, 1991; Wakimoto, 2001). However, a wet, or high-reflectivity, microburst is associated with more rainfall (more than 0.25 mm), has a peak radar reflectivity factor value of $>$ 35 dBZ, and are observed with intense precipitation (Wakimoto, 1985; Atkins and Wakimoto, 1991; Wakimoto, 2001). The general observational differences of these microbursts was detailed by Ted Fujita (1985) (Figure 1.5).

Generally speaking, either type of microburst can occur when the environmental conditions as met. Thus, dry and wet microbursts can occur anywhere that convection occurs, and the main factor that would drive regional variations is moisture availability. Regions that experience high moisture content would be less likely to experience dry microbursts as opposed to wet microbursts. However, the opposite is also true that environments with lower moisture are less likely to experience wet microbursts as opposed to dry microbursts. No study has been found describing regional variability between the two microburst types in great detail. However, previous studies have shown that both wet and dry microburst can be observed in the High Plains (Fujita, 1985; Wakimoto, 1985; Hjelmfelt, 1987; Walter, 2007) and Desert Southwest (Kuster et al., 2021). Other studies have shown wet microbursts also appear in the Southern Plains (Walter, 2007; Heinselman et al., 2015a; Kuster et al., 2021) and Southeastern US (Atkins and Wakimoto, 1991; Kingsmill and Wakimoto, 1991; Kuster et al., 2021).

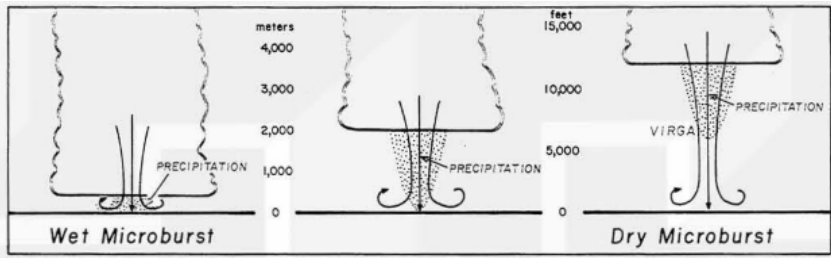

Figure 1.5: Figure 5.5 from Fujita (1985) displaying the general observational differences between both wet (left panel) and dry (right panel) microbursts.

Wet and dry microburst terminology can be confusing as both can be associated with precipitation, but they occur in different environments and are driven by different physical processes and mechanisms (Wakimoto, 1985). Thus, it is important to understand the environments surrounding each microburst type in order to fully understand the potential for one to occur. There are certain tools that can be used to help determine if an environment is favorable for a certain type of microburst to form such as atmospheric soundings and relative humidity levels below the cloud base (Brown et al., 1982; Fujita, 1983; Fujita and Wakimoto, 1983a,b; Wakimoto, 1985). However, forecasting advice is traditionally location/region specific due to many factors that can greatly impact the potential of microburst formation. Nevertheless, some generalizations can be made about favorable environments for microbursts to occur.

For dry microbursts, they are typically associated with marginal instabilities in reasonably dry environments, which result in weak convection (Wakimoto, 2001). Forecasts for the possibility of dry microbursts can typically be made using the 1200 UTC sounding, expectations of solar heating, and the forecasted maximum surface temperatures (Wilson et al., 1984; Johns and Doswell, 1992). According to Wakimoto (1985), which looked at microburst over the High Plains near Denver, CO, a favorable environment for dry micorburst development has the following four criteria:

- Shallow morning radiation inversion at the surface beneath a deep dry-adiabatic layer,

- The dry-adiabatic layer extends to approximately 500 mb,
- Mean subcloud mixing ratio should be approximately 3–5 g kg^{-1} along with the presence of midlevel moisture, and
- The convection temperature must be reached during the day.

Wet Microbursts, on the other hand, typically occur in weakly capped environments with high moisture throughout a deep surface-based layer (Wakimoto, 2001). Forecasts for the possibility of wet microbursts can generally be made using the 1200 UTC sounding and predicted moisture and thermal advection patterns. Atkins and Wakimoto (1991) have shown that using vertical profiles of equivalent potential temperature can be useful in identifying possible environments that could support wet microbursts. Ellrod (1989) showed that vertical soundings from radiance measurements from the Geostationary Operational Environmental Satellite (GOES) satellite can be useful in detecting moisture and thermal advection patterns that could lead to wet microburst environments. According to Mackey (1998) and Atkins and Wakimoto (1991), environments favorable to wet microburst formation generally can be found by looking at $\Delta\theta_e$ which is defined as the difference between the equivalent potential temperature at the surface and the equivalent potential temperature minimum in the midlevels. The breakdown of $\Delta\theta_e$ values are:

- $\Delta\theta_e \leq 15$ K - low threat,
- 15 K $< \Delta\theta_e <$ 25 K - moderate threat,
- $\Delta\theta_e \geq 25$ K - high threat.

When looking at specific atmospheric soundings associated with microbursts, Figure 1.6 shows three different examples of atmospheric soundings that were assocaited with microbursts. First, panel a) is a prime example of a dry microburst sounding profile from Tucson, AZ at 0000 UTC on 8 July 2015. The important things to notice here is the inverted “V” stretches from the surface up to above 700 mb, the overall profile is very dry, and there

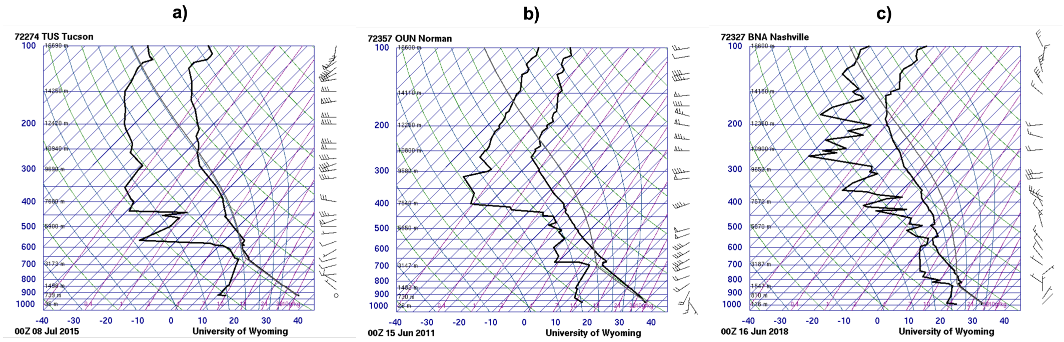

Figure 1.6: Example soundings of microburst environments (University of Wyoming, 2021) with the black lines representing temperature (right) and dewpoint temperature (left) and the grey lines representing a theoretical parcel path. Panel a) shows an ideal dry microburst sounding over Tucson, AZ at 0000 UTC on 8 July 2015. Panel c) shows an ideal wet microburst sounding over Nashville, TN at 0000 UTC on 16 June 2018. Panel b) shows an in between sounding over Norman, OK at 0000 UTC on 15 June 2011.

are marginal instabilities along the parcel path. Second, panel c) is a prime example of a wet microburst sounding profile from over Nashville, TN at 0000 UTC on 16 June 2015. The environment is weakly capped, a large amount of instability under the parcel path, and is relatively moist throughout the sounding; however, the inverted “V” at the surface is still present although much shallower compared to the dry microburst sounding in panel a) of Figure 1.6. Finally, panel b) is an in between sounding that represents an environment between an ideal wet or dry microburst environment. Something to notice here is that there is more moisture below 500 mb in this sounding compared to the dry microburst sounding in panel a), but there is less moisture than the one in panel c). Furthermore, the instability is also in between the extremely weak instabilities in panel a) and the strong instabilities in panel c), and there is a stronger cap in panel b) than there is in panel c). Thus, depending on the type of convection that occurs in this environment, it could be possible to get either a wet or dry microburst in this environment depending on how this environment changed in time. Table 1.2 provides a summary of the environmental and observation difference between dry and wet microbursts.

Table 1.2: Summary of environmental and observational differences between wet and dry microbursts.

Parameter Type	Parameter	Dry Microbursts	Wet Microbursts
Environmental	Moisture Location	$\geq$ 650 mb	Throughout
	Mixed-Layer	Surface to 500 mb	surface to 800 mb
	Instability	Marginal	Strong
Observational	Z_h Value	$<$ 35 dBZ	$>$ 35 dBZ
	Rainfall Amount	$<$ 0.25 mm	$>$ 0.25 mm
	Visible Observation	Virga Shafts	Intense Precipitation

1.3.3 Radar Observations

Microbursts can be associated with many different radar observations in both single- and dual-polarization radar variables. Most radar observations are much more prevalent for wet microbursts because of the large amounts of hydrometeors that are present within the storm cell accompanying strong to intense convection.

For a wet microburst, radar signatures can occur in both single and dual-polarization radar variables. The variables that will be analyzed within this project include Z_h, v_r, and K_{DP}. According to Doviak and Zrnic (1993), reflectivity factor is defined as the "sixth power of the hydrometeor diameter summed over all hydrometeors in a unit volume", and is represented by:

$$Z_h = \int_0^\infty N(D)D^6 dD. \tag{1.1}$$

where D represents the hydrometeor diameter, $N(D)$ represents the drop size distribution associated with each hydrometeor diameter within a unit volume, and dD represents an infinitesimally small change in hydrometeor diameter.

Furthermore, from Doviak and Zrnic (1993), radial velocity is defined as the first moment of the Doppler spectrum of the signal received by the radar, and is represented by:

$$V_r(\boldsymbol{r_0}) = \int\int\int v(\boldsymbol{r_1})\eta(\boldsymbol{r_1})I(\boldsymbol{r_0},\boldsymbol{r_1})dV_1 \Big/ \int\int\int \eta(\boldsymbol{r_1})I(\boldsymbol{r_0},\boldsymbol{r_1})dV_1 \tag{1.2}$$

where $I(\boldsymbol{r_0}, \boldsymbol{r_1})$ is the illumination function, $\boldsymbol{r_0}$ is the center of the resolution volume, $\boldsymbol{r_1}$ is some point within the resolution volume, $\eta(\boldsymbol{r_1})$ is the reflectivity, $v(\boldsymbol{r_1})$ is the point velocity, and dV_1 is the differential over the resolution volume.

Finally, K_{DP} is defined as a difference between the propagation constants for horizontally and vertically polarized electromagnetic waves as in Sachidananda and Zrnic (1986), and is represented by:

$$K_{DP} = \frac{\hat{\phi}_{DP}(r_n) - \hat{\phi}_{DP}(r_m)}{(r_n - r_m)} \qquad \text{rad} \quad \text{km}^{-1} \tag{1.3}$$

where $\hat{\phi}_{DP}$ is estimates of differential phase shift and r_n and r_m are the ranges of the differential phase shift estimates. Each variable has unique precursor signatures that are observed before the microburst reaches the surface; thus, these signatures can provide some warning to when a microburst might occur at the surface.

The most characteristic signature of a microburst is the diverging wind signature at the surface (seen in the lowest elevation angle, typically 0.5°). By definition, this signature needs to be ≥ 10 m s^{-1} in magnitude across an area of no more than 4 km to be classified as a microburst (Atkins and Wakimoto, 1991; Wakimoto, 2001). However, this signature only indicates that a microburst is ongoing.

The other important radial velocity signature associated with microbursts is the precursor of midlevel convergence that occurs within the storm (Figure 1.7) (Wakimoto and Bringi, 1988; Wakimoto, 2001; Heinselman et al., 2008; Vasiloff and Howard, 2009; Kuster et al., 2016). Generally speaking, previous studies have looked for mid-level convergence between heights of 1 km and 6 km above ground level (AGL) (Vasiloff and Howard, 2009; Kuster et al., 2016). This signature is believed to be a mass continuity response as the microburst begins its decent toward the surface. The descending air associated with the microburst is vacating a region, which must be filled in by surrounding air causing the convergence above the descending air column in order to maintain mass continuity.

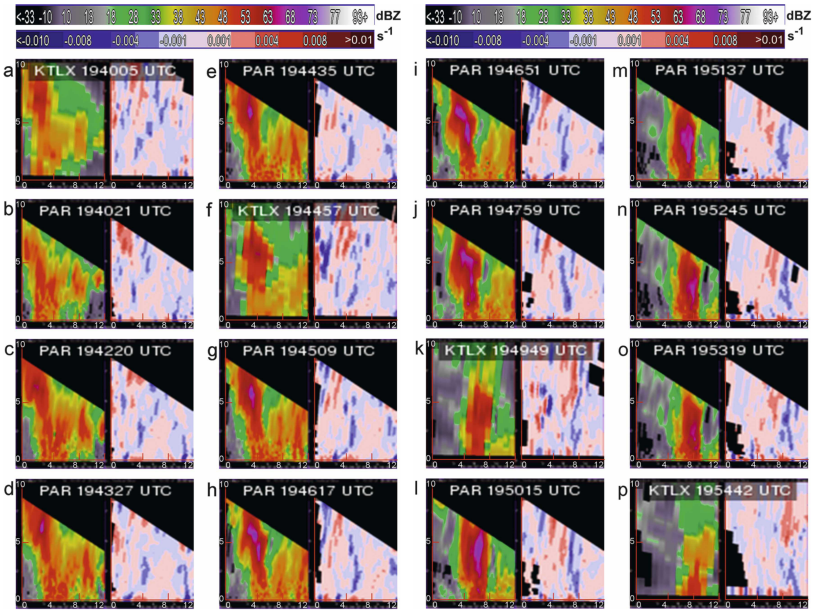

Figure 1.7: A combined Figure 5 from Heinselman et al. (2008) showing a descending reflectivity column along with co-located mid-level convergence for a microburst on 10 July 2006.

Looking at reflectivity factor (Z_h), the characteristic precursor signature is a descending reflectivity column (DRC) (Figure 1.8). As defined by Kuster et al. (2016), a DRC develops at an altitude of at least 5 km, descends to the surface, and corresponds to a near-surface divergence signature. The DRC signature is an indication of hydrometeor loading and is believed to be the starting mechanism for wet microbursts, which is then continued through melting and evaporative cooling (Atkins and Wakimoto, 1991; Wakimoto, 2001; Atlas et al., 2004; Vasiloff and Howard, 2009; Kuster et al., 2016, 2021). In his paper, Isaminger (1988) discussed that DRCs were assocaited with 95% of downbursts that were analyzed within the study, and Roberts and Wilson (1989) indicated that a DRC was associated with 88% of the downbursts within their study. Now, it is important to note that many have noticed that the DRC and midlevel convergence signatures are related, and the midlevel convergence should be associated with the DRC as it is associated with a downdraft (best seen in panel j of Figure 1.7 between 4 and 8 km range and 0 to 5 km AGL) (Roberts and Wilson, 1989; Vasiloff and Howard, 2009; Kuster et al., 2016).

While there are many dual-polarization signatures that can be analyzed, only the K_{DP} core will be analyzed within this study (Figure 1.9. K_{DP} has a very robust relationship to liquid water content, and this relationship can be exploited in the detection of wet microbursts (Kuster et al., 2021). A K_{DP} core can be indicative of hydrometoer loading and the rapid descent of melting ice below the environmental melting layer associated with a downdraft capable of producing a microburst (Kuster et al., 2021). In their paper, Kuster et al. (2021) look at changes in K_{DP} core median and maximum values as well as the size of the core for all K_{DP} values $\geq 1.0^{\circ}$ km^{-1} at the elevation angle closest to the environmental melting layer.

1.4 Goals

The main goal of this project is to develop a framework and tool set to analyze how different radar scanning techniques observe and detect microbursts and their precursor signatures. A proof-of-concept analysis of a single wet microburst is performed as a way to showcase the information that can be gathered from using this framework and tool set. Most notably, the tools developed herein look to quantitatively measure different microburst precursor signatures and compare how they are observed by different radar scanning techniques. Furthermore, the quantitative metrics developed herein could be exploited for use in the development of adaptive scanning algorithms using PARs.

In order to provide an example of how this methodology and tool set can be utilized, a proof-of-concept analysis is performed. The scanning techniques analyzed herein are related to potential strategies that could be employed by a future PAR network - or more directly by the Horus radar - and comparing them to conventional scanning strategies like the VCPs associated with WSR-88Ds. More specifically, this project will compare a pseudo-RHI from VCP 212, a traditional RHI (hereafter referred to as true RHI), and three atmospheric imaging scans at different spoiled transmit beamwidths. These scanning strategies will be compared on the basis of both qualitative observations and quantitative metrics associated with microburst precursor signature detection and evolution in time (as discussed in Section 2.3.2). The baseline scanning strategy will be set as VCP 212 as it represents the current operational capabilities of the NEXRAD system. The true RHI and imaging scanning strategies represent potential options on an operational PAR system.

The data used for this proof-of-concept analysis is a single microburst producing storm generated from a numerical weather prediction (NWP) simulation. The radar emulator, RSim, is used to emulate the different radar scanning strategies. RSim reads in pre-calculated dual-polarization variables and then applies the range weighting function and desired antenna pattern to the data to emulate the radar data. The variances of the radar variable estimators are calculated in order to introduce errors associated with estimation processes into the idealized NWP simulations. The process and methodology behind this is discussed in Section 2.3.1. This error analysis is believed to show that these results herein are applicable to real-world examples where estimation errors are present.

Using the NWP data along with RSim, the goals of this project are to:

- Introduce a methodology and framework for analysis of how PAR scanning strategies observe and detect microbursts and their precursor signatures,
- Provide metrics to quantify the size, shape, and intensity of microburst precursor signatures, and
- Perform a proof-of-concept analysis showcasing how the methodology and tools can be utilized.

The framework and tool sets developed in this research are detailed in Chapter 2. The proof-of-concept analysis will be detailed in the results and discussion of this project presented in Chapters 3 and 4, respectively. Finally, a summary of the conclusions of this paper and the implications of this research moving forward are detailed in Chapter 5.

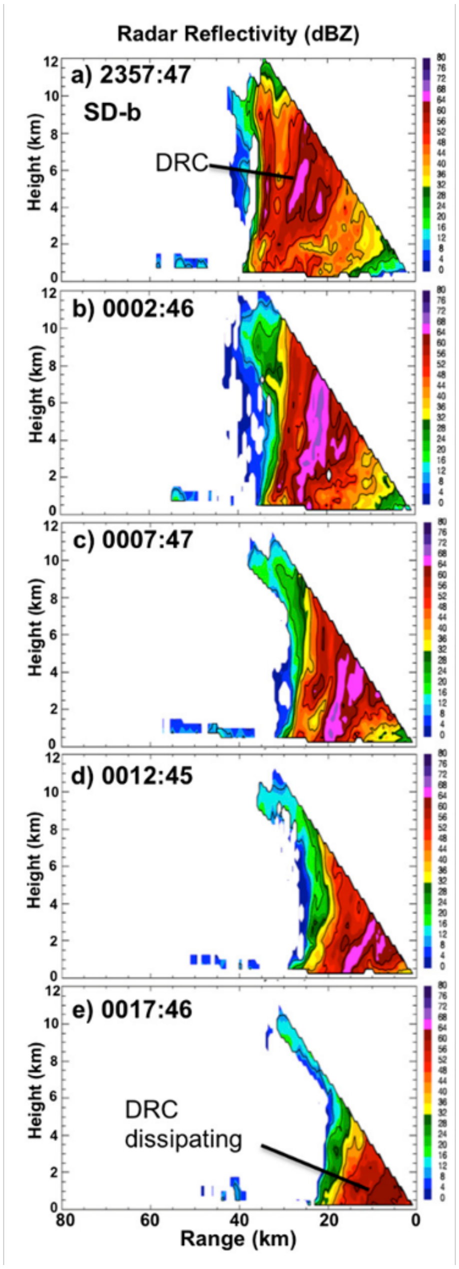

Figure 1.8: Figure 10 from Kuster et al. (2016) showing the descent of a reflectivity column with values $\geq$ 60 dBZ.

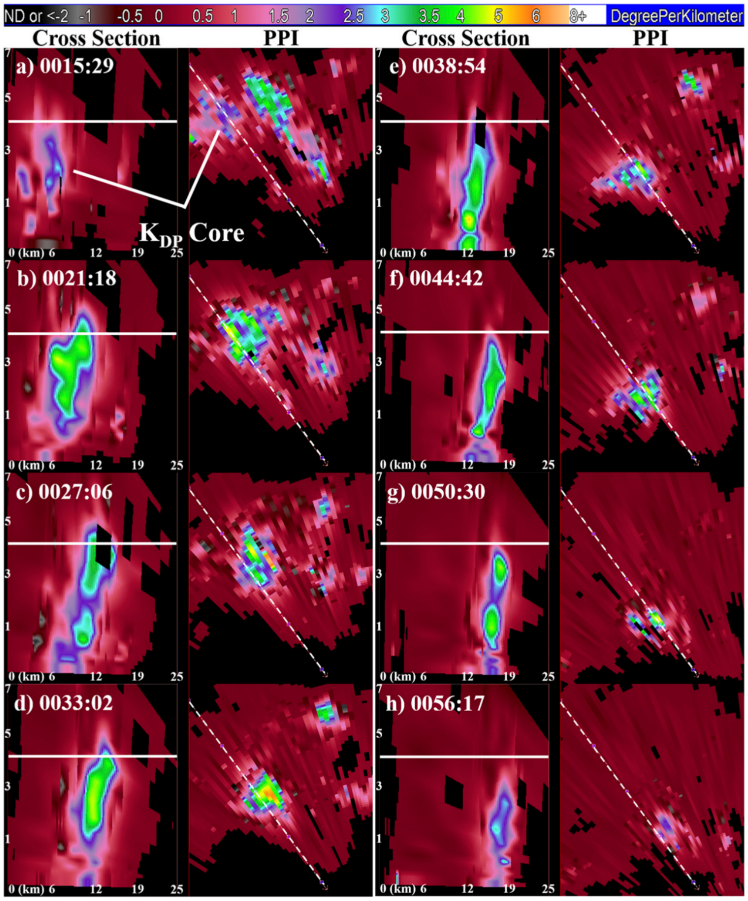

Figure 1.9: Figure 10 from Kuster et al. (2021) showing both PPIs and vertical cross-section images of a K_{DP} core associated with a microburst on 10 June 2018 using the KBMX WSR-88D radar.

Chapter 2

Data and Methods

The framework and tools developed in this project will be described below through a proof-of-concept analysis of a single wet microburst case. A flowchart of the developed framework is depicted in Figure 2.1. First, NWP simulations are utilized to generate a microburst producing storm which outputs pure hydrometeor mixing ratios and number concentrations (q, n), individual wind components (u, v, w), and eddy dissipation rate (ε). The NWP data is then used to calculate the radar variables including Z_h, Z_v, and K_{DP} and interpolate all variables onto a spherical coordinate system using a nearest neighbor method. These radar variables - along with the other variables such as u, v, w, and ε - are read in by RSim to emulate the desired scanning strategy. Once the emulations are complete, error analysis is performed to generate different sets of error that can be added into the pure data from the emulations. After these errors sets are generated, analysis is performed on each combined data set (pure data plus errors), and further errors analysis is performed between the errors from each error set.

2.1 CM1

One wet microburst was generated using the Cloud Model 1 (CM1) version 20.2 released on October 18, 2020 by National Center for Atmospheric Research (NCAR) (Bryan and Fritsch, 2002; Bryan, 2020). The microburst was generated on a uniform horizontal resolution of 250 m and extended a total of 200 km in the x and y directions (±100 km in each direction from the origin at $x = 0$ and $y = 0$). The vertical grid spacing was stretched, and it ranged from 50 m under 3 km AGL to 550 m above 9 km AGL with a total vertical extent reaching 20 km AGL. Temporally, outputs were generated every 10 s to capture as much of the evolution as possible while balancing computational complexity.

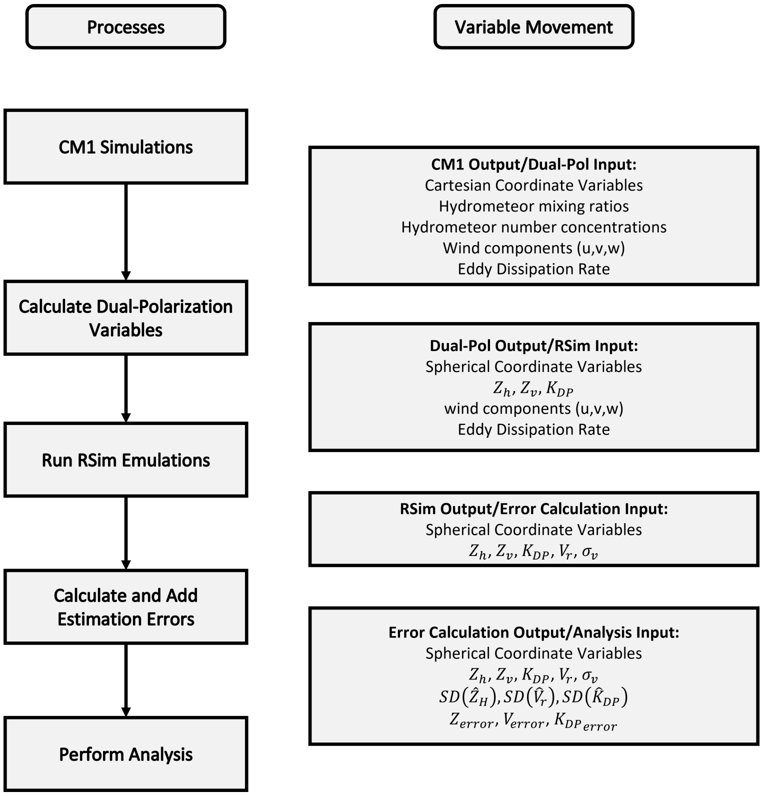

Figure 2.1: High-level flowchart of the framework developed in this work. The order of the processes are on the left column and the output/input variables for each step are on the right. Each variable movement box is located in between the two processes it corresponds to (i.e., the variable movement box has the output from the above process and the input to the process below it).

The model was run as a Large-Eddy Simulation with the Morrison double-moment microphysics scheme which outputs number concentrations and mixing ratios of rain, snow, cloud ice, and hail, and the large-ice category was set to hail. Mixed-phase precipitation is not explicitly represented in the model's output but was added into the data before radar emulation and are detailed in Section 2.2.1.1. No planetary boundary layer parameterization was used. The horizontal boundary conditions were radiatively open and the top and bottom boundary conditions were free-slip. The atmospheric sounding used was obtained from the University of Wyoming's archived atmospheric sounding data (University of Wyoming, 2021).

The one microburst simulation used herein was a wet microburst and was generated using an atmospheric sounding from KBNA, Nashville, Tennessee, at 0000 UTC on 16 June 2018 (from now on known as KBNA). On 16 June 2018, there was a microburst that occurred in the Green Hills area of Nashville, TN (NWS Nashville, 2018). Severe hazards associated with the microburst that occurred included 0.25-in hail and strong winds resulting in downed trees (NWS Nashville, 2018).

2.2 RSim

In order to test how different scanning strategies would observe the microburst generated with the CM1 models, a radar emulator was required. For this project, the radar emulator RSim was used and modified (Mahre, 2020). RSim was used to emulate radar data using the following scanning strategies: pseudo-RHIs from VCP 212, true RHIs from the PAR, and atmospheric imaging with spoiled beams of 2.5°, 5°, and 10° in elevation. A pseudo-RHI is defined as an RHI that is generated from combining different PPI elevations into an RHI image.

RSim reads in single- and dual-polarization data (Z_h, Z_v, K_{DP}) along with other variables (u, v, w, ε) in spherical coordinates to perform the emulations. Once these variables are read in, RSim then applies the range weighting function and two-way beam patterns associated with the desired scanning strategy which results in emulated values of Z_h, Z_v, K_{DP}, and V_r. Finally, RSim calculates additional variables such as σ_v, signal power (S), and Signal-to-Noise Ratio (SNR) before saving all data into an individual file for each VCP update time.

The benefits of RSim are numerous in that it can provide great flexibility to use different scanning strategies with the same input data to test how certain scanning strategies change how the radar is viewing the exact same storm. One potential problem with the RSim framework is that it does not actually use independent scatterers, as seen in emulators like SimRadar; however, the output from RSim has proven to still be realistic from both a meteorological and engineering viewpoint (Cheong et al., 2017; Mahre, 2020). RSim is further limited as it is unable to simulate impacts of signal processing such as ground clutter filtering nor is it able to more realistically simulate estimation errors. Despite these limitations, RSim is sufficient for the purpose of this study as it has be shown that RSim can accurately represent the model environment and equivalent estimation errors can be added into the data afterwards in post processing (Mahre, 2020).

2.2.1 RSim Modifications

RSim was modified from its original version to operate on CM1 model output instead of relying solely upon Weather Research and Forecasting (WRF) model data as an input (Bryan, 2020). These changes ranged from minor optimization modifications to completely reworking some of the scanning strategies and dual-pol calculations. The major modifications will be detailed below.

2.2.1.1 Dual-Polarization Calculations

One of the significant modifications of RSim was allowing it to ingest dual-polarization variables instead of calculating them on the fly during the emulation process. Calculating the dual-polarization variables before running the RSim code was paramount to reduce computational complexity because these calculations can become burdensome and time-consuming, especially when dealing with fine temporal and spatial resolution model data. Furthermore, in a break with previous work with RSim, the dual-polarization calculations were done using both a Rayleigh scattering approximation and T-Matrix lookup tables (Mishchenko, 2000). The use of the T-Matrix lookup tables was only for the rain classification, which is realistically similar between the two categories. This decision was made as there were errors in using the Rayleigh scattering approximation when dealing with small mixing ratios combined with large number concentrations of rain that led to extremely negative and positive values that were not realistic. The T-Matrix calculations were much more realistic in the areas associated with small rain mixing ratios combined with large rain number concentrations and were very similar in structure and magnitude of the other variables (Z_h, Z_v, K_{DP}). This was also done for simplicity and efficiency purposes, but are not believed to greatly impact the data as the Rayleigh approximation only breaks down for large hail. As described in Jung et al. (2008), the main limitation to using this assumption is an overestimation of the radar cross section for large hailstones, which can lead to an overestimation of reflectivity factor values.

Mixed-phase precipitation was incorporated into the data set to better represent more realistic environmental characteristics associated with microbursts. It has been shown that mixed-phase precipitation contributes to the generation of strong microbursts (Srivastava, 1987; Wakimoto and Bringi, 1988; Vasiloff and Howard, 2009; Amiot et al., 2019; Kuster et al., 2021). However, the CM1 model simulation, detailed in Section 2.1, was only run with a double-moment microphysic scheme. Therefore, generation of mixed-phase precipitation was added into the data via a similar method to the one described in Jung et al. (2008, 2010). The only difference herein is the T-matrix and Rayleigh scattering are combined where they were independent of each other in Jung et al. (2008, 2010).

The dual-polarization calculations were performed for Z_h and Z_v along with K_{DP}. The generic Rayleigh scattering equations used to calculate the three variables of interest from Jung et al. (2008, 2010) are:

$$Z_{h,x} = \frac{4\lambda^4 \alpha_{xa}^2 N_{0x}}{\pi^4 |K_w|^2} \Lambda_x^{-(2\beta_{xa}+1)} \Gamma(2\beta_{xa}+1) \qquad (\mathrm{mm}^6\mathrm{m}^{-3}) \tag{2.1}$$

$$Z_{v,x} = \frac{4\lambda^4 \alpha_{xb}^2 N_{0x}}{\pi^4 |K_w|^2} \Lambda_x^{-(2\beta_{xb}+1)} \Gamma(2\beta_{xb}+1) \qquad (\mathrm{mm}^6\mathrm{m}^{-3}) \tag{2.2}$$

$$K_{DP,x} = \frac{180\lambda}{\pi} N_{0r} \alpha_{xk} \Lambda_r^{-(2\beta_{xk}+1)} \Gamma(\beta_{xk}+1) \qquad (^\circ\mathrm{km}^{-1}) \tag{2.3}$$

where λ is the radar wavelength in radar wavelength (in mm); Γ is the complete gamma function; N_{0x} is the intercept parameter; Λ_x is the slope parameter that is diagnosed from the mixing ratio of each hydrometer species; K_w is the dielectric factor for water; and α_{xa}, α_{xb}, β_{xa}, and β_{xb} are coefficients of the power-law form of the particle size D (mm) of the backscattering amplitudes of different hydrometeor species. For the purposes of this research, the values for "dry" hydrometeors (rain, dry snow, and dry hail) are the same as those found in Jung et al. (2008), and the coefficients for mixed-phase precipitation can be found by using:

$$\alpha_{rsa} = (0.194 + 7.094 f_w + 2.135 f_w^2 - 5.225 f_w^3) * 10^{-4} \tag{2.4}$$

$$\alpha_{rsb} = (0.191 + 6.916 f_w - 2.841 f_w^2 - 1.160 f_w^3) * 10^{-4} \tag{2.5}$$

$$\alpha_{rha} = (0.191 + 2.39 f_w - 12.57 f_w^2 + 38.71 f_w^3 - 65.53 f_w^4 + 56.16 f_w^5 - 18.98 f_w^6) * 10^{-3} \tag{2.6}$$

$$\alpha_{rhb} = (0.165 + 1.72 f_w - 9.92 f_w^2 + 32.15 f_w^3 - 56.0 f_w^4 + 48.83 f_w^5 - 16.69 f_w^6) * 10^{-3} \tag{2.7}$$

where the subscripts *rha* and *rhb* represent a mixture of rain and hail, the subscripts *rsa* and *rsb* represent a mixture of rain and snow, and f_w represents the water fraction relative to each species such that a generic formula f_w is given by:

$$f_w = \frac{q_r}{q_r + q_x} \tag{2.8}$$

where q_x can be the mixing ratio for either snow or hail.

The generic equations used for the T-Matrix calculations are also directly from (Jung et al., 2008, 2010). These equations are:

$$Z_{h,r} = \frac{4\lambda^4}{\pi^4 |K_w|^2} \int N(D) \left(A|f_a|^2 + B|f_b|^2 + 2C|f_a||f_b| \right) dD \qquad (\mathrm{mm^6 m^{-3}}), \tag{2.9}$$

$$Z_{v,r} = \frac{4\lambda^4}{\pi^4 |K_w|^2} \int N(D) \left(B|f_a|^2 + A|f_b|^2 + 2C|f_a||f_b| \right) dD \qquad (\mathrm{mm^6 m^{-3}}), \tag{2.10}$$

and

$$K_{DP,r} = \frac{180\lambda}{\pi} \int N(D) C_k Re(f_a - f_b) dD \qquad (^\circ\text{km}^{-1}), \tag{2.11}$$

where

$$A = \frac{1}{8}\left(3 + 4e^{-2\sigma^2} + e^{-8\sigma^2}\right), \tag{2.12}$$

$$B = \frac{1}{8}\left(3 - 4e^{-2\sigma^2} + e^{-8\sigma^2}\right), \tag{2.13}$$

$$C = \frac{1}{8}\left(1 - e^{-8\sigma^2}\right), \tag{2.14}$$

$$C_k = e^{-2\sigma^2}, \tag{2.15}$$

f_a and f_b are the backscattering amplitudes for polarizations along the major and minor axes respectively, the mean canting angle is assumed to be zero, and the standard deviation of the canting angle is assumed to be 10° for rain.

In order to include the contributions of mixed-phase precipitation and prevent very small numbers of wet hydrometeors from resulting in unreasonable drop-size distribution estimates, the following process was done. It was assumed that all snow and hail were both dry and mixed-phase such that $q_{rs} = q_s$ and $q_{rh} = q_h$. Using this method, the same slope and intercept parameters for the drop size distributions were used for both melting and dry precipitation. Once these values were calculated, the individual contributions of each hydrometeor species were then taken into consideration by multiplying each moment variables of each hydrometeor species by a weight that is directly related to f_x which represents the fraction of rain-snow or rain-hail mixture at each point of the model domain. This fraction is the same as F in Jung et al. (2008) while still assuming an $F_{max} = 0.5$, such that

$$f_x = F = F_{max}[min(q_x/q_r, q_r/q_x)]^{0.3} \tag{2.16}$$

where x can be either h for a rain-hail mixture or s for a rain-snow mixture. It is further assumed, along with Jung et al. (2008), that the maximum amount of mixed-phase precipitation allowed at each point in the model domain is 50%.

The weights for the mixed-phase precipitation are defined by the fraction $w_{rh} = f_h$ for the rain-hail mixture and $w_{rs} = f_s$ for the rain-snow mixture. The weights for the dry precipitation are equal to $w_h = 1 - f_h$ for hail, $w_s = 1 - f_s$ for snow, and $w_r = 1 - f_s - f_h$ for rain as it contributes to the mixed phase of both ice species. The weights for each hydrometeor species were applied while the variables were still in linear units for Z_h and Z_v and in degrees per kilometer for K_{DP}.

Once the dual-polarization variables were calculated, the data was interpolated onto a spherical coordinate system using a nearest-neighbor interpolation with an angular resolution of 0.5° in azimuth and elevation and a range resolution of 250 m. This was done so the model data are more closely related to the beam patterns that are applied through the radar emulator. Every variable used by the emulator gets interpolated onto the spherical coordinate system including Z_h, Z_v, K_{DP}, u, v, w, and ε. It is within this interpolation that the model domain is moved to place the microburst at the desired distance in range, and for simplicity, the microburst was moved such that it was always oriented south of the radar ($\approx 270°$ from the x-axis).

2.2.1.2 Spectrum Width Calculations

The other major change in RSim was a separate set of equations to calculate the turbulence component of spectrum width. The previous method used in Mahre (2020) was based upon equations from Nastrom and Eaton (1997):

$$\sigma^2_{turbc} = \frac{\varepsilon A^{3/2}}{N_{bv}} \tag{2.17}$$

where $A = 1.6$ is a Kolmogorov constant, N_{bv} is the Brunt-Vaisala frequency, and ε is the eddy dissipation rate given by

$$\varepsilon = \frac{k_z N_{bv}^2}{0.3} \tag{2.18}$$

where k_z is the vertical eddy diffusion coefficient. The problem with the above equations (2.17 and 2.18) is that they are valid under the assumption that the atmosphere is stably stratified. This implies that the Brunt-Vaisala frequency is real and non-zero (i.e., $N_{bv}^2 > 0$). This assumption breaks down in the presence of convection as the intense vertical motions can result in imaginary N_{bv} such that $N_{bv}^2 < 0$. Therefore, other equations had to be used in order to properly calculate the turbulence contribution of spectrum width.

The new approach involves using equations from Doviak and Zrnic (1993) in which the Brunt-Vaisala frequency is not even considered. Thus, the assumptions are valid within convection. The equation used for the spectrum width from turbulence is given by equation (10.68) from Doviak and Zrnic (1993):

$$\sigma_t^2 = \left(\frac{r \varepsilon \sigma_\theta A^{1.5}}{0.72} \right)^{2/3} \tag{2.19}$$

where r is the range in meters, $A = 1.6$ is a Kolmogorov constant, and σ_θ is the antenna pattern induced spectrum width. The antenna pattern induced spectrum width, σ_θ, is given by equation (5.75) from Doviak and Zrnic (1993):

$$\sigma_\theta = \frac{\theta_1}{4\sqrt{\ln(2)}} \tag{2.20}$$

where θ_1 is the beamwidth assuming a circularly symmetric Gaussian pattern. This is a fine assumption for a pencil beam that has a uniform beam width in both azimuth and elevation. However, for atmospheric imaging situations, θ_1 is calculated such that $\theta_1 = \sqrt{\theta_{el}\theta_{az}}$ where $\theta_{az} = 0.96^\circ$ for all situations since the beam is spoiled only in the vertical dimension. θ_{el} varies with spoiled beamwidth and is calculated by the 3-dB beamwidth of the one-way transmit beam.

2.2.2 Brief Review of RSim Operations

Once the dual-polarization variables have been calculated, the RSim code is then run. RSim reads in precomputed Z_H, Z_V, and K_{DP} along with u, v, and w winds in spherical coordinates. This data is used to calculate all desired variables within the sector of interest set by the user. The variables that are calculated by RSim include Z_H, K_{DP}, v_r, σ_v, and SNR. The emulation takes into consideration both antenna and range weighting functions. It derives the expected radar variables at each sampling point (using spherical coordinates - azimuth, elevation, and range) within the radar scan domain based upon the range and antenna weighting patterns. According to Mahre (2020), the range weighting pattern used in RSim are based upon those in Doviak and Zrnic (1993) and Orfanidis (2016); however, in another break with the RSim from Mahre (2020), the antenna weighting pattern is generated separately and then interpolated onto the data used for emulation (more will be discussed in Section 2.2.3.1). Because both 30 km and 90 km range cases are analyzed, the movement of the storm away from the radar was handled in the interpolation associated with the dual-polarization calculation (Section 2.2.1.1). Thus, RSim is not involved in this movement in any way.

2.2.3 Concept of Operations and Specifications

Now, to lay the foundation of the methodologies and tools developed herein, a rough concept of operations was developed to provide more information regarding the assumptions of the type of radar system being used.

The assumed radar architecture is a single-faced, mechanically rotating planar PAR that supports multiple scanning modes such as PPI and RHI options. The architecture used herein is related to the Horus radar. The Horus radar's scalability will eventually be exploited by the ARRC for larger systems, and the following architecture is just one example of one such system. This architecture has a similar structure to the Transportable PAR (TPAR) system with an example of the array geometry and is provided in Figure 2.2

(Palmer et al., 2022). The TPAR system provides a reasonable and realistic geometry for this work because, like a leading candidate to replace the operational NEXRAD network, the TPAR system is a rotating, 1° beamwidth, dual-polarization PAR. All beams that are generated using this array geometry and are either intrinsically calculated from the geometry or synthesized from it. It is assumed that the radar performs normally with a mechanical rotation rate of $24^{\circ}s^{-1}$ which provides a minimum update time of 15 s.

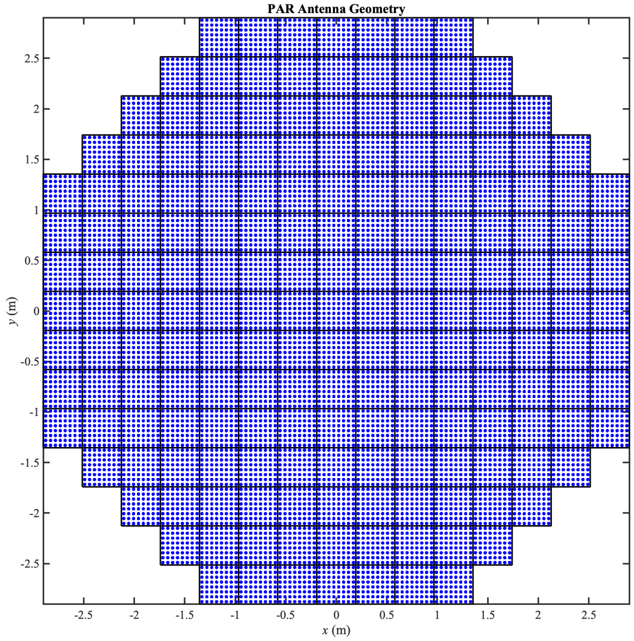

Figure 2.2: Antenna geometry for a TPAR configuration. Each black square is one of the 185 panels, and each blue dot represents a radiating element. The diameter of this configuration is 6 meters and has a total of 11,840 radiating elements.

Each scanning strategy was given the same baseline specifications within RSim so as to not impact the results (Table 2.1). The emulation was done at S-band (10.7 cm wavelength), and the volume update time for a full PPI volume varied as different scanning strategies were tested for effectiveness. However, because the vertical structure is the most important feature of microbursts and their precursor signatures, all emulations were done

Table 2.1: RSim radar parameters that were used for all PAR emulations.

System Parameter	Value
Wavelength (λ)	10.7 cm
Pulse Length	1.67μs
PRT	1 ms
Azimuthal Sampling	1°
Range Sampling	250 m

with an RHI pattern save for VCP 212 which is used as the current standard for operational observations from the NEXRAD network. However, when emulating VCP 212, which has temporal updates on the order of 4–7 min, time delays were accounted for in order to be as representative of the true observations associated with a pseudo-RHI.

Even though the different PAR scanning strategies have varied temporal resolutions, the associated dwell times at each radial do not change with each emulation because the rotation rate of the radar is assumed to be constant. This is because the radar is assumed to be utilizing additional resources within the allotted rotation rate to make the additional RHI scans over the area of interest (defined herein as a set of 5 contiguous azimuth angles at 30 km range and 3 contiguous azimuth angles at 90 km range). For example, if the normal operations of the radar take time T_1 to perform, then the additional time T_2 is available for other purposes, where $T_1 + T_2 = 15$ s. T_2 is time that can be used to perform the desired RHI scans and any other adaptive scanning tasks. T_1 is constant for every rotation, but the portion of T_2 that is available for RHI scans changes depending on how long they take to perform. Thus, if a specific RHI scanning strategy takes longer to perform, then it takes up a larger fraction of T_2 and must occur less frequently to allow for the execution of the other adaptive scanning tasks. However, if a specific scanning strategy can be performed very quickly, then it takes up a small fraction of T_2 and can be performed more frequently. The limit applied here is that using a 10° spoiled transmit beam results in the fastest scanning strategy, and scanning RHIs over the area of interest can be repeated every rotation, which yields a temporal resolution for 10° imaging of 15 s. Thus, each scanning strategy, save for VCP 212, has a fractional decrease in spoil factor compared to 10° imaging, and the temporal resolution increases by the reciprocal of that factor. That is to say, 5° imaging is one half the spoil factor associated with 10° imaging; therefore, it takes twice as long to perform RHIs over the area of interest which yields a 30 s temporal resolution (i.e., every 2 rotations of the radar). The update times for all beam patterns can be found in Table 2.2. It should be noted that VCP 212 does not fall under the adaptive scanning framework as it is used to represent the current operational capabilities.

Table 2.2: Scanning strategies analyzed and the temporal resolution associated with each. The 4.5 temporal resolution is only associated with VCP 212 and not related to any assumed scanning strategy of a PAR system utilizing adaptive scanning.

Beam Type	Beam Width [deg]	VCP Volume Update Time [min]
Pencil	1°	2.5–4.5
Imaging	2.5°	1.0
	5°	0.5
	10°	0.25

2.2.3.1 Beam Patterns

The beam patterns that are currently used for RSim are different from those used in (Mahre, 2020). The new beam patterns are generated offline and then interpolated onto the data during the emulation process.

The beam patterns are generated in two main ways depending on the style of beam desired. The pencil beam is generated based on the geometry of the TPAR antenna and is intrinsic to the antenna shown in Figure 2.2. The spoiled beam patterns are synthetically generated on a two-dimensional domain ranging from ±90° (Schvartzman et al., 2022a,b). Each transmit pattern is then combined with the same tapered receive pattern using a Taylor taper. The combination of these patterns results in a 2-way 6-dB beamwidth of 1° in both the azimuth and elevation direction for the pencil beam, and slightly larger in the spoiled beam elevation direction due to the spoiling. More specifically, Figure 2.3 shows the two-dimensional two-way beam patterns for the pencil and spoiled transmit patterns assuming

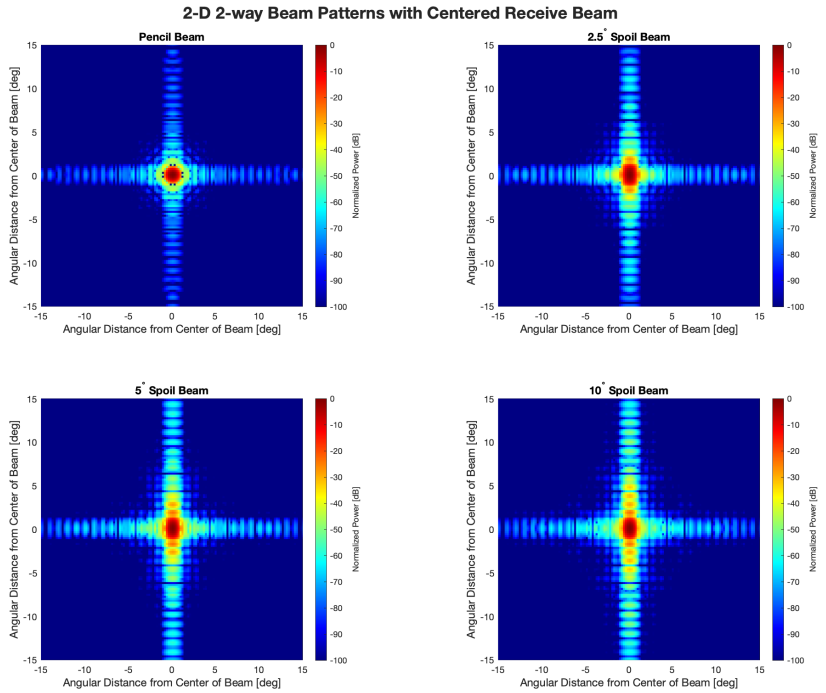

Figure 2.3: 2-dimensional 2-way Beam Patterns for a pencil (top left), 2.5° spoil (top right), 5° spoil (bottom left), and 10° spoil (bottom right) transmit beams with a centered receive beam.

a centered receive beam, and Figure 2.4 shows the same patterns but in a one-dimensional slice in the elevation direction. Notice how, in Figure 2.3, the spoiled beam patterns are elongated in the elevation direction where the pencil beam is circular. Furthermore, notice how the more the beam is spoiled the brighter the power seen in Figure 2.3. This is seen in the vertical direction with more prominent sidelobes appearing as well as a brightening along the vertical axis mainly between ±5° from the center of the beam.

The increase in the transmitted spoiled beamwidth can also be seen in the difference in the two-way 6-dB beamwidths (Table 2.3). The pencil beam has a beamwidth right around the required 1°; however, the beam spoiling makes the receive pattern and 2-way patterns almost completely merge along the mainlobe resulting in a larger beamwidth in the elevation dimension for the spoiled cases. The differences in the azimuthal 6-dB beamwidths are attributed to the fact that no explicit equation is used for the transmit beam, but rather an optimization that searches for the best set of phase weights to shape the beam. Thus,

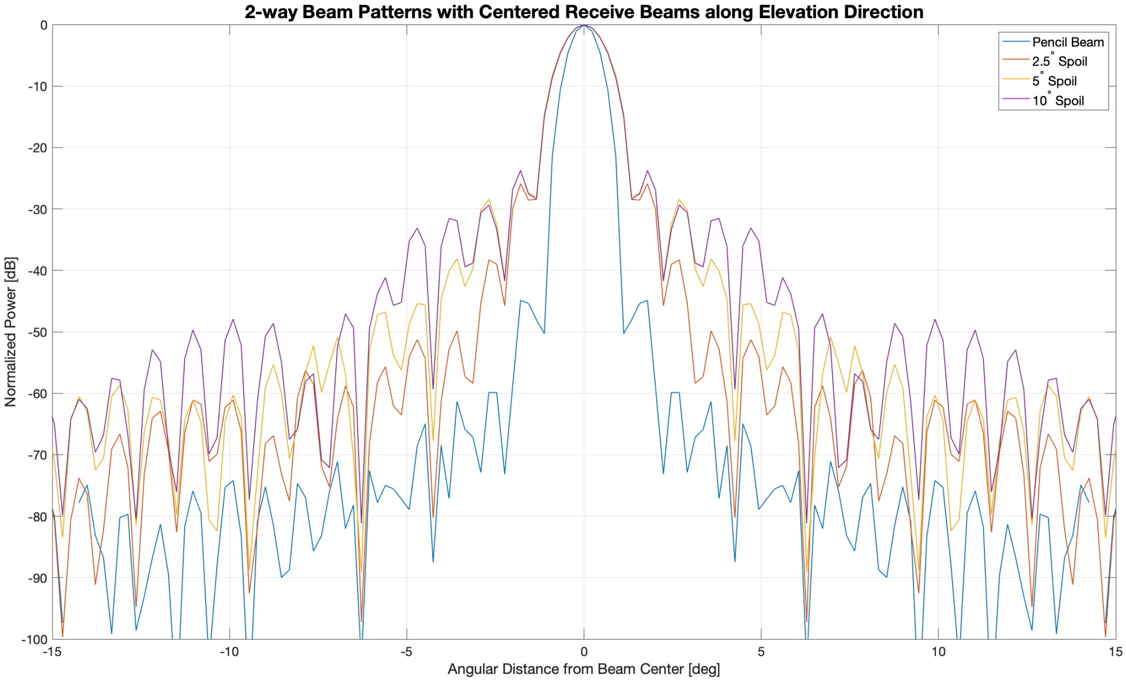

Figure 2.4: 1-dimensional 2-way Beam patterns in elevation for a pencil (blue), 2.5° spoil (orange), 5° spoil (yellow), and 10° spoil (purple) transmit beams with a centered receive beam.

small differences in the transmit beam pattern coupled with the same receive beam pattern can result in minor differences seen here (which are also seen in the elevation directions with the spoiled beams deviating by about 0.03°). However, these differences are on the order of 0.01° to 0.03° and are not believed to impact the data in any significant way.

Table 2.3: 6-dB beamwidths associated with each different transmit beam pattern coupled with a centered (0° offset) receive beam.

Beam Pattern	-6 dB BW Azimuth	-6 dB BW Elevation
Pencil	1.01°	1.01°
2.5° Spoil	0.94°	1.52°
5° Spoil	0.92°	1.52°
10° Spoil	0.94°	1.49°

Due to the fact that each beam pattern is synthesized or intrinsically calculated on transmit, utilize a Taylor taper on receive, and no other beam patterns are used, the comparisons between the beam patterns were done relative to one another. Thus, the results herein are dependent upon the use of the same tapers and generation techniques as mentioned above. However, the conclusions in this work should not be greatly impacted by a change in tapers and should be applicable with other beam patterns.

The beam patterns were compared to one another using integrated sidelobes level ratios (ISLR) over the one-dimensional domain of the two-way mainlobe elevation beam width. This was done to capture the most important change to the beam patterns which was in elevation due to the atmospheric imaging cases.

The ISLR is the same as the one found in Wang (2013) and Chatzitheodoridi et al. (2020) and is calculated by:

$$ISLR = 10 \log_{10}\left(\frac{T_s}{T_m}\right) \tag{2.21}$$

and where T_s is the integrated total sidelobe power and T_m is the integrated main lobe power and are given by:

$$T_s = \int_{-\infty}^{a} |y(\tau)|^2 d\tau + \int_{b}^{\infty} |y(\tau)|^2 d\tau \tag{2.22}$$

and

$$T_m = \int_{a}^{b} |y(\tau)|^2 d\tau \tag{2.23}$$

where $|y(\tau)|^2$ represents the two-way beam pattern in one-dimension and the interval $[a,b]$ represents the bounds of the main lobe.

The ISLRs associated with each of the beam patterns, detailed in Sections 2.2.3.2 - 2.2.3.4, can be found in Table 2.4. It includes a pencil beam pattern with a 1° beamwidth for VCP 212 and true RHI scans and spoiled beams of 2.5°, 5°, and 10° for atmospheric imaging. It should be noted that ISLRs are only computed for one direction of offsets from the central beam for the imaging cases because the ISLRs are the same for either positive or negative deviations from the transmit beam's center.

The contents of Table 2.4 indicate that the pencil beam pointing at broadside has the lowest ISLR value of -43.18 dB, and generally, the 2.5° spoiled beam case has the next

Table 2.4: ISLRs associated with a pencil beam and three different spoiled beam width for atmospheric imaging. The pencil beam will be used as the baseline ISLR to which the other beam patterns will be compared. A positive deviation indicates a higher ISLR compared to the pencil beam.

Beam Type	Beamwidth in Elevation	Receive Beam Position	ISLR [dB]	Deviation from Pencil Beam [dB]
Pencil	1°	0°	-43.18	0
Spoiled Beam	2.5°	0°	-28.07	15.11
		0.75°	-26.59	16.60
	5°	0°	-23.39	19.79
		1°	-23.86	19.33
		2°	-25.56	17.63
	10°	0°	-22.61	20.58
		1°	-22.79	20.40
		2°	-22.82	20.37
		3°	-23.12	20.06
		4°	-25.01	18.18

lowest ISLR values while the 10° spoiled beam has the highest ISLR values. This was not surprising given that spoiling a radar beam results in higher two-way sidelobe levels associated with the transmitted beam. Furthermore, the more a beam is spoiled, the higher the expected ISLR values will be as seen in the 10° spoiled beam case. Outside of the 2.5° spoiled beam, the expected pattern of decreasing ISLR values with increasing distance from transmit beam center for the atmospheric imaging cases is observed which is important for real-world applications as these patterns do match up with theoretical expectations in this regard. Furthermore, the AIR utilized a 20° spoiled beam. Thus, these spoiled beamwidth are smaller but generally more appropriate for operational purposes.

Although the beam patterns are calculated over an entire ±90° domain in both the azimuth and elevation directions, RSim only uses a ±15° two-dimensional sector to perform emulations as this area houses the majority of the beam pattern that directly impacts the emulation and for computational efficiency. The truncation of the beam pattern on this region is not believed to negatively impact the emulations as increases in the ISLRs when using the full ± 90° domain was no larger than 0.004 dB.

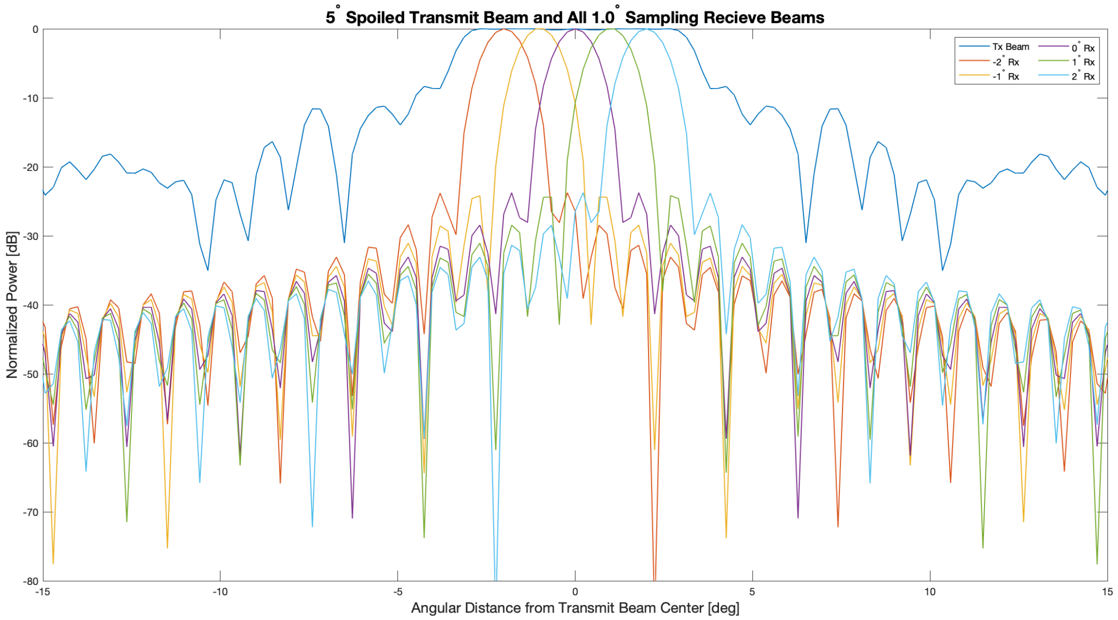

Figure 2.5: Example situation where a 5° spoiled transmit beam has five 1.0° sampling receive beams.

Given the fact that these beam patterns are generated offline to be read in by RSim, each transmit/receive pattern combination is generated individually. For a pencil beam, this is not a problem because the transmit and receive beams are always centered. However, this became more difficult for atmospheric imaging, and there are multiple receive beams used for one transmit beam. This means that a 5.0° spoiled beam has nine different combinations if looking at 0.5° sampling but would have only five different combinations if looking at 1.0° sampling (Figure 2.5).

The above beam patterns are used for all of the scanning strategies discussed below. VCP 212 and the traditional RHI scans utilize the pencil beam pattern and the atmospheric imaging scans utilize the specific beam patterns associated with the desired transmit beam spoiling.

2.2.3.2 Traditional VCP (VCP 212)

VCP 212 was chosen to represent current operational NEXRAD methods that can be used to observe microbursts. This VCP was used operationally for 36 microburst cases in

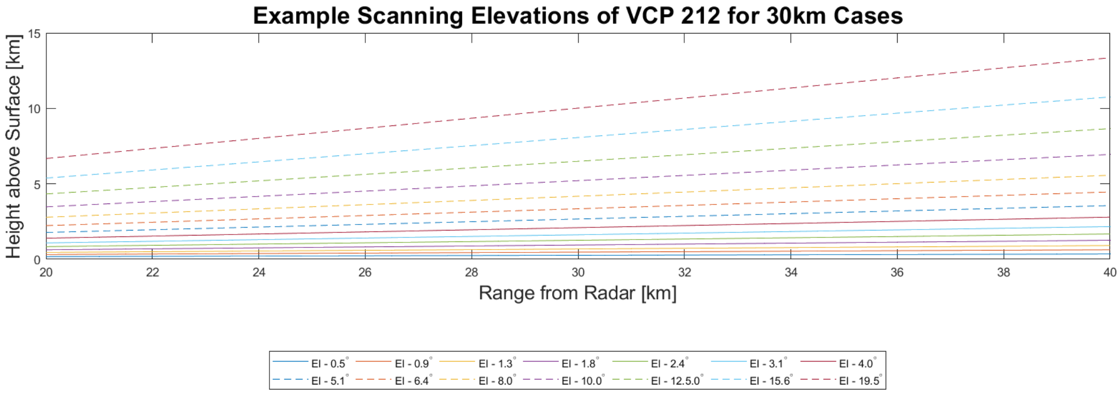

Figure 2.6: Elevation Angles of the beam center over 20 km to 40 km range. These beam heights are examples of how a VCP 212 would observe the atmosphere during the 30 km cases.

(Kuster et al., 2021). VCP 212 has an approximate update time of 4–7 min, since its true update times are dependent upon many factors including additional scanning techniques used by the radar during the time of data collection: AVSET, SAILS, MESO-SAILS, or MRLE. However, these additional features are outside the scope of this work but would be great additions in the future. Without the use of the previously mentioned techniques, the update time for the VCP 212 emulations was set to 4.5 min to be as close to optimal as possible for the NEXRAD system.

Now, VCP 212 has a total of 17 elevations because there are split cuts in the lowest three elevations (0.5°, 0.9°, 1.3°) (Figures 2.6 & 2.7). This means that the total update time of 4.5 min results in a PPI update time of approximately 16 s. Thus, each elevation will have a 16-s delay between data representation; however, the three lowest cuts will have double that because they are split cuts which comprise two PPIs (one PPI for reflectivity and dual-polarization information and one PPI for velocity and SW information). Thus, these lowest elevations have a time delay of 32 s to be properly simulated.

For a VCP 212, RSim takes the start time to emulate the the first radial associated with elevation 0.5°, it then adds on a time delay of 32 s and pulls in the necessary data to match that time frame. Now, the radar data has been generated every 10 seconds, so the code pulls in both the time before and time after the new time and performs a linear interpolation

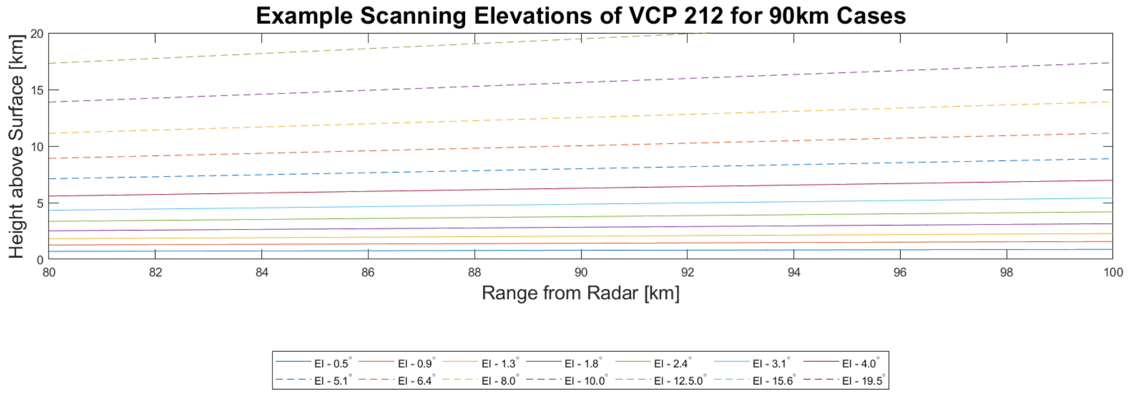

Figure 2.7: Elevation Angles of the beam center over 80 km to 100 km range. These beam heights are examples of how a VCP 212 would observe the atmosphere during the 90 km cases.

between the two times to get a representation of the meteorological state in that in-between time. This process is repeated for each elevation angle adding 32 s in between each split cut and adding 16 s between each batch cut. The VCP 212 module operates one PPI sweep at a time so it will complete the entire 20° sector 0.5° elevation, then implement the time delay and pull in the new data before moving onto the 0.9° elevation. This process generates the pseudo-RHI needed for analysis and comparison purposes.

2.2.3.3 Traditional RHI

In order to provide a general PAR alternative to the pseudo-RHIs that are currently operationally available, this project also looks at the use of true RHIs. This true RHI does not operate on the assumption of piecing together PPIs to generate the pseudo-RHIs of VCP 212. Rather, its operates by scanning the elevations from bottom to top consecutively before moving to a different azimuth angle. Thus, the data within a true RHI is much more vertically consistent than generating a pseudo-RHI from a traditional operational VCP. The true RHI has a scanning strategy with similar low level sampling to VCP 212; however, this scanning strategy has much finer vertical sampling in the mid- to upper-levels of the storm (henceforth called VCP Alpha (Figure 2.8)). It should be noted that because two

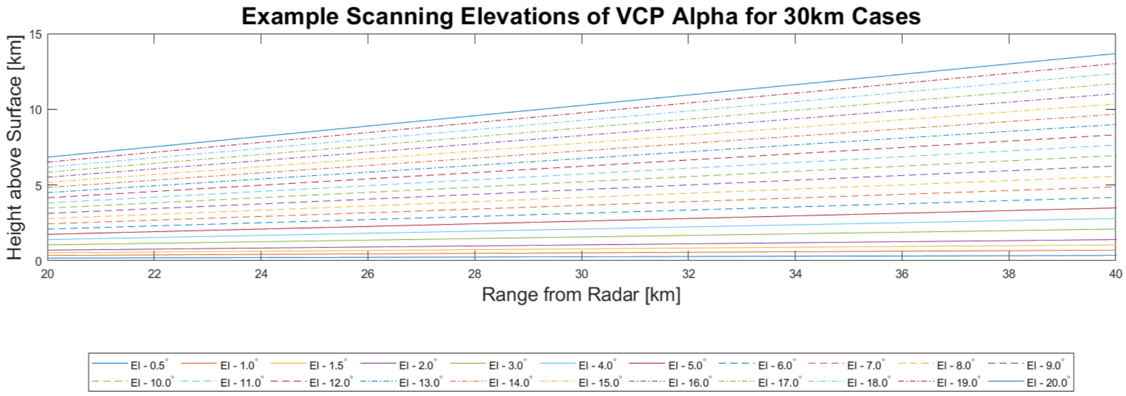

Figure 2.8: Elevation Angles of the beam center over 20 km to 40 km range. These beam heights are examples of how VCP Alpha would observe the atmosphere during the 30 km cases for both the traditional RHI and atmospheric imaging cases.

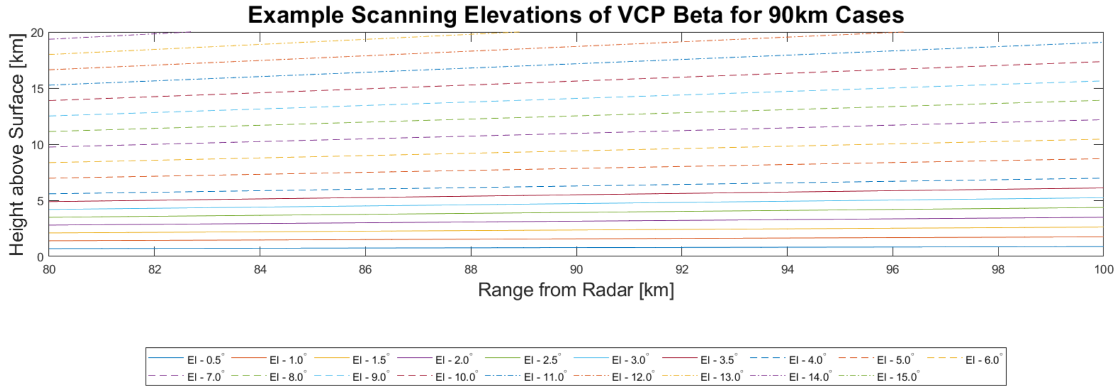

Figure 2.9: Elevation Angles of the beam center over 80 km to 100 km range. These beam heights are examples of how VCP Beta would observe the atmosphere during the 90 km cases for both the traditional RHI and atmospheric imaging cases.

different distances are used in the emulation process (30 km and 90 km), there are different true RHI scanning VCPs for each. Namely, the 90 km case uses what is called VCP Beta (Figure 2.9). VCP Beta only goes up to 15.0° in elevation and has some more elevation angles between 0.5° and 4.0° compared to VCP Alpha because scanning a full 20° elevation sector cannot be accomplished at 90 km range with data that ends at 20 km AGL.

The true RHIs are emulated such that RHIs in the area of interest can be generated every 2.5 min. Because we are only interested in one storm cell (which is the only storm cell to exist in the KBNA sounding simulation), only a 20° azimuthal sector is emulated to capture the most important parts of the storm associated with our areas of interest in order to maintain computational efficiency. However, the assumption is that the RHI scans in an adaptive-scanning implementation would be limited to just a handful of azimuth angles, which would take a very short amount of time to complete. This assumption is implemented by only analyzing the data over a set of 5 contiguous azimuth angles at 30 km range and a set of 3 contiguous azimuth angles at 90 km range, as previously mentioned in Section 2.2.3.

2.2.3.4 Imaging

Imaging is a third alternative scanning strategy that will be discussed herein. This will be accomplished by performing beam spoiling in the vertical direction. Three different beam spoil factors will be employed during analysis producing beams with 2.5°, 5°, and 10° elevation beamwidths with a constant azimuthal beamwidth. This will help showcase some of the trade-offs associated with imaging such as sensitivity issues and higher sidelobe levels.

For the purpose of this study, imaging will be very similar to those used for the true RHI generation. For the 30 km cases, the imaging will use VCP Alpha (Figure 2.8), and the 90 km cases will use VCP Beta (Figure 2.9).

One benefit to imaging is that receive beams can be generated at any point within the spoiled transmit beam which would allow for finer vertical sampling in the mid- to upper-levels of a storm without having to worry about using more radar time. However, this benefit is not currently analyzed within this study, and the main comparison between the imaging and traditional RHI is the difference in sidelobe levels, reduced sensitivity, and temporal differences in scanning limits associated with a mechanically rotating, single-faced PAR.

As previously mentioned, it is assumed that these RHI scans would occur within an adaptive-scanning framework. Thus, the radar would have some extra time to perform additional tasks (T_2) in addition to the normal operations (T_1) where T_1 is constant and $T_1 + T_2 = 15$. All adaptive-scanning techniques have to share T_2, where the RHI scans make up a portion of that time in T_2. Therefore, smaller spoil factors require a larger fraction of T_2, as they take longer to complete, and must be performed less frequently as a result. Whereas, larger spoil factors can be performed more frequently as they take up a small fraction of T_2. Also previously mentioned, the limit applied here is that using a 10° spoiled transmit beam is the fastest imaging technique and can occur every rotation yielding a 15 s temporal sampling. Because 5° imaging utilizes a spoiled transmit beam with one half the spoil factor, it would require twice as long to scan the same RHI scans which yields a 30 s temporal sampling. Finally, because 2.5° imaging utilizes a spoiled transmit beam with one fourth of the 10° spoiled beam pattern, it would require four times the amount of time to scan the same RHI scans. This means that the 2.5° imaging requires a 60 s temporal sampling.

2.2.4 Representativeness of Storm Environment

While previous literature has shown that RSim performs well as being a representative example of how a radar would observe a given storm (with no estimation errors), a brief comparison was performed to showcase RSim's capabilities and can be found in Appendix A (Mahre, 2020). These qualitative comparisons occurred at both 30 km and 90 km in range between the model data and the true RHI emulations using VCP Alpha and Beta at each range respectively and prior to any random errors being added into the true RHI data. It is shown in Appendix A that RSim can provide representative observations of the model environment.

2.3 Analysis Methods

The following analysis methods detail the analysis tools and framework set up by this project. These processes were specifically applied through a proof-of-concept case which looks at a single wet microburst case. The tools and framework dealt with ways to quantify the performance of the different scanning strategies. This quantification occurs through calculating the beam patterns' integrated sidelobe levels (done in Section 2.2.3.1); applying radar error analysis; and calculating different metrics for different precursor signatures' size, shape, and intensity. The calculation of different metrics and application of radar error analysis were done for each distance of the microburst away from the radar (30 km and 90 km).

2.3.1 Radar Error Analysis

Because this proof-of-concept analysis relied upon the use of simulations to generate a microburst and a radar emulator to generate what a radar "sees", the analysis was considered to be in an idealized situation. However, in order to make the results more realistic, the methodology first introduces random error into the data and then scanning strategy performance analysis was performed. The methodology used to add in random error based on estimation processes was as follows.

First, using the variables calculated by the emulator, the variance of the signal power and velocity estimators were calculated using equations form Doviak and Zrnic (1993) and Yu et al. (2007):

$$\frac{var(\hat{S})}{S^2} = \frac{1}{M+1}\left[\sum_{l=-M}^{M}\frac{M-|l|+1}{M+1}\rho^2(lT_s)+\frac{N_p^2}{S^2}+2\frac{N_p}{S}\right] \tag{2.24}$$

$$\begin{aligned} var(\hat{v}) = \frac{\lambda^2}{32\pi^2 M\rho^2(T_s)T_s^2}\Bigg[&(1-\rho^2(T_s))\sum_{l=-(M-1)}^{M-1}\frac{M-|l|}{M}\rho^2(lT_s) \\ &+\frac{N_p^2}{S^2}+2\frac{N_p}{S}[1-\frac{M-1}{M}\rho(2T_s)]\Bigg] \end{aligned} \tag{2.25}$$

where M is the number of pulse pairs, T_s is the pulse repetition time (PRT), ρ is the normalized sample-time autocorrelation function, S is the signal power, N_p is the noise power, and $\hat{S}$ and $\hat{v}$ are the estimators for signal power and radial velocity, respectively.

The signal power S came from the reflectivity factor calculated from the forward operator. The autocorrelation function is the same as what is given by Doviak and Zrnic (1993) and is given by:

$$\rho(mT_s) = exp\left[-8\left(\frac{\pi\sigma_v mT_s}{\lambda}\right)^2\right], \text{where} \quad m = 0,1,2,...(M-1). \tag{2.26}$$

where lambda is the radar wavelength in m.

The standard deviation of radial velocity was very straight-forward with just taking the square root of the variance. However, in order to obtain the standard deviation of the reflectivity factor in dB units, the following equation from Mahre (2020) was used:

$$SD(\hat{Z}_h) = 10\log_{10}\left(1 + \frac{SD(\hat{S})}{S}\right). \tag{2.27}$$

The last standard deviation calculated was the standard deviation for K_{DP}. The equations used for these calculations were obtained from Melnikov (2004) and are given by:

$$SD(\hat{\Phi}_{dp}) = \frac{1}{\sqrt{2}\rho}\left(\frac{SNR_h + SNR_v + 1}{M\,SNR_h\,SNR_v} + \frac{1-\rho}{M_I}\right)^{1/2} \quad \text{(rad)} \tag{2.28}$$

and

$$SD(\hat{K}_{dp}) = \frac{SD(\hat{\Phi}_{dp})}{\sqrt{2}L} \tag{2.29}$$

where M_I is the number independent pulse pairs, SNR_h (from here on SNR) is the SNR in the horizontal polarization, and SNR_v is the SNR in the vertical polarization. SNR and SNR_v are related by $SNR = Z_{DR}\,SNR_v$.

Now, the SNR is calculated using the same methodology as Mahre (2020). The SNR can be represented as:

$$SNR(r,\phi) = Z_h(r,\phi) - 20\log_{10}(r) - n_f + SNR_{reduction} \quad \text{(dB)} \tag{2.30}$$

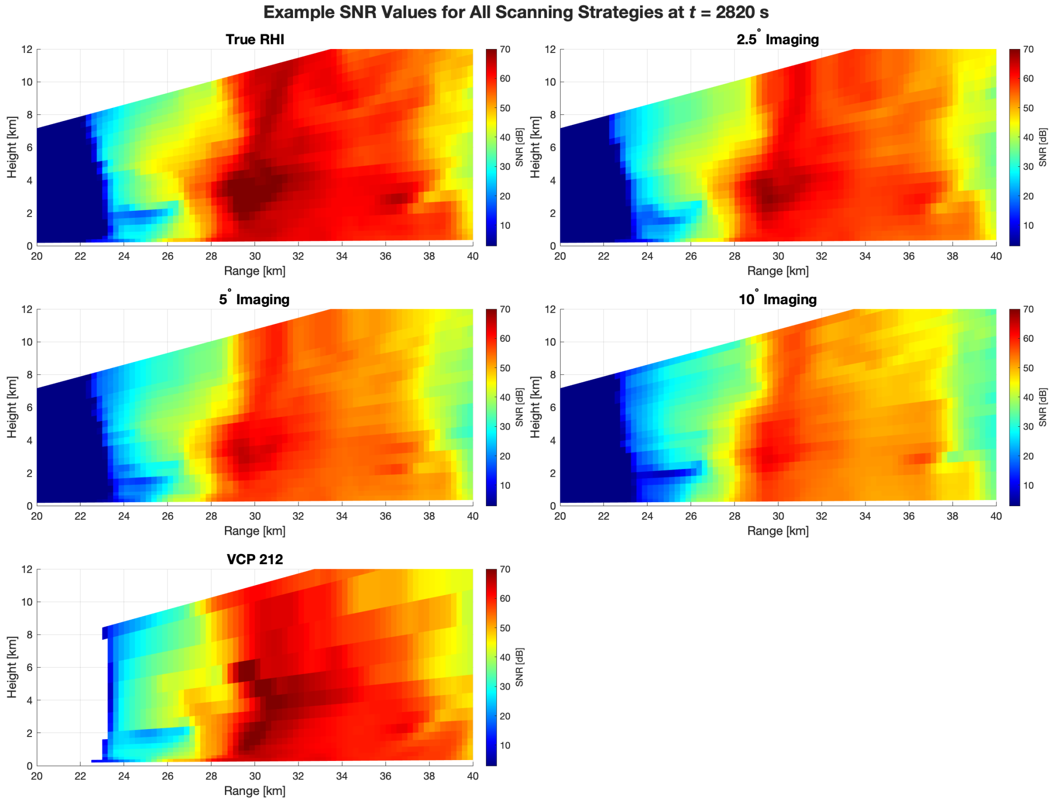

Figure 2.10: SNR values for all 5 scanning strategies at $t = 2820$ s at 30 km range.

where r is the range of the given bin, ϕ is the elevation angle, n_f is the noise floor given by $n_f = -7.5 - 20\log_{10}(50)$ in dB at 50 km range, and $SNR_{reduction}$ is the reduction in SNR dependent upon the beam pattern given by the equation:

$$SNR_{reduction} = 10\log_{10}\left(\frac{\theta_p}{max(\theta_{az}, \theta_{el})}\right) \quad \text{(dB)} \tag{2.31}$$

where θ_p represents an ideal beamwidth associated with a spherical pencil beam pattern such that $\theta_p = 1$. Example SNR calculations for the $t = 2820$ s time period within the analysis are found in Figures 2.10 and 2.11 for the 30 km and 90 km cases, respectively. Notice how as the spoiling factor increases, there is a reduction in the SNR. Most notably, the expected SNR reduction of 10 dB between the true RHI (pencil beam) and 10° imaging panels is observed.

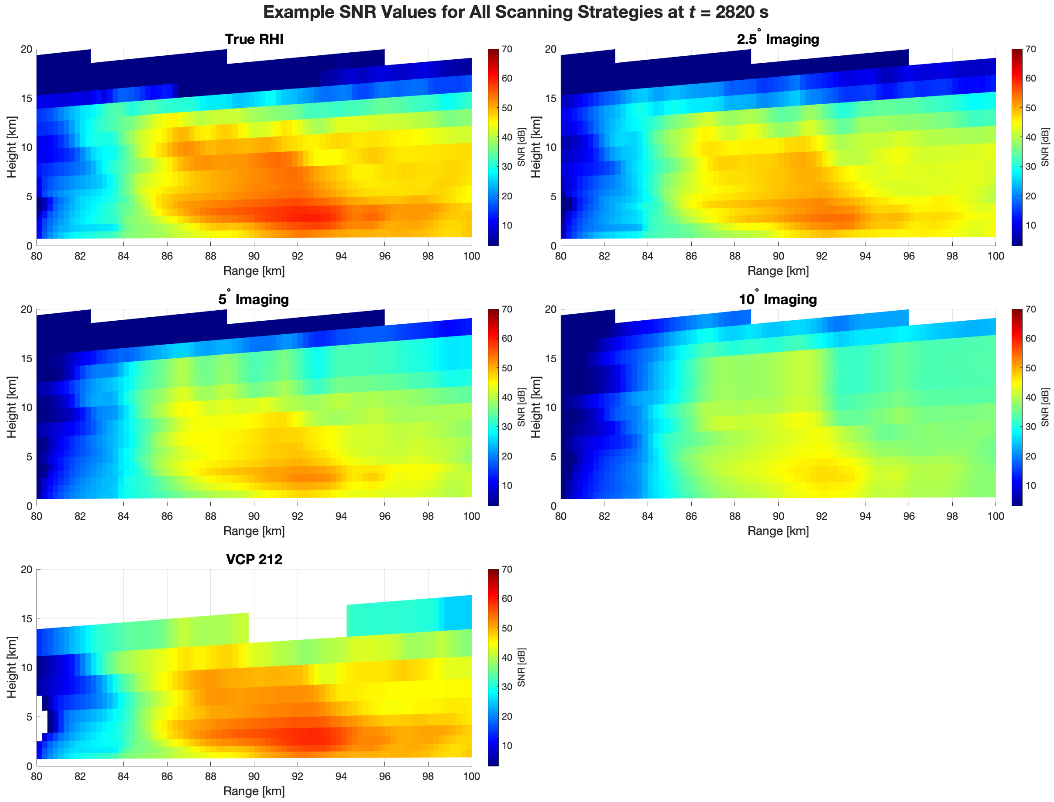

Figure 2.11: Same as Figure 2.10 but for 90 km range.

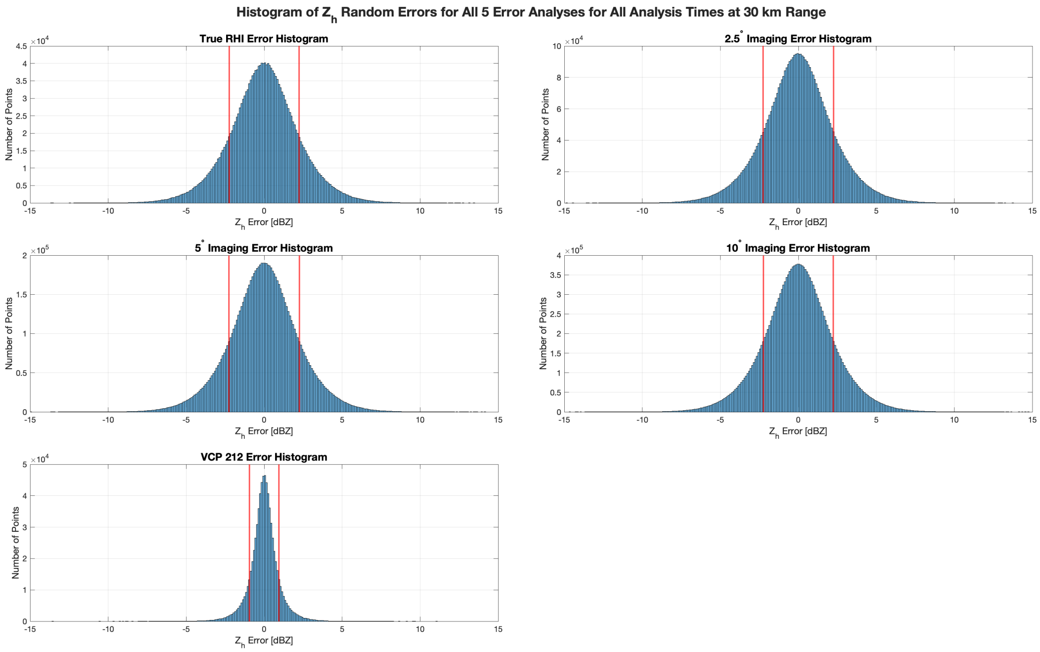

Figure 2.12: Histogram of all Z_h errors for all analysis time periods of all scanning strategies of 30 km range case. The vertical red lines represent the positive and negative location of the standard deviations associated with the errors in the histogram.

Once the emulations were completed, these standard deviations of reflectivity factor, radial velocity, and specific differential phase were used to introduce error into the data. The error was applied at each emulated range gate by using a random number generator assuming a Gaussian distribution with a mean of zero ($\mu = 0$) and a standard deviation equal to the standard deviations of Z_h, K_{DP}, and V_r. This value was then added onto the existing idealized data to generate a more realistic data set, and the analysis was performed using this new data set. This process was done for each of the cases in this study: the two different ranges (30 km and 90 km) and the 5 different scanning strategies. Figures 2.12 through 2.17 provide verification that the errors that were generated and added into the data for analysis were indeed associated with a Gaussian distribution.

Now, to become more representative, it was important to perform this process many times for each of the different cases. Thus, the error analysis included 5 different error

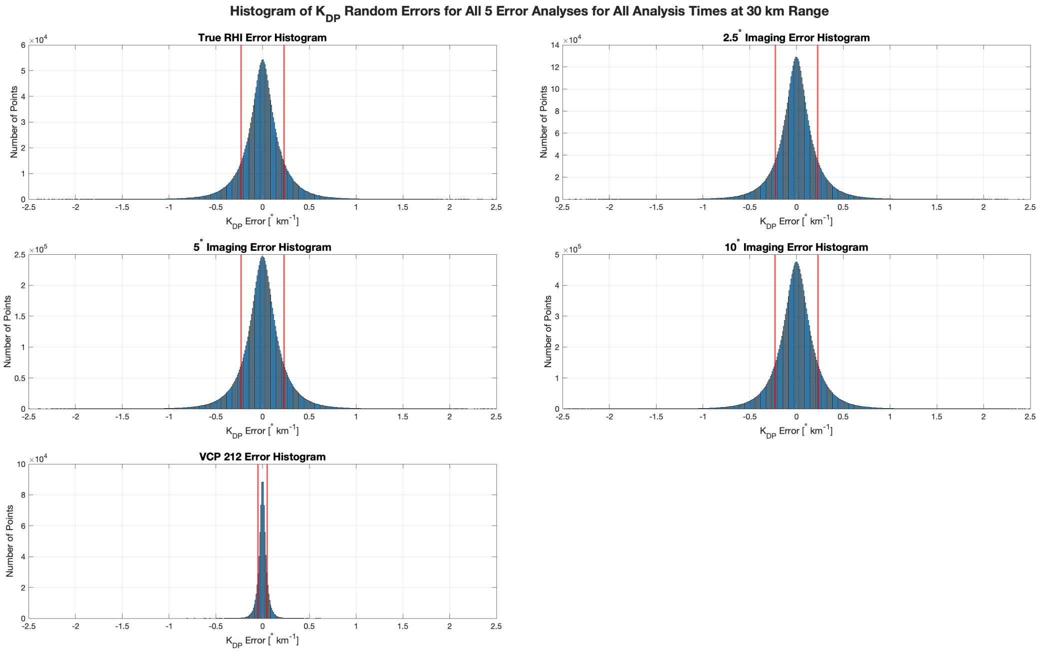

Figure 2.13: Same as 2.12 but for K_{DP} errors at 30 km range.

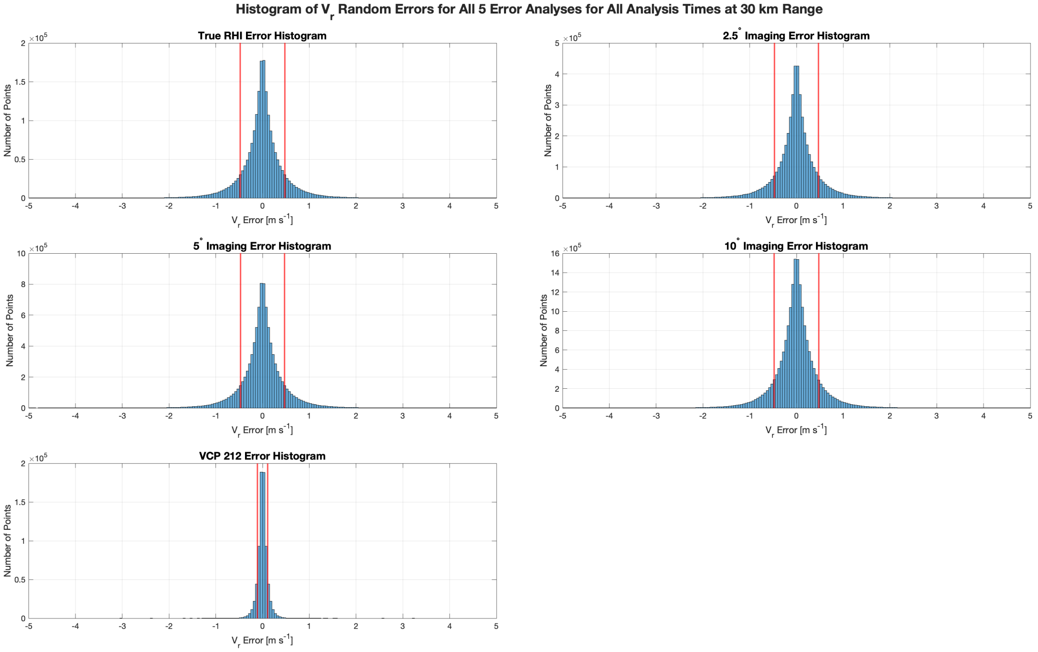

Figure 2.14: Same as 2.12 but for V_r errors at 30 km range.

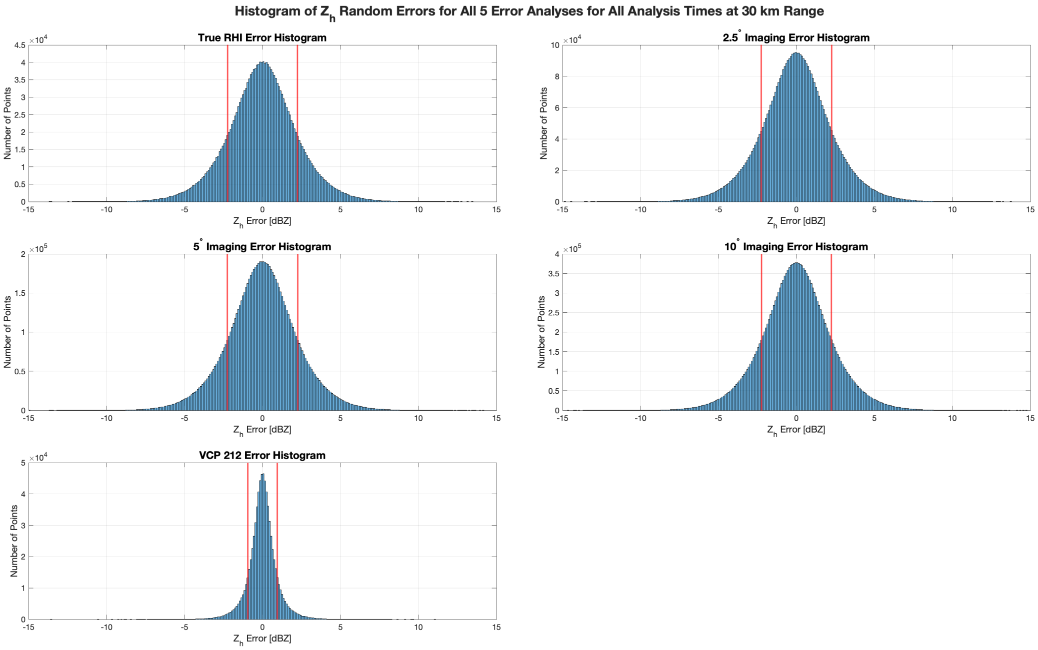

Figure 2.15: Same as Figure 2.12 but at 90 km range case.

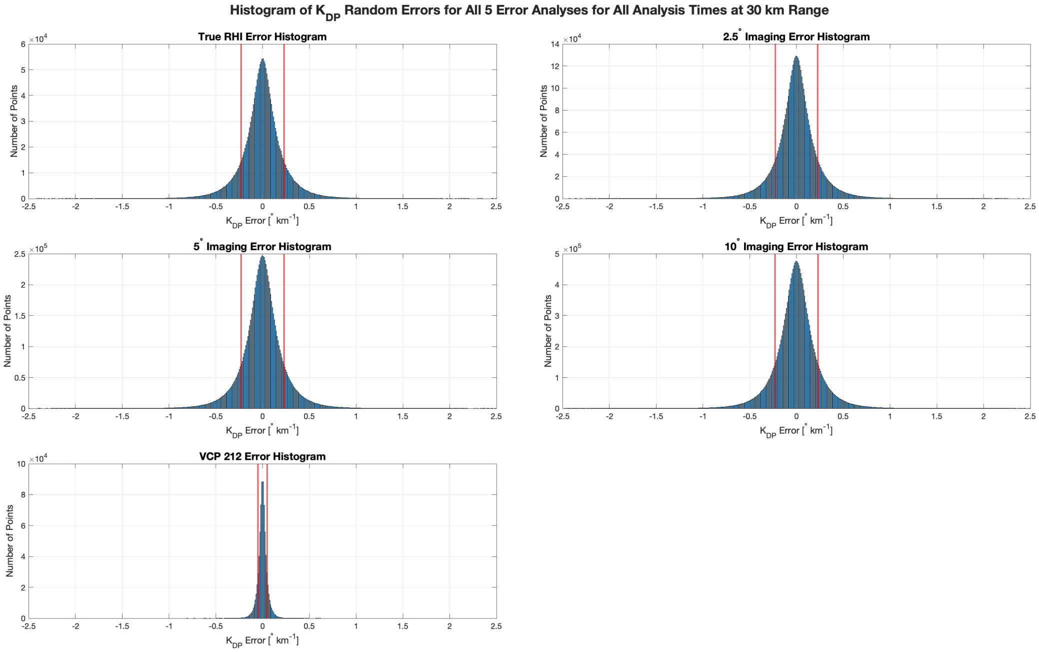

Figure 2.16: Same as Figure 2.12 but for K_{DP} errors at 90 km range case.

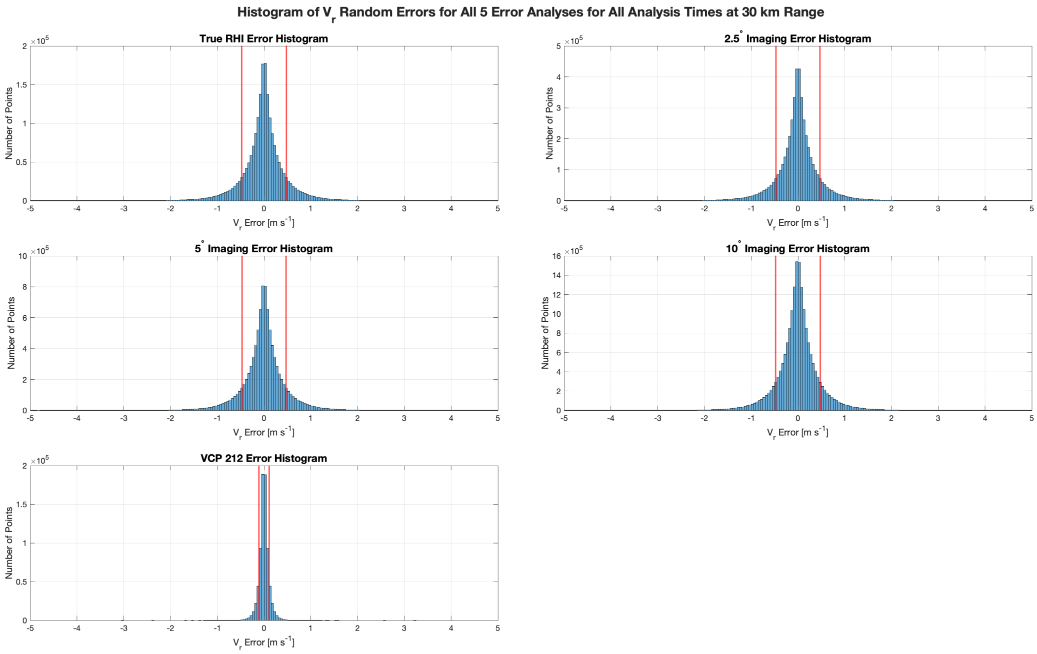

Figure 2.17: Same as Figure 2.14 but for V_r errors at 90 km range case.

analyses alongside the idealized scenario (i.e., a total of 6 analyses are performed). These error cases will be referred to as E1 through E5 throughout the remainder of this paper.

To quantify the total estimation errors added into the data of all 5 different error analyses, the mean absolute error (MAE) was calculated over all 5 different error analyses combined together and is represented as:

$$MAE = \frac{1}{N_s}\sum_{i}^{N_s}|y_{i,total} - y_{i,pure}| \tag{2.32}$$

where N_s is the total number of samples of all 5 error data sets, $y_{i,total}$ is the calculated metric with added error, and $y_{i,pure}$ is the calculated metric with no added error. The MAE provides a single value to represent the typical errors associated with each scanning strategy for each calculated metric.

It is important to note that the errors calculated by the MAE will have two distinct contributions that are combined together. First, the temporal resolution of the data will contribute to a higher MAE value as the total number of points, N_s, will be smaller for coarser temporal resolution. Second, the effects of increased imaging will be included because of the lower SNR values impact the estimator variances and standard deviations. This research does not separate these contributions. This must be considered when comparing the MAE values between the scanning strategies as there are temporal resolution differences (10° imaging at 15 s and true RHI scanning at 2.5 min).

2.3.2 Scanning Strategy Performance Analysis

Through a proof-of-concept analysis, the scanning strategy performance was quantified by determining how well each scanning strategy performed regarding detection of microbursts and their precursor signatures. The scanning strategy performance was done on one set of data which was comprised of the pure emulated data with one set of errors added in. As previously mentioned these errors represent errors associated with estimation processes and provide a more realistic look at what an actual radar would see.

The first set of comparisons were between VCP 212 at 4.5 min temporal resolution and the model data prior to any emulation at 60 s temporal resolution. This provided a baseline to how current operational radars would observe the simulated microburst with regard to precursor signature evolution and how they compared to those observed using the model domain data. Furthermore, this provided visual confirmation and explanation of the precursor signatures discussed later in the analysis.

After the above mentioned comparisons, scanning strategy performance analysis was performed for the proof-of-concept case involving the four PAR scanning techniques. This analysis focused on differences that occur between how different scanning strategies observed the storm and how the precursor signature evolution changed with the different spatial and temporal sampling between the different scanning strategies of 4.5 minutes for VCP 212, 2.5 min for traditional RHI, 1 min for imaging using a 2.5° spoiled beam, 30 s for imaging using a 5° spoiled beam, and 15 s for imaging using a 10° spoiled beam.

The precursor signatures that were analyzed within this study include:

- intensity, size, and evolution of K_{DP} columns (Kuster et al., 2021);
- intensity, size and evolution of DRCs (Heinselman et al., 2008; Vasiloff and Howard, 2009; Newman and Heinselman, 2012; Kuster et al., 2016; Amiot et al., 2019);
- intensity of mid-level convergence around 4 km AGL(Kuster et al., 2016).

While these are not all of the possible signatures that could be observed, these precursor signatures are characteristic of wet microburst formation and should be visible within the model simulations of the KBNA sounding.

For the quantitative comparisons, there were a few different measurable characteristics that are observed to describe the intensity, size, and evolution of the precursor signatures mentioned above. The quantitative comparisons occurred over a uniform region in time and space to keep the total number of range gates constant and encompasses 5 consecutive azimuth angles at 30 km range (3 consecutive azimuth angles at 90 km range), all available elevation angles, and 5 km of 250-m spaced range gates directly over the predetermined region associated with the surface divergence signature. Let it be known that "surface" divergence refers to a divergent radial velocity signature at the lowest available radar elevation angle, which is typically 0.5°. Thus, a bias exists given that these signatures were viewed knowing the end result of a microburst at the surface; however, following the signatures through space would provide similar results, and the main difference in the two methods is being microburst focused or precursor signature focused.

To quantify the intensity of the signatures, the 95^{th} percentile values of K_{DP} and Z_h were used as a measure of K_{DP} core and Z_h column intensity along with the maximum calculated radial convergence signature (radial ΔV) within the analysis domain at the elevation angle closest to the 4 km height level. As previously mentioned, the mid-level convergence signature can occur between 1 – 6 km AGL; however, the 4 km height level was chosen for simplicity and to provide as uniform a comparison between the scanning strategies as possible. It is noted that it is just as valid to choose different elevation angles within that 1 – 6 km AGL region but is not analyzed herein.

The quantification of the size of the elevated Z_h and K_{DP} regions was done by first finding the locations of the elevated regions (defined as $Z_h \geq 55$ dBZ and $K_{DP} \geq 2.0^\circ$ km^{-1}). Once these regions were found, the data was filtered into subregions based on the amount of points that are contiguous to one another - contiguous here means touching face to face as opposed to any side, edge, or corner in 3-dimensional space. If there were multiple regions, the largest of these regions - with an area of at least 10 range gates - was chosen to represent the K_{DP} core and Z_h column. From this, the total number of range gates were converted to total volume occupied by the K_{DP} core and Z_h column.

Finally, the evolution of the K_{DP} core and Z_h column was quantified in two parts. First, based on the regions identified as the K_{DP} core and Z_h column, the top and bottom were determined to track how the signature evolved vertically. This allowed for tracking the descent of the Z_h column (a DRC) along with tracking noticeable changes in the K_{DP} core as well. Second, the change in the 95^{th} percentiles per minute was tracked to showcase how the intensity of the K_{DP} core and Z_h column evolved in time.

The intensity of both V_r signatures were quantified using the magnitude of the maximum radial ΔV over the uniform region. Over all 5 azimuth angles, the maximum (minimum) radial ΔV were calculated to denote divergence (convergence), and the maximum (minimum) value from the 5 azimuth angles was kept to denote the peak intensity of the divergence (convergence) signature. The area of the surface divergence was also quantified as the total number of range gates associated with a divergent radial $\Delta\text{V} \geq 10$ m s^{-1}, and the number of range gates was then converted to an area using the range gate size at 30 km range. Furthermore, to determine when the microburst reached the surface, the radial ΔV had to be ≥ 10 m s^{-1} and the area of surface divergence had to have a relative maximum that reached the area associated with the general length scale of microbursts (≈ 4 km in diameter). No formal detection algorithm was used to determine when the microburst reached the surface.

These quantified metrics were calculated from the average of all 5 error analysis data sets. Thus, they do not represent metrics associated with just one error analysis case. Rather, they represent the average metrics associated with all error analysis cases within this proof-of-concept analysis.

Chapter 3

Results

The results shown here are preliminary results from a proof-of-concept analysis specifically designed to showcase the usability and potential value of the framework and tools developed herein. Therefore, these results should not be taken as generalized results. Future work would need to be performed utilizing the framework developed within this thesis to perform a more thorough analysis before generalized results can be accepted.

3.1 Scanning Strategy Performance

To showcase the usability and potential value of the framework developed, VCP 212, true RHI, and the three imaging cases are compared to the model field and each other to served as the proof-of-concept analysis. These comparisons involve both qualitative and quantitative comparisons and will primarily look at the evolution of three different microburst precursor signatures: DRCs, K_{DP} Cores, and Mid-level Convergence. The qualitative comparisons only look at the data with one set of errors added in. Thus, they only provide one set of observations. However, the quantified analysis is performed using average metrics calculated from all 5 error analysis cases. Further error analysis detailing all 5 different error sets will be shown in 3.2.1.

3.1.1 Microburst at 30 km Case

The 30 km case provides results that are close to the radar and allow the varying scanning strategies to perform in an ideal environment. VCP Alpha (Figure 2.8) was specifically designed to represent this case with a total of 22 elevation angles spaced 0.5° up to 2° elevation and 1° spacing from 2° to 20° elevation. At 30 km range, this scanning strategy has relatively fine vertical sampling up to 20° elevation ($\approx$ 10.26 km AGL) and is still close enough to the surface to detect the surface divergence signature at the 0.5° elevation angle (≈ 0.26 km AGL).

3.1.1.1 Qualitative Analysis

Before diving into the quantitative analysis, it is important to orient oneself in the data and the storm to see what exactly is going on. This comparison will examine the three radar variables of Z_h, K_{DP}, and V_r between the VCP 212 data at 4.5 min temporal resolution with the model data at the same times and at 60 s intervals otherwise. The analysis time frame was from $t = 2010$ s to $t = 3300$ s where t has units of seconds since the simulation starts. Thus, the total analysis time period is 21.5 min.

Figures 3.1 - 3.3 showcase RHI and pseudo-RHI from model and emulated VCP 212 data, respectively, over the entire analysis time period. All black contours represent the 55 dBZ Z_h contour used to show the location of the Z_h column. Starting off with the V_r RHI and pseudo-RHI images, the important points to look for include mid-level convergence along with diverging winds at the surface. The first noticeable signature that develops is the growth of outbound winds from the surface upward between 28 and 30 km range beginning at $t = 2100$ s (black arrow in panel d). The growth of this signature begins to create a convergence signature beginning at $t = 2220$ s (panel f) around 2.5 km AGL and close to 30 km range (black circle in panel f). This convergence signature continues to develop and intensify until $t = 2400$ s (panel j) where it stretches from around 2 km AGL to over 5 km AGL about 30 km range. As time progresses, the mid-level convergence signature begins to weaken and shrink until $t = 2550$ s (panel m). From $t = 2580$ s (panel o) through $t = 2760$ s (panel r), the mid-level convergence signature remains around 3 km AGL and 30 km range. At $t = 2820$ s (panel s), the mid-level convergence begins to stretch vertically again before shrinking and weakening for a final time from $t = 3000$ s (panel w) through $t = 3300$ s (panel dd).

Regarding the detection of the microburst, the model data, and VCP 212, capture the descend of the microburst from a “midair microburst” to a surface microburst between $t = 2580$ s to $t = 2820$ s (black squares in panels n - t). Notice at $t = 2580$ s (panel o), the model data has a small divergence couplet just above 29 km range (annotated in a black square in Figure 3.1). This signature becomes more pronounced with time and descends toward the surface at $t = 2820$ s (panel s and t). The “midair microburst” reaches the 0.5° azimuth level at $t = 2760$ s (panel r). The surface divergence signature remains present around 30 km range until $t = 3090$ s (panel y). It is during this time period that the microburst occurs at the surface and is supported by the observations seen in Figure 3.1.

The VCP 212 images scattered throughout Figure 3.1 show that the VCP 212 scans capture the essence of the storm environment, but the temporal resolution is too coarse to properly resolve the evolution of the signatures in question in a timely manner. Namely, the divergence associated with the “midair microburst” is seen at $t = 2580$ s (black square in panel o), yet VCP 212 would not detect this signature until it reaches the surface about $t = 2820$ s (black square in panel t) when the first elevation angle was completed for the next VCP 212 scan. Furthermore, with the mid-level convergence signature, there is a weak convergence signature caught at the VCP scan starting at $t = 2280$ s (panel h) about 30 km range and 4 km AGL, but a more robust mid-level convergence signature isn’t captured until the VCP scan starting at $t = 2550$ s (panel n).

Regarding the evolution of the Z_h field, the main focus is the development and evolution of the DRC, which is an indicator of hydrometeor loading within the storm. Panels a-f ($t = 2010$ s thorough $t = 2220$ s, respectively) show a region of $Z_h \geq 40$ dBZ building upward from the surface between 28 and 30 km range (see black arrows in panels a-f). After this time, the formation of a Z_h column (≥ 55 dBZ) is present beginning at $t = 2280$ s (panel g, black contours about 4 km AGL and between 28 km and 30 km range). This Z_h column is indicating the presence of hydrometeor loading occurring within the storm, and it continues to grow and intensify through $t = 2400$ s (panel j), and a secondary elevated

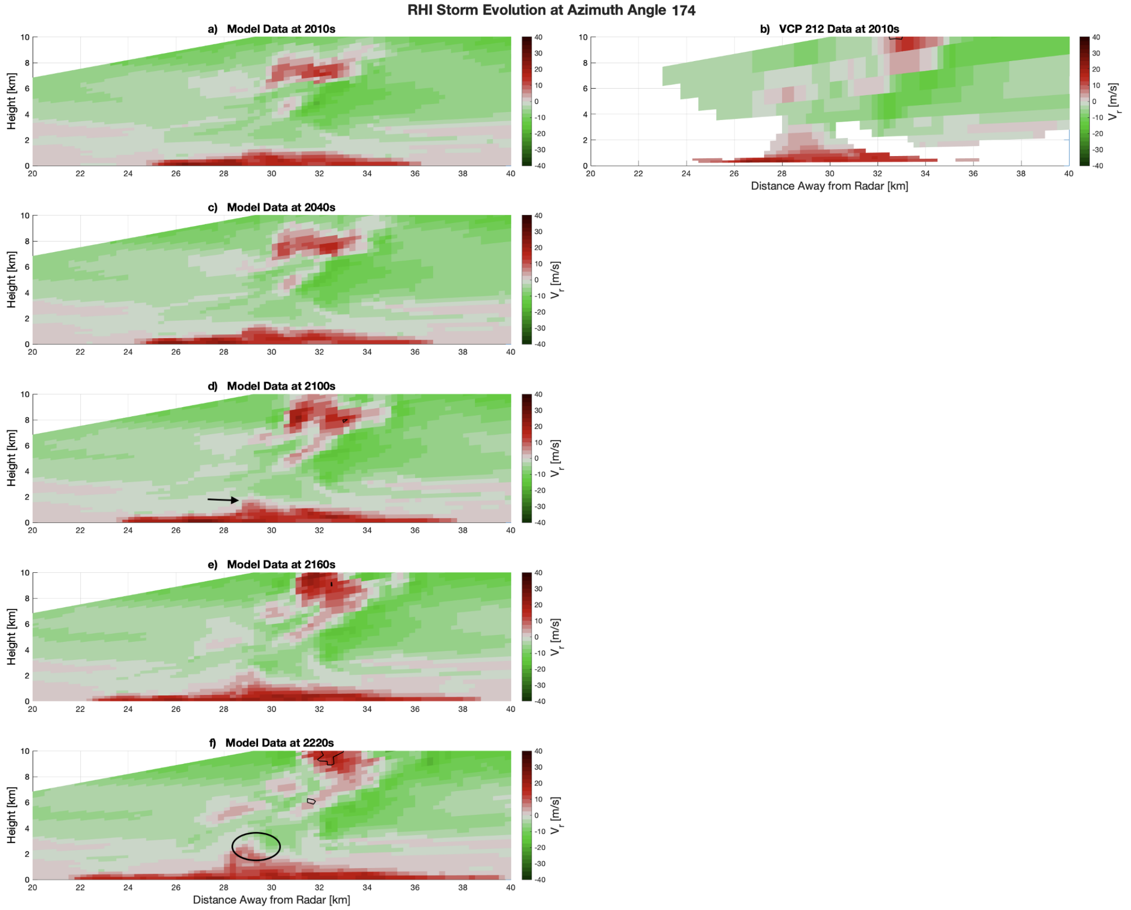

Figure 3.1: RHI images (model) and pseudo-RHI images (VCP 212) of V_r along azimuth angle 174 over the entire analysis time period. The model data is represented every 60 s while the pseudo-RHI images are interlaced every 4.5 min. The VCP scans are placed in time based on the start time of their scan. The black contours represent the 55 dBZ contour.

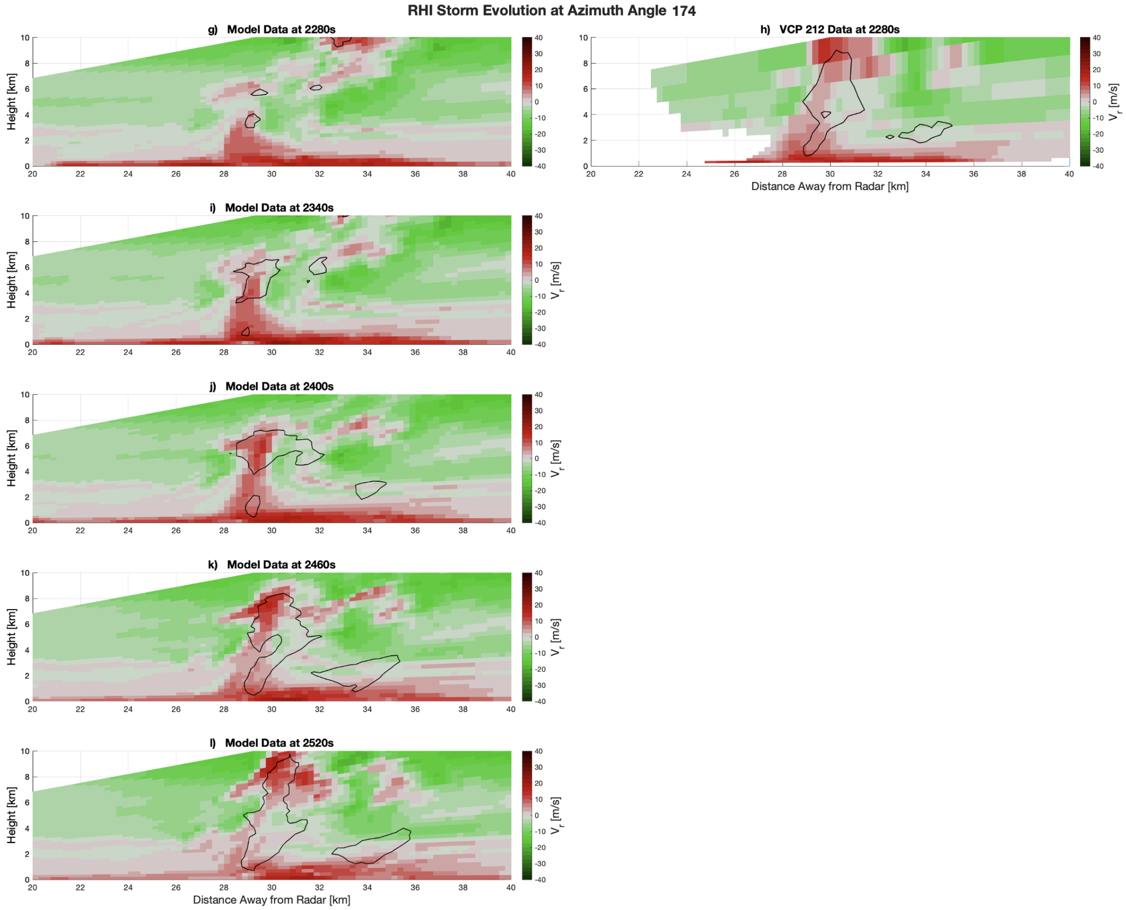

Figure 3.1 (*Continued*): The annotated black square highlights the movement of the ”midair” microburst as it transitions to a surface microburst at $t = 2820$ s.

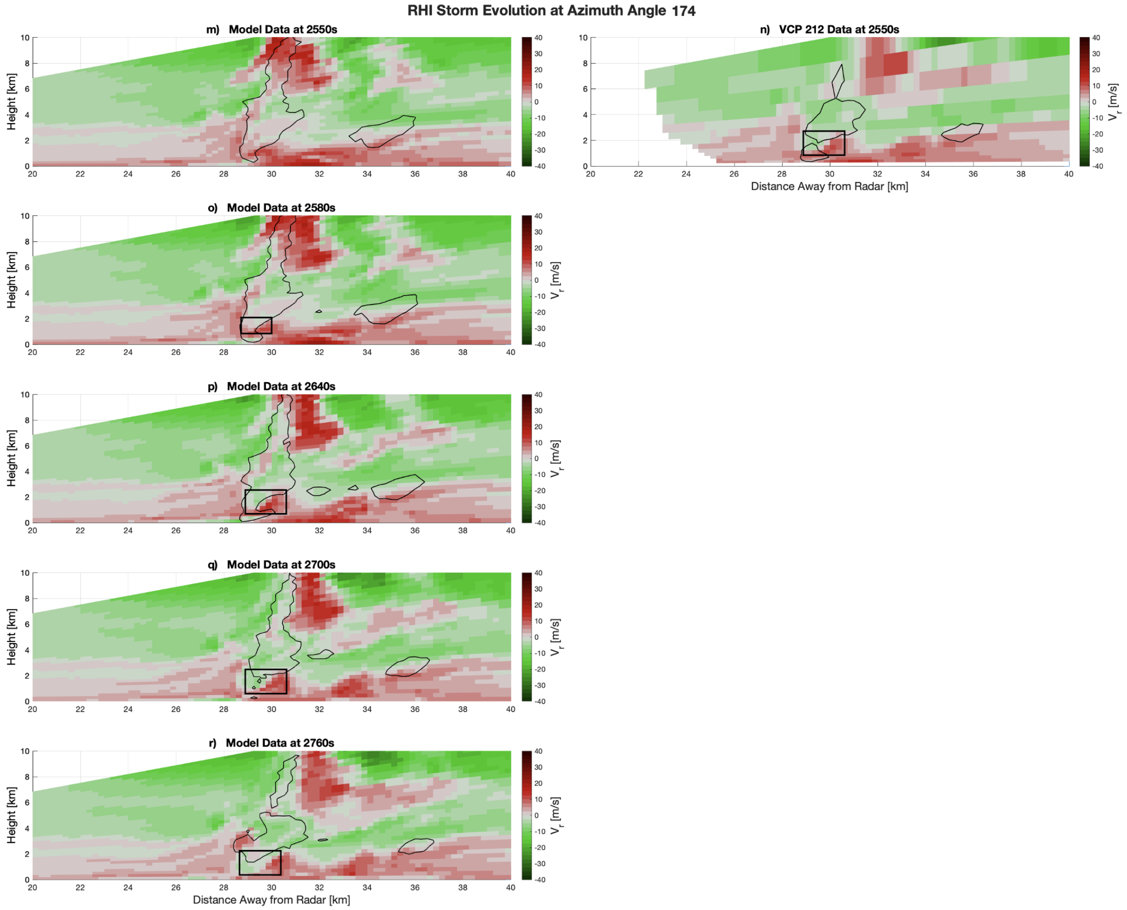

Figure 3.1 (*Continued*)

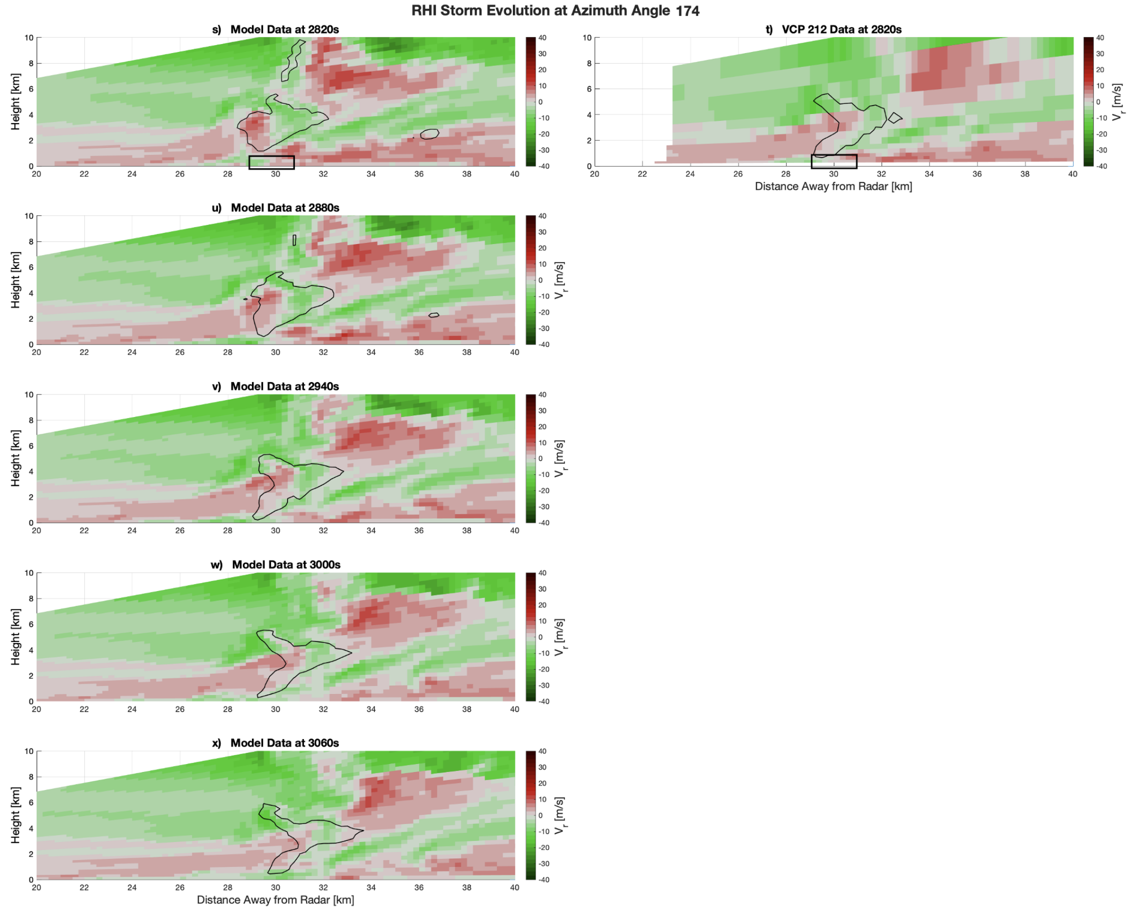

Figure 3.1 (*Continued*)

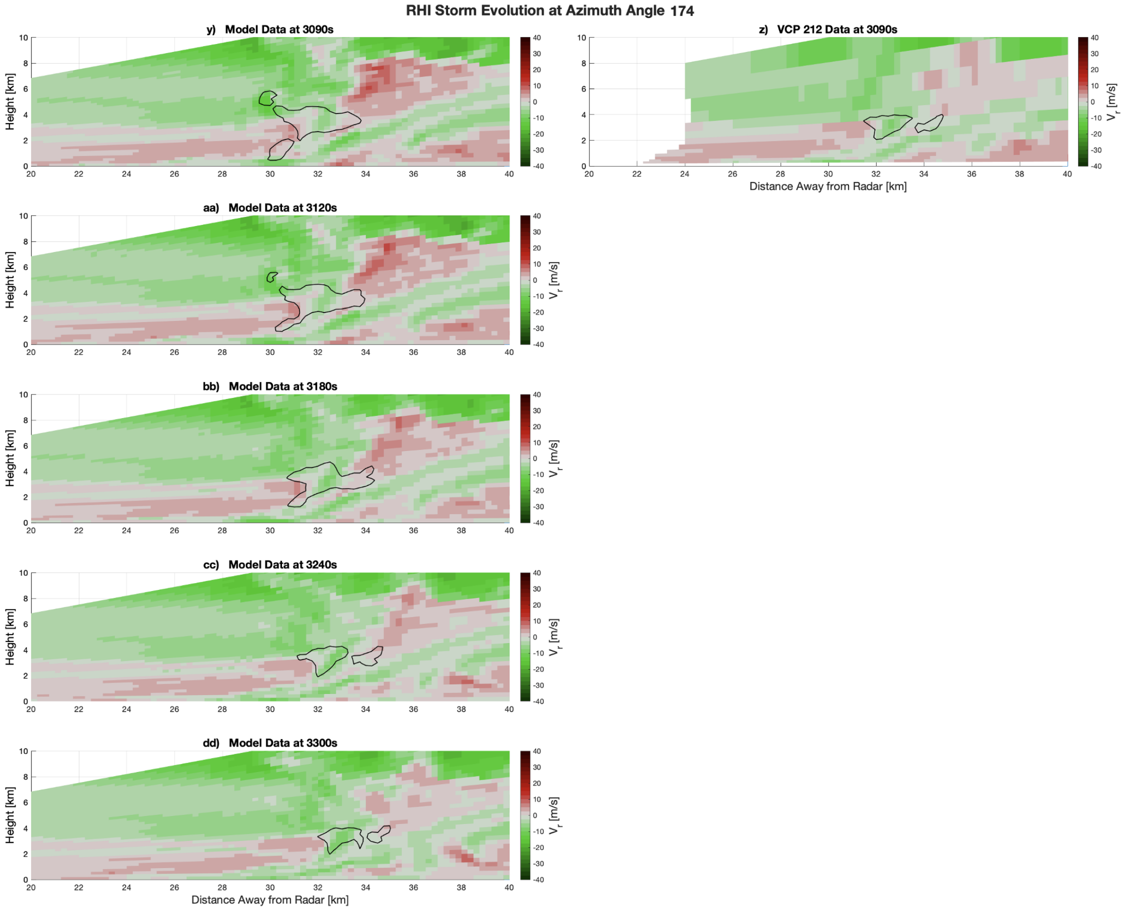

Figure 3.1 (*Continued*)

Z_h region, $Z_h \geq 55$ dBZ, is seen developing around 2 km AGL at $t = 2400$ s (black arrow in panel j). By $t = 2460$ s (panel k), the separate reflectivity regions have begun to merge together into a single Z_h column, and they are completely merged by $t = 2520$ s (panel l). Between $t = 2460$ s and $t = 2940$ s (panels i and v, respectively), the descent of the elevated Z_h column can be seen in two separate parts. The lower maximum (defined as the $Z_h \geq 60$ dBZ values below 4 km AGL (white circle in panel l)) begins its descent and disappears by $t = 2640$ s (panel p). The upper maximum (defined as the $Z_h \geq 60$ dBZ values around 6 km AGL in panel l (black circle)) begins its descent at $t = 2520$ s (panel l) where its lower bound moves closer to the 4 km AGL level. After $t = 2640$ s (panel p), this Z_h column continues its descent through $t = 2880$ s (panel u) where it eventually stalls just above the surface layer until $t = 3060$ s (panel x). Beginning at $t = 3090$ s (panel y), the broader reflectivity region (≥ 55 dBZ) begins to dissipate until the end of the analysis time period at $t = 3420$ s (not shown).

Through the VCP 212 scans, Figure 3.2, the evolution of the Z_h field shows a few different things. First, focusing on panels h through l in Figure 3.2, the VCP 212 image captures an elongated Z_h column (defined as ≥ 55 dBZ). However, as seen in panels i-l, this column is not completely connected until panel l, but the VCP 212 scanning strategy has captured the growth of the elevated Z_h region within its one scan. However, due to its temporal resolution, it only shows a drastic increase in reflectivity factor values between its initial scan (panel b) and its second scan (panel h). This can be seen again in panel sets m-r and s-x where the top of the pseudo-RHI resembles the tops of the last panels in each set and the bottom of the pseudo-RHI resembles the bottom of the model RHI image associated with the same time.

Finally, looking at the evolution of K_{DP} (Figure 3.3), the main focus is the development and evolution of a K_{DP} core, which can indicate both hydrometeor loading and development of negative buoyancy through latent heat from melting frozen hydrometeors. From $t = 2010$ s and $t = 2100$ s (panels a and d, respectively), there is not much going on except for the

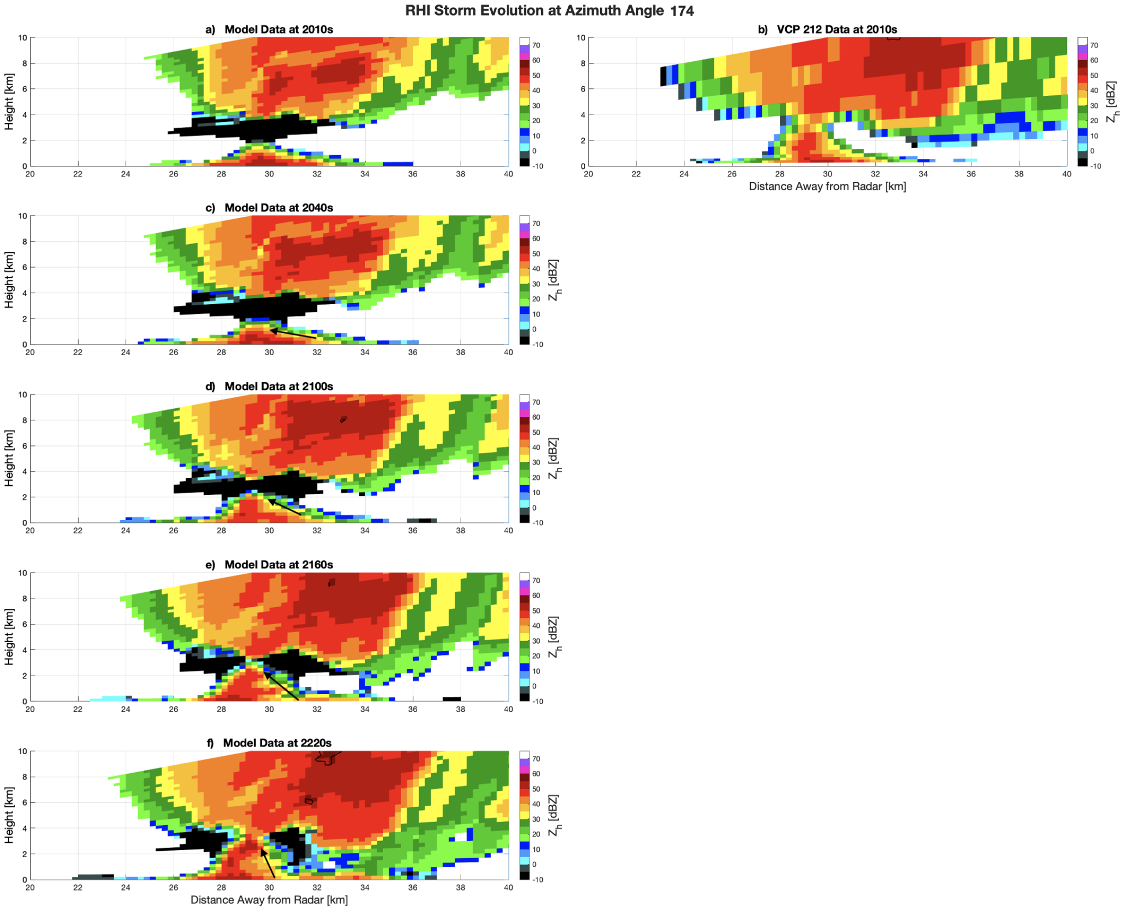

Figure 3.2: RHI images (model) and pseudo-RHI images (VCP 212) along azimuth angle 174 over the entire analysis time period. The model data is represented every 60 s while the pseudo-RHI images are interlaced every 4.5 min. The VCP scans are placed in time based on the start time of their scan. The black contours represent the 55 dBZ contour.

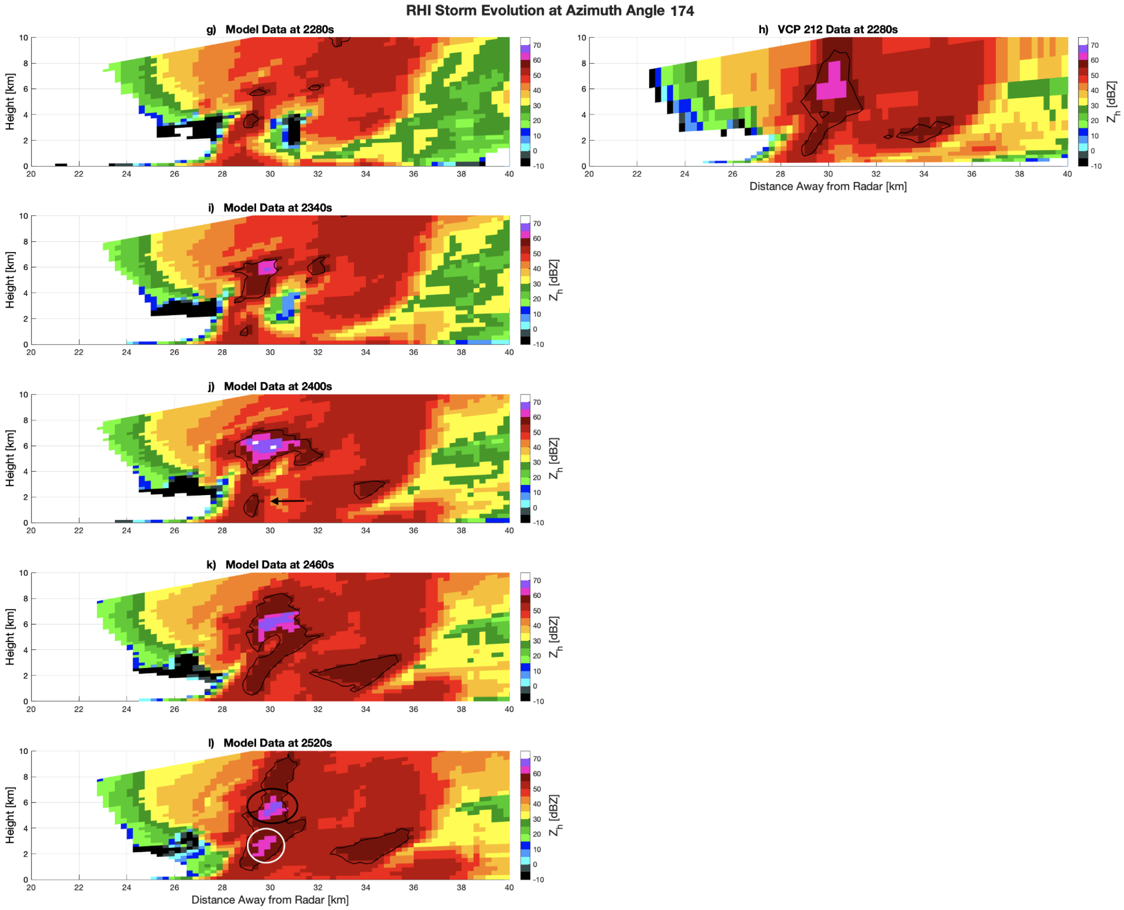

Figure 3.2 (*Continued*)

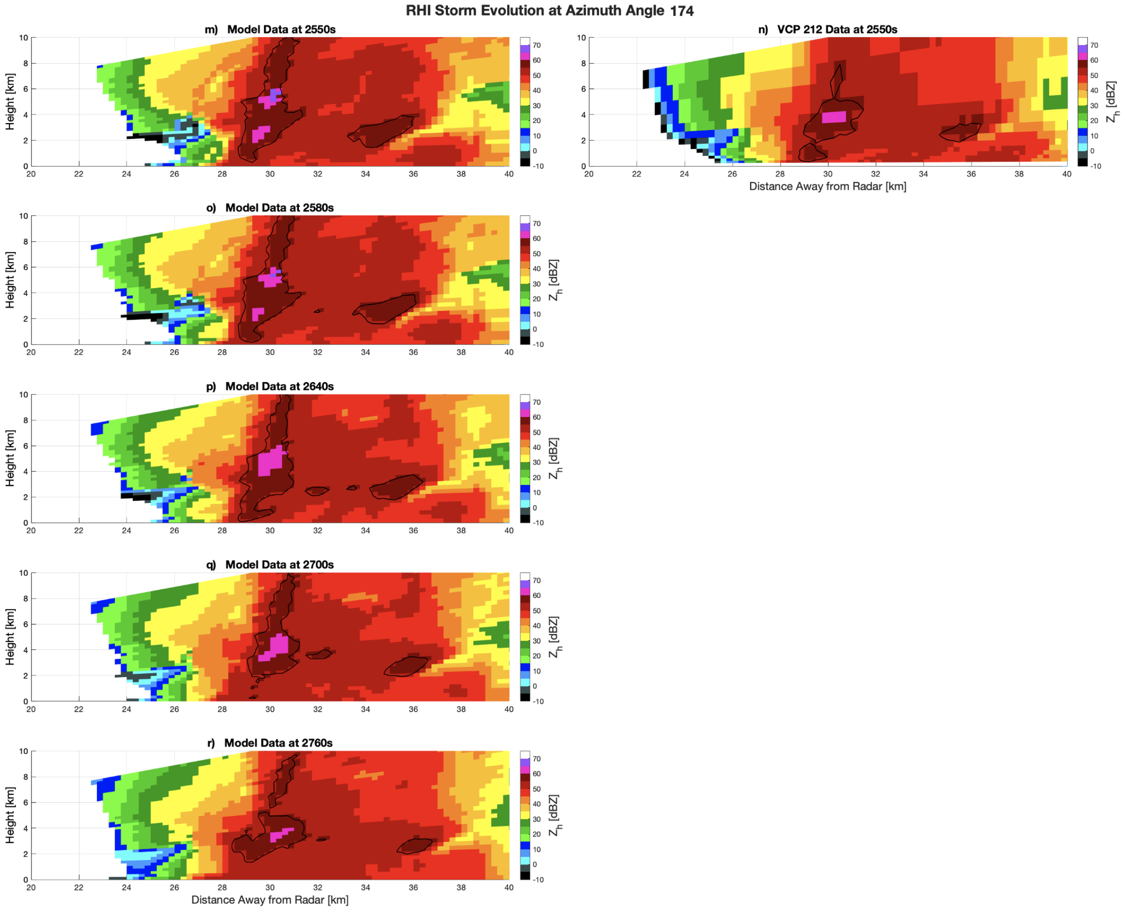

Figure 3.2 (*Continued*)

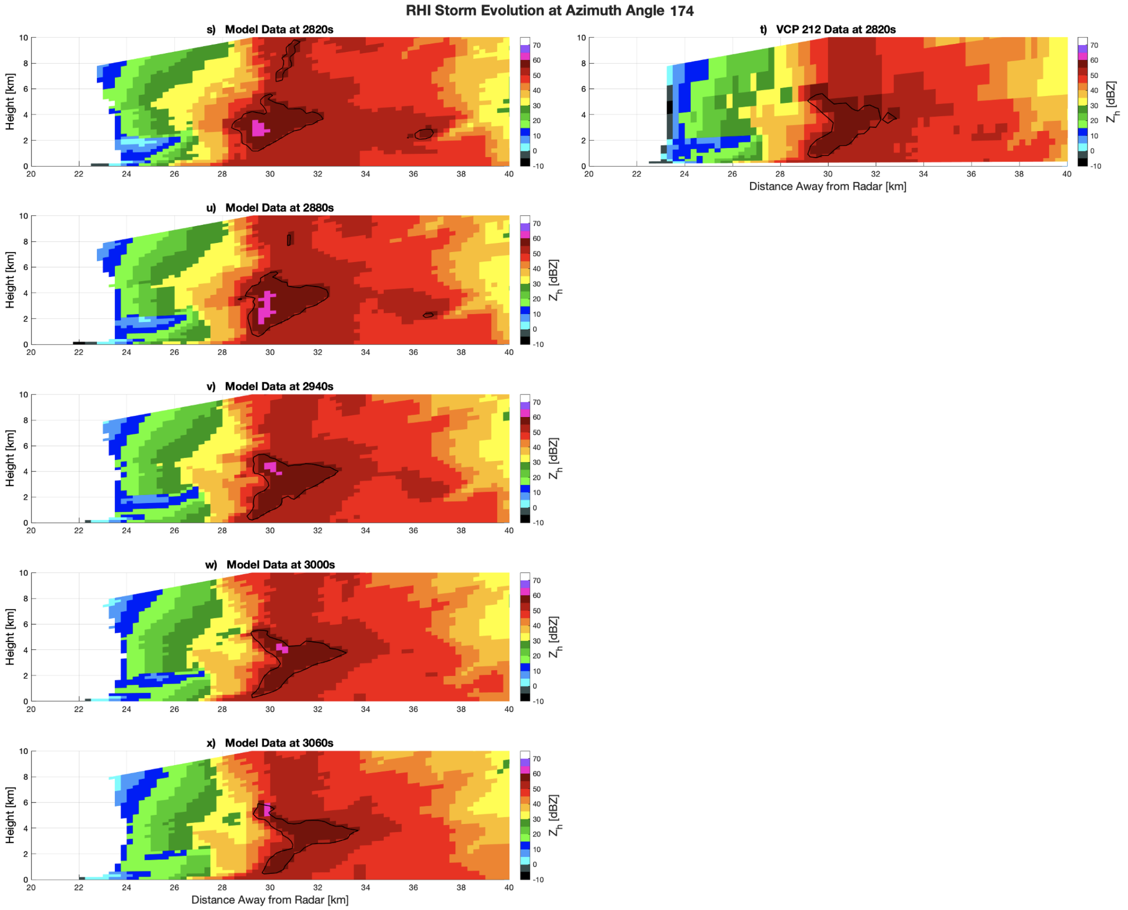

Figure 3.2 (*Continued*)

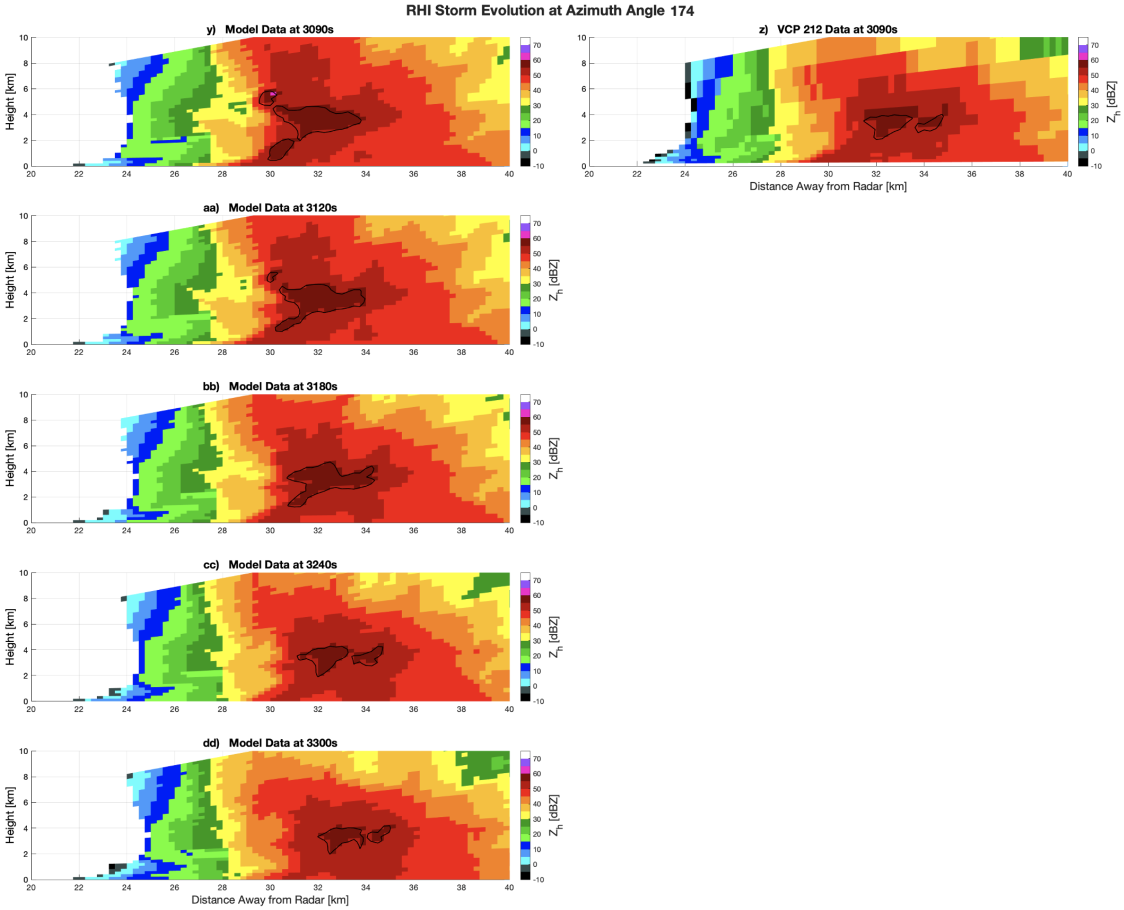

Figure 3.2 (*Continued*)

already existing elevated K_{DP} region aloft ($K_{DP} \geq 2°\text{km}^{-1}$ above 5 km AGL) from 31 to 36 km range. From $t = 2160$ s through $t = 2220$ s (panels e and f), there is a small region of K_{DP} values near 1° km^{-1} that begins to form near the surface (black arrows in panels e and f). While this region continues to develop, by $t = 2280$ s (panel g), a K_{DP} core develops around 4 km AGL and between 28 and 30 km range with values $\geq 2°$ km^{-1} (black circle in panel g). This region continues to grow and intensify through $t = 2460$ s (panel k). Furthermore, at $t = 2460$ s (panel k), an elevated K_{DP} appendage (denoted by black arrow in panel k) develops connecting the surface to the K_{DP} core, and this appendage stays in contact with the ”ground” through $t = 2820$ s (panel s). At $t = 2520$ s (panel l), the core begins to weaken before leveling off with a maximum value around 4° km^{-1} by $t = 2550$ s (panel m); however, the core continues to grow and merge with the already existing elevated K_{DP} region aloft. Also around $t = 2550$ s (panel m), the model data shows the overall descent of the elevated K_{DP} region as the bottom of the K_{DP} core begins to travel closer to the surface and the maximum in K_{DP} drops below 5 km AGL. Starting at $t = 2880$ s (panel u), the K_{DP} core is beginning to dissipate before shrinking to a small elevated K_{DP} region aloft centered around 34 km range and about 4 km AGL (panel dd).

As seen in the Z_h overview, VCP 212 does a good job of capturing the essence of the model domain. Although, the temporal resolution of VCP 212 makes it difficult to observe these features in their entirety. However, the general observations are still seen with the development, growth, and dissipation of a K_{DP} core being observed. To look at the coarseness of the VCP 212 sampling more specifically, just take the $t = 2280$ s (panel g & h) through $t = 2520$ s (panel l) time period. To be truly accurate, the pseudo-RHI for VCP 212 would not be completely available until around t = 2520 s (just after panel l) because of the temporal delay. Thus, the development of the elevated K_{DP} appendage connecting the K_{DP} core to the surface is missed until the VCP 212 scan starting at $t = 2550$ s (panel n), which would not even be completely available until close to $t = 2760$ s (panel r).

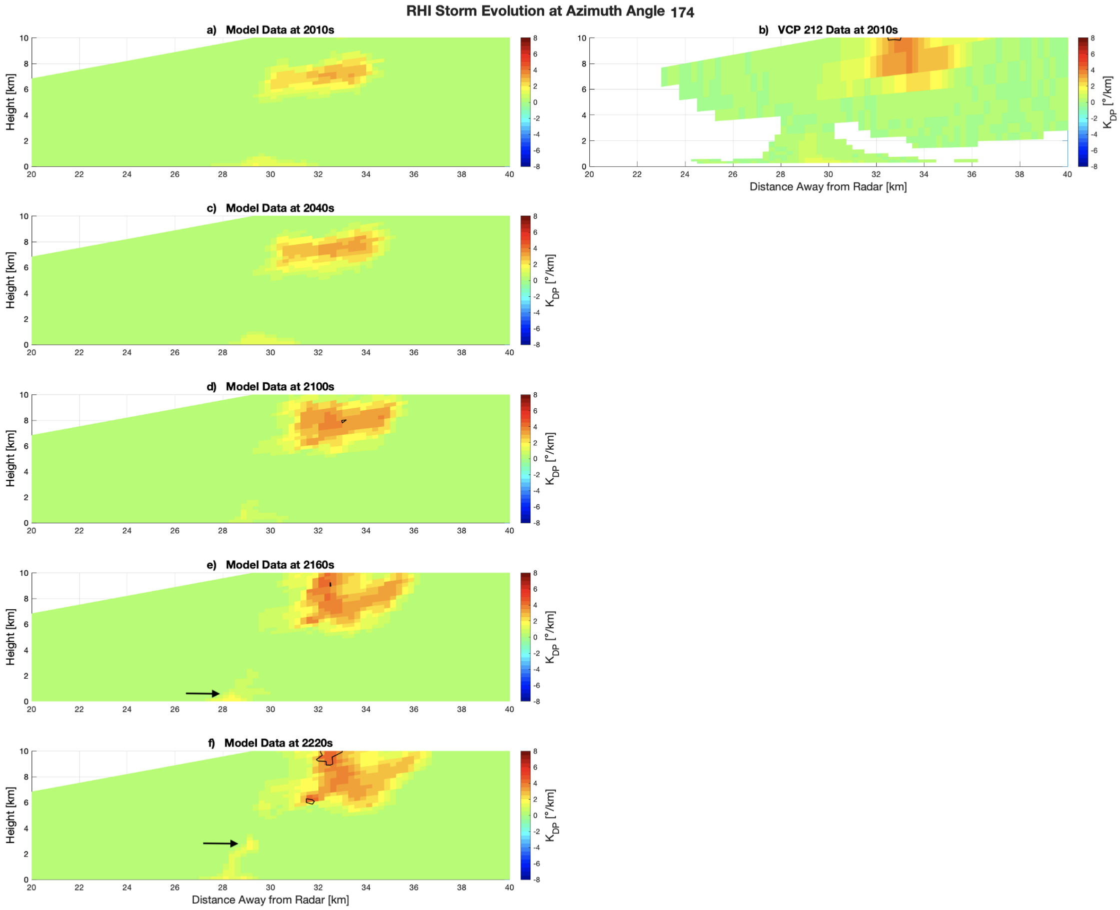

Figure 3.3: RHI images (model) and pseudo-RHI images (VCP 212) of K_{DP} along azimuth angle 174 over the entire analysis time period. The model data is represented every 60 s while the pseudo-RHI images are interlaced every 4.5 min. The VCP scans are placed in time based on the start time of their scan. The black contours represent the 55 dBZ contour.

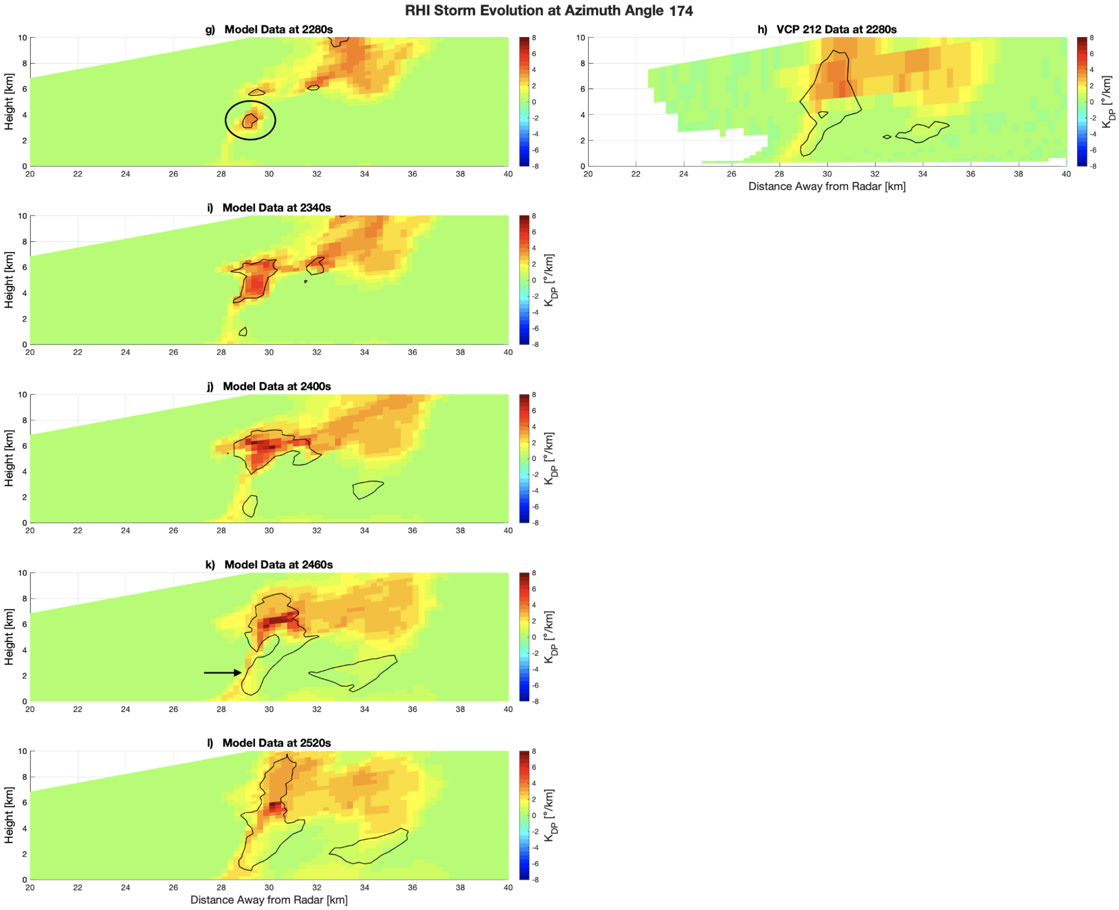

Figure 3.3 (*Continued*)

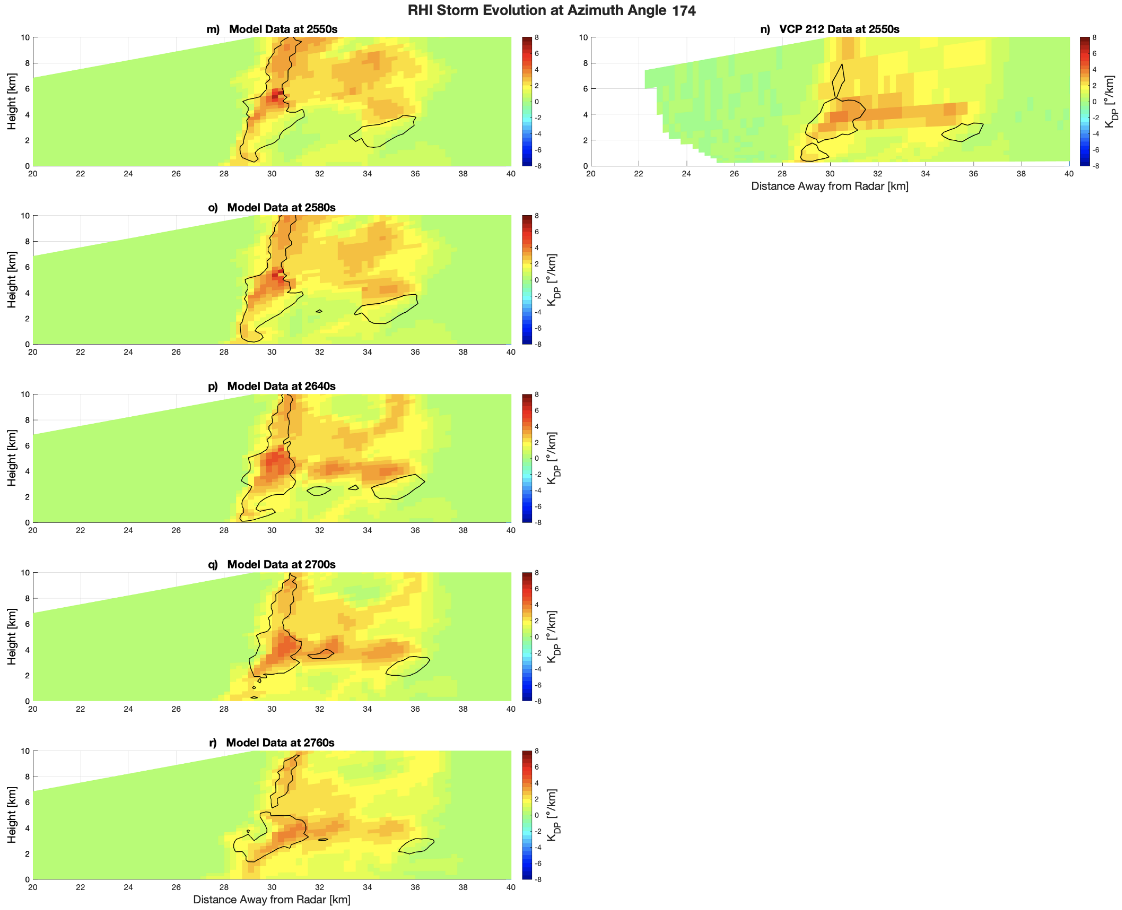

Figure 3.3 (*Continued*)

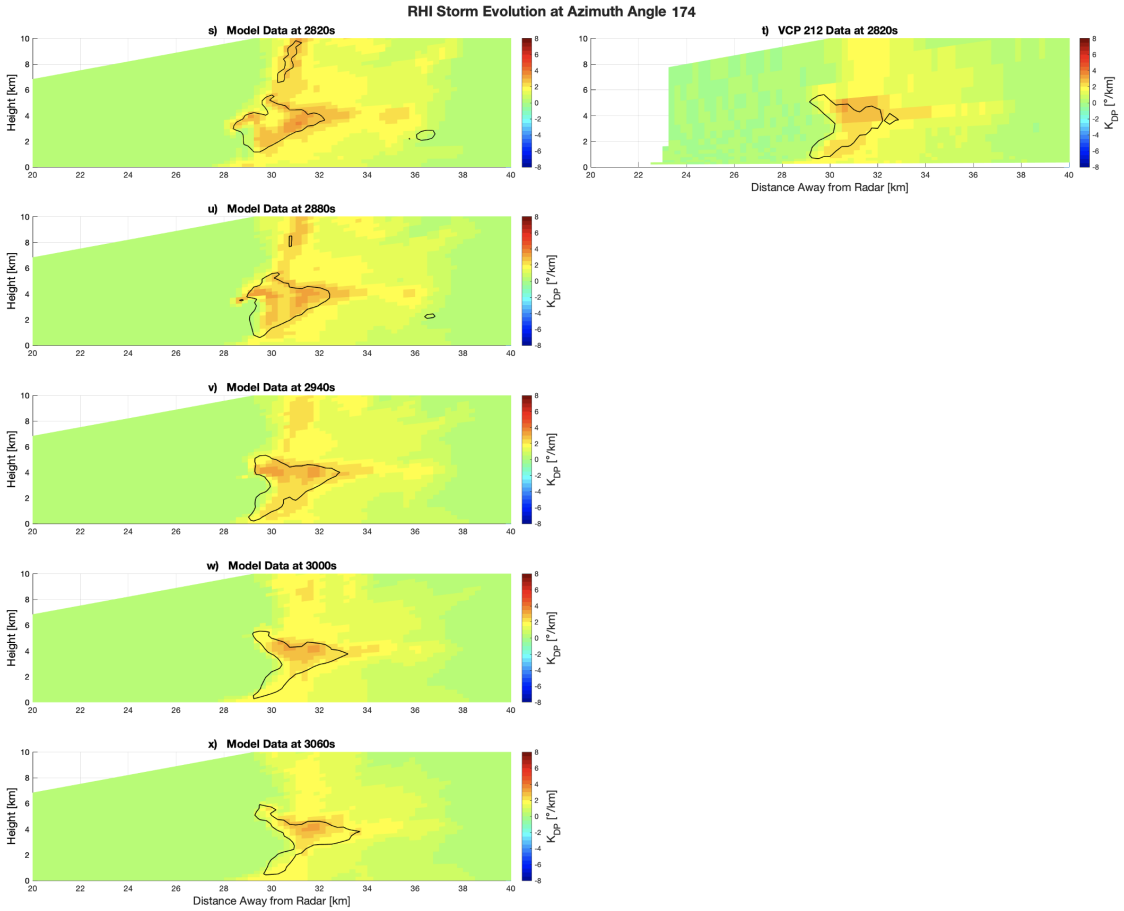

Figure 3.3 (*Continued*)

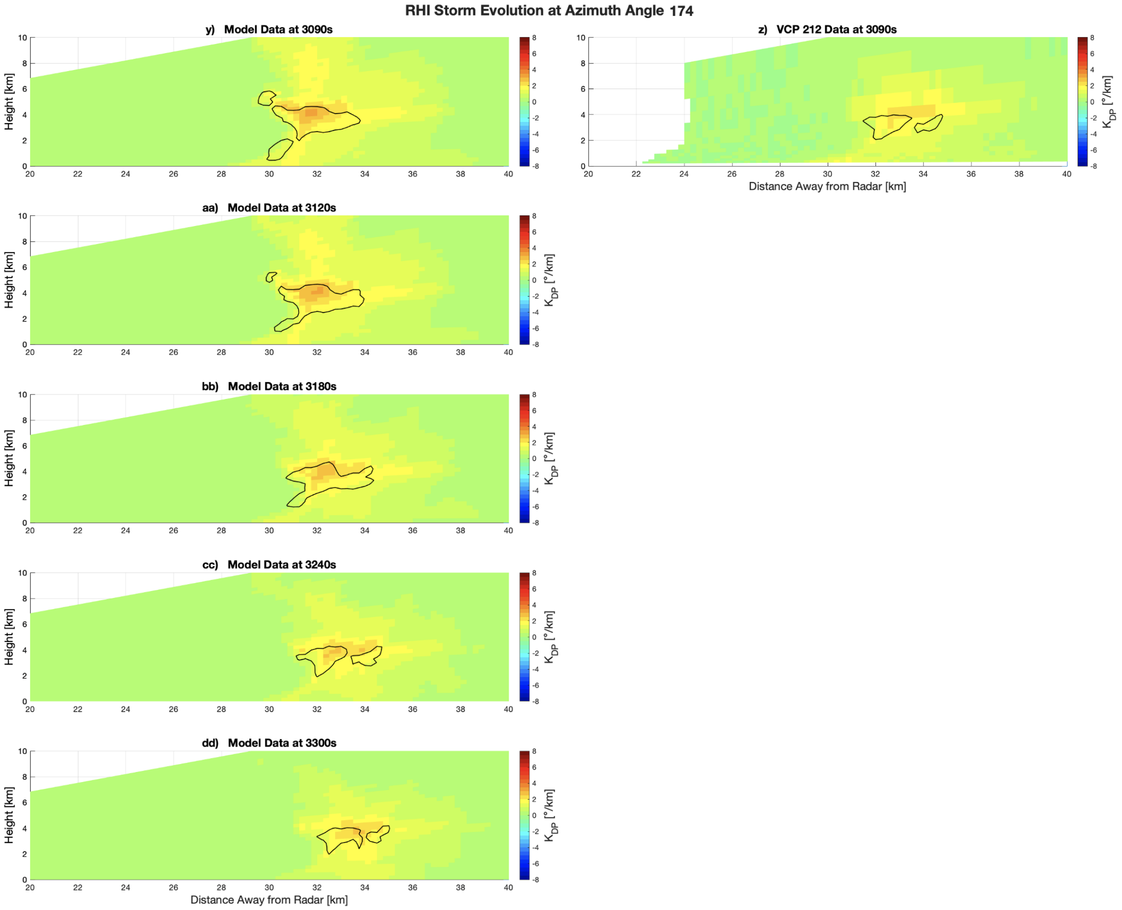

Figure 3.3 (*Continued*)

Moving into a brief qualitative comparison between the other scanning strategies and the model data, these comparisons will focus more on the observations of the microburst precursor signatures and the microburst itself as opposed to the evolution of the storm that was presented above. These comparisons will show the slower temporal resolution for the true RHI scanning strategy; however, the model data and imaging scanning strategies will be shown at 60 s temporal resolution for simplicity. The increased temporal resolution associated with the imaging cases will be analyzed more closely during the quantitative analysis in Section 3.1.1.2.

The first two signatures to be qualitatively analyzed are the mid-level convergence and surface divergence signatures in V_r (Figure 3.4). When looking at the evolution of mid-level convergence, the true RHI image does not show the development of this signature very well compared to the other scanning strategies due to its degraded temporal resolution. For example, when looking in between times $t = 2220$ s and $t = 2400$ s, the vertical development of strong outbound radial velocities leads to the development of a mid-level convergence signature in the mid-levels of the storm, but the evolution is not well captured by the true RHI scans.

Other than the temporal resolution, the true RHI scans are still more representative of the model environment compared to the imaging scans at similar times. For example, at $t = 2520$ s, as the spoiled beamwidth increases, the emulated data loses the general structure seen in the model data especially in the large area of outbound V_r values about 6 km to 10 km AGL and 30 km range (black circle in all panels at $t = 2520$ s). Furthermore, at $t = 2520$ s, there is a visible mid-level convergence signature between 4 km and 6 km AGL at 30 km range. However, this convergence signature is harder to see in the 5° and 10° imaging scans (black square in Figure 3.5). It also appears that the 10° imaging scan did not even detect a convergence signature within that region but rather has relatively uniform outbound radial velocities.

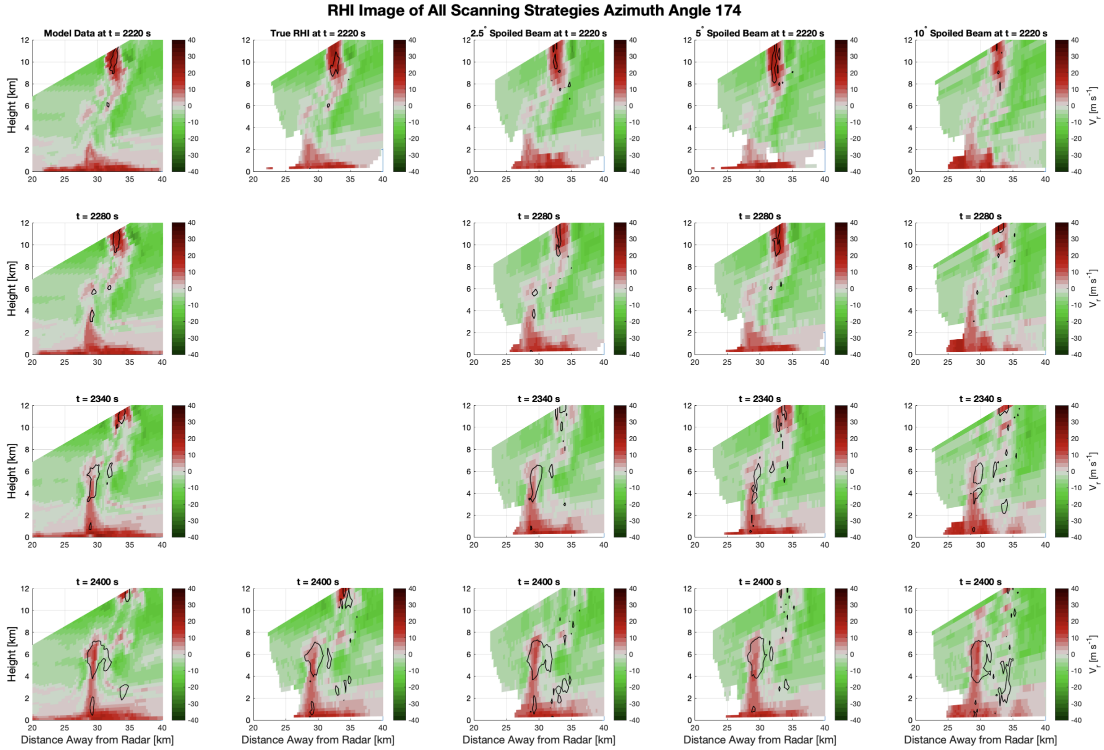

Figure 3.4: Evolution of V_r as observed by the model data (first column), true RHI scanning strategy (second column), 2.5° imaging (third column), 5° imaging (fourth column), and 10° imaging (fifth column). Resolution for all scanning strategies is 60 s except for the true RHI images which have 2.5 min resolution. For true RHI images in between two minute markers, the RHI image is placed after the actual scan time. The black contours represent the 55 dBZ contour.

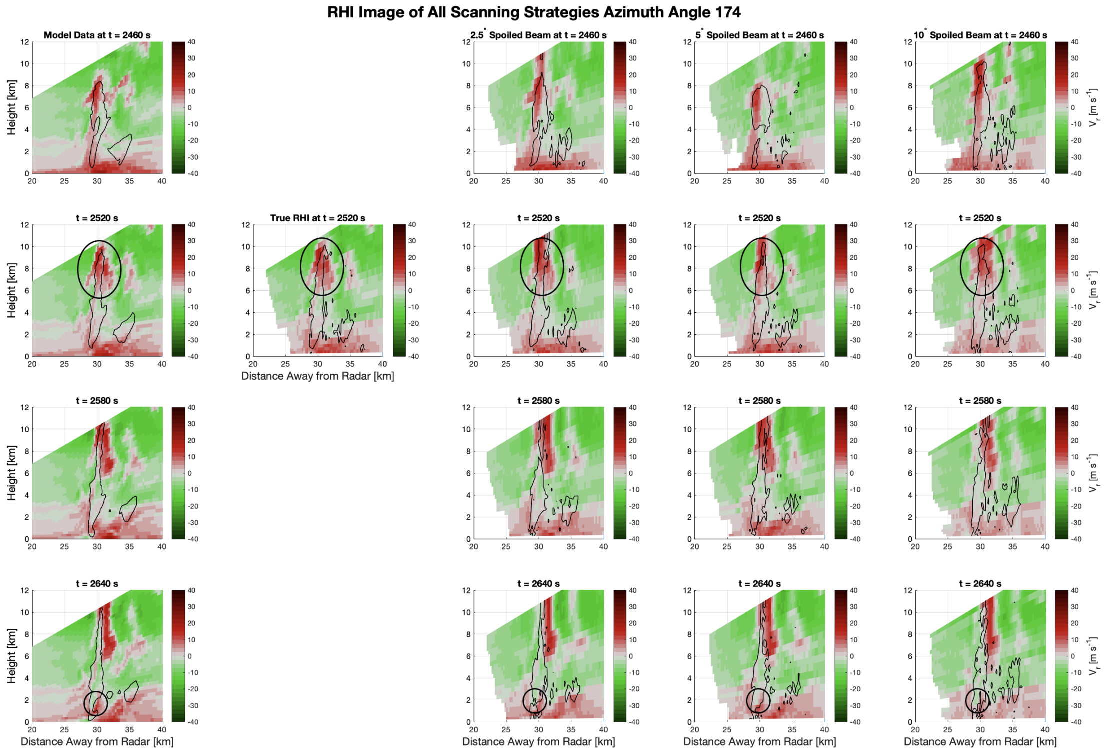

Figure 3.4 (*Continued*)

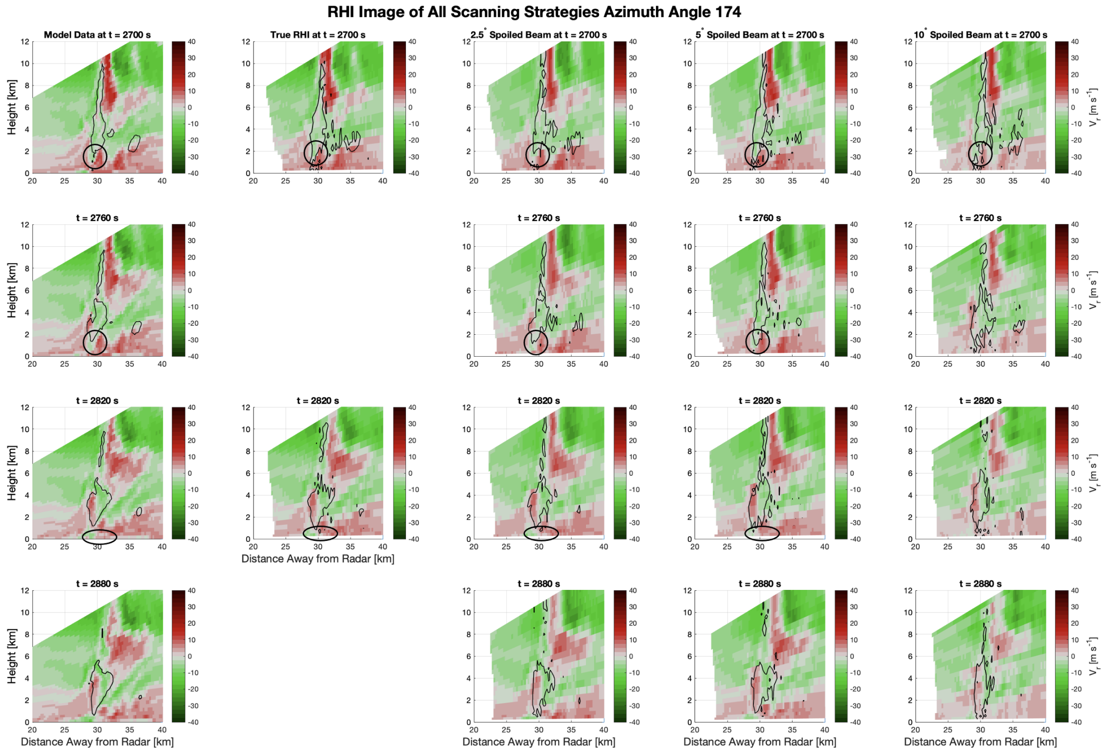

Figure 3.4 (*Continued*)

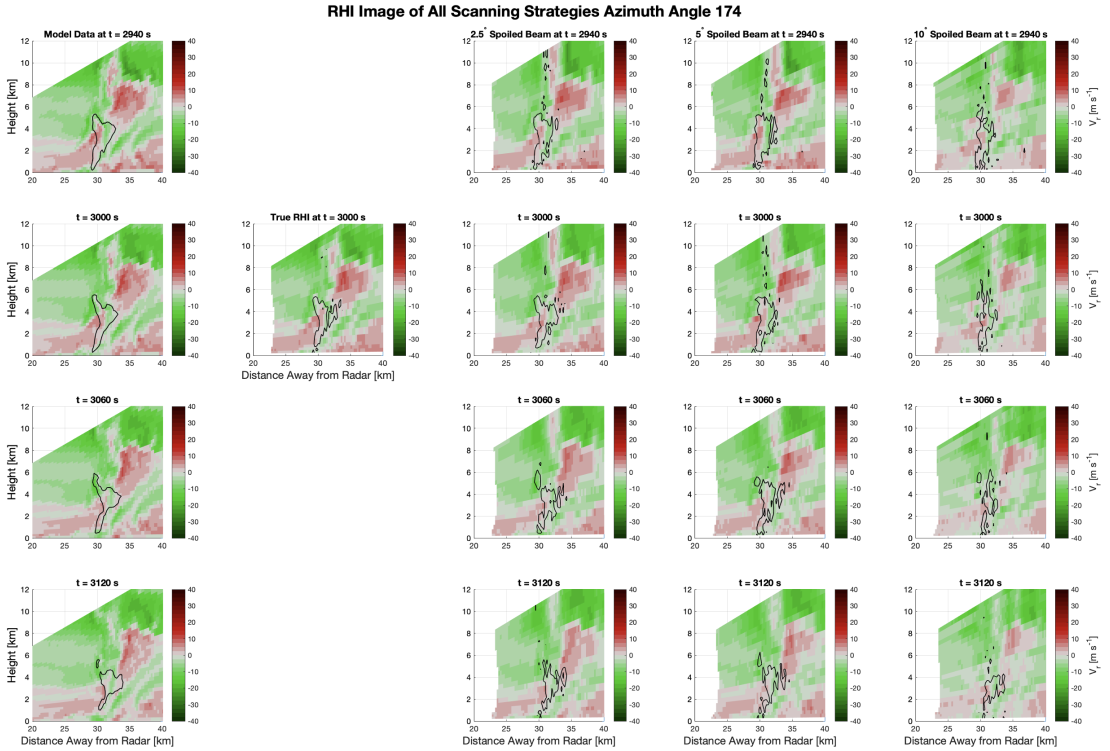

Figure 3.4 (*Continued*)

Furthermore, at the same time period, notice how the V_r values in the lowest 2 km are much more smoothed out and have a lower maximum outbound velocity around 30 km as spoiled beamwidth increases (black circles in Figure 3.5). This greatly impacts the 10° imaging scans ability to detect any important velocity signatures below the 2 km AGL level. This is extremely problematic as this is the region associated with both the “midair” and surface microbursts. The “midair” microburst is first observed at $t = 2640$ s by all scanning strategies (black circle annotations at $t = 2640$ s). However, the “midair” microburst can be tracked descending to the surface in the model, 2.5° imaging, and 5° imaging from the initial time $t = 2640$ s to $t = 2820$ s when it fully reaches the surface; however, the 10° imaging only detects the “midair” microburst through $t = 2700$ s instead of observing it all the way to the surface (black circle annotations from $t = 2640$ s through $t = 2820$ s). The surface divergence lasts until at least $t = 3120$ s in all scanning strategies except the 10° imaging, which never fully resolves the observations of the “midair” or surface

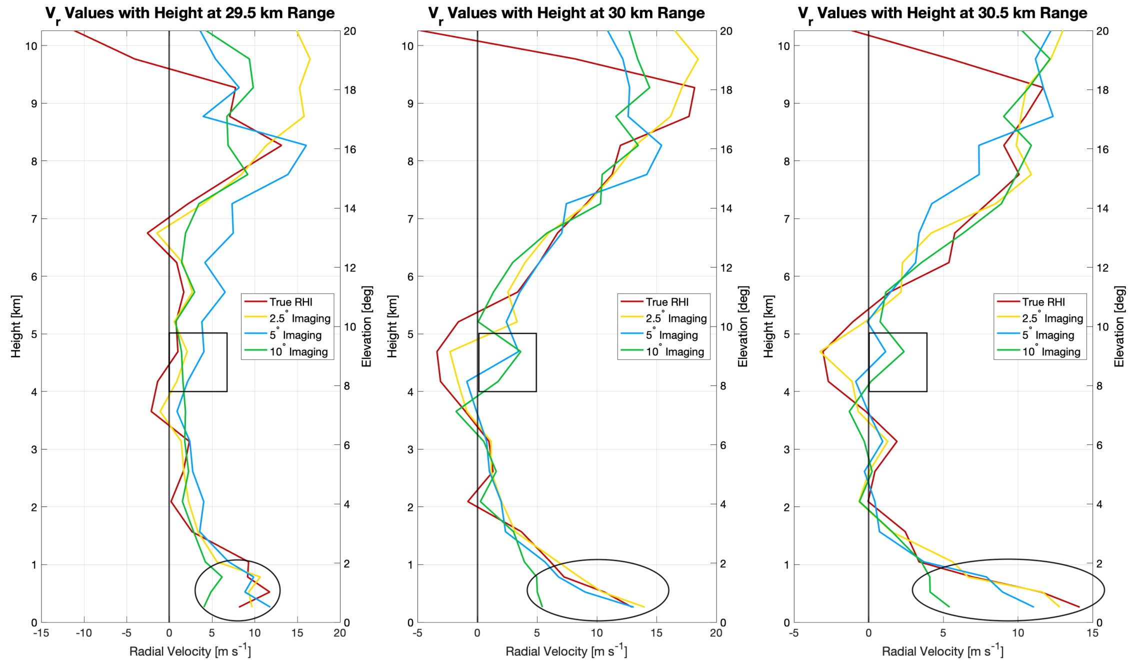

Figure 3.5: Vertical profiles of V_r at three ranges (29.5 km, 30 km, and 30.5 km) along azimuth angle 174. Black square annotations show region in the midlevels (4 - 5 km AGL) where true RHI and 2.5° imaging show a convergent signature where 5° and 10° imaging do not. Black circle annotations show where 10° imaging struggled with detecting radial velocity signatures below 1 km AGL.

microbursts likely due to sidelobe contamination effects (example of this effect can be seen in Figure 3.5). Even with the coarse temporal sampling associated with the true RHI scans, the “midair” microburst is observed at $t = 2700$ s before the surface microburst is detected at $t = 2820$ s.

There are a few things that become apparent when examining the evolution of the DRC (Figure 3.6). First, when comparing the RHI images of the true RHI scans (second column in Figure 3.6), the 2.5 minute resolution misses a large amount of the evolution of the DRC. For example, the development of a Z_h column occurs between the true RHI images shown at $t = 2220$ s and $t = 2400$ s, yet the true RHI images just show that the Z_h column appears without showing the evolution of how the signature appeared. Furthermore, the merger of the lower and upper elevated Z_h regions ($t = 2340$ s to $t = 2520$ s) is not as apparent in the true RHI scans as it is in the other scanning strategies, even with only 60 s temporal resolution.

However, what the true RHI scans lack in temporal resolution, it makes up for by capturing the essence of the storm the best. When comparing the images at $t = 2220$ s, $t = 2520$ s, and $t = 2820$ s, the true RHI scans capture the model environment the best with similarities between the size and shape of the Z_h column, while the imaging cases have a harder time picking up smaller features as a result of sidelobe contamination. This is most notably observed at $t = 3000$ s where the true RHI barely observes the ≥ 60 dBZ region around 4 km AGL and 30 km range, yet neither the 5° or 10° imaging cases detected this signature. This lack of peak detection was most prevalent in the 10° imaging case where missed detections of ≥ 60 dBZ also occurred at $t = 2760$ s. This decrease in peak detection was likely caused by sidelobe contamination due to the large spoiled beamwidth of the 10° imaging averaging down the maximum value between 3 – 4 km AGL (Figure 3.7).

Another thing to notice is the presence of smearing in the imaging cases not seen in the true RHI scans, and this smearing occurs from sidelobes located within the Z_h column influencing the observations at various other locations within the scanning domain. When

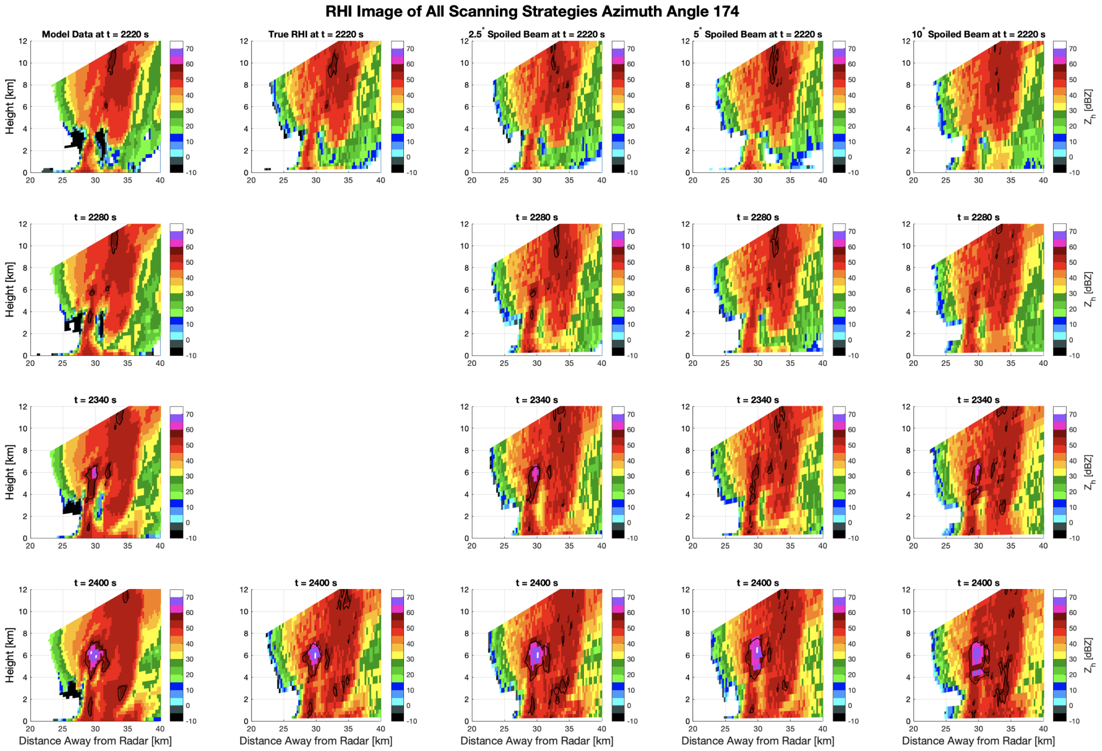

Figure 3.6: Evolution of the DRC as observed by the model data (first column), true RHI scanning strategy (second column), 2.5° imaging (third column), 5° imaging (fourth column), and 10° imaging (fifth column). Resolution for all scanning strategies is 60 s except for the true RHI images which have 2.5 min resolution. For true RHI images in between two minute markers, the RHI image is placed after the actual scan time. The black contours represent the 55 dBZ contour.

looking at $t = 2520$ s, it is evident that some smearing is occurring, which is likely caused by sidelobe contamination. At $t = 2520$ s, only the 10° imaging case has the Z_h column stretching toward the surface to below 1 km AGL (Figure 3.8). Furthermore, at $t = 2520$ s, there is evidence of smearing that occurs at the top of the Z_h column in all imaging cases. The 2.5° imaging case has the elevated Z_h region reaching the top of the scanning environment (20° elevation) seen at $t = 2520$ s in Figure 3.6. However, the 5° and 10° imaging cases do not have these signatures reaching 20° elevation ($\approx$ 10 km AGL), but smearing is still present with $Z_h \geq 50$ dBZ at the 19° elevation not seen in the model data nor true RHI scans. Figure 3.8 shows that all imaging cases have $Z_h \geq 50$ dBZ stretching to the 20° elevation angle ($\approx$ 10 km AGL) at a range of 29.75 km.

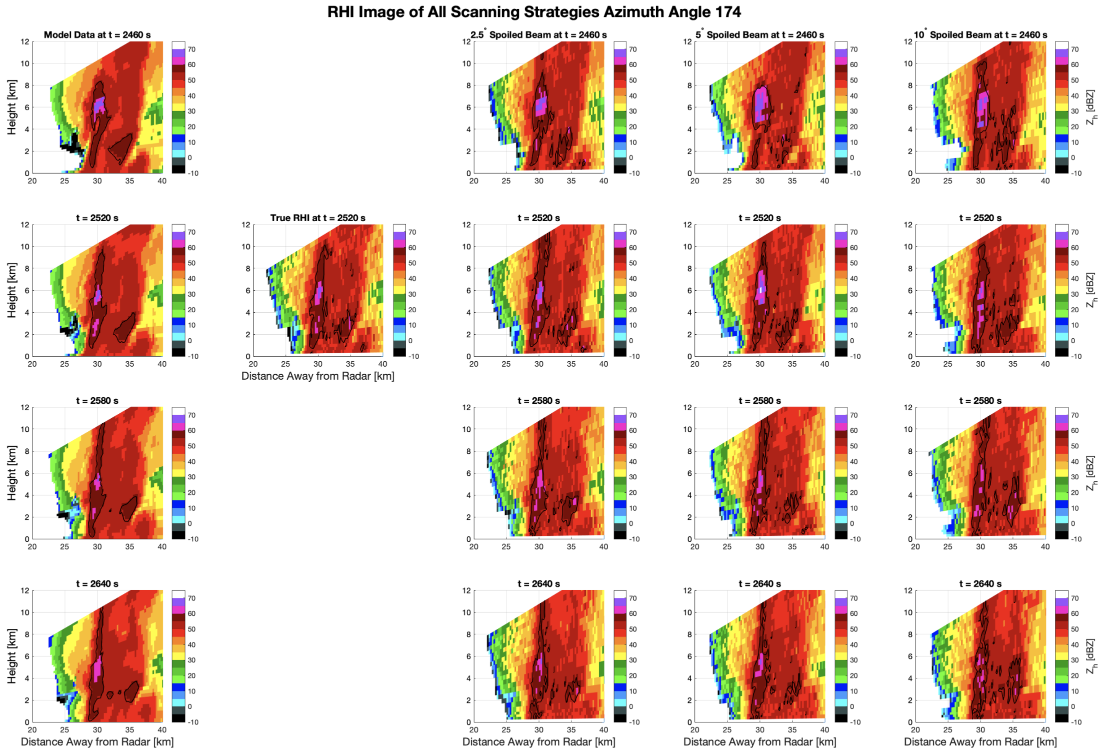

Figure 3.6 (*Continued*)

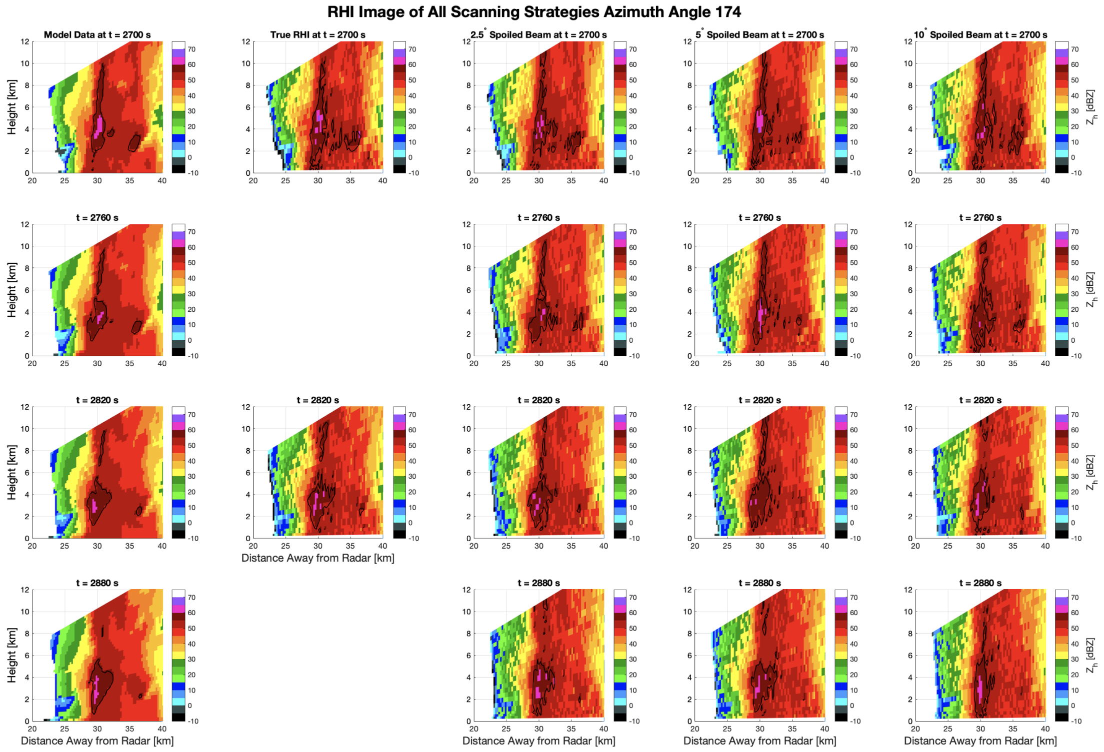

Figure 3.6 (*Continued*)

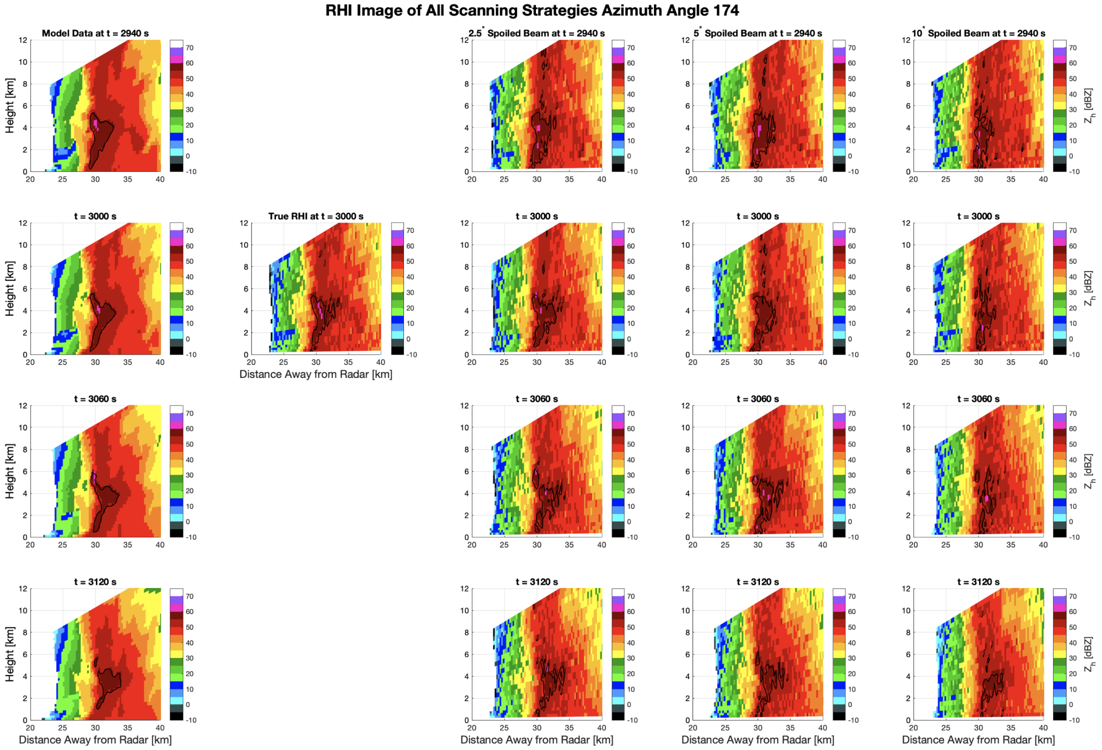

Figure 3.6 (*Continued*)

Finally, moving on to the K_{DP} core, the qualitative analysis is similar to the one for the DRC above. The temporal resolution associated with the true RHI scans (second column in Figure 3.9) greatly hinders the observations of the development and evolution of the K_{DP} core. Between $t = 2220$ s and $t = 2400$ s, the imaging scans and model data show the development of an elevated K_{DP} region ($K_{DP} \geq 2.0^\circ$ km^{-1}) where the true RHI scans only show it present at $t = 2400$ s. Furthermore, the true RHI scans miss much of the evolution of the K_{DP} core due to the temporal resolution. Between $t = 2520$ s and $t = 2700$ s, the true RHI scan misses the descent of the peak K_{DP} values from being around 6 km AGL at $t = 2520$ s to being around 4 km AGL at $t = 2700$ s, and this descent is captured by the imaging scans even with only 60 s temporal resolution.

The true RHI scans do the best job of representing the model environment when compared at the same times such as $t = 2220$ s, $t = 2520$ s, and $t = 2820$ s. This representativeness tends to decrease with increasing spoiling beamwidth as seen at $t = 2520$ s where

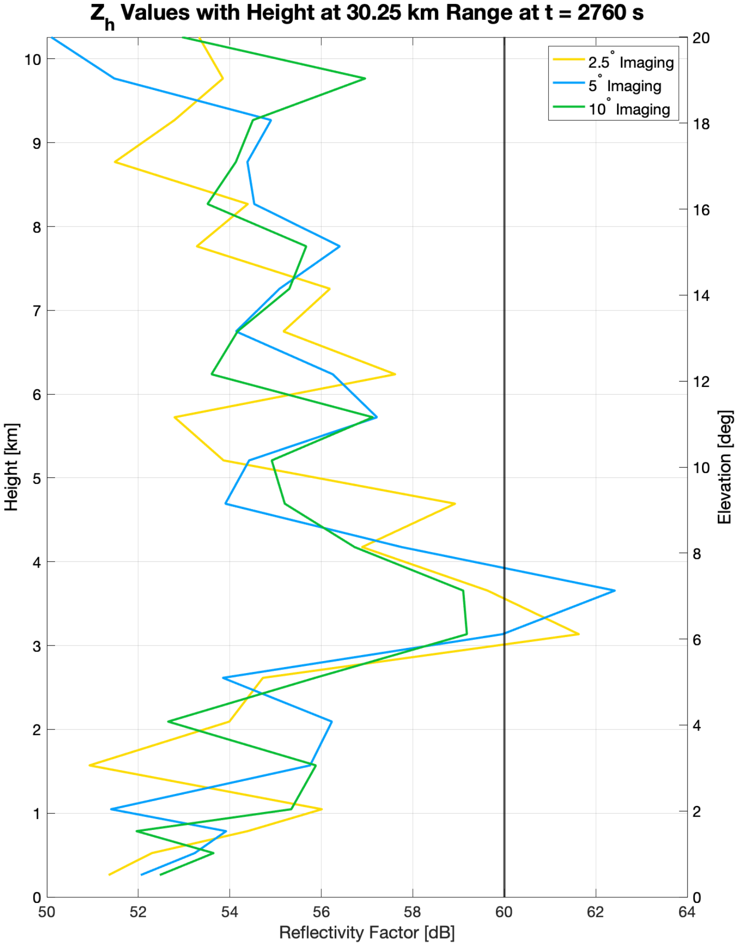

Figure 3.7: Vertical profile of Z_h at $t = 2760$ s at 30.25 km range along azimuth angle 174 that shows the 10° imaging miss the detection of ≥ 60 dBZ values between 3 – 4 km AGL. There was no true RHI scan at this time.

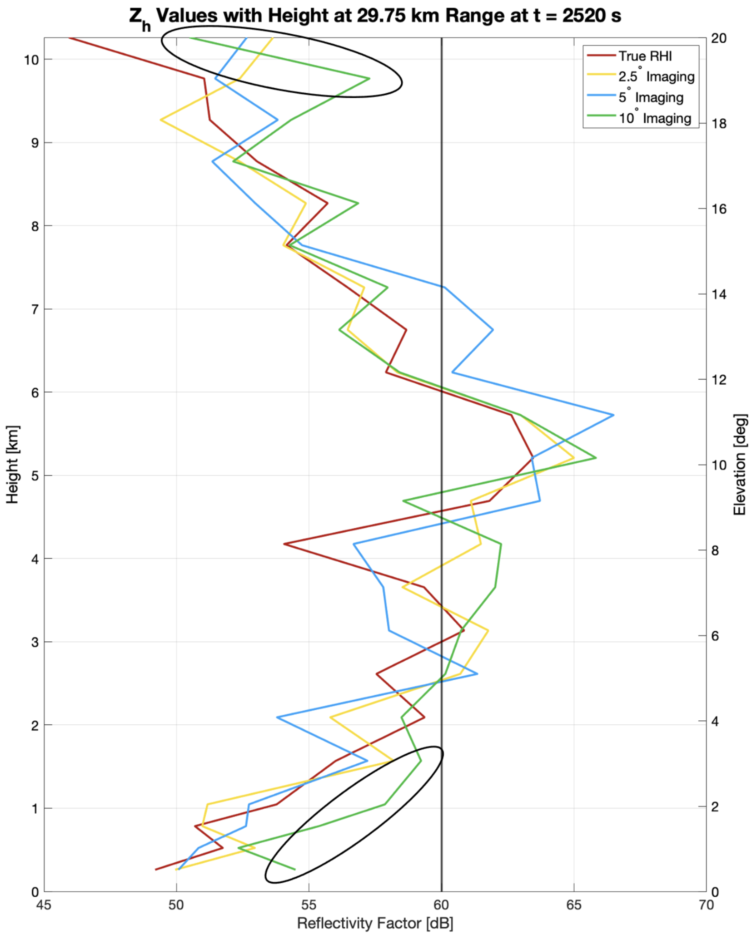

Figure 3.8: Vertical profile of Z_h values with height at 29.75 km range along azimuth angle 174 for true RHI (red), 2.5° imaging (yellow), 5° (blue), and 10° (green). Smearing effects are annotated with black circles. The vertical black line denotes the 55 dBZ level.

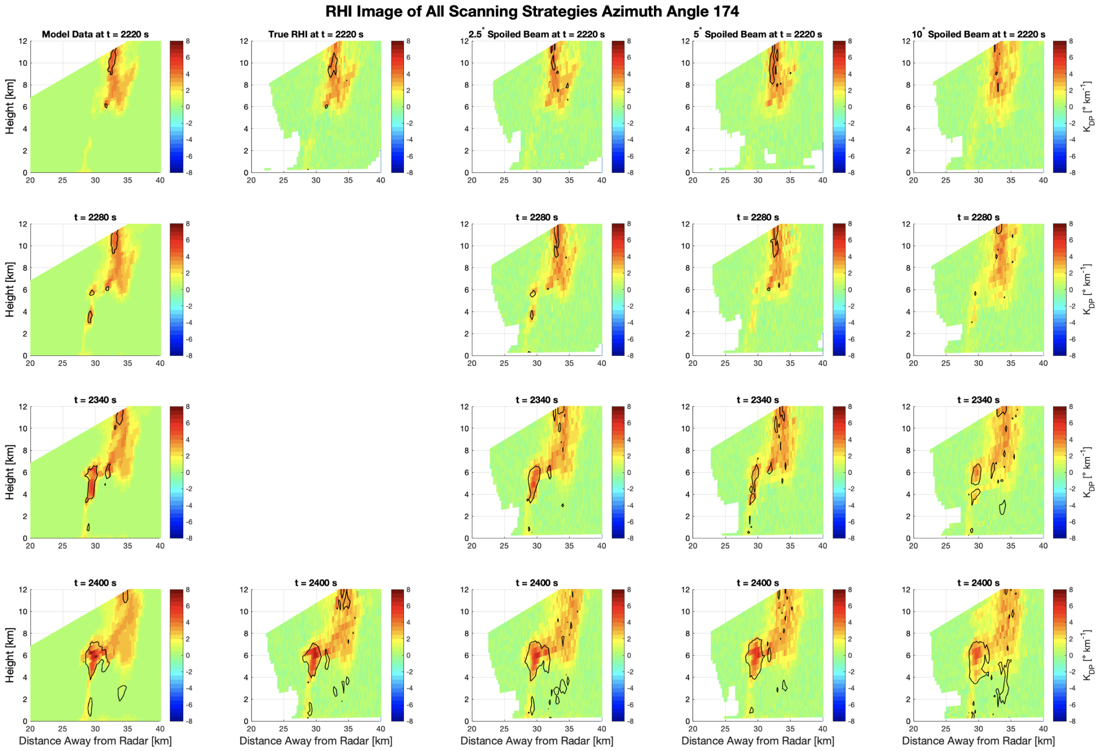

Figure 3.9: Evolution of the K_{DP} core as observed by the model data (first column), true RHI scanning strategy (second column), 2.5° imaging (third column), 5° imaging (fourth column), and 10° imaging (fifth column). Resolution for all scanning strategies is 60 s except for the true RHI images which have 2.5 min resolution. For true RHI images in between two minute markers, the RHI image is placed after the actual scan time. The black contours represent the 55 dBZ contour.

the bottom of the K_{DP} core is under-detected by both the 5° and 10° imaging scans (Figure 3.10). This decrease is again seen in at $t = 3000$ s where the elevated K_{DP} region centered around 4 km AGL loses its size and shape with increasing spoiled beamwidth. Furthermore, at $t = 2820$ s, the effects of smearing are again present in the 10° imaging scan where the elevated K_{DP} values ($\geq 2^\circ$ km^{-1}) reach the surface which is not seen in either the model data nor the other scanning strategies.

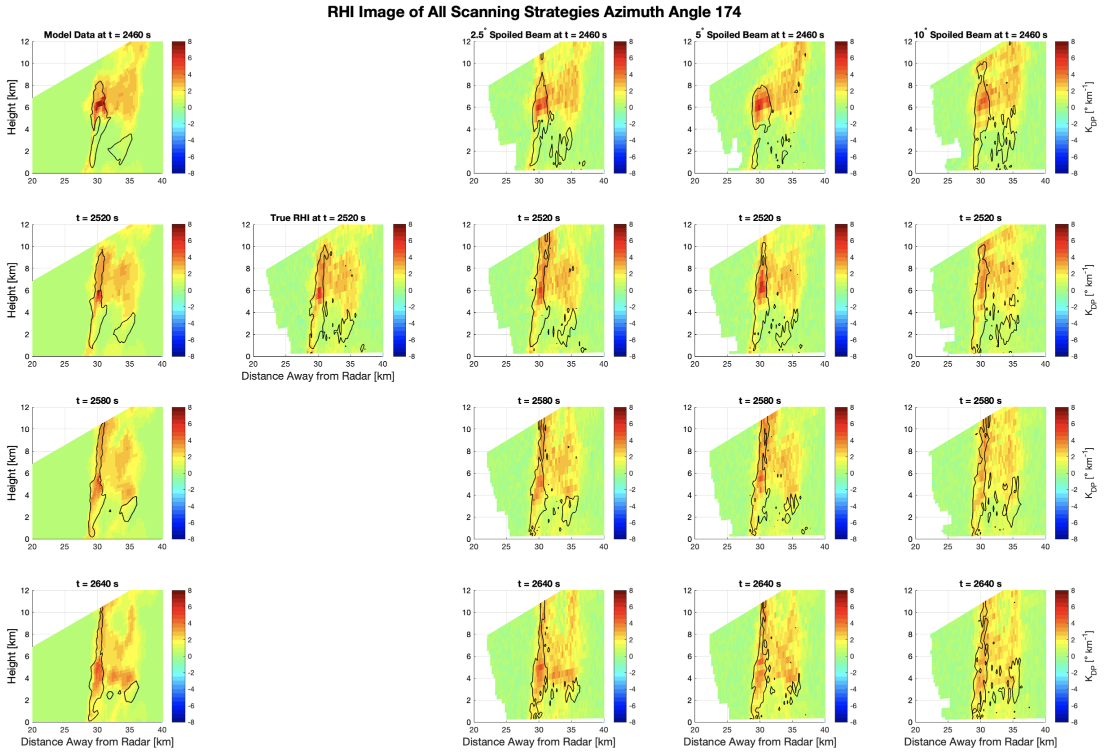

Figure 3.9 (*Continued*)

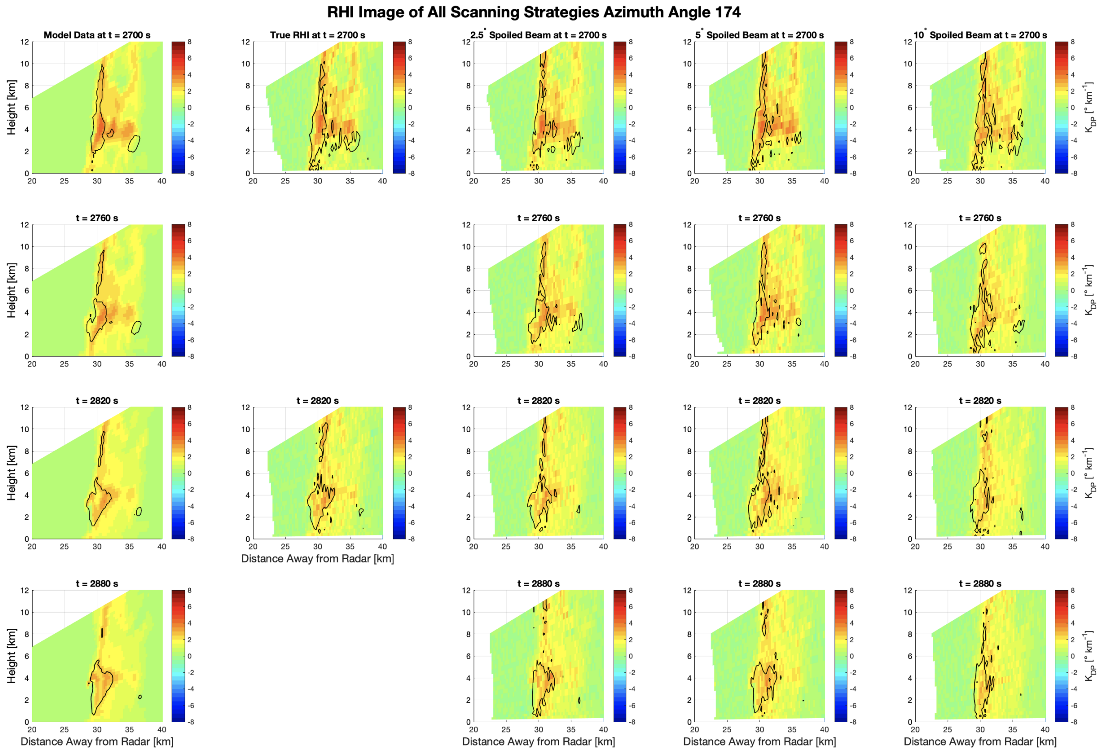

Figure 3.9 (*Continued*)

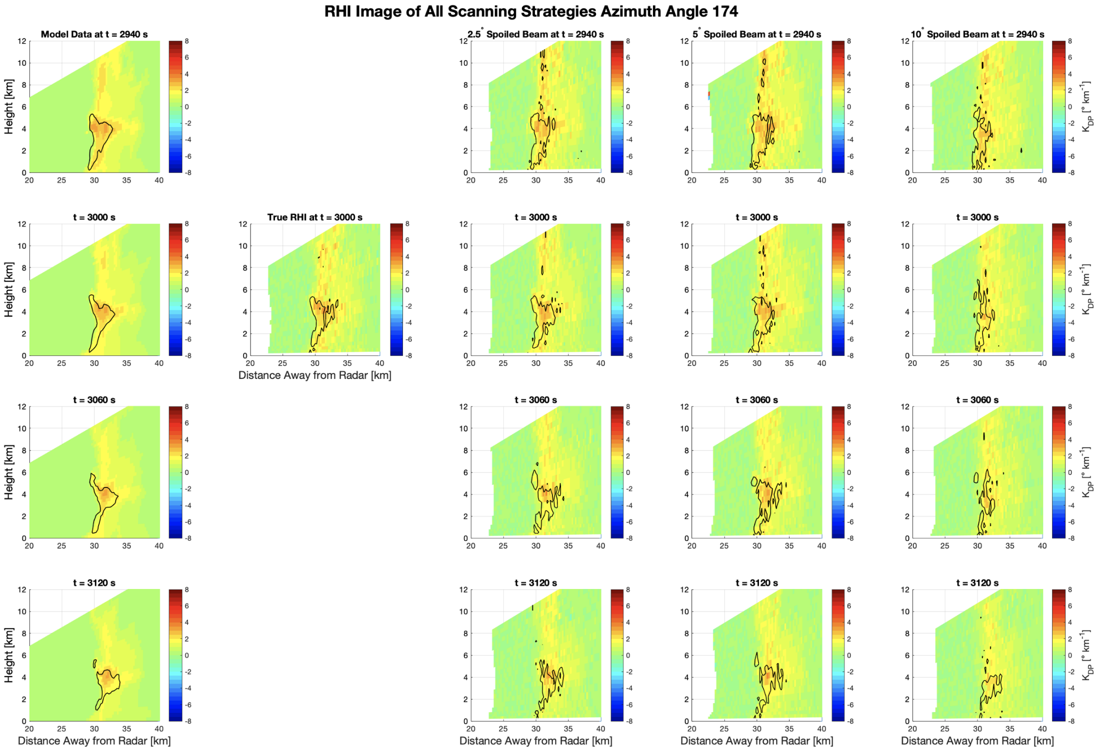

Figure 3.9 (*Continued*)

3.1.1.2 Quantitative Analysis

The previous qualitative analysis proved the presence of microburst precursor signatures consistent with theory and past observations associated with a wet microburst generated from a NWP simulation. In this section, further analysis is performed to quantify these different signatures into measurable quantities that provide an empirical baseline for comparisons between the different scanning strategies. An explanation of the different signatures discussed below can be found in 2.3.2. It is worth repeating that these quantified measures are based on average metrics calculated from all 5 errors sets, and because of this, may not fully represent the previous observations from the qualitative analysis in Section 3.1.1.1.

The first signature to be quantified is the surface divergence to help orient oneself into the evolution of the storm into two main parts: before and after the microburst reaches the surface. This distinction is important because the point of a precursor signature is to warn

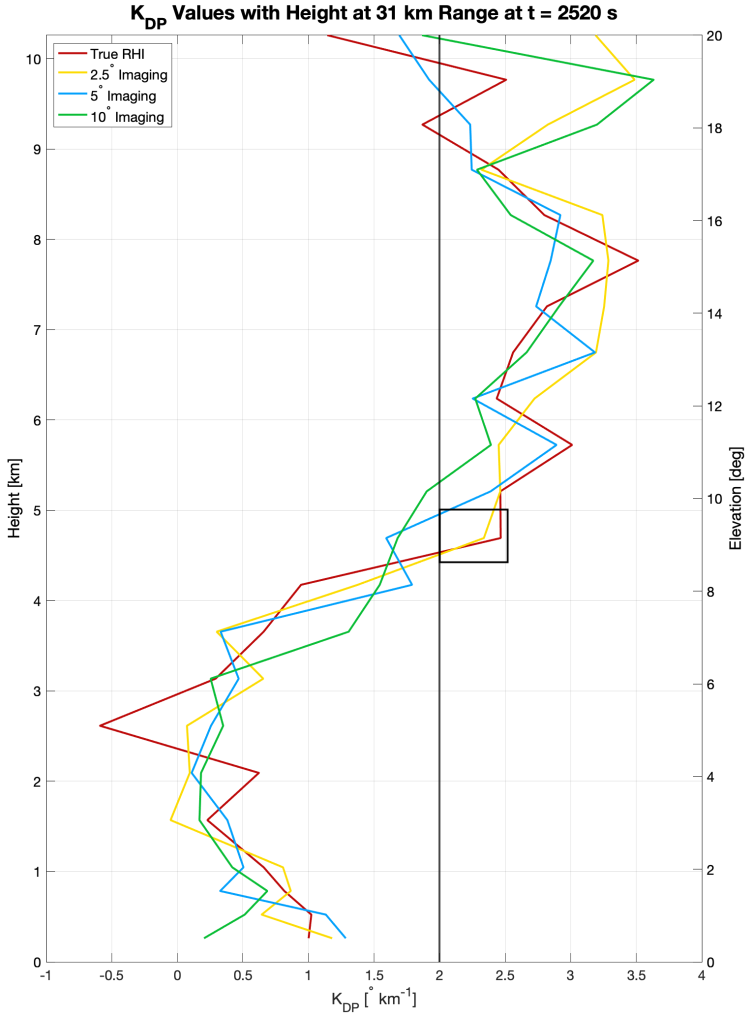

Figure 3.10: Vertical Profile of K_{DP} at $t = 2520$ s at 31 km range along azimuth angle 174. Black square showcases the under-detection of the bottom of the K_{DP} Core bottom by the 5° and 10° imaging scanning strategies.

of an impending microburst. Thus, the evolution of the precursor signatures will analyzed as either before or after the microburst reaches the surface. All plots showcase the temporal resolution of the data by plotting only the last known data point available at any given time. For example, VCP 212 remains constant for 4.5 min of data until the next full update is available (18 data points at 15 s resolution) while 2.5° imaging is only constant for 1 min of data (4 data points at 15 s resolution). That is, at any given time, the plots indicate the last measured value of the quantity plotted. Furthermore, for all plots presented below, the same color will represent each scanning strategy throughout (i.e., model data is orange, true RHI is red, 2.5° imaging is yellow, 5° imaging is blue, 10° imaging is green, and VCP 212 is grey.)

When looking at Figure 3.11, we see the maximum radial ΔV plotted for each scanning strategy along with a plot of the total area associated with $\Delta V \geq 10$ m s^{-1}. Looking at the figure, the first thing that is apparent is the presence of maximum $\Delta V \geq 10$ m s^{-1} throughout much of the analysis period in the model data (orange line); however, the coupling of the ΔV calculation with the total area covered by said signature helps shed light into when the microburst actually occurs at the surface. Namely, when looking at the evolution of the maximum radial ΔV along with the total area covered by a $\Delta V \geq 10$ m s^{-1} is is seen that the time period between $t = 2760$ s and $t = 3000$ s is characterized by not only a relative maximum in ΔV, but also an area that is consistent with the size of a microburst ≈ 4 km in diameter. Thus, for the purposes of further discussion, the time $t = 2760$ s (denoted with a black vertical line in all quantitative figures) will be used to denote the time when the microburst reaches the surface.

One important thing to note is that the lack of a surface divergence signature during the microburst time that was seen qualitatively in Figure 3.4 is again seen here for the 10° imaging data. Notice how the 10° imaging ΔV and area diverge from the other scanning strategies and decrease after $t = 2760$ s to below the microburst radial ΔV threshold of $\geq$

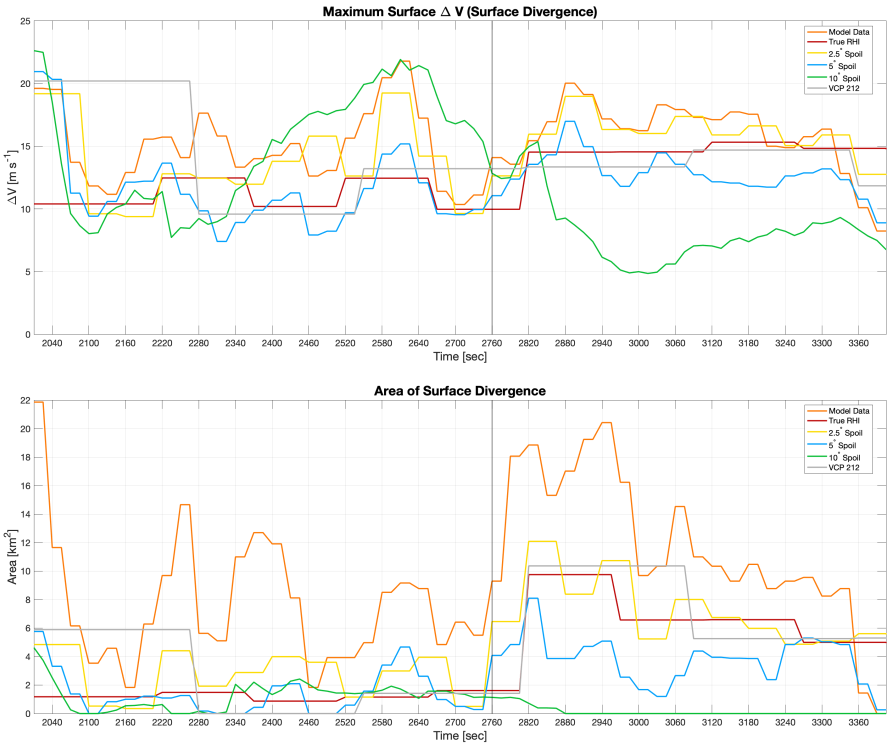

Figure 3.11: Plot of ΔV and area of ΔV that is ≥ 10 m s^{-1} on the 0.5° elevation angle in the area of interest throughout the entire analysis period (23.5 min). The black line at $t = 2760$ s denotes the start of the surface microburst.

10 m s^{-1}. This will be discussed in more detail in Section 4.2.1; however, it is classified as a missed detection of the surface microburst.

Staying with V_r signatures, the evolution of the mid-level convergence signature is presented in Figure 3.12. From the start of the analysis period, it can be seen that the maximum mid-level convergence increases in magnitude until reaching a peak between $t = 2400$ s and $t = 2520$ s for all scanning strategies except for VCP 212 and 10° imaging. The delay in VCP 212 is due to its coarser temporal resolution where it does not complete its second scan until after $t = 2520$ s, and as seen in Figure 3.11, the 10° imaging case had difficulty picking up the peak in the magnitude of the mid-level convergence signature. However, the 10° imaging is able to recover slightly to a peak closer to $t = 2640$ s and $t = 2700$ s. In all scanning strategies, the maximum mid-level convergence ΔV begins to decrease right

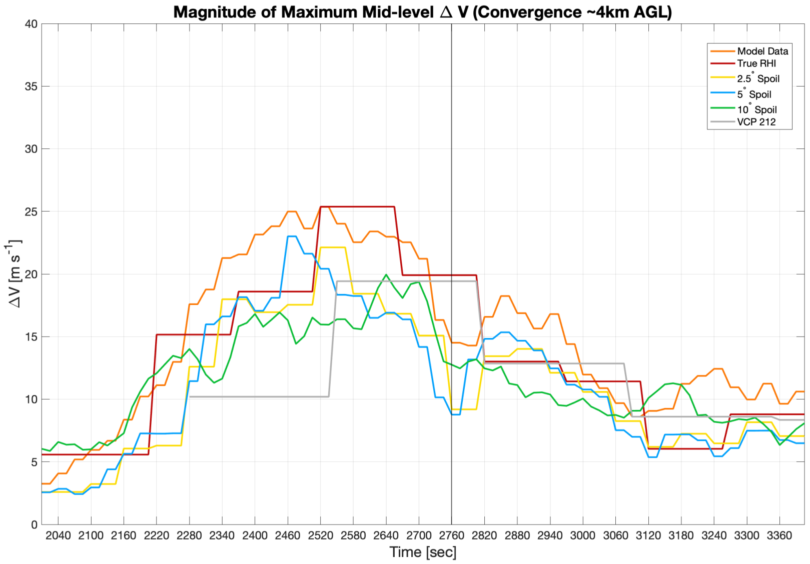

Figure 3.12: Plot of the magnitude of ΔV associated with mid-level convergence at the elevation angle closest to 4 km AGL within the area of interest throughout the entire analysis period. For VCP 212 and VCP Alpha at 30 km in range, this was the 8° elevation angle. The black line at $t = 2760$ s denotes the start of the surface microburst.

after reaching its initial peak, but this decrease in magnitude is much more evident after the microburst reaches the surface around $t = 2760$ s (black vertical line in Figure 3.12). This decrease in magnitude continues until the end of the analysis period where all scanning strategies are detecting weak convergence signatures ($\Delta\text{V} < 10$ m s^{-1}) while the model ΔV generally remains between 10 m s^{-1} and 12 m s^{-1}.

Moving on to Z_h, the evolution of the intensity (Figures 3.13 & 3.14), size (Figure 3.15), and shape (Figure 3.16) of the observed DRC are presented. As with before, all figures will indicate the start of surface divergence associated with the microburst with a black vertical line.

When looking at the intensity of the DRC, a rapidly evolving process can be observed. Namely, in Figure 3.13, it is apparent that prior to the microburst at the surface, the 95th percentile Z_h values rapidly increase between $t = 2280$ s and $t = 2460$ s, and this is believed to be an indicator of the presence of hydrometeor loading. Prior to $t = 2280$ s, the 95th percentile Z_h values were relatively constant in the different scanning strategies and was

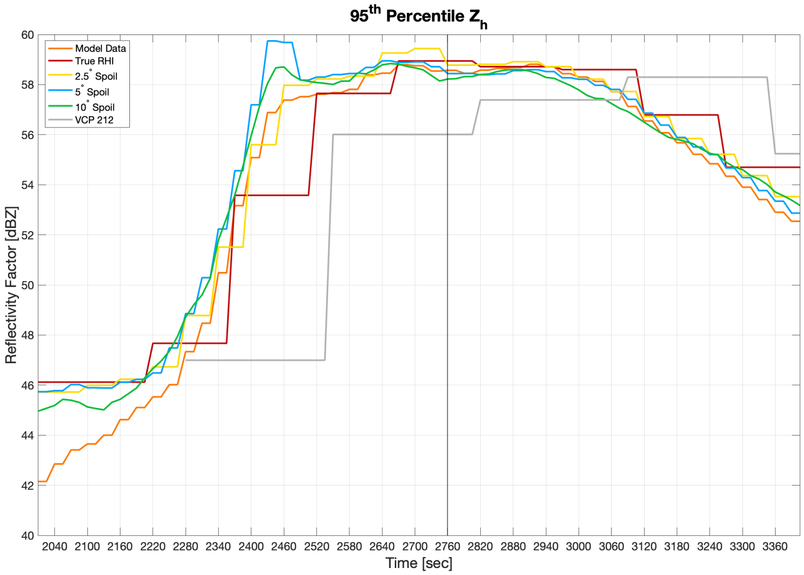

Figure 3.13: Evolution of 95^{th} percentile Z_h values over the analysis period for all scanning strategies and model data.

steadily increasing in the model data from around 42 dBZ at t = 2010 s to around 46 dBZ at $t = 2220$ s. After the rapid increase from $t = 2280$ s to $t = 2460$ s, the 95^{th} percentile Z_h values remain relatively constant around 58 dBZ until around $t = 3000$ s when they start to slowly decrease to around 54 – 56 dBZ by the end of the analysis period for all scanning strategies except VCP 212, which is delayed due to its temporal resolution. The rapid increase observed, from $t = 2280$ s to $t = 2460$ s, occurs over a 3 min window of time, which is less than the typical VCP 212 update time; thus, this rapid increase cannot be properly resolved by VCP 212.

This rapid increase in the 95^{th} percentile Z_h values can also be seen in Figure 3.14 where the change in the 95^{th} percentile Z_h values per unit time is plotted for all scanning strategies. Here, it can be seen that the change in the 95^{th} percentile Z_h per unit time is strongly reflective of the model processes for all scanning strategies with temporal resolutions less than 1 min (5° & 10° imaging). However, there is still a noticeable change in the 95^{th} percentile Z_h per unit time in the true RHI, but this change has a smaller magnitude, due to normalization in time, although it is still located in a similar position to the other peaks.

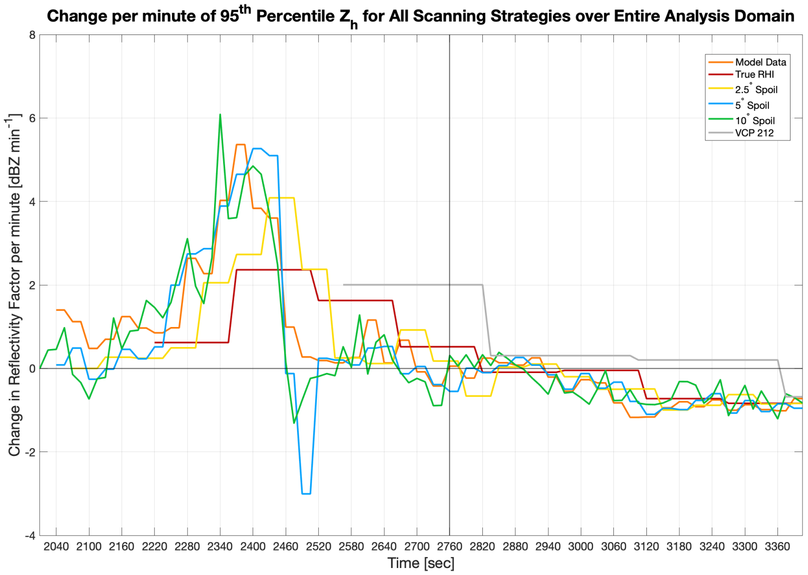

Figure 3.14: Evolution of the change in the 95^{th} percentile Z_h values over the analysis period for all scanning strategies and model data. This change is a simple difference between the previous 95^{th} percentile value at time t-1 and the current 95^{th} percentile value at time t. This change is then normalized by the temporal resolution such that the units are in dBZ min^{-1}.

The 2.5° imaging scans, which have a temporal resolution of 1 min, are still closely aligned with the other imaging cases regarding the magnitude of change in the 95^{th} percentile Z_h per unit time values; however, the effects of the longer temporal resolution are still seen as its peak has a magnitude of about 1 dBZ min^{-1} smaller than the other imaging cases and the model data.

Regarding the volume of the Z_h column, it evolves rather interestingly in time throughout the analysis (Figure 3.15). It is seen in Figure 3.15, that the Z_h column begins to develop between $t = 2280$ s and $t = 2340$ s. VCP 212 is severely delayed by its temporal resolution as it does not complete a full volume scan that detected the Z_h column until $t = 2550$ s, which corresponds to a 4.5 min delay. After $t = 2340$ s, the Z_h column steadily increases in volume before reaching a relative maximum around $t = 2640$ s in the model data and all scanning strategies except for VCP 212. This relative maximum occurs prior to the microburst detection at the surface; however, there is a secondary Z_h column volume

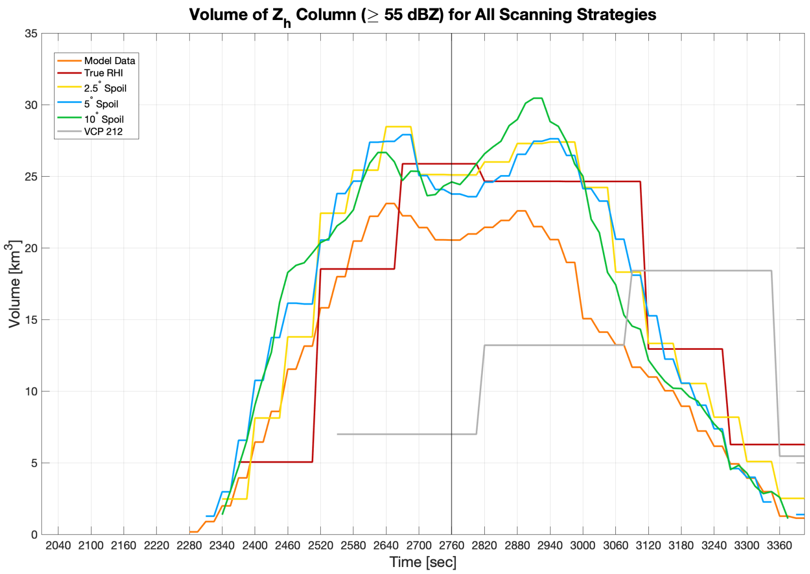

Figure 3.15: Evolution of elevated Z_h column volume (in km^3) within the analysis domain over the analysis time for all scanning strategies and model data.

maximum after the initial microburst detection at the surface. This secondary maximum is located between $t = 2880$ s and $t = 2940$ s and occurs during the time of the microburst as seen in Figure 3.11. There are some discrepancies between the maximum volumes observed by the model data and the different scanning strategies; however, these are likely due to sampling difference in the scanning strategies which represent a roughly 1° by 1° receive beamwidth where the model data is at a finer 0.5° by 0.5° resolution.

The last measurements associated with the Z_h column are the movements of the bottom and top of the column through time (Figure 3.16). In Figure 3.16, it can be seen that the Z_h column begins at $t = 2280$ s between 6° and 10° elevation ($\approx$ 3–5 km AGL) while the imaging scanning strategies first detect it between 10° and 12° elevation ($\approx$ 5–6 km AGL) at the same time. The true RHI emulations do not pick up the signatures for about 1.5 min until $t = 2370$ s and detect the top and bottom to be 13° and 7° elevation, respectively ($\approx$ 6.7 and 3.6 km AGL, respectively). As time progresses, the Z_h column grows to eventually stretch from the surface (0.5° elevation) to 20° elevation ($\approx$ 10.2 km AGL) by $t = 2580$ s. However, as noted in the qualitative analysis (Figure 3.2), there was a secondary elevated Z_h

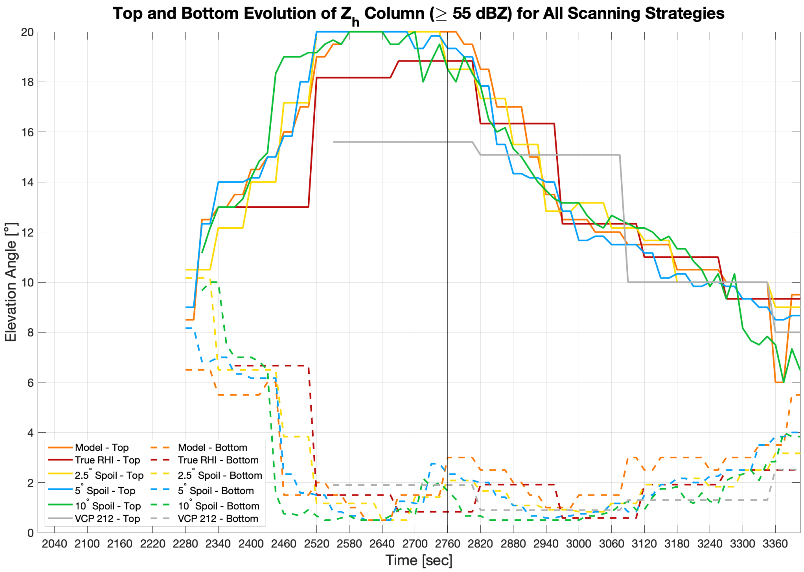

Figure 3.16: Evolution of the maximum and minimum elevation angles of the Z_h column within the analysis domain over the analysis time for all scanning strategies and model data.

region in the lower levels of the storm that merged with the original and larger Z_h column. This is why the bottom of the Z_h column drastically plummets to the surface in all scanning strategies and the model data around $t = 2460$ s to $t = 2520$ s. As the lower elevated Z_h column dissipated (Figure 3.2 panel q), the bottom of the Z_h column "lifts" from the surface before continuing the descent associated with the primary DRC. This descent is best observed in the 2.5°, 5°, and model data as it continues throughout the microburst time period of $t = 2760$ s to $t = 3000$ s. The temporal resolution of the true RHI images is too coarse to properly capture this evolution, but the secondary descent is still present at the end of the microburst time period with the scan at $t = 2970$ s. The 10° imaging has the localized maxima in Z_h smeared to the surface between $t = 2790$ s and $t = 2910$ s (seen in Figure 3.6 at times $t = 2820$ s and $t = 2880$ s), and thus, does not capture the descent between $t = 2760$ s and $t = 3000$ s. As the microburst begins to occur at the surface, the descent of the Z_h column is also apparent in the top of the Z_h column as it begins to descend below the 20° elevation angle before reaching roughly 12° elevation by the end of the microburst

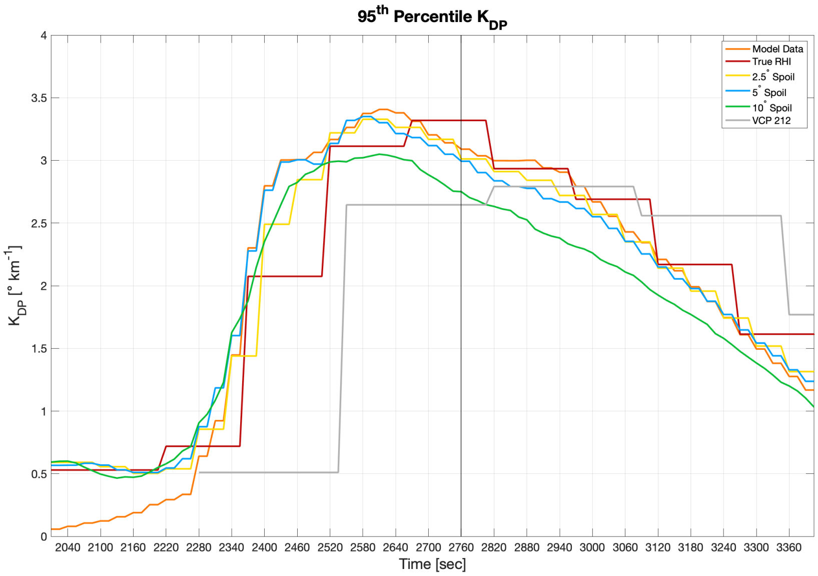

Figure 3.17: Evolution of 95^{th} percentile K_{DP} values over the analysis period for all scanning strategies and model data.

at the surface ($t = 3000$ s) in all scanning strategies except VCP 212. Throughout the rest of the analysis period, the top and bottom of the elevated Z_h column continue to sink and lift, respectively, through the analysis period.

The last precursor signature for quantitative analysis are the intensity (Figures 3.17 & 3.18), size (Figure 3.19), and shape (Figure 3.20) of K_{DP} cores. First looking at the intensity of the K_{DP} cores measured by the 95^{th} percentile of K_{DP} over the analysis area (Figure 3.17). As was seen in Figure 3.13 with Z_h, the 95^{th} percentile of K_{DP} evolves in a similar manner. Until $t = 2280$ s, the 95^{th} percentile remains at or below 0.5° km^{-1}. However, beginning at $t = 2280$ s, the 95^{th} percentile values rapidly increase to over 2.5° km^{-1} by $t = 2400$ s and continue to increase steadily before reaching a peak at or above 3.0° km^{-1} between $t = 2580$ s and $t = 2640$ s. This peak is delayed in the true RHI scans until $t = 2670$ s, but it reaches a similar magnitude to the model data along with 2.5° and 5° imaging. After this peak is reached, the 95^{th} percentile K_{DP} values begins to decrease even before the microburst reaches the surface at $t = 2760$ s, and this decrease appears to be

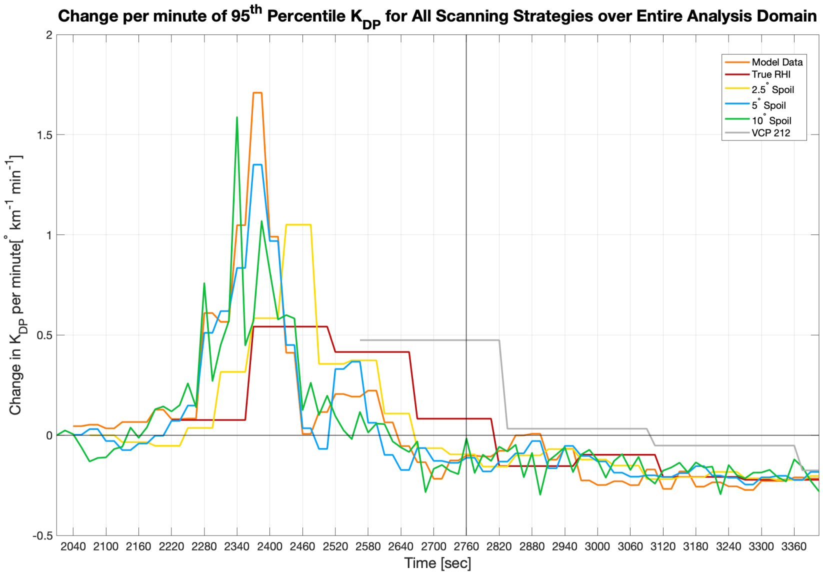

Figure 3.18: Same as Figure 3.14, but for the change in the 95th percentile Z_h values over the analysis period for all scanning strategies and model data.

relatively linear with time from around 3.0° km^{-1} at its peak to closer to 1.0 – 1.5° km^{-1} by the end of the analysis period at $t = 3420$ s.

However, the most noticeable thing in Figure 3.17 is the rapid increase in K_{DP} values between $t = 2280$ s and $t = 2400$ s, and this rapid increase is also seen in Figure 3.18 which shows the change in the 95th percentile K_{DP} values per unit time. This figures shows a similar evolution of the change of the 95th percentile K_{DP} values per unit time as was seen in Figure 3.14 for Z_h. Namely, there is relatively little change in the 95th percentile K_{DP} values until around $t = 2280$ s where the change ramps up to $\geq 0.5°$ km^{-1} min^{-1} and even $\geq 1.5°$ km^{-1} min^{-1} between $t = 2340$ s and $t = 2400$ s for the model data, 5° imaging, and 10° imaging scans. Furthermore, due to the temporal resolution associated with the true RHI, the increase in the change per unit time of the 95th percentile K_{DP} values only reaches a peak magnitude of about 0.5° km^{-1} min^{-1}. A similar magnitude decrease is seen in the 2.5° imaging scans due to the slightly longer temporal resolution; however, it reaches a peak magnitude of 1.0° km^{-1} min^{-1}, which is only 0.5° km^{-1} min^{-1} lower than the other imaging cases. After the peak for each scanning strategy, the change in 95th percentile

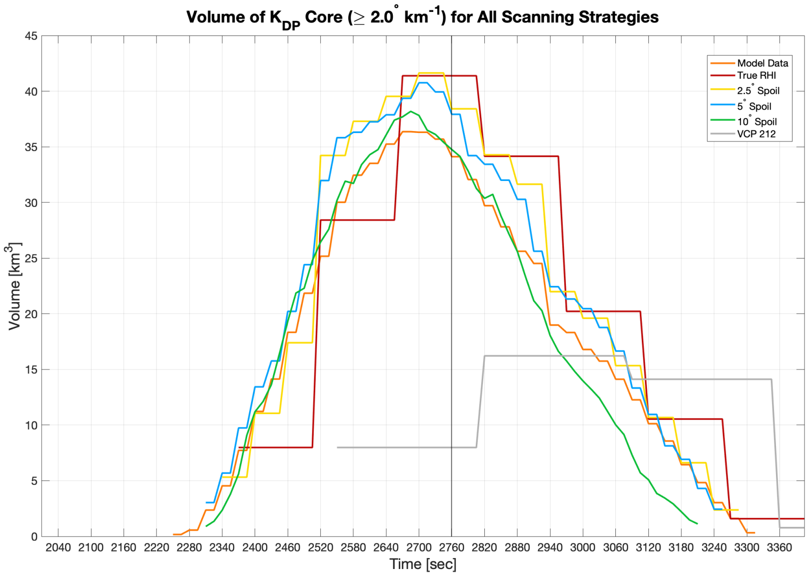

Figure 3.19: Evolution of elevated K_{DP} column volume (in km^3) within the analysis domain over the analysis time for all scanning strategies and model data.

K_{DP} values per unit time decrease almost as quickly as they increased and remain relatively constant and negative for the model data and all imaging scanning strategies from about $t = 2700$ s onward through the analysis period. This bolsters the previous comment that the decrease in the change of 95th percentile K_{DP} values is relatively linear after the peak is reached, and the decrease also occurs prior to the microburst occurring at the surface. This decrease is also seen in the true RHI and VCP 212 scans; however, the observation is delayed in time because of the coarser temporal resolutions.

Moving onto the volume of the K_{DP} core, it evolves rather parabolically in time (Figure 3.19). The volume of the K_{DP} core passes the 10 range gate threshold around $t = 2280$ s in the model data, 5° imaging, and 10° imaging scans. Because of their coarser temporal resolution, this signature is not picked up until $t = 2340$ s for the 2.5° imaging scans, $t = 2370$ s for the true RHI scans, and $t = 2550$ s for VCP 212. However, once the K_{DP} core was detected, its volume began to quickly increase until around $t = 2580$ s where its volumetric increase slows until the peak is reached at $t = 2700$ s, which is just before the microburst reaches the surface at $t = 2760$ s. After the peak is reached, the volume

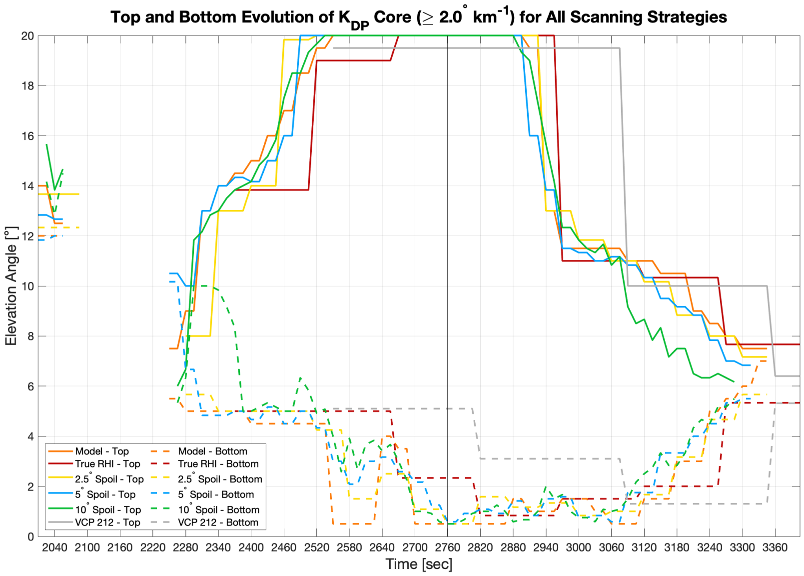

Figure 3.20: Evolution of the maximum and minimum elevation angles of the elevated K_{DP} core within the analysis domain over the analysis time for all scanning strategies and model data.

of the K_{DP} core quickly begins to descend until it disappears around $t = 3300$ s for the model data, 2.5° imaging, and 5° imaging. The 10° imaging lost the signature as early as $t = 3210$ s, and the signature was almost completely gone by $t = 3270$ s and $t = 3360$ s for the true RHI and VCP 212 scanning strategies, respectively. As stated previously, the discrepancy between K_{DP} core volume in the model data and scanning strategies is likely due to sampling differences between the scanning strategies (roughly 1.0° by 1.0° by 250 m sampling) and interpolated model data (0.5° by 0.5° by 250 m resolution).

Finally, the evolution of the top and bottom of the K_{DP} core signature can be seen in Figure 3.20. In Figure 3.20, most scanning strategies detected the K_{DP} core signature between $t = 2250$ s and $t = 2280$ s except for the true RHI emulations at $t = 2370$ s and VCP 212, which did not complete the volume scan containing the signature until $t = 2550$ s. As with the Z_h column, the K_{DP} core first appears around 5° to 8° elevation in the model data ($\approx$ 2.6 and 4.2 km AGL, respectively). This is a similar region detected by the 10° imaging and 2.5° imaging scans, but the 5° imaging scans detected the region starting closer to 11° in elevation at $t = 2250$ s, but quickly recovering to match the other imaging scans at $t = 2280$ s. Generally speaking, the bottom of the K_{DP} core remains constant until $t = 2550$ s where the small appendage seen in Figure 3.3 in panel m and at $t = 2550$ s in Figure 3.9 connects the K_{DP} core to the surface. However, the 10° imaging case does not keep the bottom of the K_{DP} core constant, but rather moves it up and down between 5° and 8° elevation between $t = 2280$ s and $t = 2520$ s ($\approx$ 2.6 and 4.2 km AGL, respectively). However, at $t = 2550$ s, the 10° imaging bottom lines fall in line with the other imaging and the model data. After the small appendage disappears, the model and imaging scans quickly rise back up to levels similar to the ones seen in the true RHI scans before descending to the surface again at $t = 2700$ s just before the microburst reaches the surface. The true RHI data finally reaches the surface at $t = 2820$ s, which is delayed almost 2 min due to its coarser temporal resolution. The K_{DP} core remains in contact with the surface until $t = 2880$ s before bouncing up and down between the 0.5° and 2.0° elevation angles, and this movement in the bottom of the K_{DP} core is seen in all imaging scans along with the model data. After $t = 3120$ s, the bottom of the K_{DP} core begins to quickly climb until the signature predominantly disappear between $t = 3300$ s and $t = 3360$ s.

The top of the K_{DP} core does not move as much as the bottom of the K_{DP} core does. Once the K_{DP} core is detected, the top of the K_{DP} core increases in elevation until reaching the 20° elevation angle between $t = 2460$ s and $t = 2550$ s for the imaging scans and model data; however, the true RHI data is delayed until $t = 2670$ s. The top of the K_{DP} core remains at the 20° elevation angle ($\approx$ 10.2 km AGL) until quickly dropping down to about 12° elevation ($\approx$ 6.2 km AGL) right before the end of the microburst at the surface at $t = 3000$ s. After $t = 3000$ s, the top continues to slowly sink until the K_{DP} core disappears between $t = 3000$ s and $t = 3360$ s.

3.1.2 Microburst at 90 km Case

The scanning strategy comparisons at 90 km range are reported in a similar manner to the 30 km comparisons presented in Section 3.1.1. The most notable difference is the lack of surface velocity comparisons due to the distance of the storm from the radar. This occurs because the lowest scanning elevation (0.5°) is located approximately 0.8 km AGL. Thus, this beam is too high to detect the surface divergence associated with the microburst, and all references to the microburst winds at the surface will come from Section 3.1.1 as both represent the same base data just interpolated to different ranges from the radar. VCP Beta (Figure 2.9) was specifically designed for this case to provide as much vertical sampling as possible with 0.5° sampling up to 4° elevation and 1° sampling above that.

3.1.2.1 Qualitative Analysis

Similar to the qualitative analysis in Section 3.1.1.1, the qualitative analysis below will detail the evolution of the storm by first looking at the evolution through model data compared directly with VCP 212 pseudo-RHI scans. Then more focus will be brought onto the precursor signatures by looking how they were observed by the other scanning strategies: true RHI and imaging. As at 30 km , the contours on all qualitative figures represent the 55 dBZ region which is the threshold used in this study to determine the Z_h column.

First, looking at V_r, it is important to note that the surface divergence signature will be visible in the model data as there is a 0° elevation angle in the model data that is not present in VCP 212. Thus, VCP 212 is already at a disadvantage in detecting the surface microburst winds at this range. As seen in Figure 3.1, there is an upward growth of outbound V_r values (denoted by the black arrows in panels d-k) from the surface to about 10 km AGL by $t =$ 2460 s (panel k). This signature ultimately generates mid-level convergence seen between 88–90 km range from around 4 – 6 km AGL. As time progresses, the mid-level convergence signature continues to remain present about 90 km range, but fluctuates in magnitude with its peak value appearing to occur around $t = 2580$ s (panel o). After $t = 2880$ s (panel

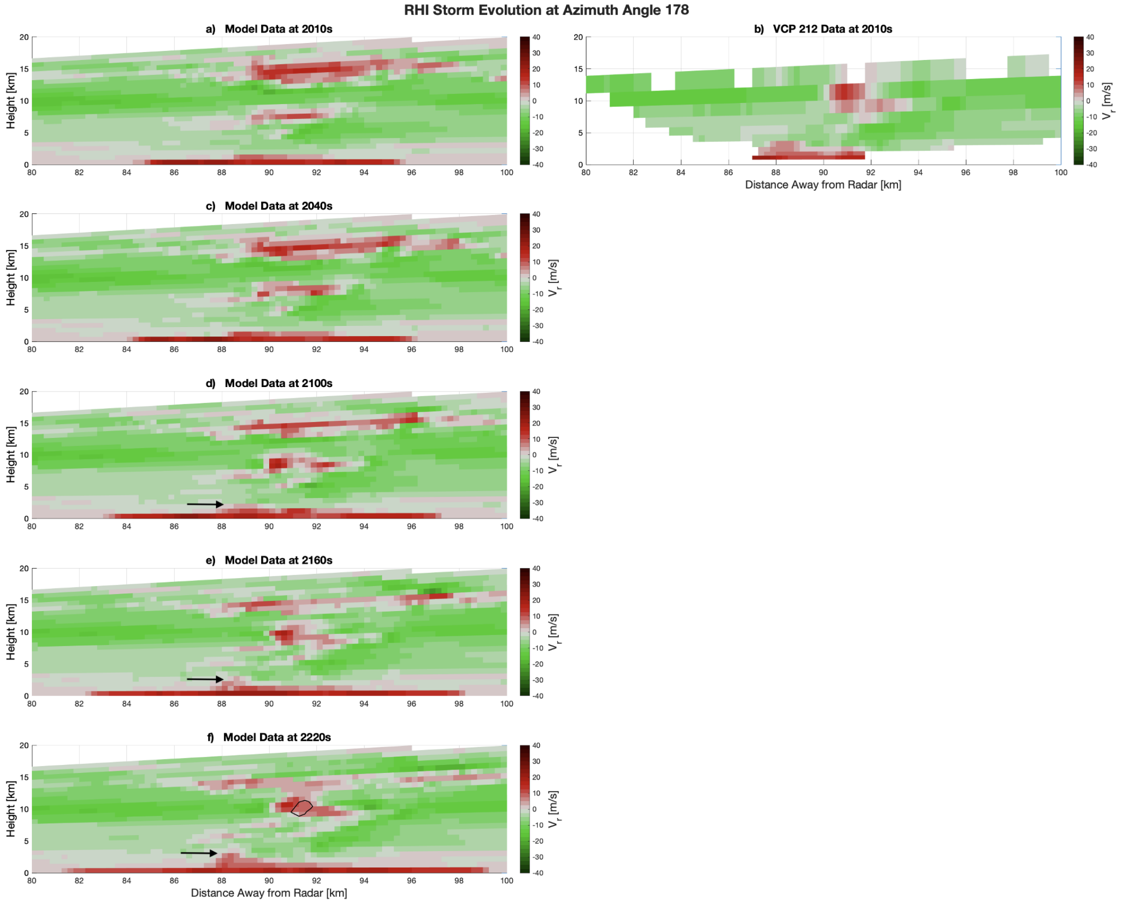

Figure 3.21: Same as Figure 3.1 but at 90km range and azimuth angle 178.

u), the mid-level convergence signature is observed to propagate away from the radar and weaken significantly. By $t = 3300$ s (panel dd), it is located approximately 92 km range.

The microburst is first observed here at $t = 2640$ s as a “midair” microburst (black circle in panels p-s). This signature continues to descend toward the ground before reaching the surface and becoming a surface microburst around $t = 2820$ s (black circle in panel s). The tracking of the “midair” microburst is a little more difficult at this range; however, this was to be expected given the larger range gate volume at 90 km. After reaching the surface at $t = 2820$ s, the surface microburst is observed at 89.5 km range and continues to propagate away from the radar throughout the analysis period. The signature is strongest between $t = 2820$ s (panel s) and $t = 2940$ s (panel v) when looking at the region between 88 km and 92 km range.

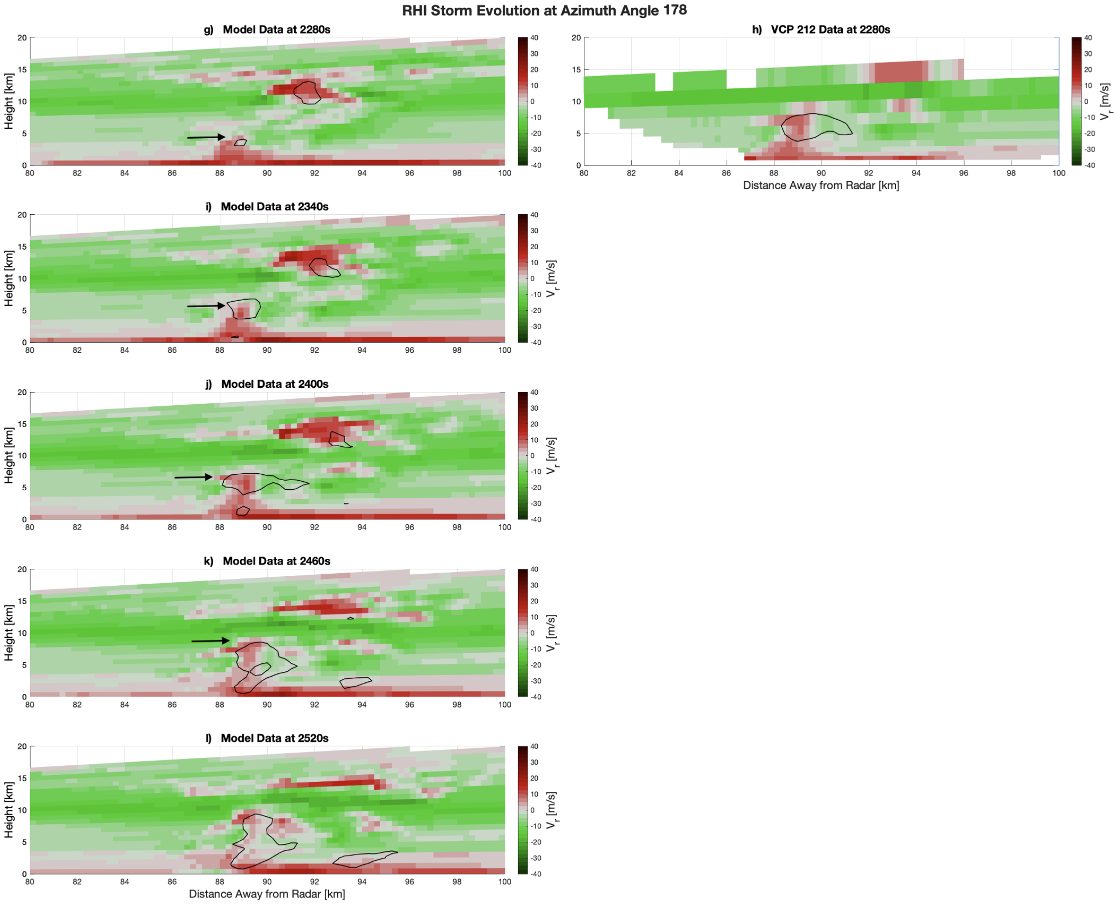

Figure 3.21 (*Continued*)

VCP 212 is again severely hindered by the temporal resolution, but continues to capture the essence of the storm from a qualitative standpoint. For example, VCP 212 captures the mid-level convergence signature in the volume scan starting at $t = 2220$ s (panel h); however, this data is not completely available until $t = 2550$ s, and the fluctuations seen in the mid-level convergence signature observed in the model data between $t = 2220$ s (panel g) and $t = 2550$ s (panel m) are not captured.

Looking at Z_h, the 90 km data provides a full view of the storm where both the top and bottom are visible. This was not the case at 30 km range where the data terminated around 10 km AGL. From $t = 2010$ s to $t = 2220$ s (panels a-f) in Figure 3.22, there is a small region of ≥ 45 dBZ that builds upward from the surface around 88 km range (denoted by black arrows). By $t = 2280$ s (panel g), the origins of the Z_h column are seen about a range

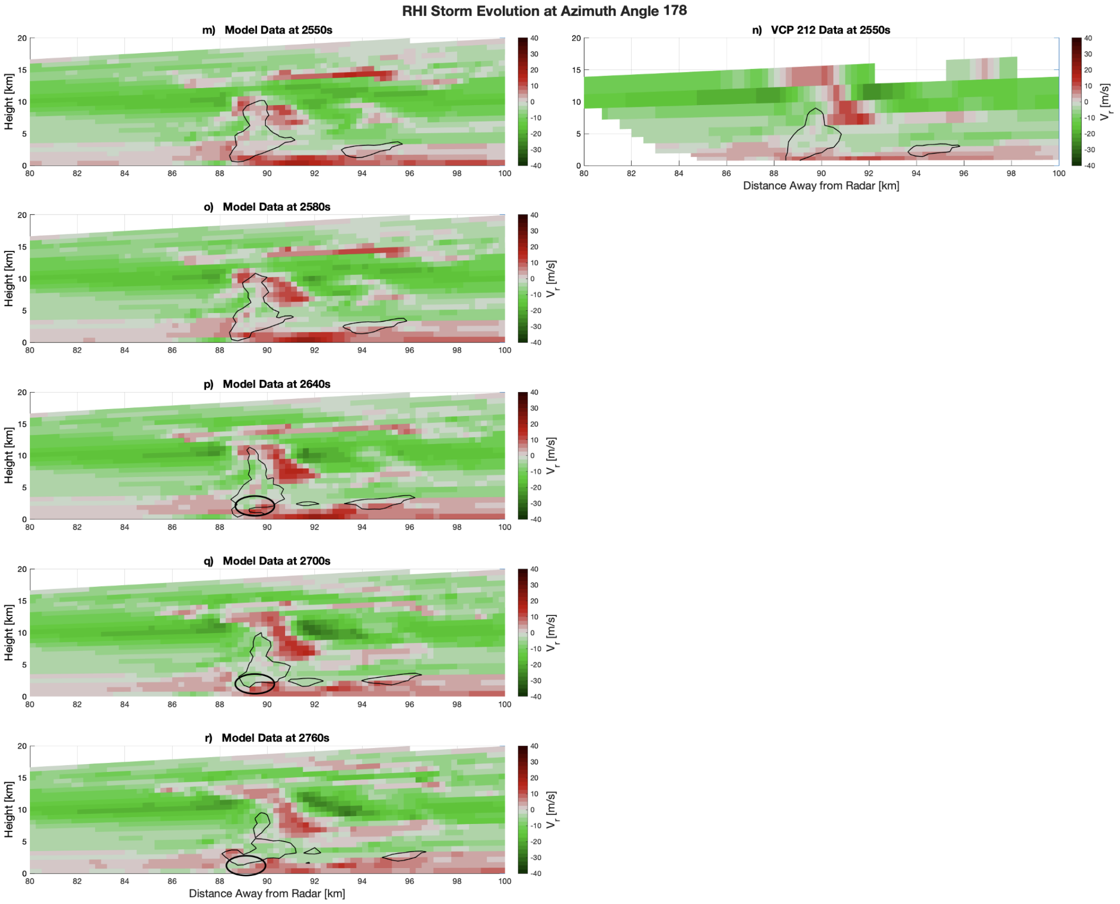

Figure 3.21 (*Continued*)

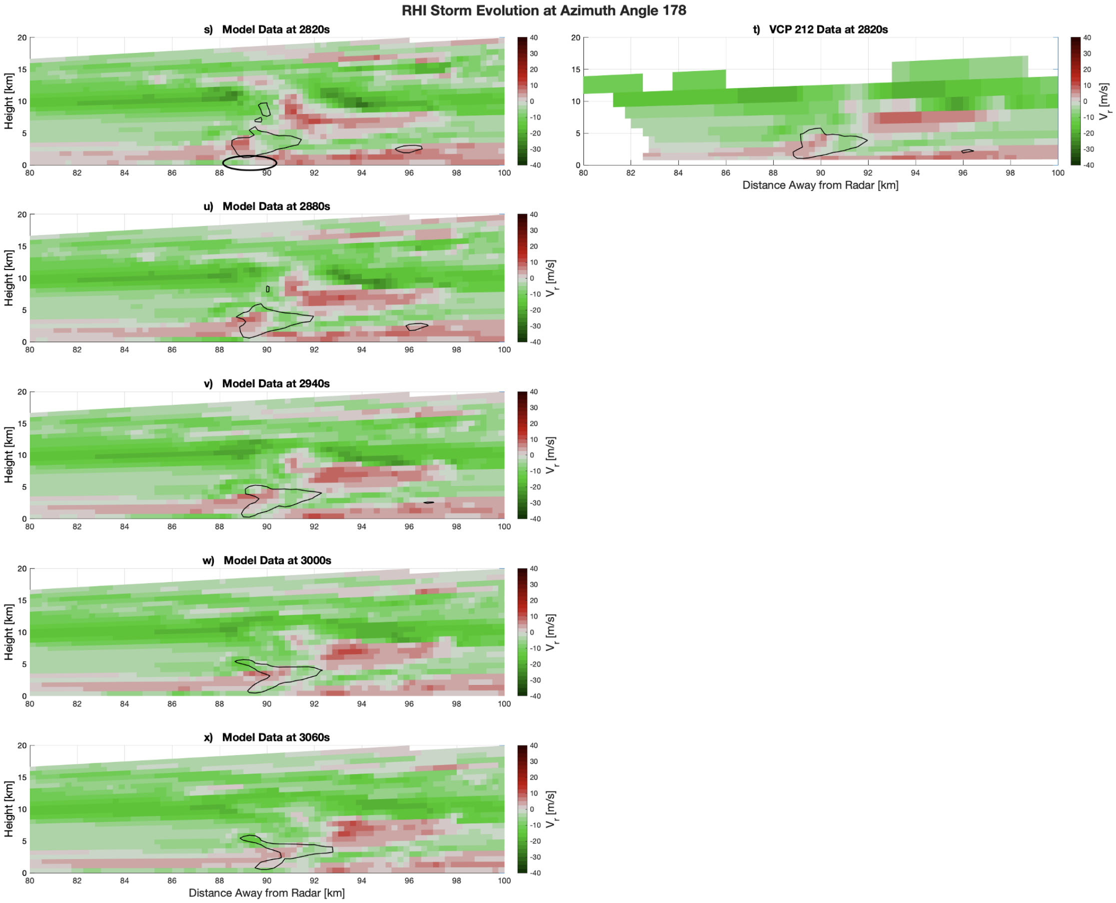

Figure 3.21 (*Continued*)

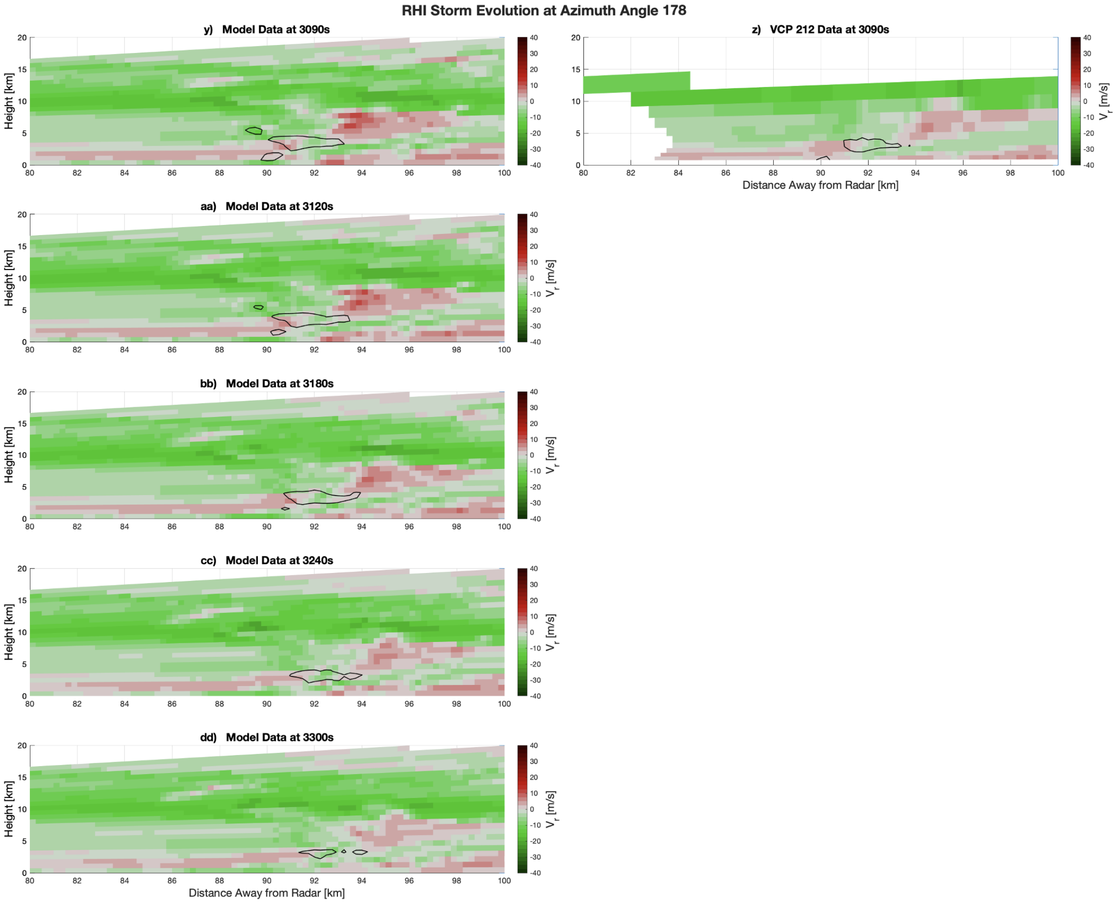

Figure 3.21 (*Continued*)

of 89 km and just below 5 km AGL (black contour). At $t = 2400$ s (panel j), the origins of the lower elevated reflectivity region are seen and are likely tied to the upward build of Z_h ≥ 45 dBZ. These signatures continues to grow and eventually merge together at $t = 2460$ s (panel k). They become indistinguishable at $t = 2520$ s (panel l), and this new combined Z_h column becomes relatively stable in size and position until $t = 2640$ s (panel p) where the lower portion begins to dissipate. With this dissipation, the downward transition of the entire Z_h column ($Z_h \geq 55$ dBZ) becomes more apparent as opposed to having to observe the ≥ 60 dBZ region descent. This descent of the entire Z_h column can be tracked after the dissipation of the lowest portion of said region from $t = 2700$ (panel q) through $t = 2820$ s (panel t) when the signature reaches the 0.5° elevation angle (≈ 0.78 km AGL) and remains there until $t = 3090$ s (panel y). The dissipation of the Z_h column begins around $t = 2940$ s and continues through $t = 3300$ s (panel dd).

When looking at the evolution of VCP 212, it does a good job of capturing the model environment as a whole relating to the structure and size of the signatures; however, its temporal resolution is too coarse to properly resolve the evolution of the features seen in the model data. For example, between times $t = 2280$ s and $t = 2550$ s (panels h and n), VCP 212 correctly captures the increase in the area of elevated Z_h values, but it does not show how the storm evolved to get there. Namely, using only the VCP 212 data, it is not obvious that there were two high Z_h regions that merged together. Furthermore, at times $t = 2550$ s and $t = 2820$ s (panels n and t), VCP 212 shows a general weakening of the Z_h column; however, one would not know that the lower portion of the Z_h column had dissipated, and the column had descended after this dissipation which occurred in between volume scans.

Finally, looking at K_{DP}, the evolution is similar to the one detailed in Section 3.1.1.1. There is little development in elevated K_{DP} values until $t = 2280$ s (panel g) when the origins of a K_{DP} core begin to form just under 5 km AGL and between 88–90 km range (black circle in panel g). This core continues to grow until it merges with an already existing

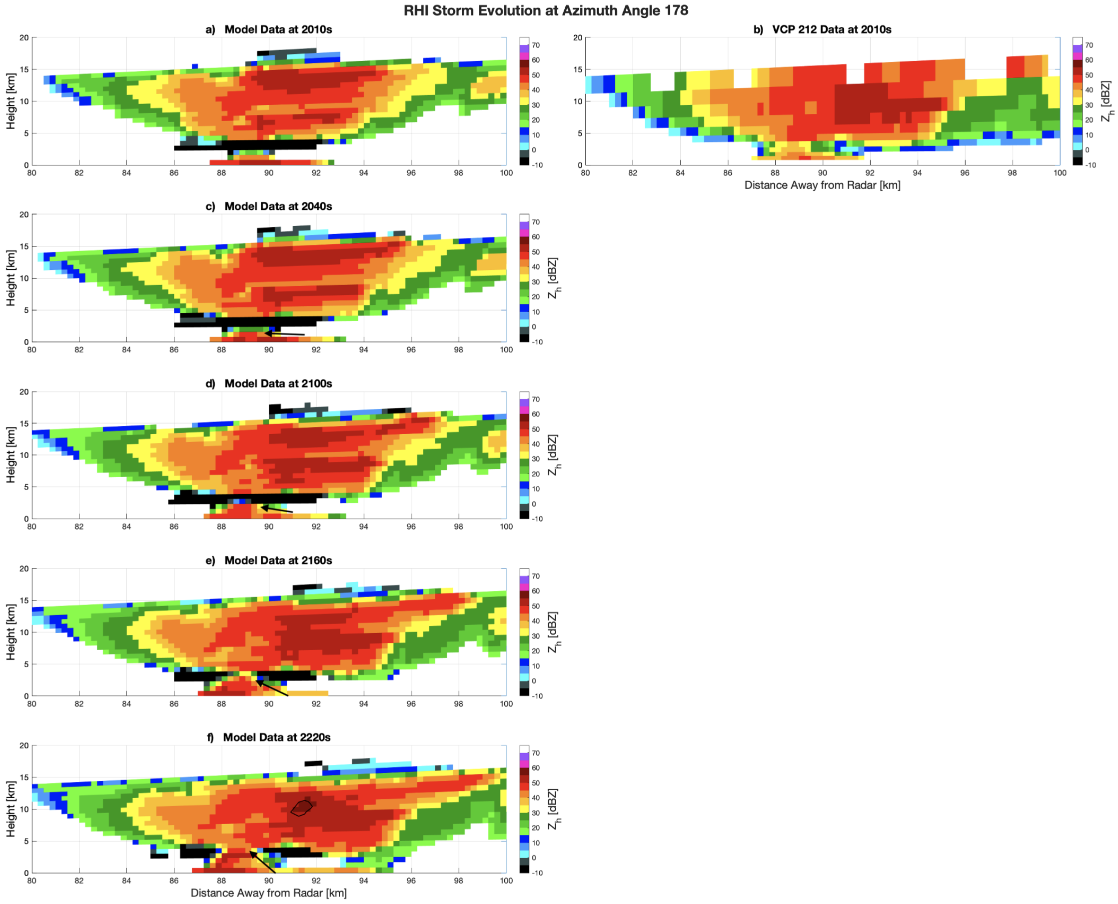

Figure 3.22: Same as Figure 3.2 but at 90km range and azimuth angle 178.

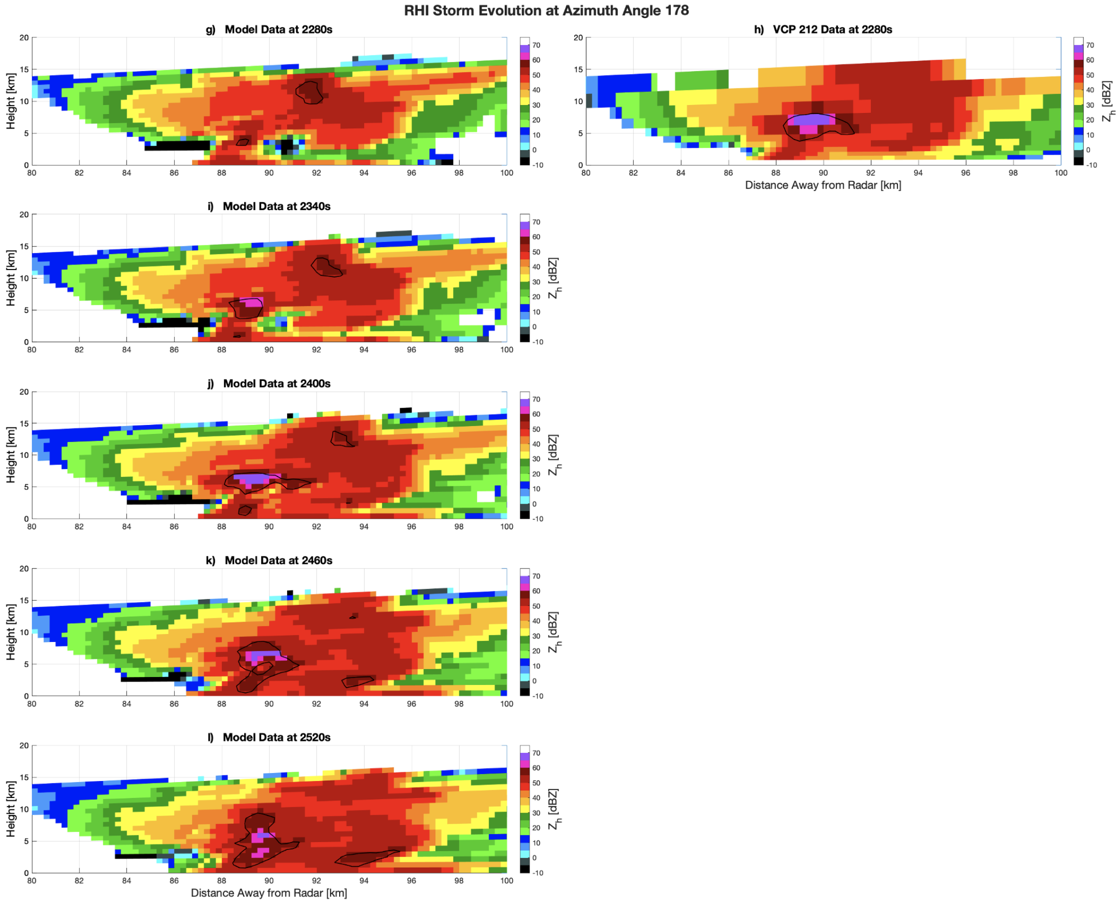

Figure 3.22 (*Continued*)

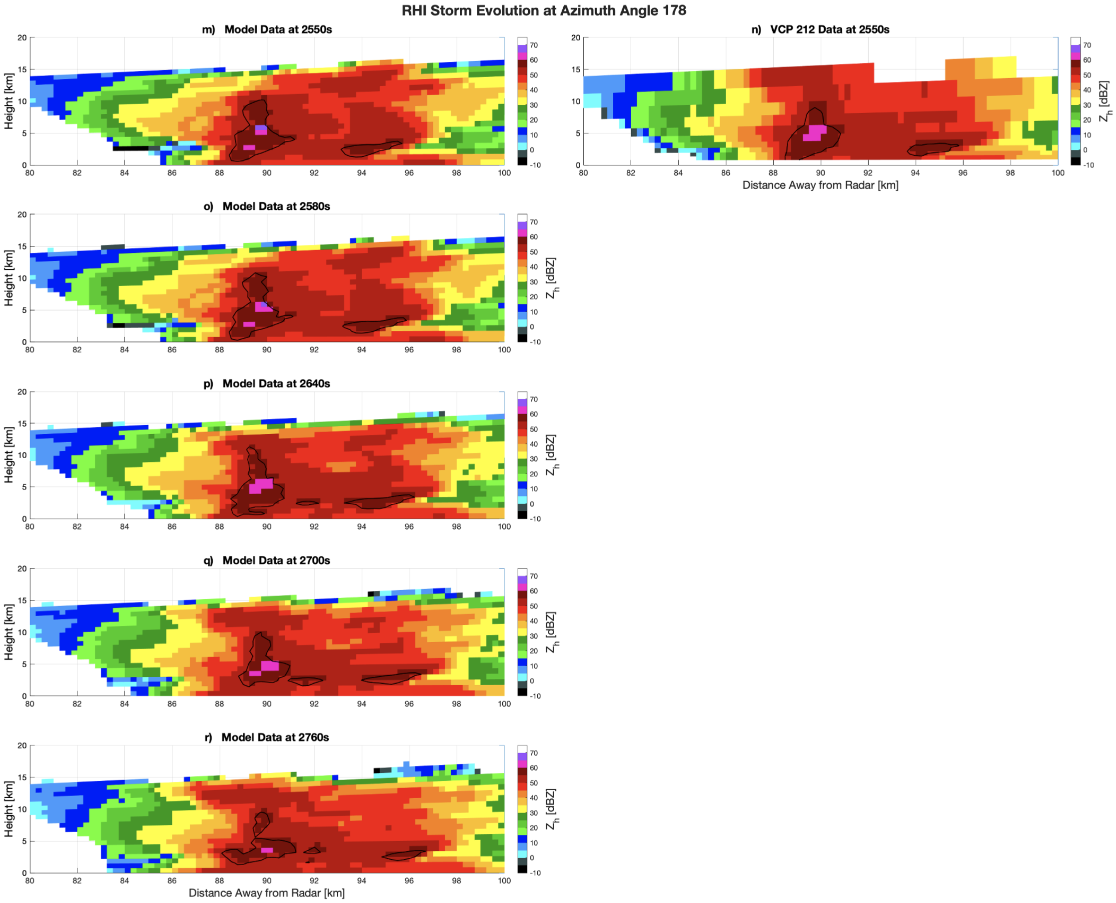
RHI Storm Evolution at Azimuth Angle 178

m) Model Data at 2550s

n) VCP 212 Data at 2550s

o) Model Data at 2580s

p) Model Data at 2640s

q) Model Data at 2700s

r) Model Data at 2760s

Figure 3.22 (*Continued*)

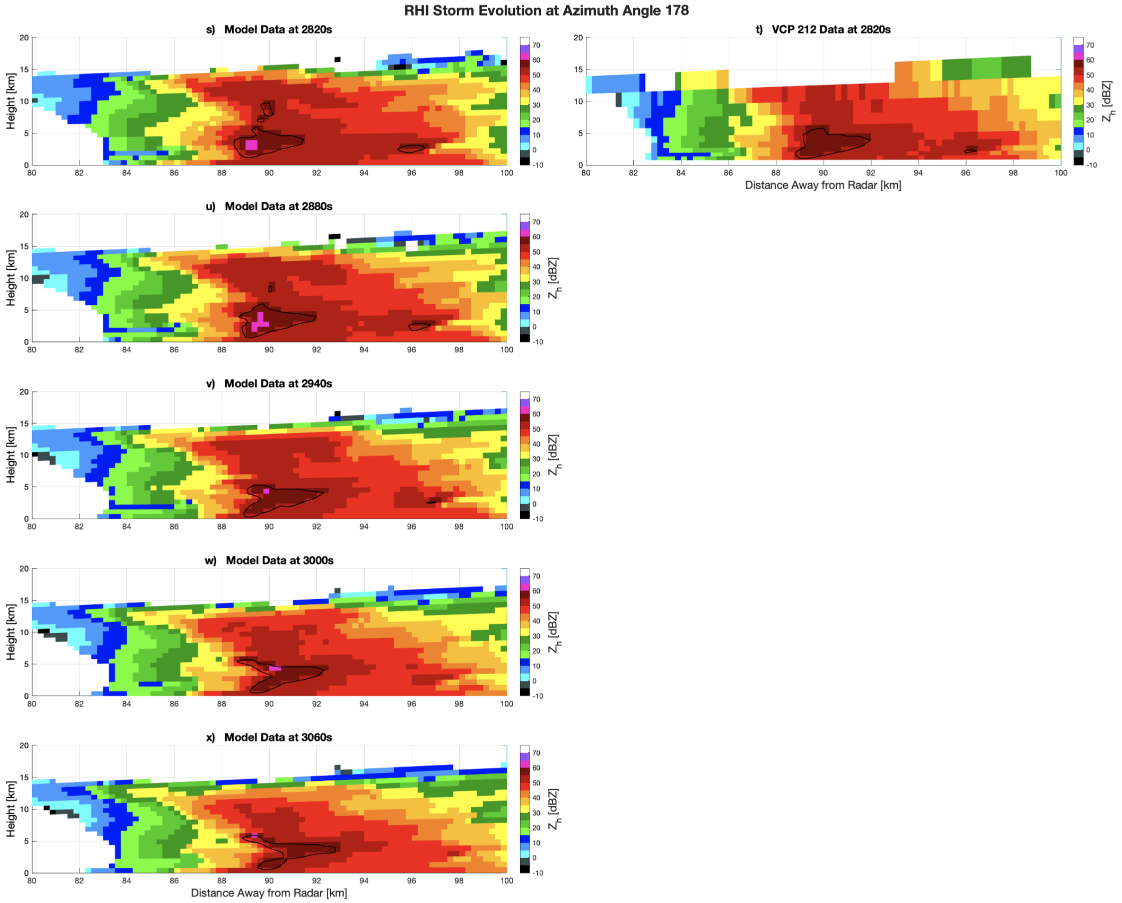

RHI Storm Evolution at Azimuth Angle 178

s) Model Data at 2820s

t) VCP 212 Data at 2820s

u) Model Data at 2880s

v) Model Data at 2940s

w) Model Data at 3000s

x) Model Data at 3060s

Figure 3.22 (*Continued*)

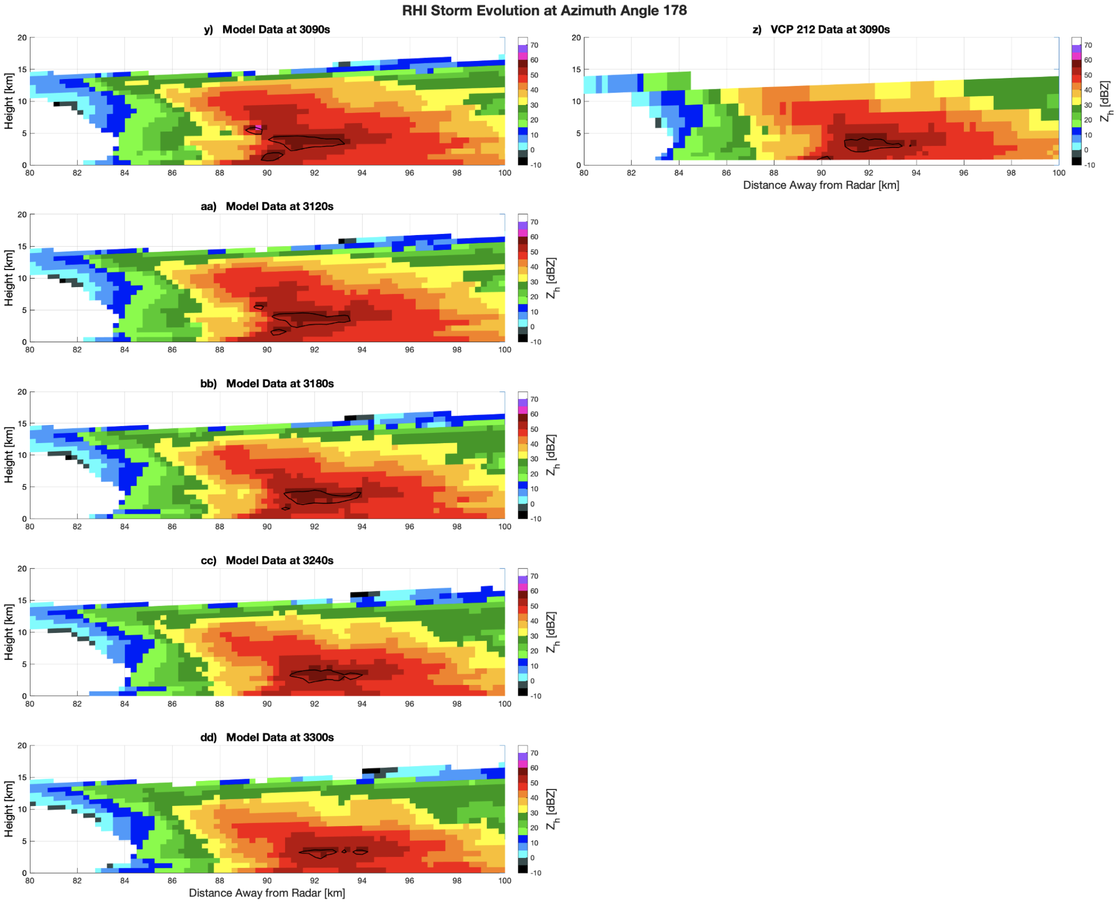

Figure 3.22 (*Continued*)

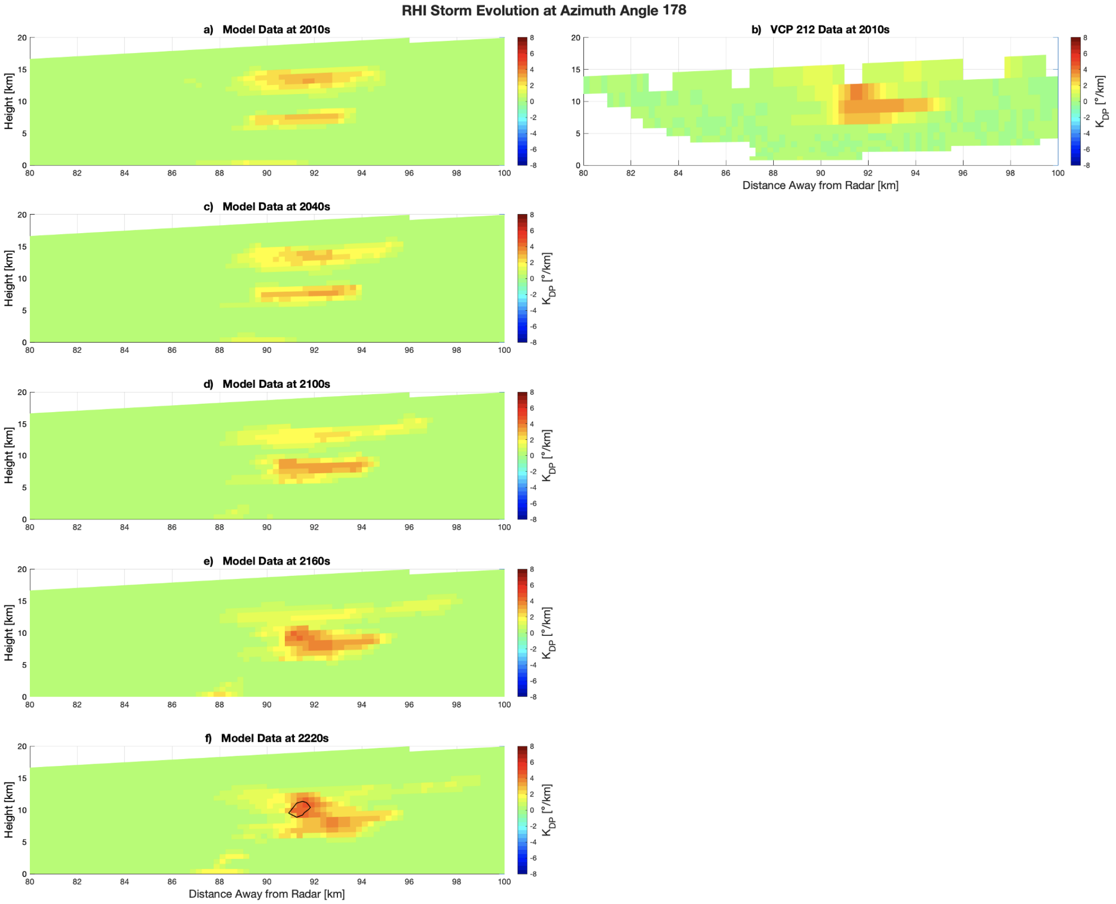

Figure 3.23: Same as Figure 3.3 but at 90km range and azimuth angle 178.

elevated K_{DP} region aloft at $t = 2400$ s (panel j). During this same time, a small appendage of elevated K_{DP} connects the K_{DP} core to the surface beginning at $t = 2400$ s (panel j), and it remains in contact with the surface until $t = 2580$ s (panel o). At $t = 2640$ s (panel p), this small appendage breaks away from the surface before reaching again at $t = 2760$ s (panel r). The size of the K_{DP} core increases until about $t = 2640$ s (panel p) before slowly decreasing steadily until $t = 3300$ s (panel dd). The intensity of the K_{DP} core increased from formation until $t = 2460$ s (panel k) before slightly decreasing to around 4.0° km^{-1} until $t = 2700$ s (panel q). After $t = 2700$ s (panel q), the intensity continues to decrease until hovering just above 2.0° km^{-1} from $t = 3000$ s (panel x) through $t = 3300$ s (panel dd).

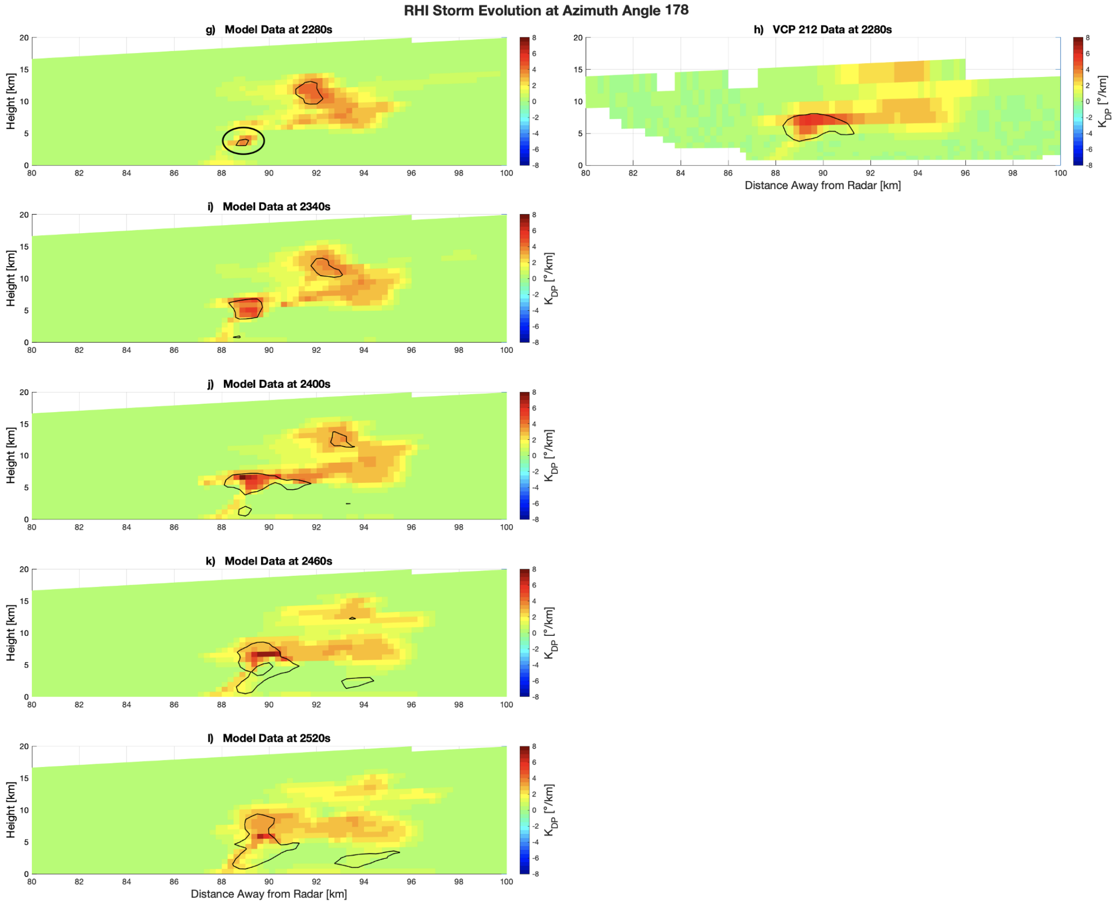

Figure 3.23 (*Continued*)

VCP 212 performed similar to the observations in the Z_h analysis above. The observations VCP 212 did make, captured the structure seen in the model environment; however, the temporal resolution is severely lacking. Namely, at time $t = 2220$ s (panel h), VCP 212 shows a K_{DP} core aloft between 88 km and 92 km range; however, the entire volume scan would not have been completed until $t = 2550$ s which would be in line with panel m. This is a severe delay in the availability of data, and this resolution does not capture the evolution seen in the model data. Furthermore, VCP 212 does not observe the small appendage connecting the K_{DP} core to the surface until the volume scan starting at $t = 2550$ s which would not be completed until close to $t = 2760$ s which is panel r.

Moving on to how the other scanning strategies observed specific microburst precursor signatures, these figures will be set up similar to Figures 3.4 - 3.9. The first signature

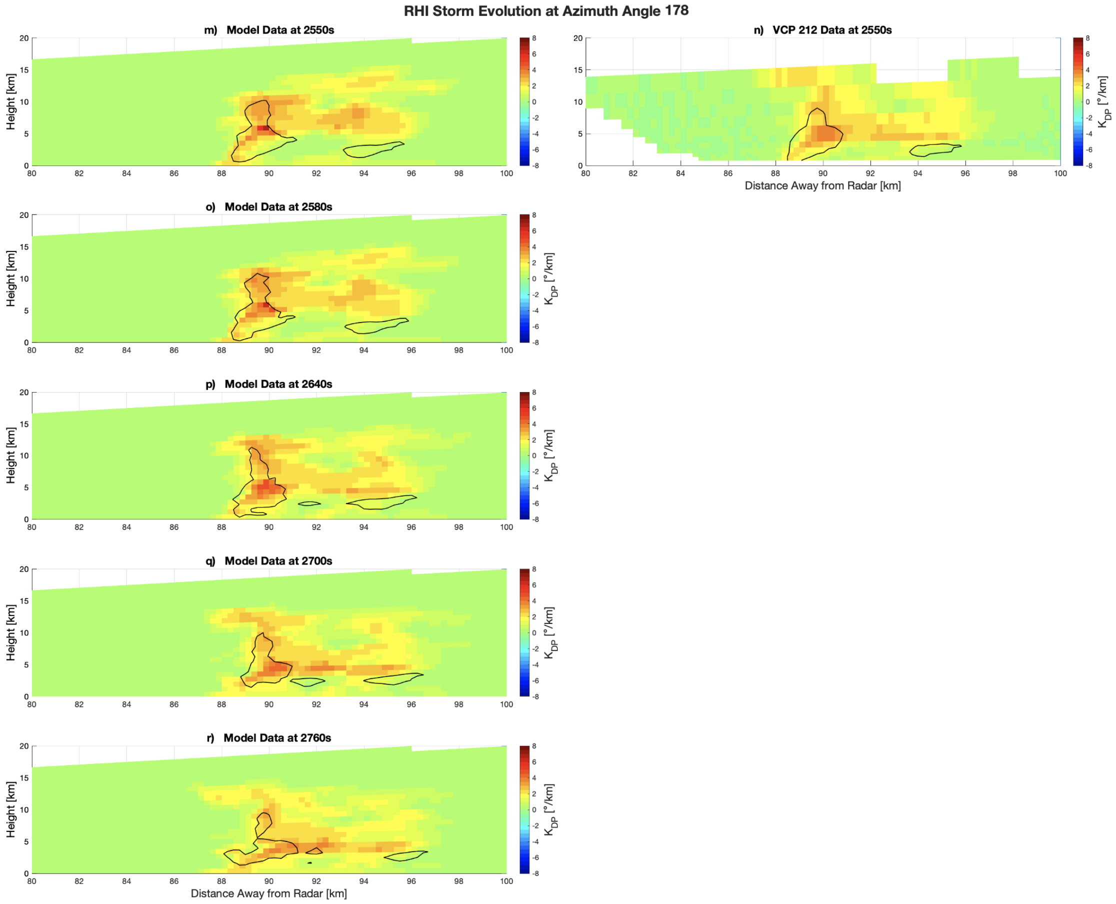

Figure 3.23 (*Continued*)

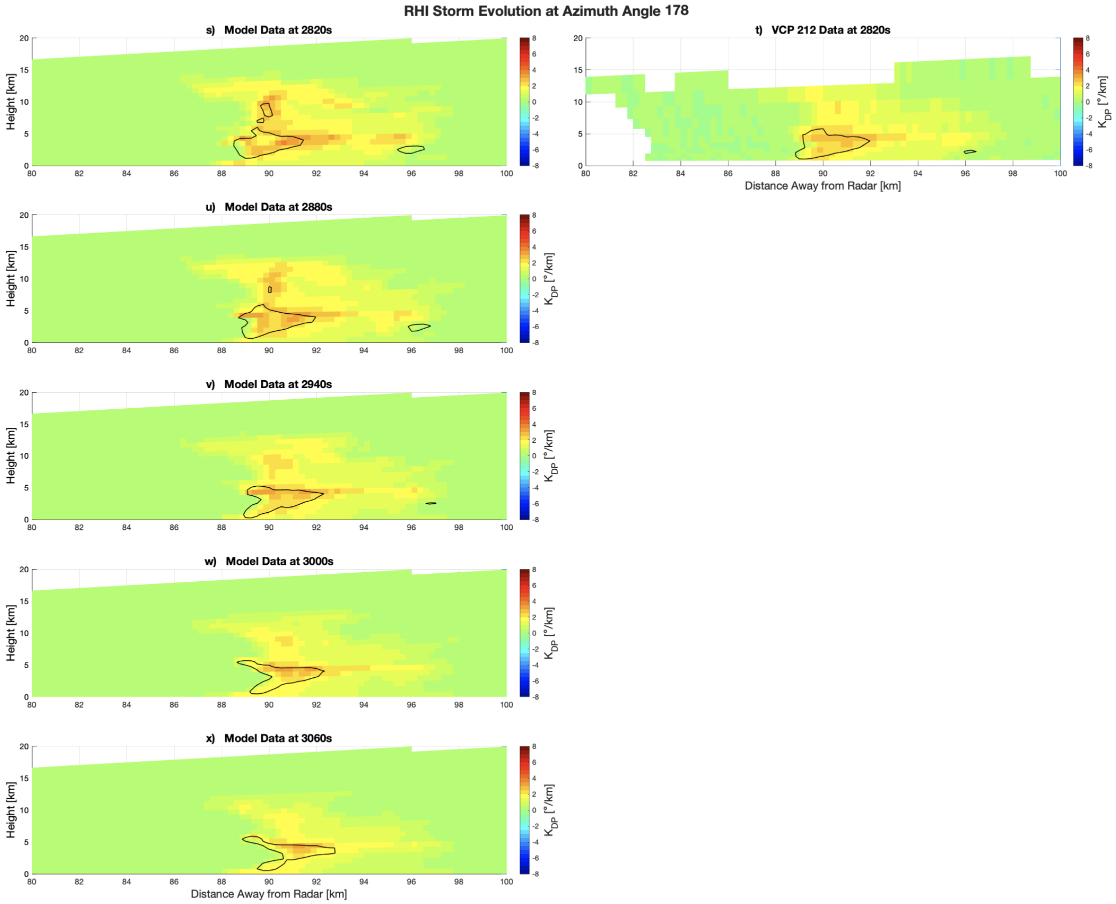

Figure 3.23 (*Continued*)

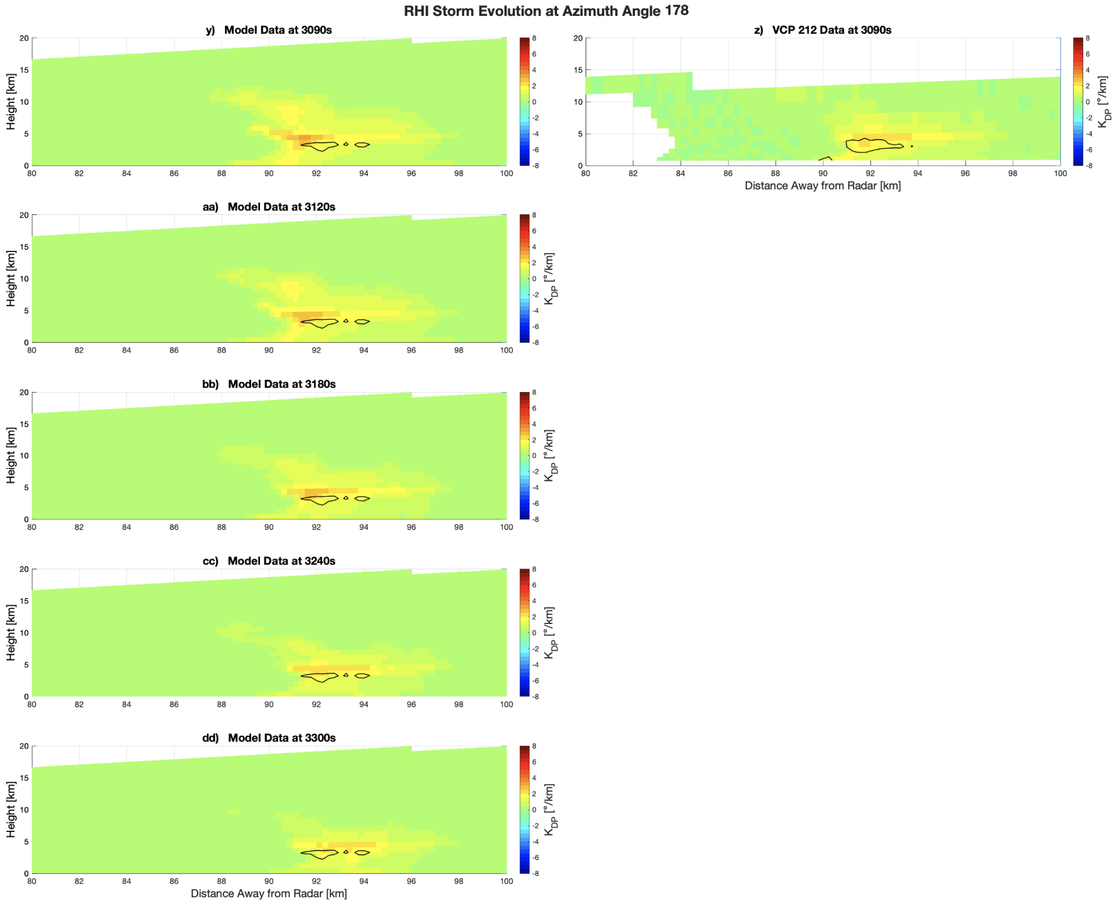

Figure 3.23 (*Continued*)

for qualitative analysis is the mid-level convergence signature (Figure 3.24). As seen in Figure 3.21, the vertical development of outbound V_r values from the lower levels to about 8 km AGL really contributes to the early observations of mid-level convergence right at 90 km range (black arrows in the model data of Figure 3.24). This vertical development can be traced through all scanning strategies. After $t = 2400$ s, the mid-level convergence signature fluctuates similar to what was seen in Figure 3.21. It should be noted that the observation of the "midair" microburst is still visible at this range due to its height above the surface (black box in all panels of Figure 3.24 where visible). This signature is present in the model data from $t = 2580$ s to $t = 2760$ and is observed by the 2.5° imaging data. It is also captured by the one true RHI image at t = 2700 s. Both the 5° and 10° imaging data doe not detect the "midair" microburst signature. After the microburst reaches the surface, as seen in the model data at $t = 2820$ s, the surface divergence signature is not observed at the elevation angle above in either the model data nor any of the other scanning strategies, which bolsters the point to avoid using surface divergence analysis at this range for microburst detection.

Generally speaking, the true RHI images captured the structure of the model environment, yet have the worst temporal resolution leading to little aid in observing the evolution of the mid-level convergence signature. Just like at 30 km range (Section 3.1.1.1), the 10° imaging tends to be least representative of the model processes. First, the 10° imaging data had a spurious outbound velocity detection around 90 km range between 10 km and 15 km AGL during the $t = 2400$ s to $t = 2520$ s time period (black circle in 10° imaging panels). Furthermore, throughout the time period shown ($t = 2220$ s through $t = 3060$ s), the V_r returns from the lowest elevations are not good representations of the model environment with much of the observations not aligning with the model data or other scanning strategies because the signatures are smoothed out and weakened. This representativeness problem is also seen in the 5° imaging case, but not to the same extent or magnitude seen in the 10° imaging case.

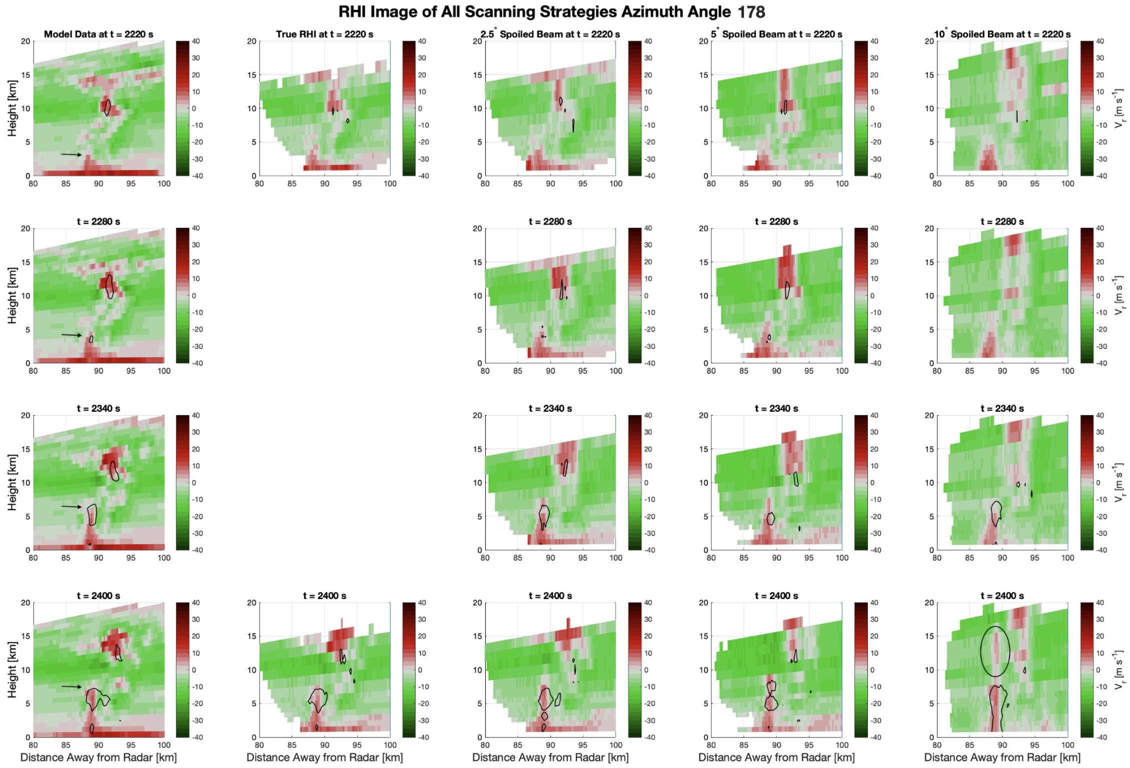

Figure 3.24: Similar to Figure 3.6 but at 90 km range and azimuth angle 178.

In Figure 3.25, the origins of the Z_h column are first detected at $t = 2280$ s just to the left of 90 km range and under 5 km AGL in the model data (black arrow); however, the elevated Z_h in the imaging cases do not meet the necessary threshold of $Z_h \geq 55$ dBZ, and there is no true RHI scan at this time. By $t = 2340$ s, all imaging scanning strategies have detected the Z_h column with 10° imaging having the largest signature. By $t = 2400$ s, the second true RHI scan occurs, and provides the best representative view of the model environment of the scanning strategies. 5° imaging has a hard time resolving the signature with a small Z_h column area shown around 5 km AGL, and 10° imaging still has the largest signature area, which could be attributed to smearing effects. The Z_h column continues to grow and elongate until $t = 2580$ s where it stretches from the surface (0.5° elevation) to around 10 km AGL. In the model data, there are two distinct Z_h regions associated with ≥ 60 dBZ values (both just around 90 km range with one around 5 km AGL and the other around 2.5 km AGL). Starting at $t = 2700$ s, it appears that the top of the reflectivity column begins

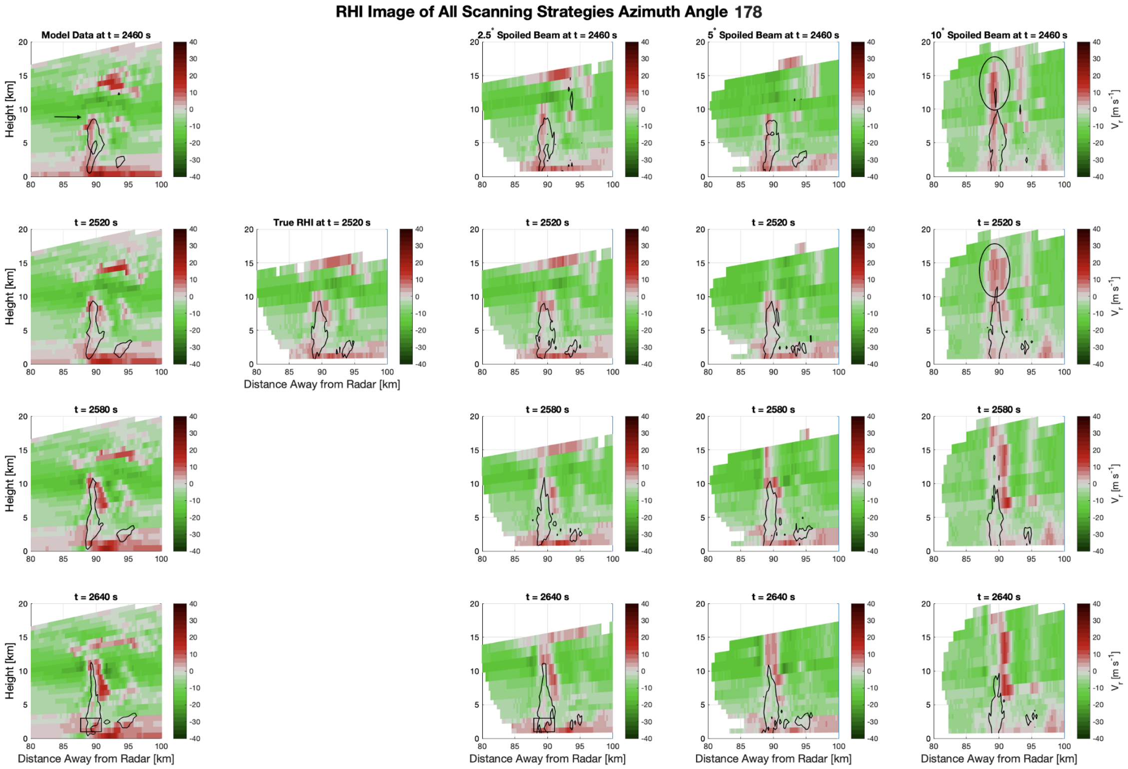

Figure 3.24 (*Continued*)

to descend from the 10 km AGL level and the bottom of the signature is no longer at the 0.5° elevation angle (0.26 km AGL) as the lower portion of the Z_h column has dissipated, which is similar to what was observed in Figure 3.6. Also observed at $t = 2700$ s, the Z_h values ≥ 60 dBZ are barely detected by the 10° imaging scans. The 2.5° imaging loses this signature just 60 s later at $t = 2760$ s, but recovered at $t = 2880$ s and $t = 2940$ s with a small detection of this region. From $t = 2700$ to 2880 s, the descent of the Z_h column is explicitly observed in the model, 2.5°, and 5° imaging data where as the 10° imaging data never saw the dissipation of the lowest Z_h column signature, which is likely a smearing effect (confirmed by Figure 3.26). During the final frames of Figure 3.25, the dissipation of the Z_h column has already begun with the size of the Z_h column decreasing drastically - especially in the 10° imaging case.

Of all scanning strategies, the true RHI data was the most representative of the size, shape and intensity of the Z_h column observed in the model data, even though its temporal

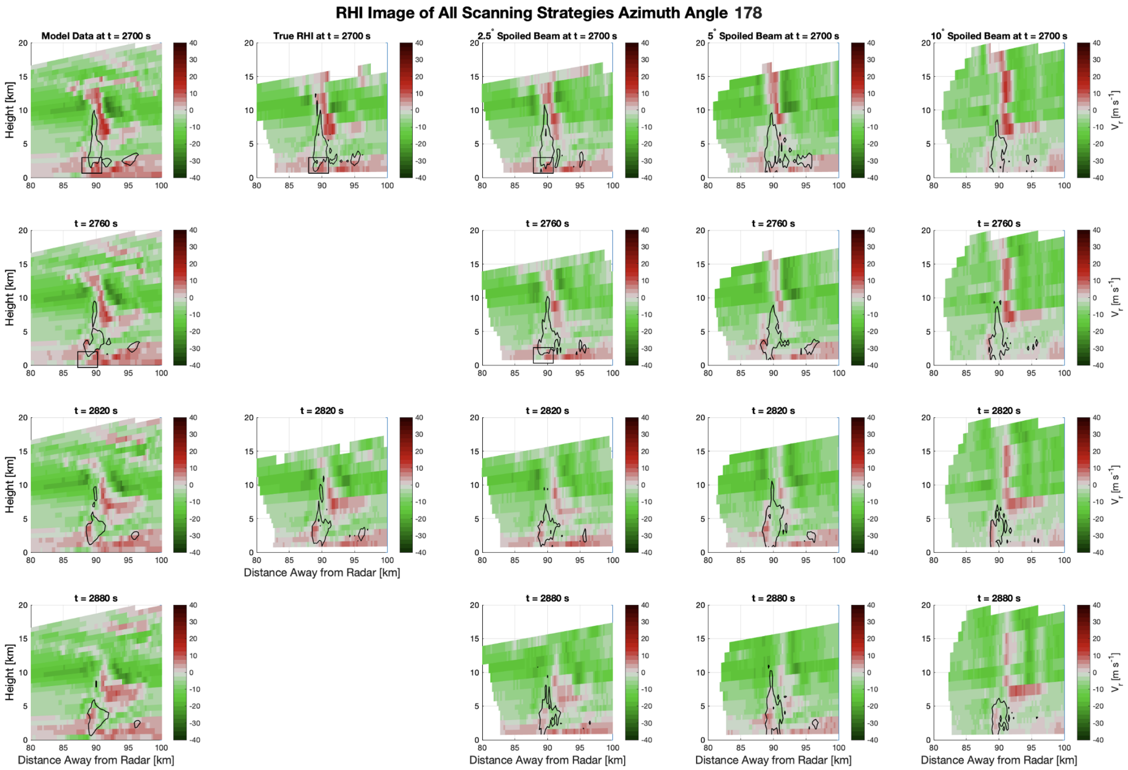

Figure 3.24 (*Continued*)

resolution was very coarse. The least representative scanning strategy was the 10° imaging scans. These scans were subject to smearing throughout the period showing the Z_h in contact with the ground from $t = 2400$ s through $t = 3000$ s and not capturing the dissipation of the lowest portions of the Z_h column around $t = 2640$ s. Furthermore, in all panels of Figure 3.25, the 10° imaging data actually smears the top of the storm higher in altitude than is seen in any of the other scanning strategies or the model data. This smearing is also present occasionally in the 5° imaging data (see $t = 3000$ s at the upper edge of the Z_h column), but is not as obvious and severe as seen in the 10° imaging data (top black circle in Figure 3.26).

Moving into the evolution of the K_{DP} core in Figure 3.27, the earliest detection of the K_{DP} core is seen at $t = 2280$ s around 90 km range and just under 5 km AGL (black arrow in model panel). This signature is detected best by the 5° imaging case, but is still visible in the 2.5° imaging data and slightly in the 10° imaging data. As time progresses, the

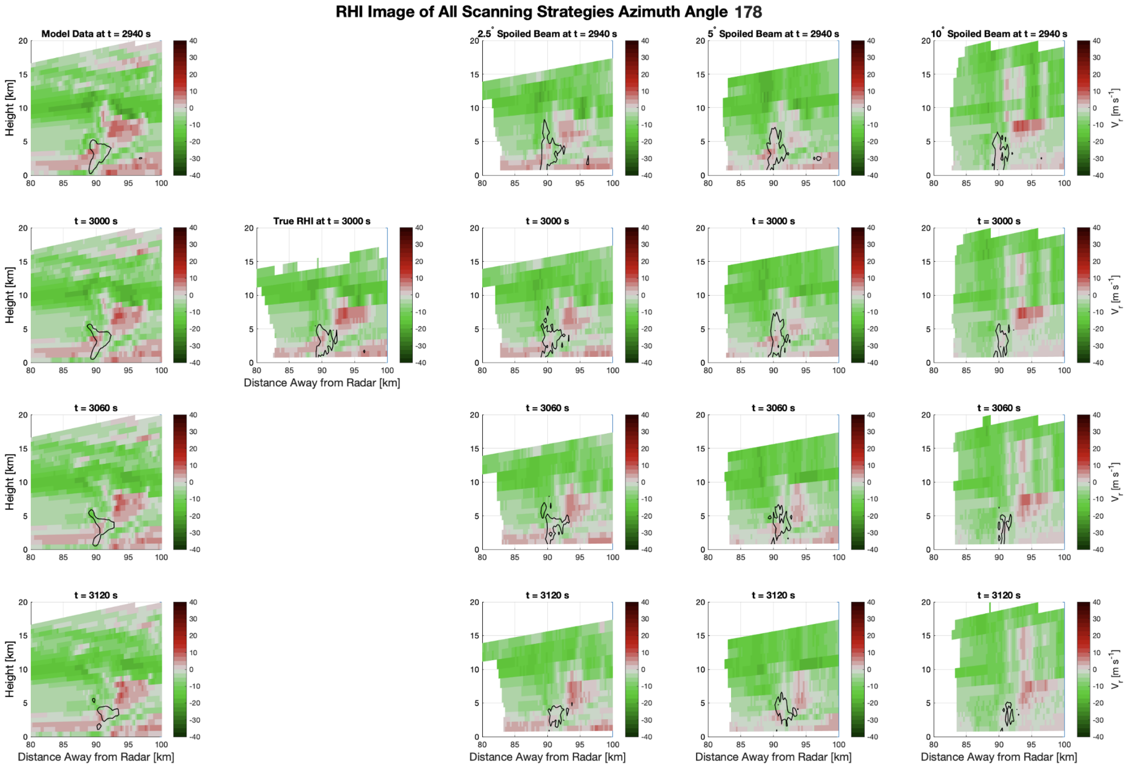

Figure 3.24 (*Continued*)

K_{DP} core continues to grow and is detected best by the true RHI and 10° imaging data at $t = 2400$ s. By $t = 2520$ s, the small elevated K_{DP} appendage that connects the K_{DP} core to the surface is detected by all scanning strategies save for the 10° imaging data (black arrows at $t = 2520$ s). The K_{DP} core continues to grow before reaching a maximum height around 12.5 km AGL around $t = 2700$ s. By this time, the small appendage has dissipated, but it reappears briefly at $t = 2760$ s. From $t = 2700$ s through $t = 3060$ s, the K_{DP} core begins to quickly shrinks vertically before settling around 4 km AGL just outside 90 km range.

As seen in previous qualitative analysis, the true RHI data best represents the observations seen in the model data; however, it performs the worst in capturing the evolution of the K_{DP} core due to its temporal resolution. Smearing effects are still seen in the 10° imaging case, and they are most notable from $t = 2700$ s to $t = 2940$ s. As noted earlier at $t = 2400$ s, the K_{DP} core is best observed by the true RHI and 10° imaging data. This

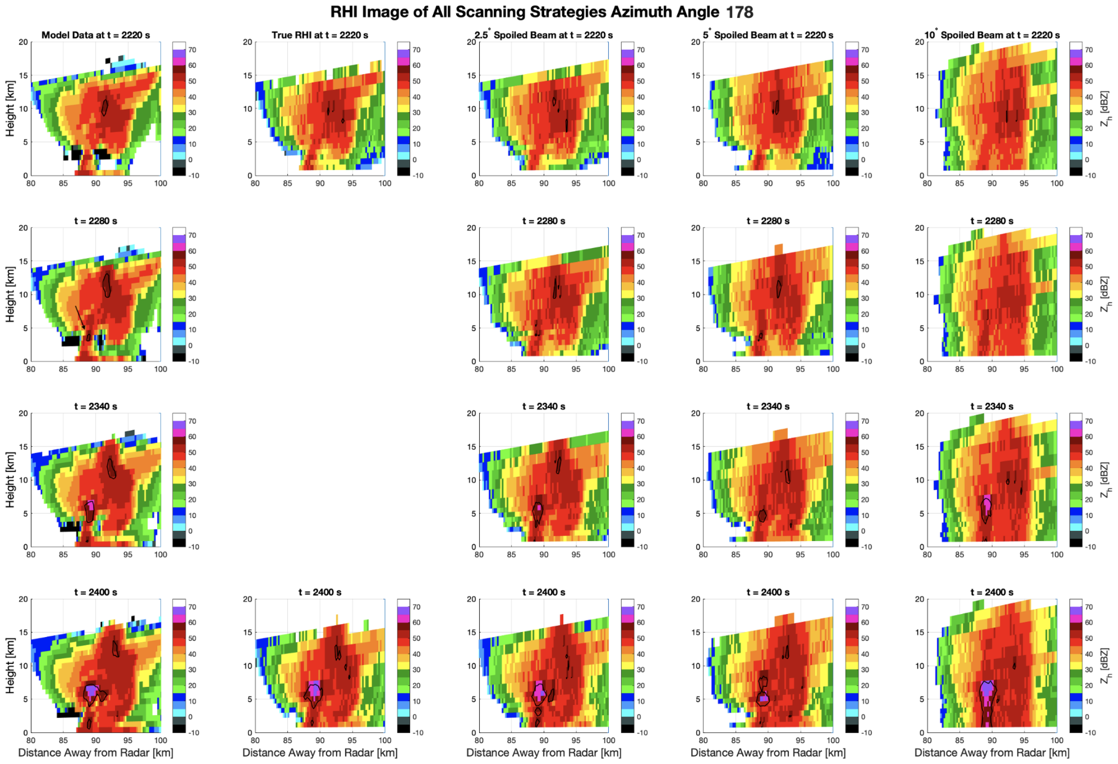

Figure 3.25: Similar to Figure 3.6 but at 90 km range and azimuth angle 178.

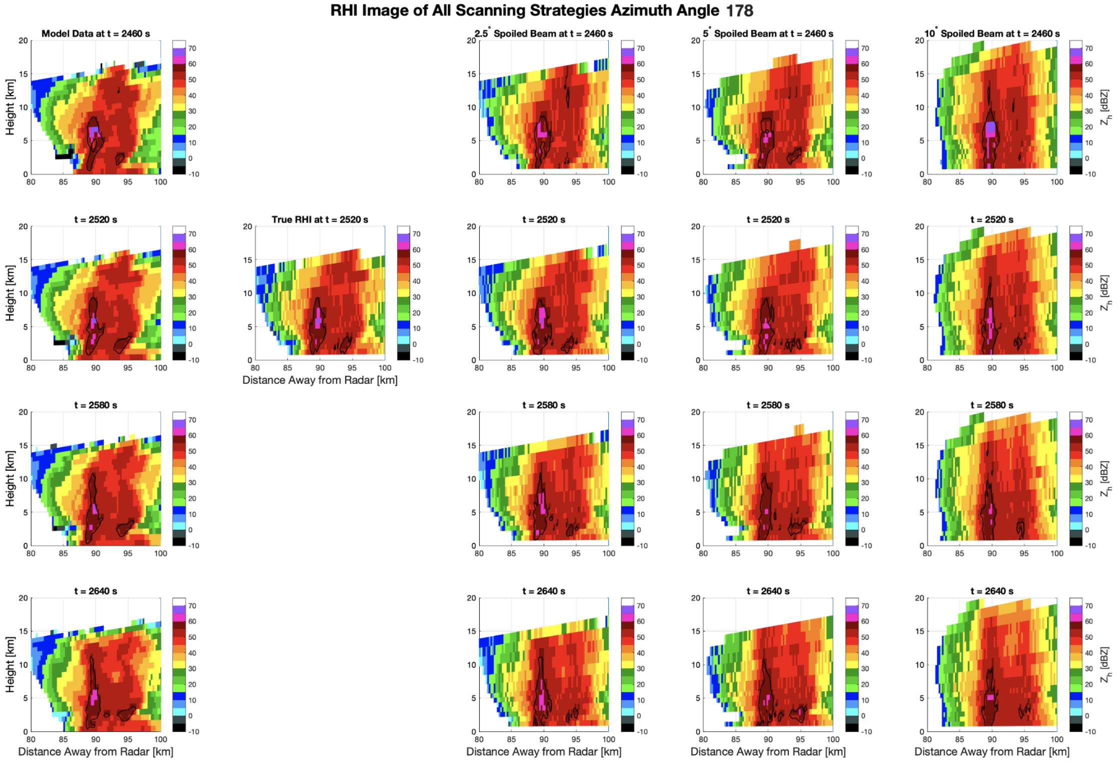

Figure 3.25 (*Continued*)

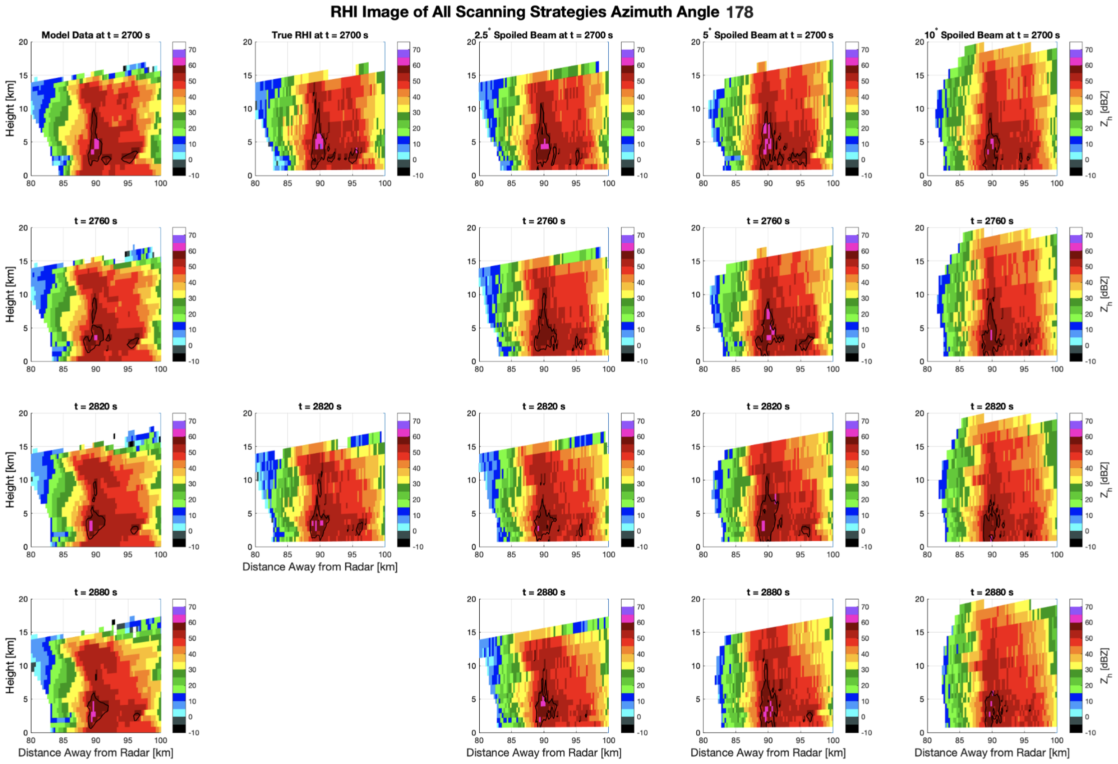
RHI Image of All Scanning Strategies Azimuth Angle 178

Figure 3.25 (*Continued*)

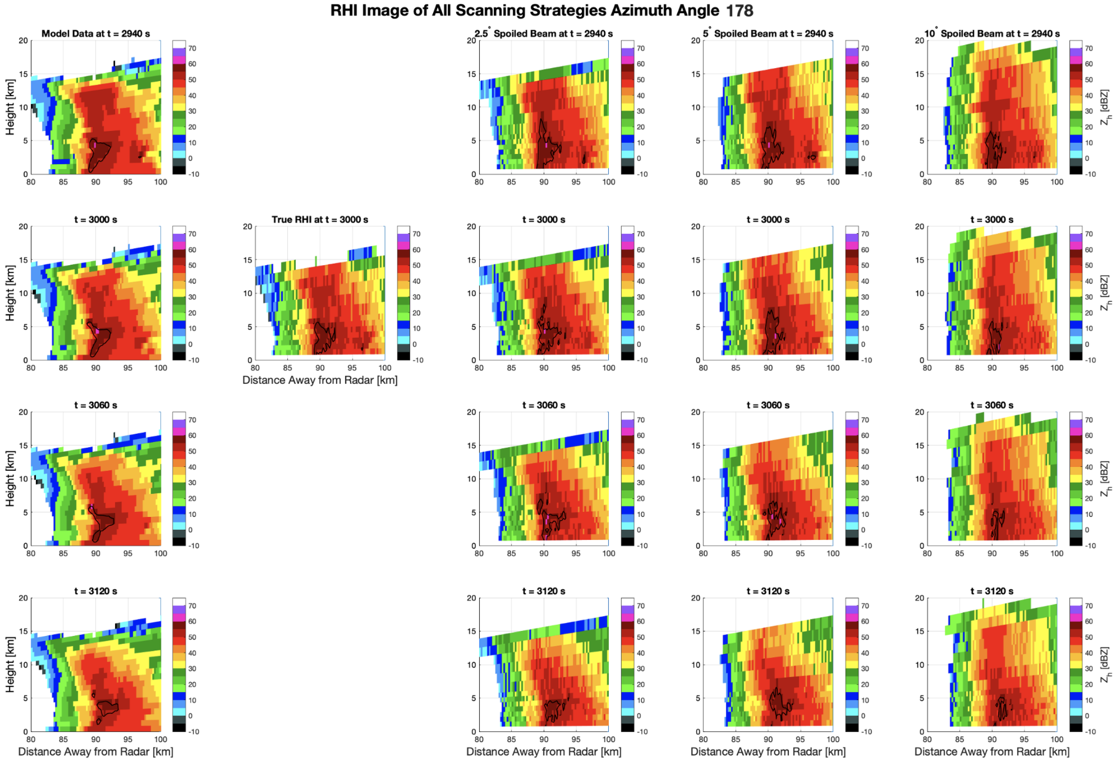
RHI Image of All Scanning Strategies Azimuth Angle 178

Figure 3.25 (*Continued*)

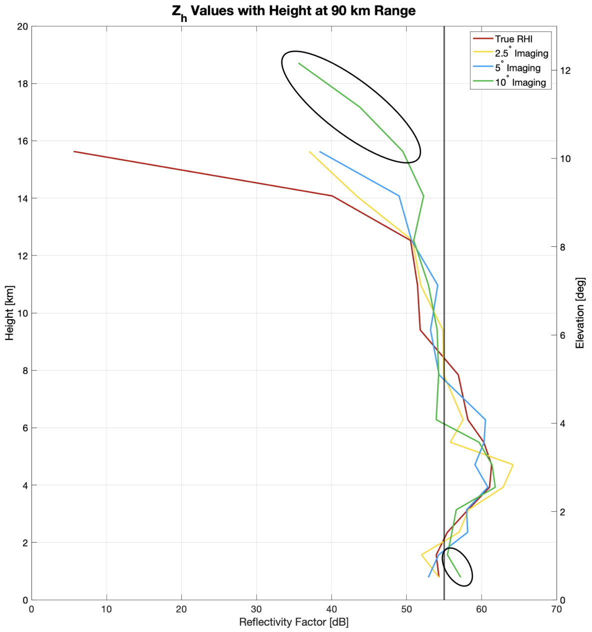

Figure 3.26: Scatter plot of Z_h values with height at 90 km range along azimuth angle 178 for true RHI (red), 2.5° imaging (yellow), 5° (blue), and 10° (green). Smearing effects are annotated with black circles. The vertical black line denotes the 55 dBZ level.

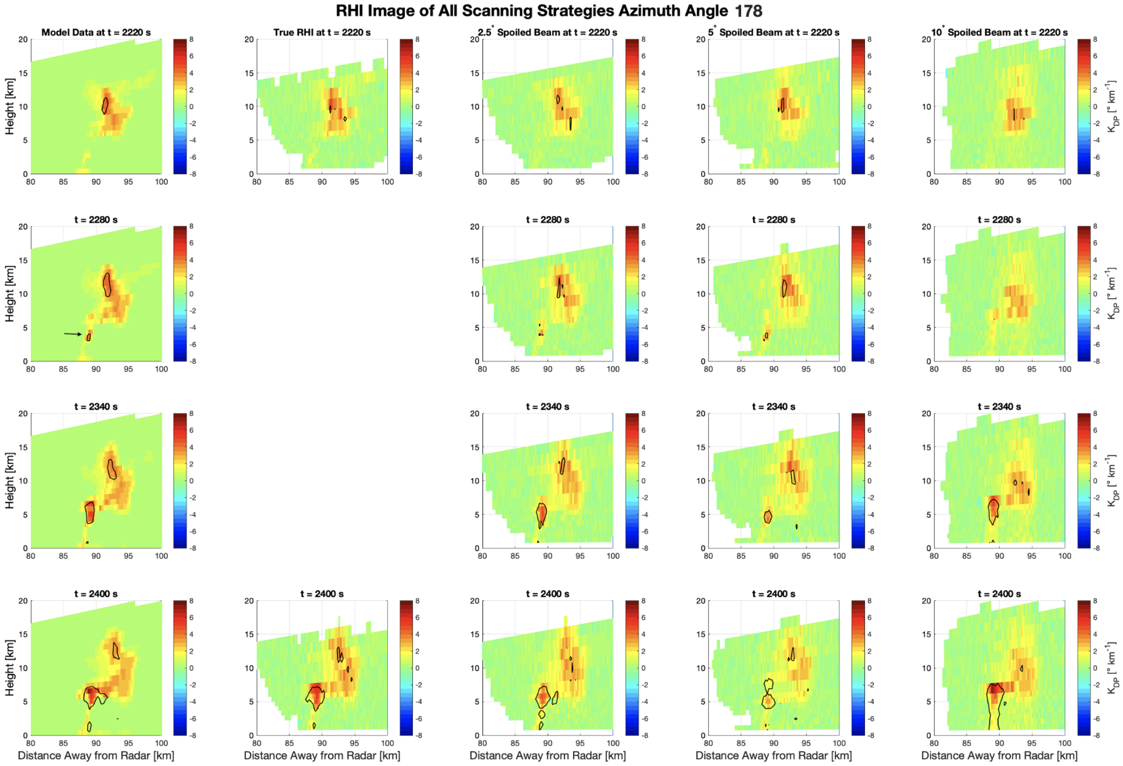

Figure 3.27: Similar to Figure 3.9 but at 90 km range and azimuth angle 178.

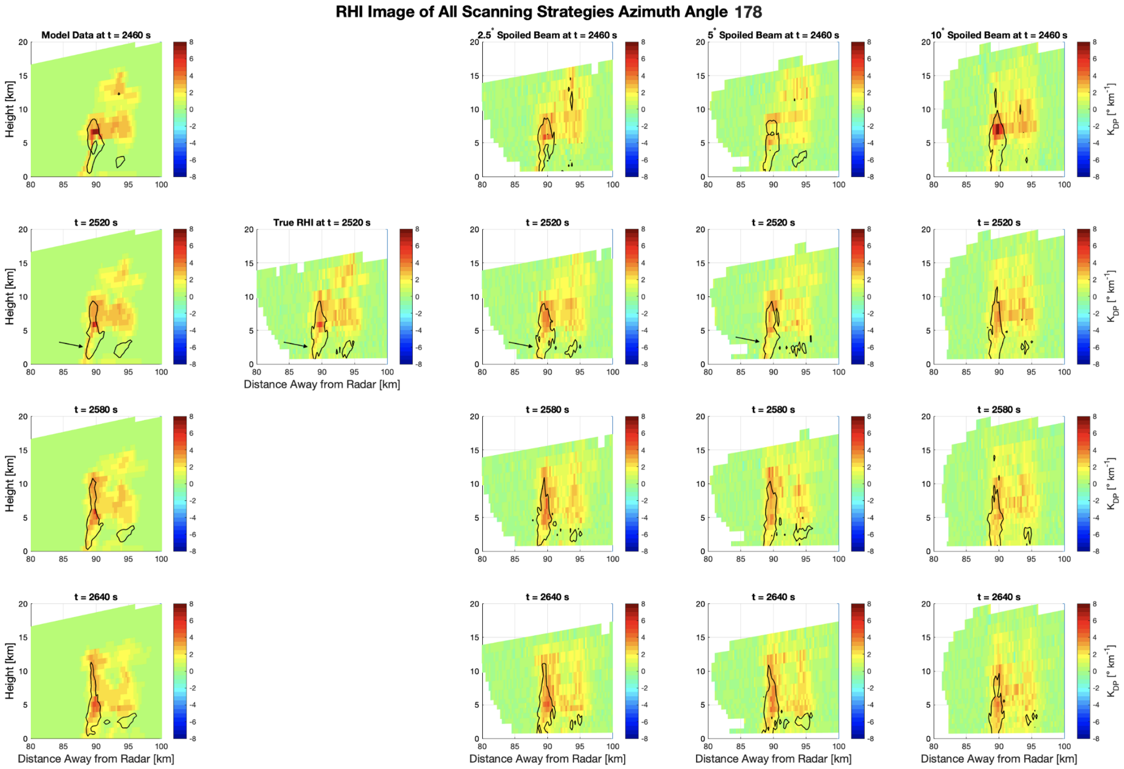

Figure 3.27 (*Continued*)

phenomenon was also observed in Figure 3.25, and the root cause is believed to be the same for both observations. Namely, that the signatures are on the edge of the 2.5° and 5° imaging transmit beams, which makes it harder for them to properly observe that centralized signature. As also seen in Figure 3.25, when moving forward in time, the signature stretches vertically, and it becomes easier and easier for the 2.5° and 5° imaging cases to detected the signature; then, by $t = 2520$ s, they better represent the K_{DP} core compared to the 10° imaging data.

3.1.2.2 Quantitative Analysis

The same variables discussed in Section 3.1.1.2 were recalculated and are shown below for the 90 km case. These variables are average measures of the intensity, size, and shape of the DRC, K_{DP} core, and mid-level convergence from all 5 error analysis data sets. Because of the location of the 0.5° elevation angle, surface divergence is not quantified below for

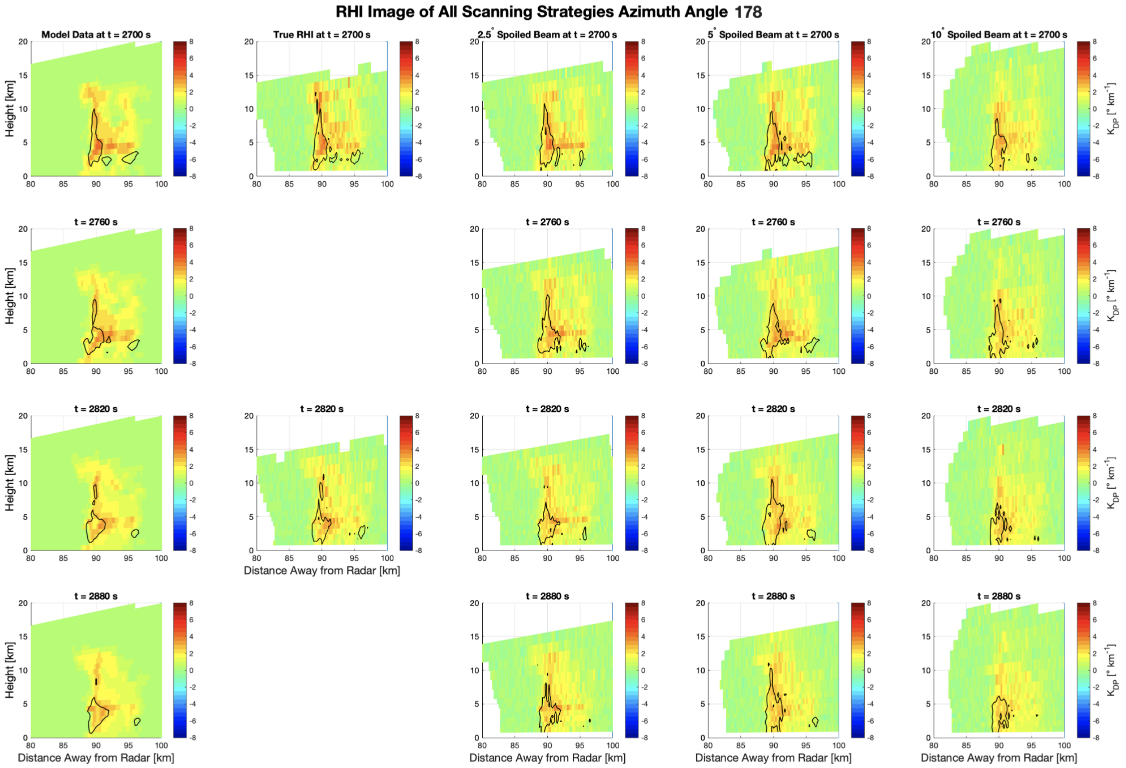

Figure 3.27 (*Continued*)

the 90 km data; however, the time of the surface microburst will be the same as the one determined in Section 3.1.1.2, and is displayed as a vertical black line.

Starting with the mid-level convergence signature (Figure 3.28), it evolves similarly to the mid-level convergence at 30 km (Figure 3.12); however, the magnitude of the signature is much stronger than what was seen at 30 km. This could be caused by two things: the interpolation using the nearest neighbor method grabbed different points between 30 km and 90 km interpolations, or the closest elevation to 4 km AGL has different data than at 30 km due to differences in beam height of closest elevation (e.g., looking at 3.7 km AGL as opposed to 4.1 km AGL). The maximum mid-level convergence still occurs around $t = 2400$ s; however, the decrease in mid-level convergence after the maximum occurs much more rapidly here than at 30 km. Furthermore, none of the scanning strategies observe mid-level convergence ΔV of > 25 m s^{-1} likely due to decreased sampling resolution at 90 km range. From this figure, it implies that the 2.5° imaging data best captures the

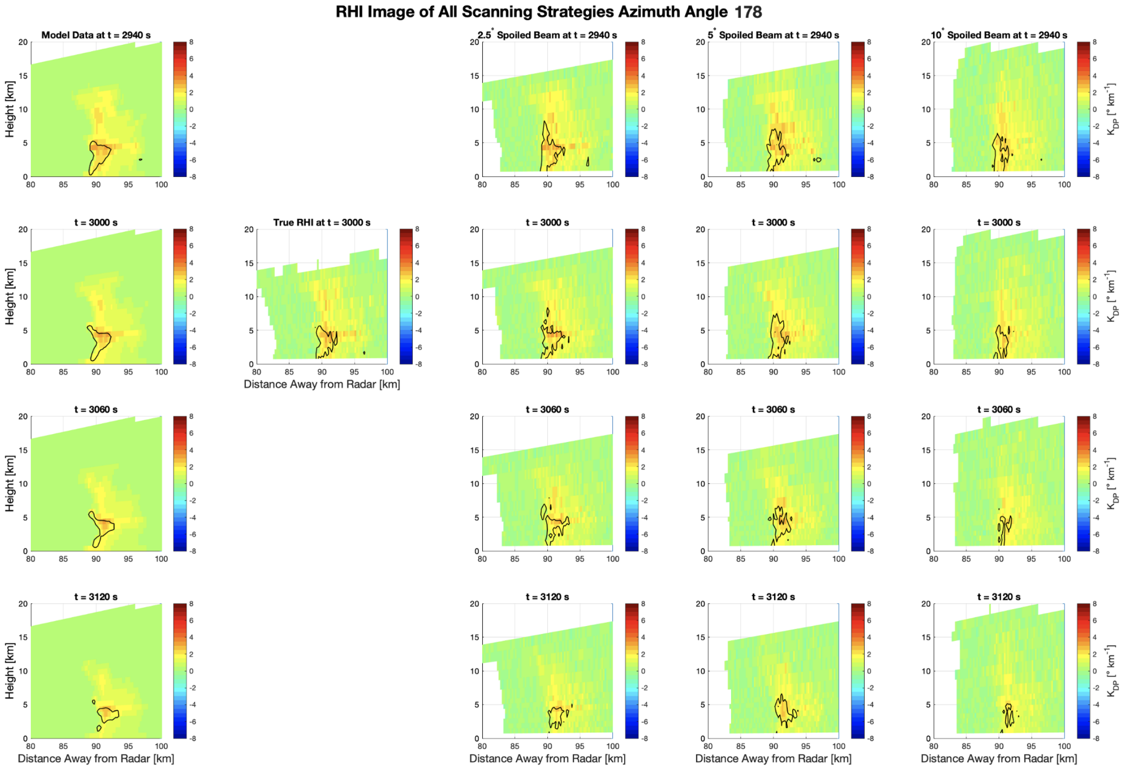

Figure 3.27 (*Continued*)

evolution of the mid-level convergence signature having the highest ΔV value. There is a noticeable increase in mid-level convergence ΔV in the true RHI data at $t = 2370$ s, but it has a magnitude under half of the magnitude observed in the model data. Finally, at this distance, both the 5° and 10° imaging cases did not observe the mid-level convergence ΔV well but rather remained rather consistent between 10–15 m s^{-1} from $t = 2280$ s through the analysis period. This lack of observation in 10° imaging was also seen at 30 km range; however, the lack of detection by the 5° imaging scans was vastly different from the 30 km range case. This implies that larger spoiling factors could struggle with V_r signatures at further ranges from the radar, but I digress.

Looking at Z_h, the first quantitative analysis is for the intensity of the Z_h column that develops. This was measured as the 95th percentile Z_h value over the analysis domain and the change per unit time of the 95th percentile Z_h value (Figure 3.29). The 95th percentile Z_h values evolve similarly to the values at 30 km (Figure 3.13). They start off low ($\leq$ 45

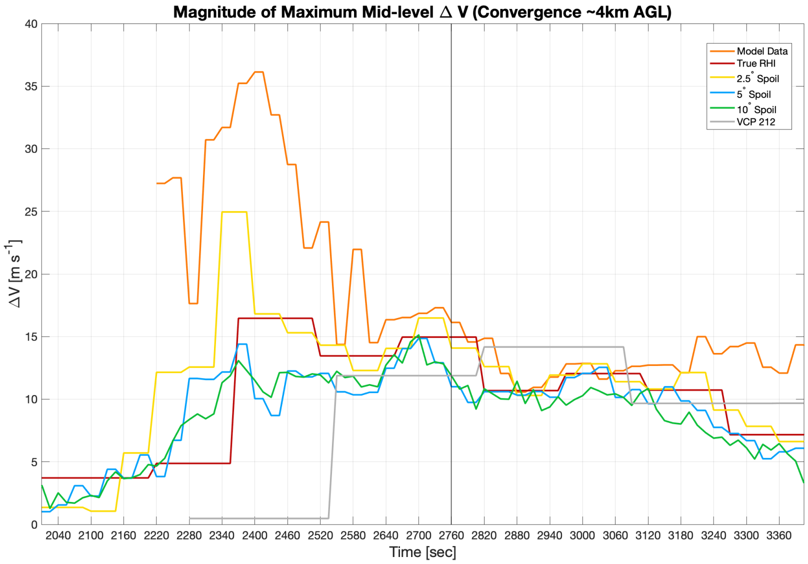

Figure 3.28: Same as Figure 3.12 but at 90 km range.

dBZ) but start to rapidly increase in magnitude from $t = 2280$ s to $t = 2460$ s; however, this increase is not as drastic as was seen at 30 km. Around $t = 2520$ s, the 95^{th} percentile Z_h values generally level off and remain between 56 dBZ and 60 dBZ before starting to decrease in magnitude around $t = 3060$ s (which corresponds to the ending of the microburst at the surface seen in Figure 3.11). Throughout the analysis period, all scanning strategies, except for VCP 212, observed a higher 95^{th} percentile Z_h value than observed in the model data, and this could be caused by the sampling differences resulting in a smaller sample size of points and increasing the Z_h value if a similar maximum is detected. However, it could also be due to added random errors which are not present in the model data.

The rapid increase observed in Figure 3.29 is also seen when looking at the change per unit time of the 95^{th} percentile Z_h values (Figure 3.30). By unit time, the largest increase in the 95^{th} percentile Z_h values most drastically increases between $t = 2340$ s and $t = 2400$ s. In Figure 3.30, the temporal resolution greatly impacts the values seen as the fastest temporal resolution, 10° imaging, is associated with the largest maximum change and the lowest temporal resolution, VCP 212, is associated with the smallest maximum change. However, for all potential PAR scanning strategies - true RHI and all imaging data - the

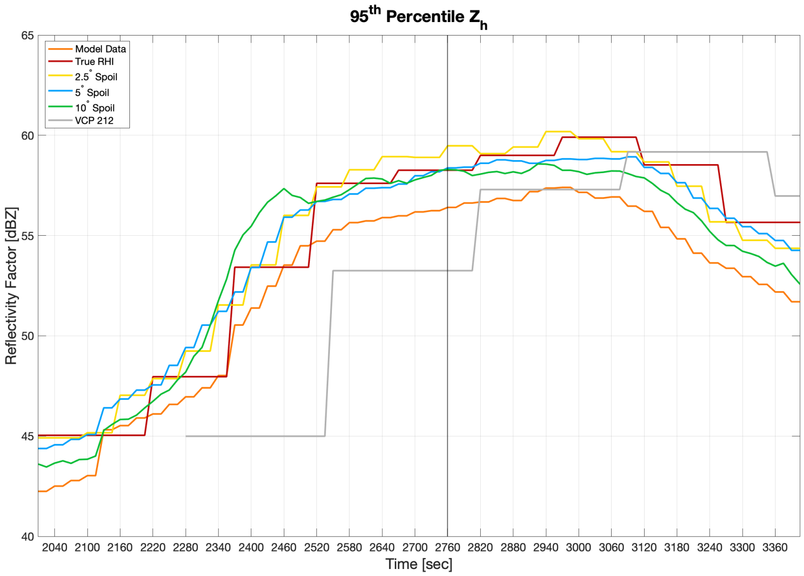

Figure 3.29: Same as Figure 3.13 but at 90 km range.

change in 95^{th} percentile Z_h values reaches > 2 dBZ $\min^{-1}$ approximately 6 min prior to the microburst reaching the surface. This sharp increase is believed to be a sign of ongoing hydrometeor loading being observed with the Z_h column.

The volume of the Z_h column behaves differently from the behavior observed at 30 km range (Figure 3.15), and this is likely because the full storm is observed at 90 km as opposed to 30 km. In Figure 3.31, once the Z_h column is detected, the total volume of the signature continues to increase rather linearly until reaching a maximum around $t = 2940$ s. This point is right at the end of the microburst at the surface, and after $t = 2940$ s, the size of the Z_h column drastically decreases to less than 15 km^3 by the end of the analysis period at $t = 3420$ s. All scanning strategies observed a higher maximum volume of the Z_h column than the model data, and it is because of the sampling differences. This peak at 90 km corresponds to the secondary peak observed at 30 km range (Figure 3.31), which could imply the need for higher scanning angles at 30 km range to properly capture this entire signature at close range.

The evolution of the shape of the Z_h column appears similar to the 30 km case (Figure 3.16); however, the added range allowed for the actual maximum height observations as

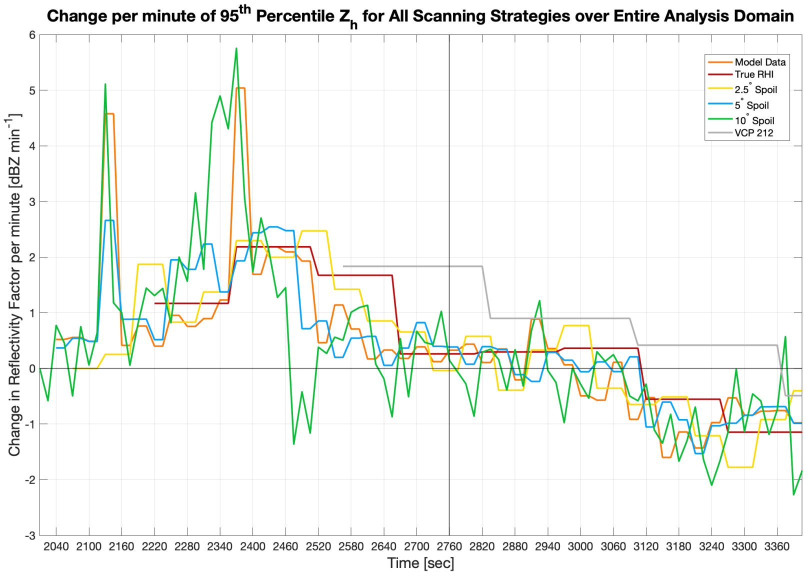

Figure 3.30: Same as Figure 3.14 but at 90 km range.

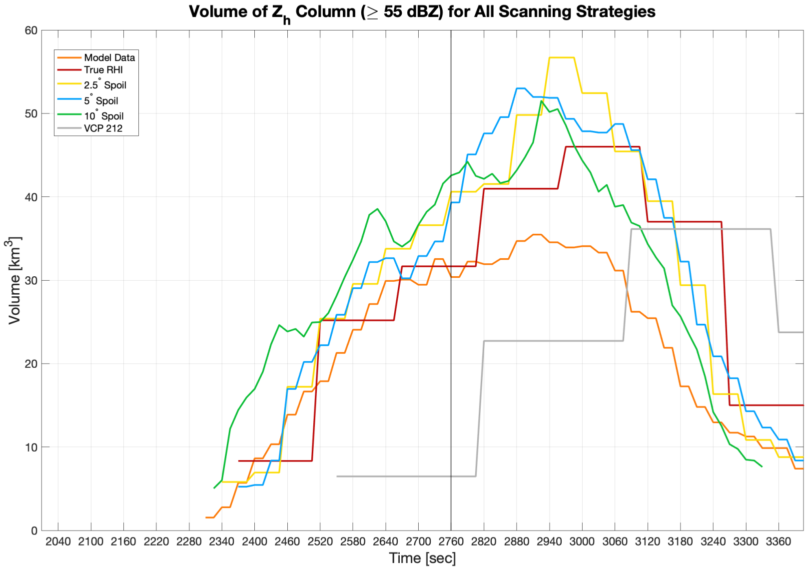

Figure 3.31: Same as Figure 3.15 but at 90 km range.

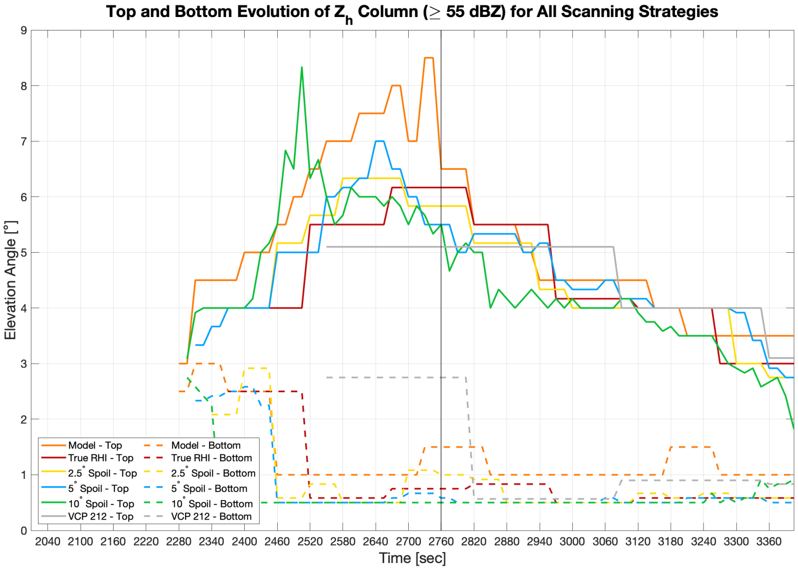

Figure 3.32: Same as Figure 3.16 but at 90 km range.

opposed to the 20° scanning elevation limit at 30 km. In all scanning strategies, the Z_h column reaches a maximum height prior to microburst formation at the surface, and evidence of descent in the upper limit of the signature can be observed. The spurious detection of a maximum height at 9° elevation ($\approx$ 14.1 km AGL) in the 10° imaging data is likely caused by smearing effects. These smearing effects also contribute to the lack of observations in the evolution of the bottom limit of the Z_h column as the 10° imaging data reaches the surface just after $t = 2340$ s and remain there until $t = 3300$ s. Otherwise, the other scanning strategies follow the general trend in the model data and what was discussed with Figure 3.16.

Moving into the quantification of the K_{DP} core, the first thing analyzed was the intensity measurements from the storm (Figures 3.33 & 3.34). The 95th percentile K_{DP} again behaves similarly to the observations seen at 30 km (Figure 3.17). The 95th percentile K_{DP} start off very small before steadily increasing to their maximum before the microburst occurs at the surface; however, this increase in the 95th percentile K_{DP} is not as drastic as observed at 30 km range. Once the microburst occurs at the surface, these values steadily decrease throughout the remainder of the analysis period.

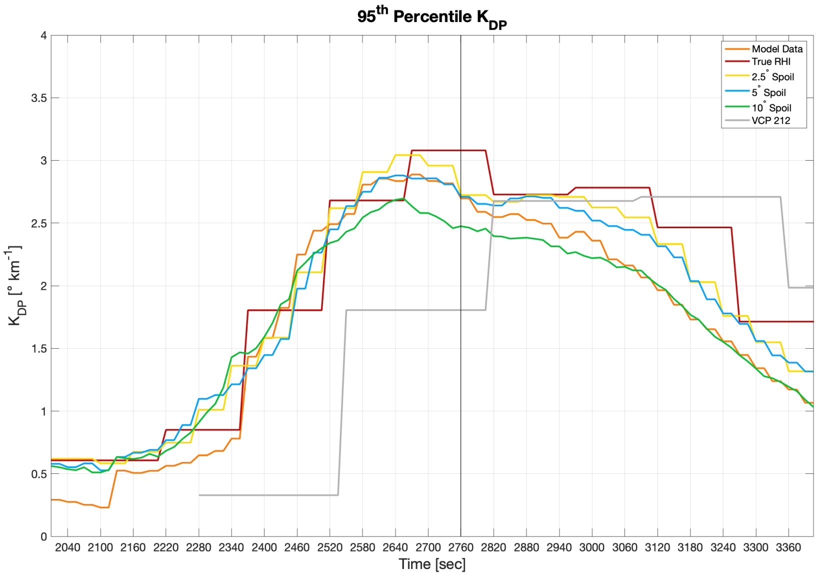

Figure 3.33: Same as Figure 3.17 but at 90 km range.

When looking at the change in the 95^{th} percentile K_{DP} (Figure 3.34), there are a few relative maxima observed. First, the scanning strategies with less than 1 min resolution - 5° and 10° imaging - detect the relative maximum at t = 2130 s. The next relative maximum has little agreement on actual timing of the increase; however, all but one potential PAR scanning strategy detect it within approximately 1 min of the model data. The final relative maximum is detected by all imaging cases, but the true RHI data does not have fine enough resolution to observe this increase. Once these maxima occur, the change in the 95^{th} percentile trends downward until reaching and generally remaining negative after the microburst reached the surface. Thus, the overall trend is similar to the 30 km case (Figure 3.18).

The total volume of the K_{DP} core at 90 km (Figure 3.35) also evolves similarly to the 30 km case. Once the K_{DP} core is detected, it continued to grow rapidly before reaching a maximum just before the onset of microburst winds at the surface. After the maximum is reached, the K_{DP} core volume quickly decreases with most scanning strategies no longer show the signature by $t = 3300$ s except VCP 212 and true RHI scanning which do not detect this dissipation due to temporal resolution restrictions. The most interesting thing

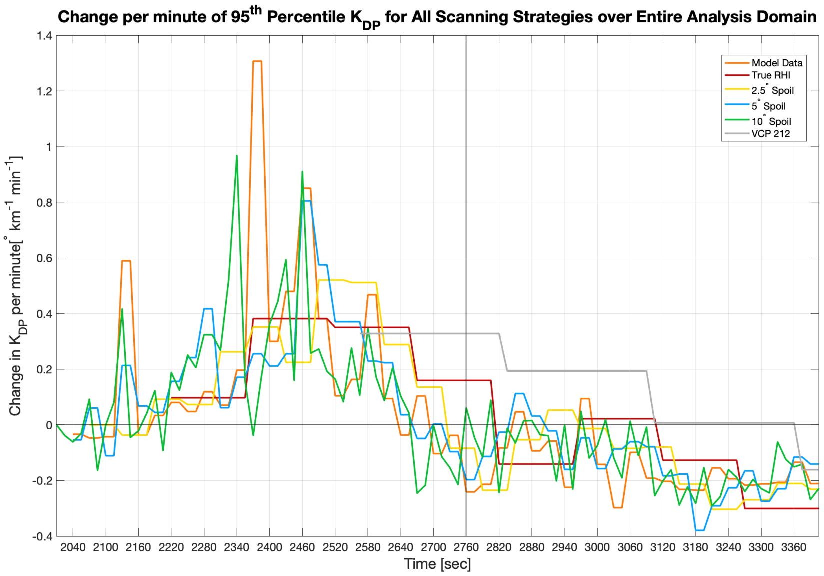

Figure 3.34: Same as Figure 3.18 but at 90 km range.

seen here is that the 5° imaging case actually has a maximum volume located after the microburst occurs at the surface as opposed to prior like the other scanning strategies. A small increase in volume is also seen in the 2.5° imaging around the same time; however, it is not as pronounced.

Finally, the observations of the vertical structure of the K_{DP} core were quantified and shown in Figure 3.36. Because of the distance from the radar, the entire K_{DP} core signature can be observed as was seen for the Z_h column; however, a similar evolution of the shape of the K_{DP} core is observed to the observations at 30 km range. Namely, after the K_{DP} core is detected, the top of the K_{DP} core builds upwards before reaching a maximum height. The top of the K_{DP} core remains relatively constant until after the microburst occurs at the surface and then quickly decreases starting around $t = 2940$ s when the top drops from around 7° elevation to closer to 4° elevation ($\approx$ 11 km and 6.3 km AGL, respectively). Regarding the bottom, it evolves similarly to the observations at 30 km with remaining relatively constant until $t = 2520$ s. After that time, the bottoms of different scanning strategies bob up and down until finally lifting from the surface around $t = 3090$ s. It should be noted that the 10° imaging line never raises from the surface until around $t = 3090$ s,

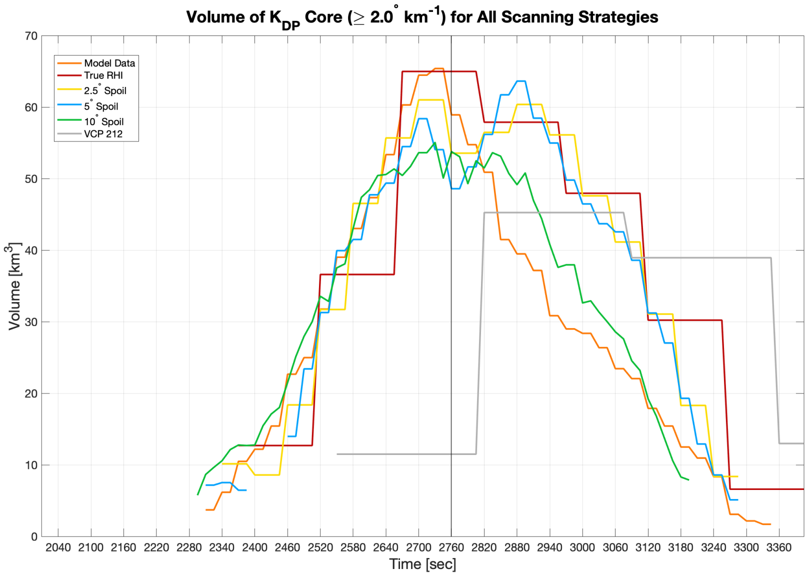

Figure 3.35: Same as Figure 3.19 but at 90 km range.

and this deviation from the other scanning strategies is likely a smearing effect and can be corroborated in Figure 3.27.

3.1.3 Summary of Qualitative and Quantitative Analyses

The previous sections dealt with both the qualitative and quantitative scanning analysis at both 30 km and 90 km range for a proof-of-concept test case. Thus, these results should be considered preliminary; however, the results were relatively similar for many of the scanning strategies between the two different ranges. Because of the distance from the radar, the 90 km range data was less optimal to observe the microburst, especially at large spoil factors, which was expected. The 90 km range data struggled with observing the signatures as accurately as the 30 km range data due to increases in range gate size in both azimuth and elevation. The main takeaways from the above analysis can be summarized as:

- The 30 km data showed the best overall picture of the microburst as the resolution/sampling allowed for tracking the descent of the microburst to the surface,

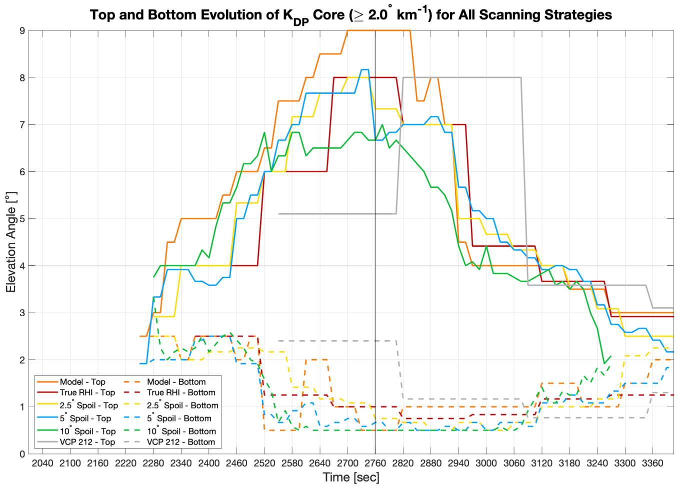

Figure 3.36: Same as Figure 3.20 but at 90 km range.

  - However, to properly observe the entirety of the signatures, higher scanning angles than 20° are needed.

- The qualitative observations were more ideal for tracking signatures at 30 km range because of the increased sampling of the low to mid-levels of the storm.

- Even though magnitudes varied, the general trends observed in the quantitative data were similar between both the 30 km and 90 km data.

  - However, certain signatures, such as the volume of the Z_h column and K_{DP} core, had different trends because the 90 km case was able to observe the entirety of the storm where the 30 km case only observed up to around 10–12 km AGL.

3.2 Error Analysis

The error analysis focuses on the evolution changes when adding error into the data of the same variables analyzed in Sections 3.1.1.2 & 3.1.2.2. There were a total of 5 sets of error analysis completed for each the 30 km and 90 km cases in this proof-of-concept analysis, and this error analysis dives into comparisons between these 5 error analysis data sets.

3.2.1 Microburst at 30 km Case

When adding error into the data, the general observation was that the 10° imaging had the highest errors while VCP 212 scans had the lowest. However, some calculated variables were more greatly impacted with these errors compared to others. Table 3.1 shows the MAE over all 5 error sets associated with each measured variable analyzed in 3.1.1.2 in relation to the pure emulation data for each scanning strategy and not to the model data itself. As seen for the majority of the quantitative observations, the 10° imaging data has the largest MAE associated with the 5 different error analyses.

Table 3.1: MAEs of calculated measurements associated with the precursor signatures in each radar variable along with error for observation of the microburst at the surface. The abbreviation "Perc." represents percentile. The bold values represent largest MAEs associated with each quantified metric.

Variable	Observation	Units	Scanning Strategy				
			True RHI	2.5° Spoil	5° Spoil	10° Spoil	VCP 212
Z_h	95^{th} Perc.	dBZ	0.42	0.50	0.53	**0.63**	0.14
	95^{th} Perc. Change	dBZ	0.08	0.24	0.38	**0.74**	0.04
	Elevated Volume	km^3	0.60	0.81	0.74	**1.25**	0.25
	Region Top	°	0.63	0.57	0.64	**0.73**	0.16
	Region Bottom	°	0.53	**0.80**	0.71	0.57	0.07
K_{DP}	95^{th} Perc.	° km^{-1}	0.10	0.11	**0.12**	0.10	0.02
	95^{th} Perc. Change	° km^{-1}	0.02	0.05	0.07	**0.13**	0.01
	Elevated Volume	km^3	0.82	0.90	0.99	**1.16**	0.19
	Region Top	°	0.31	0.32	0.46	**0.61**	0
	Region Bottom	°	0.54	0.53	0.68	**0.89**	0.07
V_r	Mid-level Conv.	m s^{-1}	**0.87**	0.59	0.73	0.65	0.21
	Surface Div.	m s^{-1}	**1.18**	0.96	0.87	0.75	0.23
	Surface Div. Area	km^2	**0.92**	0.74	0.70	0.14	0.30

However, looking more specifically into the contents of Table 3.1, there are a few things that jump out. First, for both 95^{th} percentile calculations - Z_h and K_{DP} - the average error associated with imaging is roughly similar to the true RHI scans. Thus, it appears that when operating on similar dwell times, intensity observations show little difference in errors between the true RHI and small imaging cases with the largest difference in errors for Z_h being 0.21 dBZ and for K_{DP} being 0.02° km^{-1}. Furthermore, looking at the general trend of the MAE for each calculated observation, it is typically seen that, once imaging is used, the errors increase with increasing spoiled beamwidths. That is to say that the 10° imaging tends to have the largest MAE of any of the scanning strategies. There are some notable exceptions to this such as all V_r signatures, Z_h column bottom, and 95th percentile K_{DP}, and these signatures will be analyzed in more detail below. Similar plots for the other calculated observations can be found in Appendix B.

The increase in errors associated with the increase in spoil factor could be caused by a couple factors that directly influence the standard deviations of the radar variable estimators: $SD(\hat{v})$, $SD(\hat{Z}_h)$, and $SD(\hat{K}_{dp})$. First, the σ_v (Eqn. 2.19) calculations rely on σ_θ (Eqn. 2.20) which is a function of beamwidth. Thus, larger spoiled beamwidths increase the value of σ_θ. This also increases σ_v, which in turn increases the standard deviations of the V_r and K_{DP} estimators. In a similar process, SNR is calculated such that an increased spoil factor decreases the SNR. This reduction in SNR also acts to increase the standard deviations of the estimators as well.

One thing to note when diving into the following comparisons is that these MAEs are only relative to the original emulated data and not the model data. Thus, smaller errors imply that the estimates provided by the original emulations were "more precise"; however, if a scanning strategy did not properly observe a signature to begin with, then having smaller MAEs is a problem.

Starting off with the V_r signatures, Figure 3.37 shows 6 different panels for each scanning strategy along with an average of ΔV over the 5 realizations from the different scanning strategies in the bottom right panel for mid-level convergence observations. Each panel contains the pure observations, each error analysis observation and an average of all observations of the signature. The most notable thing observed in Figure 3.37 is the similarities in the behavior of the errors between each of the PAR scanning strategies: true RHI and all imaging cases. There is little difference between the true RHI and all imaging cases, and the errors associated with the true RHI data actually perform worse than all imaging cases. It can be seen that the true RHI data is generally observed to have higher errors throughout the analysis period compared to the other scanning strategies over the 5 error data sets used here. There are some instances where the 2.5° imaging data also has higher fluctuations, but these are more rare and can be seen at $t = 2220$ s and $t = 2340$ s. However, as previously seen in Figure 3.12, 10° was not necessarily well representative of the model environment. Thus, having slightly lower MAEs does not bolster its average estimation as being more accurate.

When looking at the error analysis of surface divergence (Figure 3.38) and area of surface divergence ≥ 10 m s^{-1} (Figure 3.39), the VCP 212 scans have the lowest MAE. However, among the PAR scanning strategies, the 10° imaging has the lowest MAE while the true RHI actually has the highest. Now, this is likely a similar issue to the observation associated with the mid-level convergence. Namely, the 10° imaging had smaller errors due to lower ΔV values associated with a missed detection of the microburst at the surface, and had the 10° imaging actually observed the microburst at the surface, it would likely have had the highest MAE of all scanning strategies. This same line of reasoning applies to the area of surface divergence ≥ 10 m s^{-1} because once the microburst reaches the surface around $t = 2760$ s, the 10° imaging area disappears because the ΔV drops below the threshold. Thus, it is hard to have large errors when the signature is not even calculated because a threshold has not been met. Also notice in Figure 3.39 that, generally speaking, the larger the area detected, the larger the errors were. This is seen in all scanning strategies regardless of beam pattern or scanning technique.

Looking at the other radar variables, it can be seen that the effects of smearing are actually benefiting the 10° imaging case with regard to errors associated with the Z_h column

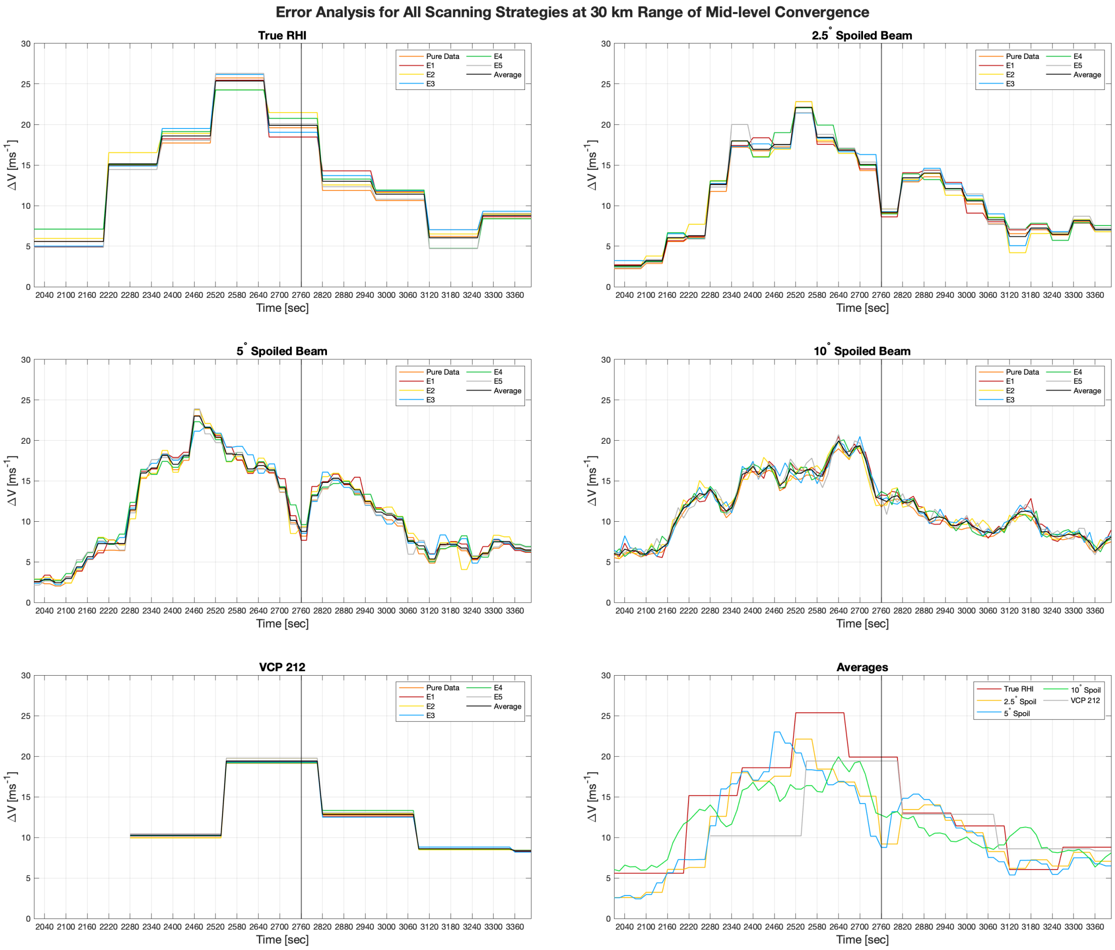

Figure 3.37: Display of the mid-level convergence observations for each error analysis for each scanning strategy. Each panel shows the pure emulation observations, each error analysis observation, and an average of all observations. The bottom right panel is a compilation of the averages from each of the other 5 panels to compare with each other.

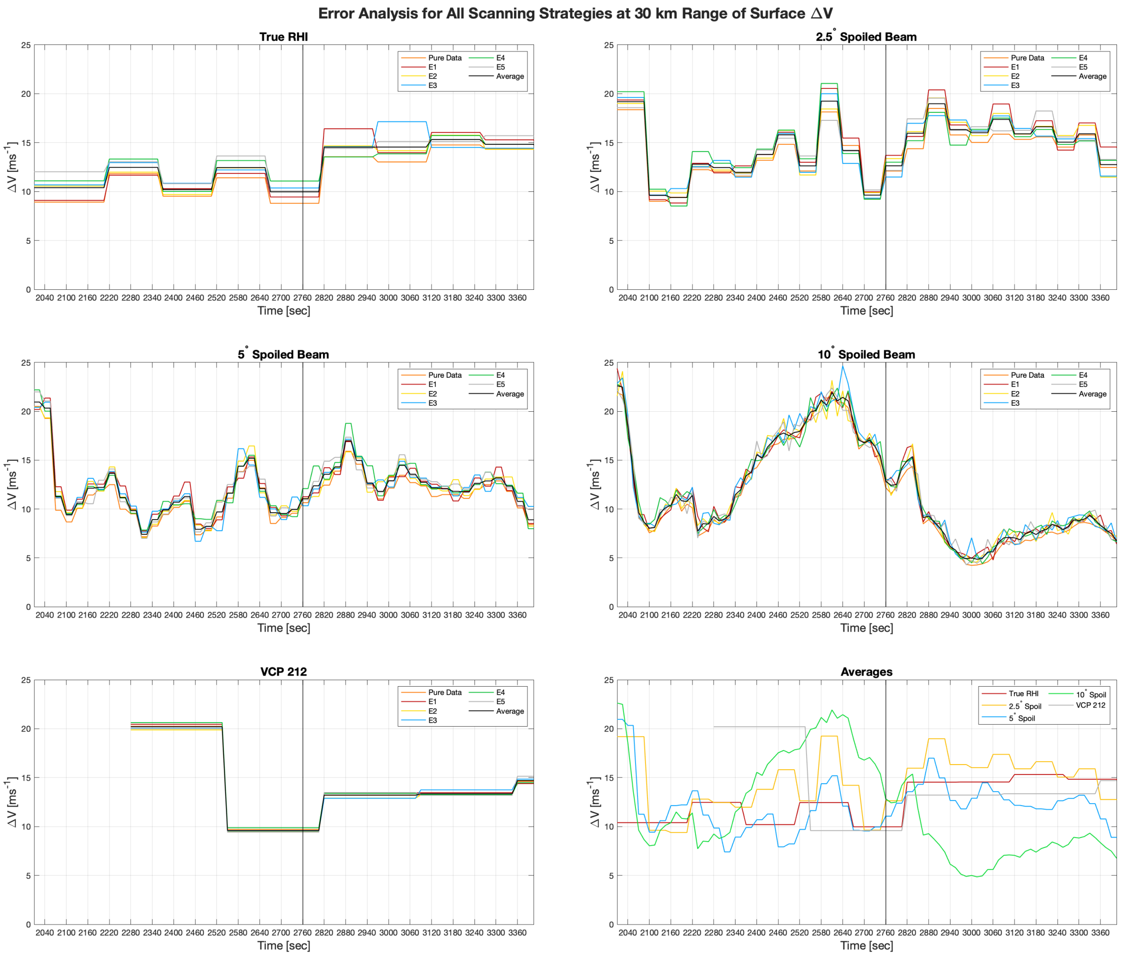

Figure 3.38: Same as Figure 3.37 but for surface divergence.

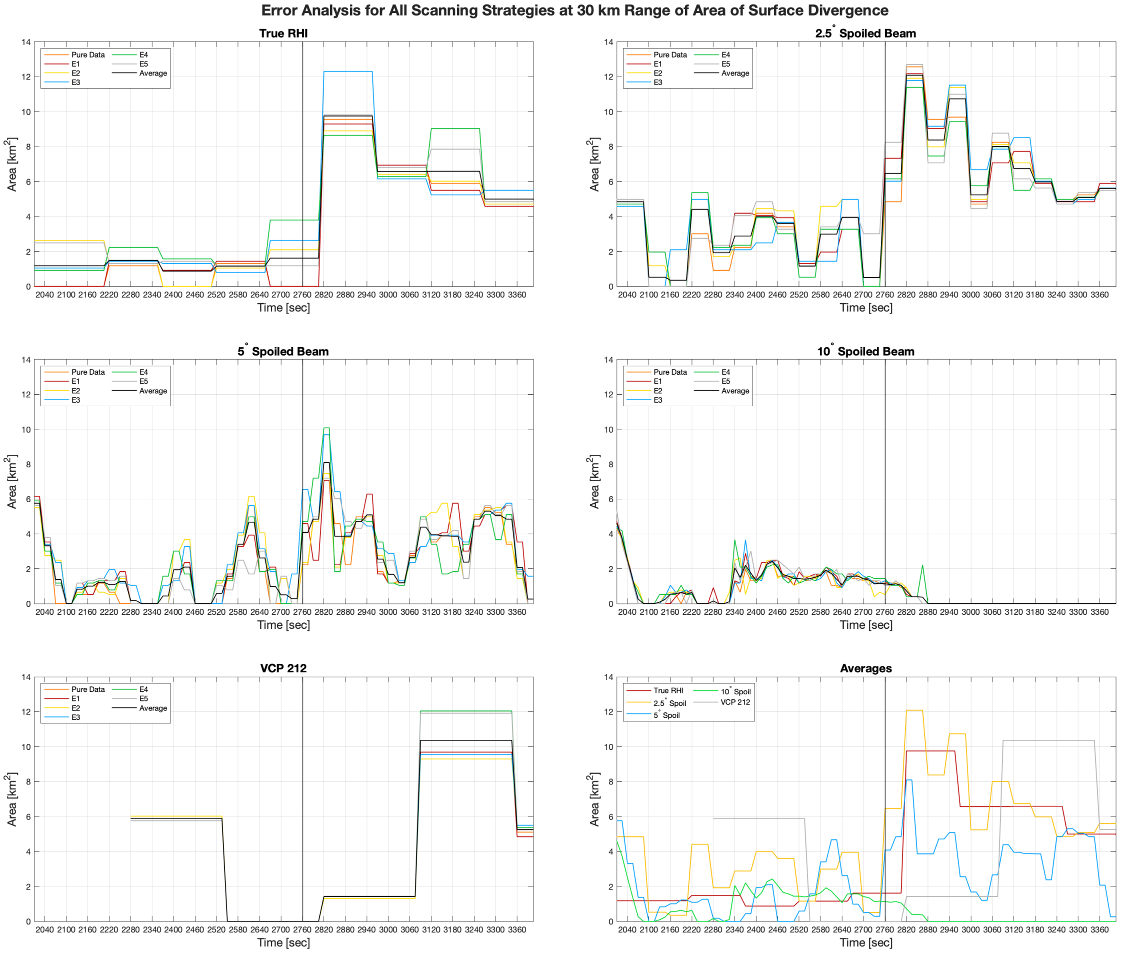

Figure 3.39: Same as Figure 3.37 but for the area of surface divergence that is associated with a $\Delta V \geq 10$ m s^{-1}.

bottom height. In Figure 3.40, notice how between $t = 2460$ s and $t = 2640$ s along with $t = 2820$ s and $t = 3000$ s the 10° imaging data rarely deviates from the surface in these two time frames. These two time frames were observed to be associated with smearing effects at the lower levels of the Z_h column that were corroborated in Figure 3.6. Furthermore, without these smearing effects, a similar phenomenon would be observed with the bottom of the Z_h column as seen with the top of the Z_h column where the 10° imaging data has the highest MAEs (Table 3.1). Therefore, although there was a perceived ”benefit” in the 10° imaging by having smaller errors in the Z_h column bottom height, this was only because the signature was not properly observed and was obstructed by smearing effects.

The 95^{th} percentile K_{DP} errors are interesting to say the least. Namely, the 5° imaging data has the highest MAEs; however, this is not by a wide margin. Looking back at Table 3.1, it can be seen that there is little variation between the PAR scanning strategies when compared with one another. Between the lowest and highest errors there is only a 0.02 ° km^{-1} difference in the error value. This lack of deviation in the MAEs between the PAR scanning strategies can be seen in Figure 3.41 where there is generally a uniform increase in the measured 95^{th} percentile K_{DP} value for all cases. This increase is typically no larger than approximately 0.2° km^{-1}, but is largest at the beginning of the analysis period before $t = 2280$ s, which happens to coincide with the formation of the K_{DP} core (Figure 3.9). However, this uniform increase in 95^{th} percentile K_{DP} is not observed in VCP 212. The reason this is not observed in VCP 212 is likely due to the fact that the MAE for the 95^{th} percentile K_{DP} value in VCP 212 is almost 5.5 times smaller than the next smallest MAE with a magnitude of $< 0.02°$ km^{-1}. This increase is likely caused by looking at the 95^{th} percentile K_{DP} value as opposed to the actual data itself which have been shown to have a Gaussian distribution (Figure 2.16).

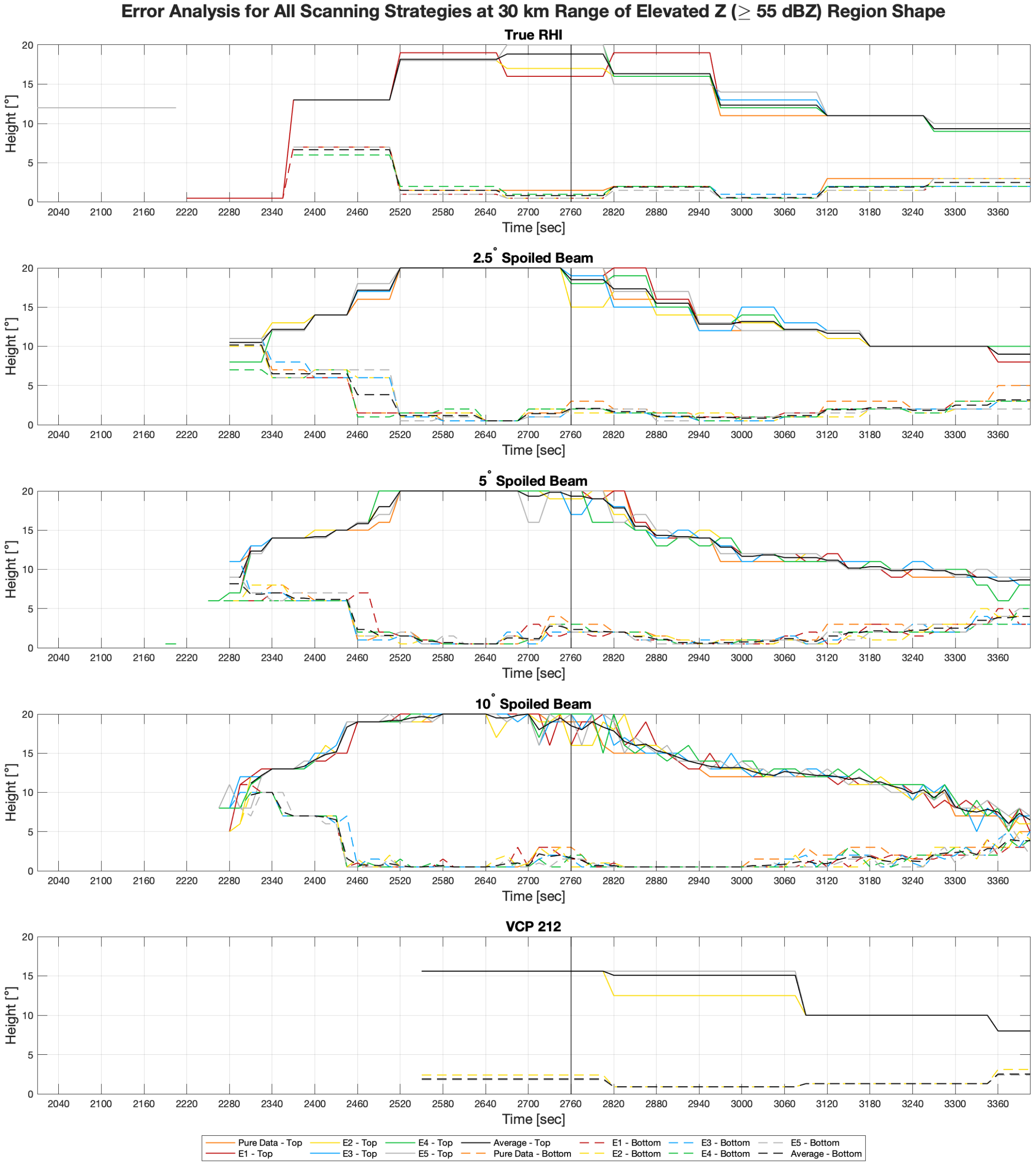

Figure 3.40: Same as Figure 3.37 but for the shape of the Z_h column.

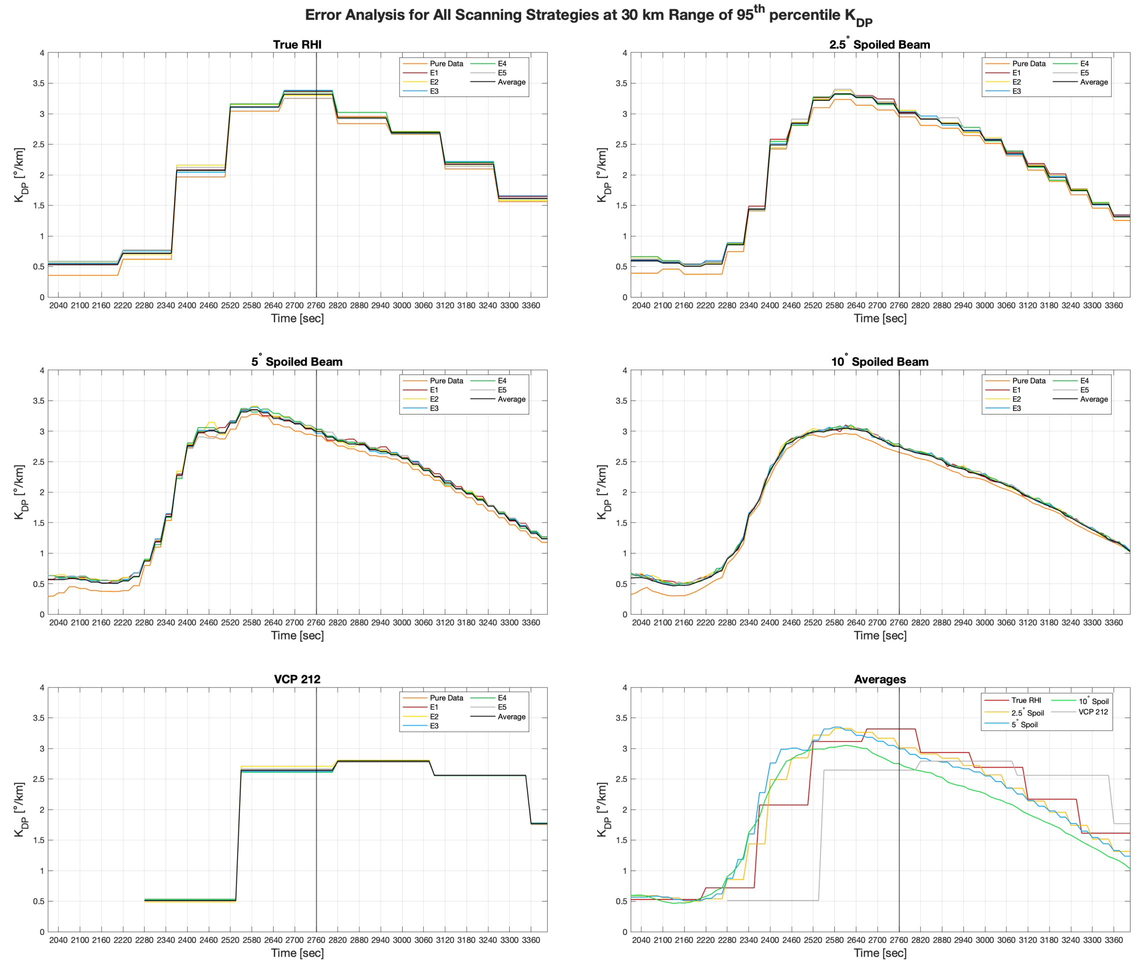

Figure 3.41: Same as Figure 3.37 but for 95th percentile K_{DP}.

3.2.2 Microburst at 90 km Case

There was generally a noticeable increase in the MAEs in all scanning strategies when compared to the 30 km error analysis (Section 3.2.1). When comparing Table 3.2 to Table 3.1, it can be seen that the MAEs for all scanning strategies tended to increase at increased range. However, the same general trend within the scanning strategies can be observed with 10° imaging typically having the highest MAEs, but this trend breaks down for different observations at 90 km compared to 30 km. Notice how the the change in 95^{th} percentile Z_h follows the general trend whereas the K_{DP} bottom and 95^{th} percentile Z_h do not. The error analyses that will be discussed in more detail include K_{DP} bottom height, 95^{th} percentile Z_h, and Z_h column total volume. Additional figures similar to those below will be located in Appendix B.

Table 3.2: Same as Table 3.1 but for MAEs at 90 km range.

Variable	Observation	Units	Scanning Strategy				
			True RHI	2.5° Spoil	5° Spoil	10° Spoil	VCP 212
Z_h	95^{th} Perc.	dBZ	0.33	0.33	**0.37**	**0.37**	0.15
	95^{th} Perc. Change	dBZ	0.09	0.29	0.57	**1.06**	0.04
	Elevated Volume	km^3	**1.76**	1.29	1.70	1.61	0.47
	Region Top	°	0.29	0.29	0.32	**0.39**	0.02
	Region Bottom	°	**0.17**	0.12	0.09	0.07	0.14
K_{DP}	95^{th} Perc.	° km^{-1}	**0.14**	0.13	0.12	0.13	0.02
	95^{th} Perc. Change	° km^{-1}	0.03	0.07	0.12	**0.20**	0.01
	Elevated Volume	km^3	2.80	2.49	2.49	**2.90**	0.64
	Region Top	°	0.32	0.28	0.39	**0.54**	0.14
	Region Bottom	°	**0.36**	0.25	0.21	0.16	0.08
V_r	Mid-level Conv.	m s^{-1}	2.34	1.71	1.92	**2.47**	0.43

Starting with the bottom height of the K_{DP} core observations, a similar story to what occurred at 30 km for the Z_h column bottom appears. Namely, when tracking the bottom of the K_{DP} core in each scanning strategy, there is a lack of movement in the 10° imaging data between $t = 2640$ s and $t = 3000$ s. During this time, there is also little movement detected in the 5° imaging data; however, there is more movement than was detected by the 10° imaging data. Looking back at Figure 3.27, this is most likely caused by the smearing effect observed in the 10° imaging data to be uniform throughout the different error analyses. This lack of movement contributes to the lower MAE even though the 10° imaging is not properly detecting the signature when compared to the model data. Furthermore, if the smearing effects were taken out, the MAEs for the bottom of the K_{DP} core would be similar to the top of the K_{DP} core signature and follow the general trend having the highest MAE (Table 3.2).

Examining two variables associated with Z_h, the first looks at the 95^{th} percentile Z_h values (Figure 3.43). In Figure 3.43, the magnitudes of error associated with the 5° and 10° imaging cases are the same. Furthermore, when looking at Figure 3.43, similarities between all scanning strategies can be observed with fairly little deviation from the average line by any of the given scanning strategies. The 5° and 10° imaging do occasionally experience large departures from the average; however, these do not greatly impact the MAEs with the 5° and 10° only being roughly 0.4 dBZ larger than the true RHI and 2.5° imaging. It should be noted that a uniform increase in the 95^{th} percentile Z_h is not observed at 90 km range as was seen in the 95^{th} percentile K_{DP} at 30 km range.

Finally, looking at the volume of the Z_h column in time, it becomes obvious why the true RHI data has the highest MAE (Figure 3.44). In RHI scans located at $t = 2820$ s and $t = 2970$ s, there are large departures in the E1 and E3 error analysis data from the pure data where E1 and E3 represent error data sets 1 and 3, respectively. The E1 departures at $t = 2820$ s is almost 5 km^3 lower than all other analyses during that time period for the true RHI scans. Furthermore, the E3 departures at $t = 2970$ s is almost 5 km^3 higher than all other analyses. None of the other scanning strategies really deal with such large departures on a consistent basis. The 5° and 10° imaging cases do have a couple of similar deviations; however, the larger deviation in the 5° or 10° imaging data never lasts longer than about

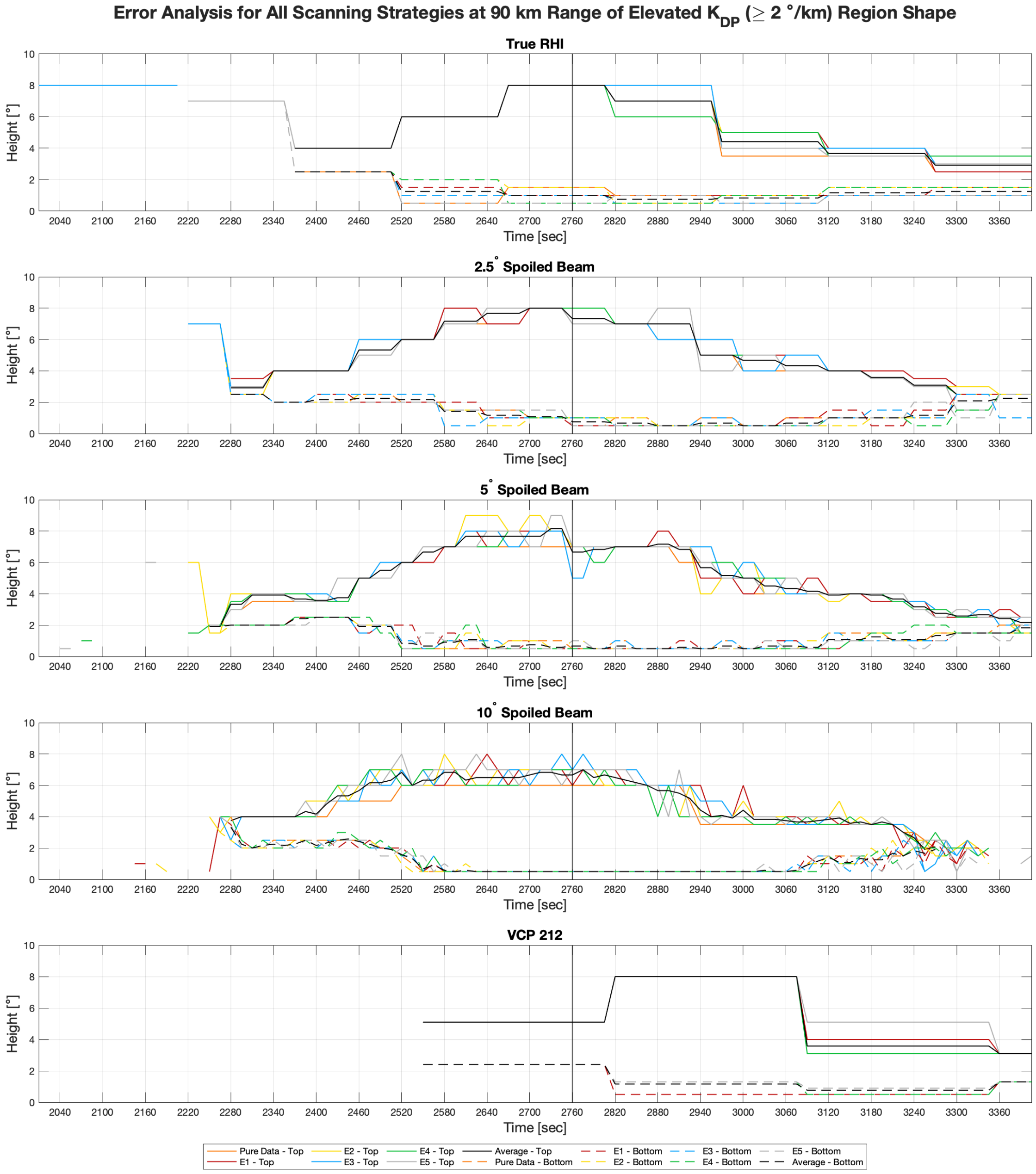

Figure 3.42: Same as Figure 3.37 but for the shape of the K_{DP} core at 90 km range.

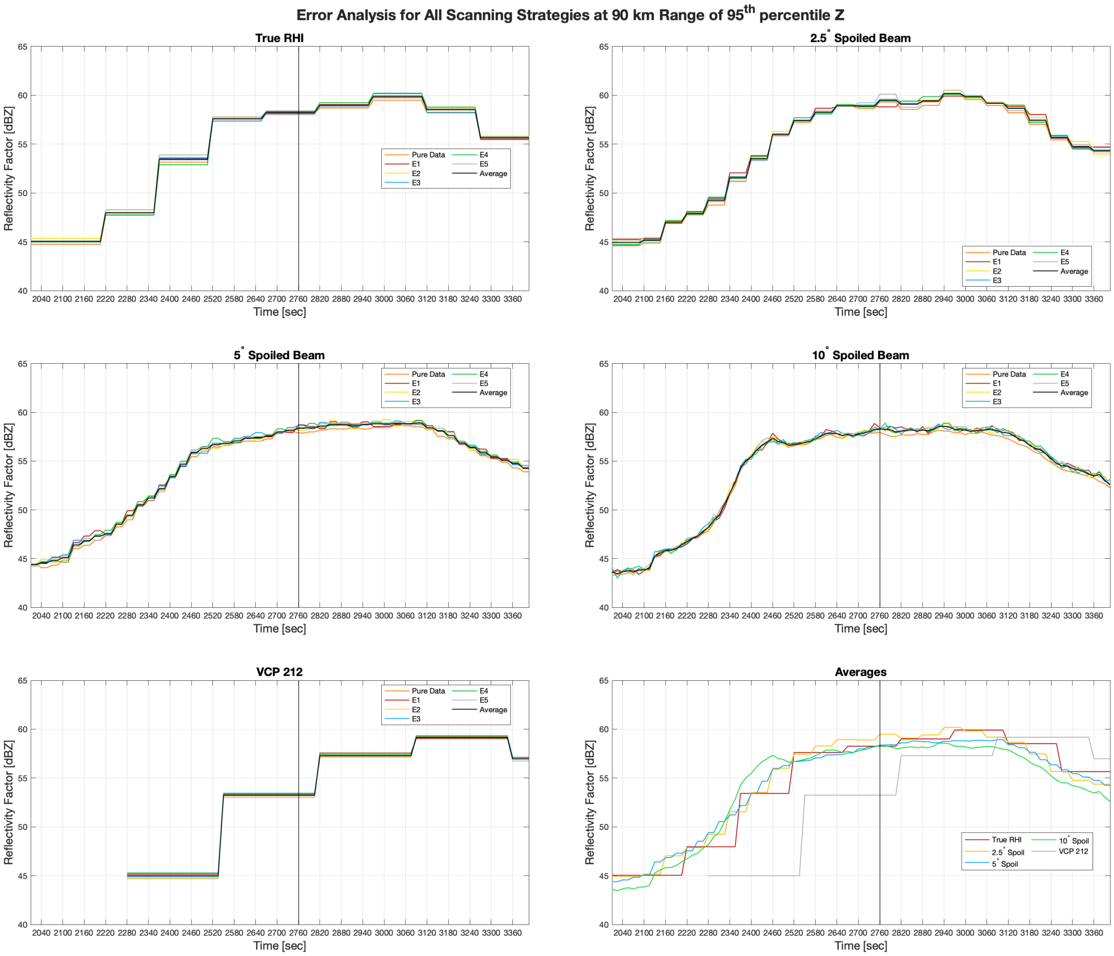

Figure 3.43: Same as Figure 3.37 but for 95th percentile Z_h at 90 km range.

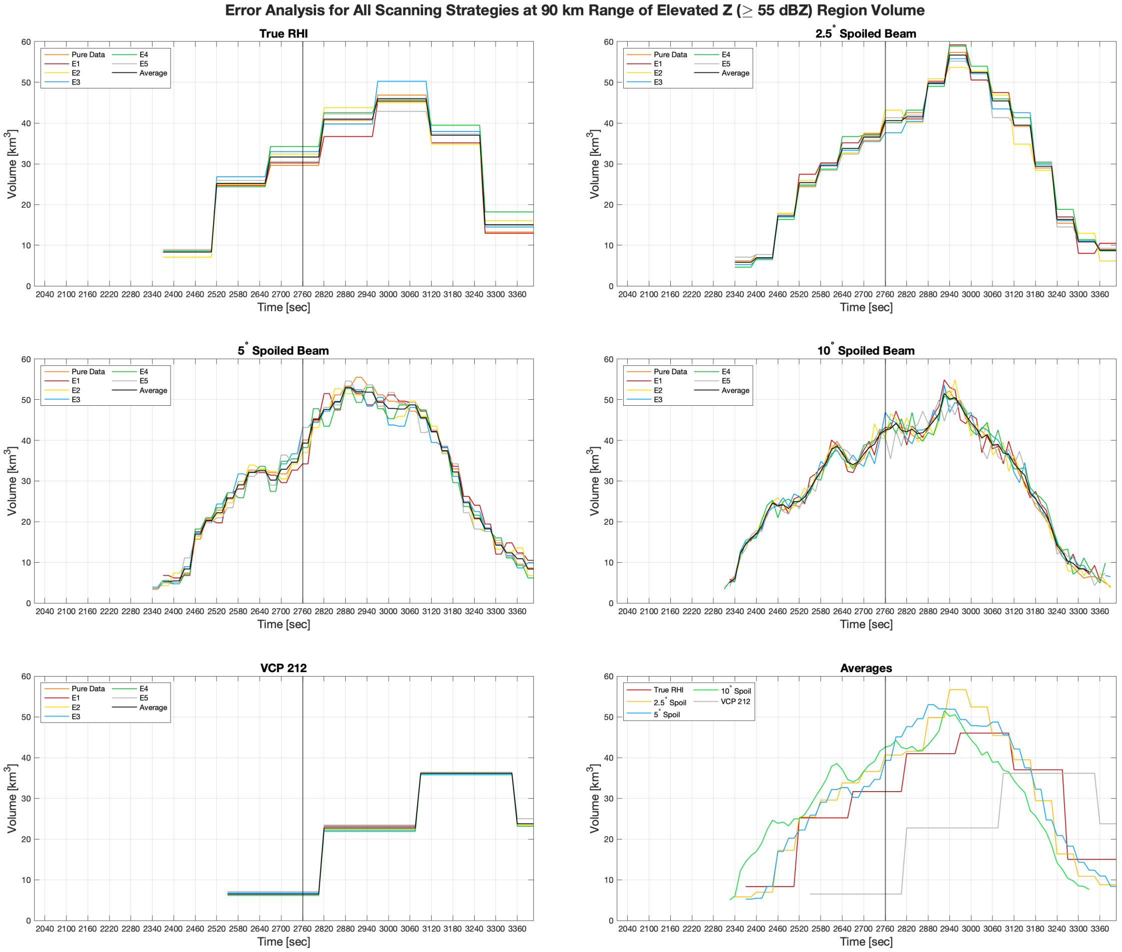

Figure 3.44: Same as Figure 3.37 but for the area of the Z_h column at 90 km range.

1 min, and does not impact the MAE as much. There are also some moderate deviations observed in the 2.5° imaging data, but these errors are never generally more than 1 – 2 km^3 at a time.

Chapter 4

Discussion: Recommendations for a Future Operational PAR

This discussion focuses on the analysis associated with a proof-of-concept test case that utilized the methodology and tools developed herein. This discussion looks to show the usability and potential value associated with this framework and tool set. With that said, any recommendations discussed below should not be applied broadly and can only be applied to this one specific proof-of-concept analysis at this time.

4.1 Direct Beam Pattern Comparisons

With the beam pattern comparisons, it is not surprising that the pencil beam was associated with the lowest ISLR and the 10° imaging case had the highest ISLR (Table 2.4). Furthermore, the pencil beam patterns had an ISLR that was less than 15 dB lower than even the smallest imaging beam pattern: 2.5° spoil factor. This implies that for direct comparisons of the beam patterns with similar temporal and spatial resolution, the scanning strategies that utilize a pencil beam would have less contamination from beam pattern sidelobes than those associated with any imaging case. This impact from sidelobe contamination would get worse as the spoiling factor increases; however, no jump is as large as seen between the pencil beam and the 2.5° imaging beam patterns.

The large increase in ISLR values indicates that the imaging cases will typically be expected to have more data degradation than the pencil beam cases and thus, should have higher biases associated with the data. The higher ISLRs can result in smearing of the data and impact observations along strong reflectivity gradients. These higher ISLRs can also impact velocity estimates in weak reflectivity regions or in regions with clutter contamination. Furthermore, maximum reflectivity values could be diminished with the increase in spoiling factor as a result of smearing out the signature over a broader area. Not to mention that increases in imaging spoil factor can also decrease the radars sensitivity to weak Z_h echos.

Although there is a large increase in ISLR levels for the imaging beam patterns, the increase in the ISLR levels greatly diminishes once spoiling has occurred. That is to say, the difference between the ISLR of 2.5° imaging and 5° imaging is only 4.68 dB where as the increase in ISLR between the pencil beam pattern and 2.5° imaging is 15.11 dB. Thus, once the decision has been made to utilize imaging, it might be most beneficial to go ahead and utilize as large a spoiled beam as possible - so long as the data is not severely degraded in other ways like smearing effects or sensitivity loss - such that the increase in temporal resolution can be exploited for the largest gain to the observer or forecaster.

4.2 Scanning Strategy Performance

For scanning strategy performance, there are two things that become extremely important. First, the update time of the data which impacts the observations of how the radar signatures evolve in time. This is extremely beneficial for forecasting if or when the signature could indicate impending severe weather and require issuance of a warning. Second, the representativeness of the model signatures. If the temporal resolution is extremely fast but the observed signatures are not accurate, then the increase in temporal resolution provides little benefit. Therefore, the performance of each scanning strategy will be discussed with these two qualifications in mind. Thus, the best performing scanning strategy should have both a fast enough temporal resolution to properly observe the evolution of the signatures, but also still represent the physical processes accurately.

4.2.1 Microburst at 30 km Cases

From a qualitative standpoint, the true RHI data best captured the structure and size of the signatures in the model environment; however, its temporal resolution was too coarse to properly resolve the evolution of the signatures (Figures 3.6 - 3.4). Of the imaging cases, the 2.5° imaging data provided the best representativeness of the model environment, and the 10° imaging data was least representative at the 30 km range, and was seen in all three radar variables analyzed. In the 10° imaging data, there were noticeably lower detections of maximum values along with different observed spatial structures and evolutions of the given precursor signatures.

From a quantitative stand point, the smaller imaging spoil factors of 2.5° and 5° performed the best in representing the microburst and microburst precursor signatures. The true RHI scans did generally perform well; however, they were significantly hindered by the 2.5-min temporal resolution, which limited observations of the evolution of the analyzed signatures. More specifically, the 2.5° imaging generally performed better with the microburst detection at the surface while the 5° imaging generally performed slightly better with the detection and observation of the precursor signatures.

Looking first at the microburst detection at the surface, the 2.5° imaging is the best representation of the surface ΔV calculation of any of the scanning strategies even though the temporal resolution is 60 s. Furthermore, the 2.5° imaging has similar, and sometimes better, observations than the true RHI and VCP 212 observations of the area of surface ΔV that is ≥ 10 m s^{-1}. The 5° imaging does make better surface ΔV estimates than the true RHI and VCP 212 scans because it better captures the temporal evolution. However, this improvement decreases in the area of surface ΔV. The worst scanning strategy for the surface divergence signature was the 10° imaging scans, as it failed to properly detect the increase in surface divergence and the increase in the area of surface divergence of the microburst likely due to sidelobe contamination effects. This is extremely concerning as a missed detection at the surface could prove extremely problematic for the aviation and operational weather community even if other precursor signatures are present. Thus, even if the 10° imaging case performs well in the observation of precursor signatures, the lack of detection at the surface is a huge negative in using a large degree of beam spoiling at low elevations, even if the temporal resolution is 15 s.

For the mid-level convergence signature, all scanning strategies had the same general trend except for the 10° imaging data. The 10° imaging data had a maximum mid-level convergence ΔV that was delayed in time and never reached the 20 m s^{-1} threshold that was observed by every other scanning strategy except for VCP 212. This delay in maximum mid-level convergence was on the order of 3 – 4 minutes and places the mid-level convergence signature only 1–2 minutes prior to the microburst reaching the surface. This is a significant reduction in potential lead time if certain mid-level convergence criteria were to be utilized in a warning situation.

For the other radar variables, the imaging data actually outperformed the true RHI imaging for all observations. The intensity of the Z_h column and K_{DP} core were closely aligned with what was seen in the model data, and the increased temporal resolution of the imaging cases greatly benefited their performance in this regard for the Z_h and K_{DP} precursor signatures. However, the 10° imaging still struggled significantly in capturing certain observations such as the 95^{th} percentile K_{DP} values along with the evolution of the shape of the Z_h column and K_{DP} core. Otherwise, the quantitative observations associated within Z_h and K_{DP} were not greatly hindered by using 10° imaging as was seen in the V_r data.

Only certain radar variables benefited from very high temporal resolution (e.g., subminute volumetric sampling). Namely, these observations were most beneficial when looking at how the top and bottom of the Z_h and K_{DP} core evolved in time; however, the fastest updates of 15 s only performed marginally better than the 30 s observations by the 5° imaging and 60 s observations by 2.5° imaging. In other variables that looked at the intensity of the signatures, the 15 s temporal resolution did not provide much in the way of benefits and provided similar results to the other imaging cases, or actually performed worse as seen in the 95^{th} percentile K_{DP} values (Figure 3.17). Overall, the benefit of increased temporal resolution decreases once the temporal resolution drops below 30 s, and in some cases, 60 s temporal resolution did provide similar or more accurate results (Figures 3.13, 3.15, 3.16, and 3.19).

Therefore, when looking at data degradation, temporal resolution, and qualitative representativeness, it would be most advantageous to utilize either 2.5° or 5° imaging to observe a potential microburst region depending on the situation at 30 km range. There were a lot of similarities between these two cases, and the evolution of all signatures both qualitatively and quantitatively were fairly similar for each. Thus, there was little difference in the observation and detection of the microburst and its precursor signatures between utilizing 60 s and 30 s temporal resolution data. With that in mind, it comes down to two main concerns in determining to use 2.5° or 5° imaging. If temporal resolution is the most important factor, then utilizing 5° imaging would be most advantageous as the observations would occur twice as frequently as the 2.5° imaging data. However, if data quality and accuracy of the observations is most important, the utilizing the 2.5° imaging scans would be most advantageous as data quality is better and the 60 s temporal resolution has shown effective in observing the evolution of the microburst and its precursor signatures.

The determination on what is more important - temporal resolution or data quality - should typically be left up to the individual forecaster as they would have the most up-to-date information regarding the operational needs at that specific time. However, it could be argued that, if other significant severe threats are on going - such as a potential tornado, significant hail, or significant winds - then completing the additional RHI scans as quickly as possible might be more advantageous. This would allow more of the extra resources to be allocated to the more important hazards. On the other hand, if there are not many other hazards, then having better data quality might be most advantageous as resolving the microburst and its precursor signatures would likely be the top priority at the time. Additionally, if the storm being observed has noticeably large Z_h gradients in the vertical, then having better data quality - corresponding to a smaller spoil factor - to better observe these large gradients could prove more beneficial.

4.2.2 Microburst at 90 km Case

Qualitatively speaking, the true RHI data is still the best representative of the model domain signatures when compared at the same time periods (as seen at 30 km range Section 4.2.1). However, it is still hindered by the temporal resolution of 2.5 min. During this time, there are changes in the precursor signatures that are not observed by the true RHI scans, and even if they are, they are delayed.

Looking at the qualitative comparisons of the imaging cases, there appears to be two separate instances for imaging performance. This distinction occurs in the Z_h and K_{DP} data at or before t = 2460 s and scans after t = 2460 s. At t = 2340s, t = 2400 s, and t = 2460 s, the 10° imaging data more accurately detects the strongest reflectivities ($\geq$ 60 dBZ) compared to the other imaging scans. The $\geq$ 60 dBZ region is located roughly at 5° elevation which makes it right on the edge of both the 2.5° and 5° imaging transmit beam patterns; however, this region is right in the middle of the 10° imaging transmit pattern. This could explain this specific observation as to why the smaller spoiled transmit scans have a harder time detecting this initial observation. The 2.5° and 5° imaging observations of the Z_h column recover quickly once the signature becomes more vertically oriented and not centralized at the location near 5° elevation. This observation also occurs in the K_{DP} observations at the same time periods such that the 10° imaging is most representative prior to t = 2460 s. However, after t = 2460 s in both Z_h and K_{DP}, the 10° imaging performs similarly to the 30 km case where smearing effects occur and the 10° imaging becomes the least representative of the model environment.

Because of the height of the 0.5° elevation angle, there is no surface divergence data to make comparisons of the observation at this range from the radar. Thus, it is unknown at this range how each scanning strategy would observe the surface divergence signature. However, the other available signatures paint an interesting story.

First, the evolution and magnitude of the mid-level convergence signature is best observed by the 2.5° imaging data. At 30 km range, all scanning strategies but 10° imaging and VCP 212 observed a mid-level convergence signature ≥ 20 m s^{-1}; however, this is not the case at 90 km. The model data has a maximum mid-level convergence ΔV on the order of 35 m s^{-1}; however, the only scanning strategy to come close was the 2.5° imaging data which passed the ≥ 20 m s^{-1} threshold and almost reached 25 m s^{-1} at its peak. None of the other scanning strategies came close to observing a maximum mid-level convergence value of ≥ 20 m s^{-1}. Although, in every scanning strategy, there was a noticeable increase in mid-level convergence prior to the microburst occurring at the surface, yet the general trend observed in the model data and at 30 km range was not observed except in the 2.5° imaging data.

Overall, as seen in the 30 km case in the quantified observations of Z_h and K_{DP}, the imaging scans generally outperformed the true RHI emulations in observing the evolution of the intensity, size, and shape of the precursor signatures. This performance by the imaging cases is mostly related to the temporal resolution differences as the evolution of these signatures are similar to those observed in the model data.

The temporal benefits observed result in similar conclusions to those in Section 4.2.1. Namely, the increase in temporal resolution with larger spoiled beamwidth typically leveled off after 30 s temporal resolution. Anything faster showed the same or worse observations than what was seen at 30 s temporal resolution - 5° imaging. The 10° imaging, which was the fastest scanning strategy, actually performed worse when observing the 95^{th} percentile of K_{DP} (lowest maximum magnitude), top and bottom of the Z_h column (smearing), and top of the K_{DP} core. Thus, when looking at imaging to increase temporal observations, the benefits from increased temporal resolution could outweigh potential observational losses up to about 30 s temporal resolution. Beyond that point, there is little difference in the observations of microbursts, and the impacts of imaging start greatly hindering the overall observations of the storm and precursor signatures.

An argument can be made that at 90 km range, these benefits level off after 60 s temporal resolution as the 2.5° imaging performed similarly to the 5° imaging in all Z_h and

K_{DP} calculated observations and even outperformed 5° imaging in the mid-level convergence signature observation. However, with the similarities between 2.5° and 5° imaging, utilizing the faster temporal resolution could provide additional insights into the evolution of the precursor signatures at 90 km range without greatly hindering the observations. Thus, determining whether data quality or temporal resolution is more important would drive whether to utilize either 2.5° or 5° imaging at 90 km range. As mentioned in Section 4.2.1, the determination on what is most important - temporal resolution or data quality - should typically be left up to the individual forecasters. However, as also mentioned in Section 4.2.1, there are likely situations such as multiple severe hazards or intense vertical Z_h gradients that might make one scanning technique more advantageous than other.

4.3 Error Analysis

4.3.1 Microburst at 30 km Cases

Throughout the different observations at 30 km range, the first guess is actually fairly accurate as most estimation errors are generally less than 1 of each calculated variable's given unit at 30 km range. However, it should be noted that this becomes more problematic for certain measurements. For example, when looking at total volume of the Z_h column, an error of ≤ 1 km^3 is not outrageous whereas an error of 1° is large when wanting to observe the elevation angle associated with the bottom of the Z_h column.

From a data quality perspective, the true RHI scans were rather disappointing. Although they best represented the model environment from a qualitative perspective, they were also associated with similar, or sometimes larger, estimation errors as the small spoiling factor imaging cases. Thus, given the rapidly evolving nature of microbursts and their precursor signatures, the temporal resolution of the true RHI, and having similar errors to small imaging spoil factors, the true RHI scanning strategy is not ideal for use in the detection and observations of microbursts. Therefore, within the proof-of-concept analysis in this project, utilizing imaging would be more advantageous to properly capture the evolution of the microburst precursor signatures.

As seen above in Section 3.1.1, qualitatively there were a lot of similarities between the 2.5° and 5° imaging such that the signatures were quantified and observed to evolve similarly utilizing these two scanning strategies. Thus, the spoil factor becomes a preference of the forecaster once imaging is utilized. If having lower estimation errors in the quantitative variables is most important to the forecaster, the the utilization of 2.5° imaging will typically be the best scanning strategy when utilizing imaging even though the temporal resolution is 60 s. However, if the forecaster wants, or needs, faster temporal updates, then utilizing 5° imaging will provide the most benefit as the increase in estimation errors is not too significant, and the qualitative observations of the storm still are not extremely impacted by the spoiling.

Regarding 10° imaging, it is the most concerning when considering the estimation errors. Namely, having low errors associated with incorrect observations does not make the observations any more accurate. It makes the observations precise, but that is not always beneficial when wanting to observe the evolution and intensity of rapidly evolving meteorological phenomena. Thus, even though some variables saw a more precise 10° imaging calculation, these observations are still not accurate and having a slightly higher error with more accurate measurements would be preferable. Therefore, it is recommended the largest spoil factor for 30 km range should be near 5° imaging.

4.3.2 Microburst at 90 km Case

Overall, the average first guess at 90 km range is generally less precise than those at 30 km; however, this is to be expected as signal and SNR are lower with increasing range which raise the errors associated with estimation. It was observed that the errors follow a similar trend as observed at 30 km. This implies that although the true RHI scans best represented the model environment from a qualitative perspective, it is not recommended for use in the observation and detection of microbursts and their precursor signatures given the current constraints of adaptive scanning used herein. This is because errors are similar to, or sometimes worse than, the small imaging spoil beamwidths, and the temporal resolution is much too coarse to properly resolve the evolution of the important signatures. Thus, utilizing imaging would be most advantageous as the temporal resolutions associated with imaging provide the best observations of the evolution of the microburst and its precursor signatures, and the associated errors are similar between the true RHI and small spoil factor imaging cases.

Even at 90 km range, there were qualitative similarities between the 2.5° and 5° imaging scanning strategies. Furthermore, the quantitative evolution of the storm is similar between both scanning strategies except in the mid-level convergence signature. At this range, needing to see all precursor signatures of a microburst becomes more important as surface detection is extremely difficult to near impossible without ground observations due to the 0.5° elevation angle beam height. Thus, the more accurate and precise observations by the 2.5° imaging would likely become more advantageous as it is able to detect all three precursor signatures the best, even with 60 s temporal resolution. If temporal resolution was such a main factor that less than 1 min temporal resolution was required, then 5° imaging would suffice. However, it would have to be remembered that the mid-level convergence observations could be hindered, and it would become more important to rely on the Z_h column and K_{DP} column observations as the difference in 2.5° and 5° imaging are smaller within these signatures.

The 10° imaging data has the same accuracy versus precision problem here as seen in the 30 km error analysis (Section 4.3.1). Namely, in some calculated variables, the 10° imaging was more precise than the 5° imaging and even 2.5° imaging data in some instances. However, the signatures observed qualitatively were not representative of the model environment. Thus, the 10° imaging data was more precise as some of the errors suggested, but the 10° imaging data was not as accurate and fails to capture the vertical evolution of the signatures. Therefore, as at 30 km range, although the temporal resolution improves to 15 s, the data degradation and lack of accuracy imply that the largest spoiling factor for the observation of microbursts and their precursor signatures should be 5° imaging which maximizes the benefit of temporal resolution while still limiting the effects of data degradation.

Chapter 5

Conclusions and Future Work

5.1 Summary and Conclusions

In this thesis, a framework for the quantification of a microburst and its precursor signatures is developed. This methodology framework is not only for qualitative comparisons between how various scanning strategies observe and detect microbursts and their precursor signatures, but it also allows for the quantification of various metrics related to the intensity, size, and shape of various microburst precursor signatures. Utilizing this framework, a proof-of-concept analysis was performed, and preliminary recommendations are made regarding the use of different scanning strategies to optimize not only fast temporal resolution but also to maintain data quality in a way that supports early detection of microbursts.

The framework developed herein starts with generating a microburst producing storm in a NWP simulation utilizing a real atmospheric sounding associated with an actual microburst. The output data from the sounding is then used to calculate dual-polarization variables using a combination of T-matrix and Rayleigh scattering approximation equations. These dual-polarization variables - along with other variables - are then sent through the radar emulator RSim. RSim takes these variables and emulates radar observations using different scanning strategies. The radar emulations, and the use of different scanning strategies, are accomplished by applying the range weighting function along with precalculated beam patterns for the given scanning strategy selected.

The scanning strategies analyzed herein operate under certain assumptions regarding a concept of operations for a potential PAR network. This concept of operations can best be summarized as the utilization of adaptive scanning on a single-faced, mechanically rotating S-band PAR. The RHI scans generated through RSim are believed to be part of adaptive scanning techniques made using any additional radar resources available. Thus, any implemented RHI scanning strategy would have to operate within, and share, this extra time with any other adaptive scanning techniques being utilized at that time. Therefore, any RHI scanning strategy that requires a large portion of the extra resources will ultimately have to have a coarser temporal resolution; however, if an RHI scanning strategy only requires a small portion of the extra resources, it can be performed more frequently.

Once all scanning strategies were emulated, both qualitative and quantitative analyses were performed. The qualitative analysis was done by comparing RHI images at the same azimuth angle for each scanning strategy on one set of data with added errors. For quantitative analysis, different measures of the intensity, size, and shape of mid-level convergence, DRC, and K_{DP} core were analyzed on the average metric from all 5 error data sets. After initial analysis, error analysis was performed to study the effects of inherent random estimation errors.

Because there was only one microburst simulation analyzed within this study, the results should be considered preliminary and cannot be generalized. However, this project serves as a proof-of-concept for future analysis and study of microbursts and their precursor signatures. The metrics utilized herein provide a way to quantify the microburst's precursor signatures, and they show promise in being able to alert forecasters of microburst potential.

The preliminary results associated with the one microburst test case can be summarized as follows. When considering both qualitative and quantitative analyses, it was generally found that the true RHI data was qualitatively the most representative of the model environment. However, its temporal resolution was much too coarse to properly resolve the evolution of the microburst and its precursor signatures. Furthermore, the errors associated with the true RHI scanning were too close to the imaging cases to justify the coarser temporal resolution. Thus, imaging provides an adequate way to utilize faster temporal resolution for observing microbursts and their precursor signatures. However, due to increases in data degradation associated with increasing spoiling factor for imaging, there was a limit to the benefits of the increased temporal resolution. It was found that the data degradation associated with 10° imaging significantly outweighed any benefits of its 15-s temporal resolution. Thus, a trade-off exists between the two best performing scanning strategies. Because of similarities in the qualitative, quantitative, and error analyses, either the 2.5° or 5° imaging are better options to scan microbursts and their precursor signatures. If faster temporal resolution is the most important aspect of the data to the forecaster, then the 5° imaging scanning strategy is the best to use; however, if better data quality is the most important aspect to the forecaster, then the 2.5° imaging scanning strategy is the best option.

5.2 Future Work

With the groundwork laid here, there is a lot of potential for future work. First, since there is only one wet microburst simulation utilized herein, it would be beneficial to increase the number of wet microburst simulations analyzed through RSim, with varying environmental conditions. This would be the first step in helping to provide generalized results associated with the observations made here, and it could help provide robust recommendations regarding which scanning strategies would be most beneficial in observing and detecting microbursts and their precursor signatures.

Second, generating a dry microburst simulation would provide a great step into future work. These results focus solely on one wet microburst and its precursor signatures, but research regarding the observations and detection of dry microbursts is few and far between. Thus, generating and analyzing a dry microburst simulation would be the first step in determining potential precursor signatures and detection strategies for dry microbursts which is an unexplored topic up to this point.

Third, further modifying RSim, or a similar radar emulator, to analyze other potential PAR scanning techniques, such as beam-multiplexing, would also be a great next step. This would broaden the scanning strategies to be analyzed, and it could provide new insights into how different techniques would observe microbursts and their precursor signatures.

Finally, because this research is the first to explicitly quantify the precursor signatures associated with microbursts, future work could utilize these quantified values in a microburst detection algorithm. Of course, generalization of these quantified signatures would need to be performed; however, the quantified results do show promise as a potential method to determine when adaptive scanning might become necessary if a storm is showing signs of potential microburst formation.

Bibliography

Adachi, T., K. Kusunoki, S. Yoshida, K.-I. Arai, and T. Ushio, 2016: High-Speed Volumetric Observation of a Wet Microburst Using X-Band Phased Array Weather Radar in Japan. *Monthly Weather Review*, **144 (10)**, 3749–3765.

Amiot, C. G., L. D. Carey, W. P. Roeder, T. M. McNamara, and R. J. Blakeslee, 2019: C-band Dual-Polarization Radar Signatures of Wet Downbursts around Cape Canaveral, Florida. *Weather and Forecasting*, **34**, 103–131.

Atkins, N. T., and R. M. Wakimoto, 1991: Wet Microburst Activity over the Southeastern United States: Implications for Forecasting. *Weather and Forecasting*, **6**, 470–482.

Atlas, D., C. W. Ulbrich, and C. R. Williams, 2004: Physical Origin of a Wet Microburst: Observations and Theory. *Journal of the Atmospheric Sciences*, **61 (10)**, 1186–1196.

Bleistein, A. J., 2010: An Historical Look at NEXRAD. Radar Operations Center, URL https://www.roc.noaa.gov/WSR88D/PublicDocs/NNOW/NNDec2010/31-35.pdf.

Bluestein, H. B., M. M. French, I. PopStefanija, R. T. Bluth, and J. B. Knorr, 2010: A Mobile, Phased-Array Doppler Radar for the Study of Severe Convective Storms. *Bulletin of the American Meteorological Society*, **91**, 579–600.

Bowden, K. A., 2014: The Phased Array Radar Innovative Sensing Experiment 2013. M.S. thesis, School of Meteorology, The University of Oklahoma.

Bowden, K. A., and P. L. Heinselman, 2016: A Qualitative Analysis of NWS Forecasters' Use of Phased-Array Radar Data during Severe Hail and Wind Events. *Weather and Forecasting*, **31**, 43–55.

Bowden, K. A., P. L. Heinselman, D. M. Kingfield, and R. P. Thomas, 2015: Impacts of Phased-Array Radar Data on Forecaster Performance during Severe Hail and Wind Events. *Weather and Forecasting*, **30**, 389–404.

Brown, J. M., K. R. Knupp, and F. Caracena, 1982: Destrucive Winds form Shallow, High-based Cumulonimbi. American Meteorological Society, 272-275 pp., Preprint, 12th Conference Severe Local Storms.

Bryan, G. H., 2020: CM1 Homepage. National Center for Atmospheric Research and National Science Foundation, URL https://www2.mmm.ucar.edu/people/bryan/cm1/.

Bryan, G. H., and J. M. Fritsch, 2002: A Benchmark Simulation for Moist Nonhydrostatic Numerical Models. *Monthly Weather Review*, **130**, 2917–2928.

Butler, J. M., 1998: Tracking and Control in Multi-Function Radar. Ph.D. thesis, University College London.

Byers, H. R., and R. R. Braham, 1949: *The Thunderstrom: Report of the Thunderstorm Project*. U.S. Government Printing Office.

Caracena, F., J. McCarthy, and J. Flueck, 1983: Forecasting the Likelihood of Microbursts along the Front Range of Colorado. American Meteorological Society, 624-629 pp., Preprint, 13th Conference on Severe Local Storms.

Chatzitheodoridi, M., A. Taylor, and O. Rabaste, 2020: A Mismatched Filter for Integrated Sidelobe Level Minimization over a Continuous Doppler Shift Interval. IEEE, 2020 IEEE Radar Conference.

Cheong, B. L., D. J. Bodine, C. J. Fulton, S. M. Torres, T. Maruyama, and R. D. Palmer, 2017: SimRadar: A Polarimetric Radar Time-Series Simulator for Tornadic Debris Studies. *IEEE Transactions on Geoscience and Remote Sensing*, **55**, 2858–2870.

Crum, T., and R. Alberty, 1993: The WSR-88D and the WSR-88D Operational Support Facility. *Bulletin of the American Meteorological Society*, **74**, 1669–1687.

Doviak, R. J., and D. S. Zrnic, 1993: *Doppler Radar and Weather Observations*. Dover Publications, Inc.

Dranidis, D. V., 2003: Backboards of the Fleet: Shipboard Phased-Array Radars; a Survey of Requirements, Technologies, and Operational Systems. *Journal of Electronic Defense*.

Dynamic Sealing Technologies, Inc., 2020: Fastest, Most Advanced Weather Radar Aims to Improve Warning Times. Dynamic Sealing Technologies, Inc., URL https://www.dsti.com/company/news/2020/article/fastest-most-advanced-weather-radar-aims-to-improve-warning-times/.

Ellrod, G., 1989: Environmental Conditions Associated with the Dallas Microburst Storm Determined from Satellite Soundings. *Weather and Forecasting*, **4**, 469–484.

FAA, 2017: Spectrum Efficient National Surveilance Radar Program (SENSR) - Formal Request for Information (RFI). Tech. rep., Federal Aviation Administration. URL {https://faaco.faa.gov/index.cfm/attachment/download/73825}.

Forsyth, D. E., and Coauthors, 2005: The National Weather Radar Testbed (phased array). American Meteorological Society, Albuquerque, NM, Preprints, *32nd Conference on Radar Meteorology*.

French, M. M., H. B. Bluestein, I. PopStefanija, C. A. Baldi, and R. T. Bluth, 2013: Reexamining the Vertical Development of Tornadic Debris Signatures in Supercells. *Monthly Weather Review*, **41**, 4576–4601.

Fujita, T. T., 1976: Spearhead Echo and Downburst Near the Approach End of a John F. Kennedy Airport Runway, New York City. Tech. Rep. 1st ed., University of Chicago.

Fujita, T. T., 1981: Tornadoes and Downbursts in the Context of Generalized Planetary Scales. *Journal of the Atmospheric Sciences*, **38**, 1511–1534.

Fujita, T. T., 1983: Andrews AFB Microburst. Department of Geophysical Science, University of Chicago, 38 pp.

Fujita, T. T., 1985: The Downburst: Microburst and Macroburst. SMRP Research Paper 210, The University of Chicago.

Fujita, T. T., and H. R. Byers, 1977: Spearhead Echo and Downbursts in the Crash of an Airliner. *Monthly Weather Review*, 1164–1181.

Fujita, T. T., and F. Caracena, 1977: An analysis of three weather-related aircraft accidents. *Bulletin of the American Meteorological Soceity*, 1164–1181.

Fujita, T. T., and R. Wakimoto, 1981: Five Scales of Airflow Associated with a Series of Downbursts on 16 July 1980. *Monthly Weather Review*, 1438–1456.

Fujita, T. T., and R. M. Wakimoto, 1983a: Microbursts in JAWS Depectied by Doppler radars, PAM, and aerial photographs. American Meteorological Society, 638-645 pp., Preprint, *21st Conference on Radar Meteorology*.

Fujita, T. T., and R. M. Wakimoto, 1983b: JAWS Microbursts Revealed by Triple-Doppler Radar, Aircraft, and PAM Data. American Meteorological Society, 97-100 pp., Preprints, *13th Conference Severe Local Storms*.

Fulton, C., and W. Chappell, 2010: Calibration of Panelized Polarimetric Phased Array Radar Antennas: A Case Study. *2010 IEEE International Symposium on Phased Array Systems and Technology*, IEEE.

Fulton, C., J. Salazar, D. Zrnic, D. Mirkovic, I. Ivic, and D. Doviak, 2018: Polarimetric Phased Array Calibration for Large-Scale Multi-Mission Radar Applications. *2018 IEEE Radar Conference*, IEEE.

Fulton, C., M. Yeary, D. Thompson, J. Lake, and A. Mitchell, 2016: Digital Phased Arrays: Challenges and Opportunities. *Proceedings of the IEEE*, **104**, 487–503.

Griffen, C. B., D. J. Bodine, J. M. Kurdzo, A. Mahre, and R. D. Palmer, 2019: High Temporal Resolution Observations of the 27 My 2015 Canadian, Texas, Tornado using the Atmospheric Imaging Radar. *Monthly Weather Review*, **147**, 873–891.

Heinselman, P., K. Bowden, D. Kingfield, and C. Kuster, 2015a: 2015 Phased Array Radar Innovative Sensing Experiment. American Meteorological Society, URL https://ams.confex.com/ams/96Annual/webprogram/Manuscript/Paper283240/Heinselman_etal_AMS_ExtendedAbstract_final.pdf, Extended Abstract, 32nd Conference on Environmental Information Processing Technologies.

Heinselman, P., D. Ladue, and H. Lazrus, 2012: Exploring Impacts of Rapid-Scan Radar Data on NWS Warning Decisions. *Weather and Forecasting*, **27**, 1031–1044.

Heinselman, P. L., D. S. LaDue, D. M. Kingfield, and R. Hoffman, 2015b: Tornado Warning Decisions Using Phased-Array Radar Data. *Weather and Forecasting*, **30**, 57–78.

Heinselman, P. L., D. L. Priegnitz, K. L. Manross, T. M. Smith, and R. W. Adams, 2008: Rapid Sampling of Severe Storms by the National Weather Radar Testbed Phased Array Radar. *Weather and Forecasting*, **23**, 808–824.

Heinselman, P. L., and S. M. Torres, 2011: High-Temporal-Resolution Capabilities of the National Weather Radar Testbed Phased-Array Radar. *Journal of Applied Meteorology and Climatology*, **50**, 579–593.

Hjelmfelt, M., 1987: The Microbursts of 22 June 1982 in JAWS. *Journal of the Atmospheric Sciences*, **44**, 1646–1665.

Hondl, K. D., and M. J. Emanuel, 2019: The Advanced Technology Demonstrator: An S-Band, Dual Polarization, Phased Array Radar at the National Weather Radar Testbed. *35th Conference on Environmental Information Processing Technologies*, American Meteorological Society.

Isaminger, M. A., 1988: A Preliminary Study of Precursors to Huntsville Microbursts. Tech. rep., Lincoln Laboratory. URL https://www.ll.mit.edu/r-d/publications/preliminary-study-precursors-huntsville-microbursts.

Isom, B., and Coauthors, 2013: The Atmopheric Imaging Radar: Simultaneous Volumetric Observations Using a Phased Array Weather Radar. *Journal of Atmospheric and Oceanic Technology*, **30**, 655–675.

Ivic, I., C. Curtis, E. Forren, R. Mendoza, D. Schvartzman, S. Torres, D. J. Wasielewski, and F. A. Zahrai, 2018: An Overview of Weather Calibration for the Advanced Technology Demonstrator. *2018 IEEE Radar Conference*, IEEE.

Johns, R., and C. Doswell, 1992: Severe Local Storms Forecasting. *Weather and Forecasting*, 588–612.

Jung, Y., G. Zhang, and M. Xue, 2008: Assimilation of Simulated Polarimetric Radar Data for a Convective Storm Using the Ensemble Kalman Filter. Part I: Observation Operators for Reflectivity and Polarimetric Variables. *Monthly Weather Review*, **136**, 2228–2245.

Jung, Y., G. Zhang, and M. Xue, 2010: Simulations of Polarimetric Radar Signatures of a Supercell Storm using a Two-Moment Bulk Microphysics Scheme. *Journal of Applied Meteorology and Climatology*, **49**, 146–163.

Kingsmill, D., and R. Wakimoto, 1991: Kinematic, Dynamic, and Thermodynamic Analysis of a Weakly Sheared Severe Thunderstorm over Northern Alabama. *Monthly Weather Review*, **119**, 262–297.

Kirker, S., 2018: OU Research Team Developing Advanced Radar Designed to Improve Weather Predictions. *OU Daily*, URL https://www.oudaily.com/news/ou-research-team-developing-advanced-radar-designed-to-improve-weather-predictions/article_f538847e-cbfa-11e8-8704-8712cbaac60e.html.

Kurdzo, J. M., B. L. Cheong, R. D. Palmer, G. Zhang, and J. B. Meier, 2014: A Pulse Compression Waveform for Improved-Sensitivity Weather Radar Observations. *Journal of Atmospheric and Oceanic Technology*, **31**, 2713–2731.

Kurdzo, J. M., and Coauthors, 2017: Observations of Severe Local Storms and Tornadoes with the Atmospheric Imaging Radar. *Bulletin of the American Meteorological Society*, **98**, 915–935.

Kuster, C., P. Heinselman, and M. Austin, 2015: 31 May 2013 El Reno Tornadoes: Advantages of Rapid-Scan Phased-Array Radar Data from a Warning Forecaster's Perspective. *Weather and Forecasting*, **30**, 933–956.

Kuster, C. M., B. R. Bowers, J. T. Carlin, T. J. Schuur, J. W. Brogden, R. Toomey, and A. Dean, 2021: Using K_{DP} Cores as a Downburst Precursor Signature. *Weather and Forecasting*.

Kuster, C. M., P. L. Heinselman, and T. J. Schuur, 2016: Rapid-Update Radar Observations of Downbursts Occurring within an Intense Multicell Thunderstorm on 14 June 2011. *Weather and Forecasting*, **31 (3)**, 827–851.

Mackey, J. B., 1998: Forecasting Wet Microbursts Associated with Summertime Airmass Thunderstorms over the Southeastern United States. M.S. thesis, Graduate School of Engineering, Air Force Institute of Technology.

Mahre, A., T. Yu, and D. J. Bodine, 2020: A Comparison of Scan Speedup Strategies and Their Effect on Rapid-scan Weather Radar Data Quality. *Journal of Atmospheric and Oceanic Technology*, **37**, 1955–1972.

Mahre, W. A., 2020: Quantitative Analysis of Rapid-Scan Phased Array Weather Radar Benefits and Data Quality Under Various Scan Conditions. Ph.D. thesis, University of Oklahoma.

Mailloux, R. J., 2005: *Phased Array Antenna Handbook*. Artech House, Inc., Norwood, MA.

Melnikov, V. M., 2004: Simultaneous Transmission Mode for the Polarimetric WSR-88D: *Statistical Biases and Standard Deviations of Polarimetric Variables*. Tech. rep., National Severe Storms Laboratory, Norman, OK.

Melnikov, V. M., R. J. Doviak, and D. S. Zrnic, 2015: A Method to Increase the Scanning Rate of Phased-Array Weather Radar. *IEEE Transactions on Geoscience and Remote Sensing*, **53**, 5634–5643.

Miller, R., 1972: Notes on analysis and severe-storm forecasting procedures of the Air Force Global Weather Central. Tech. rep., Air Weather Service, USAF, Offutt AFB, Nebraska, 199 pp.

Mishchenko, M. I., 2000: Calculation of the amplitude matrix for a nonspherical particle in a fixed orientation. *Appl. Opt.*, **39**, 1026–1031, doi:10.1364/AO.39.001026.

Morin, A., J. George, and V. Chandrasekar, 2019: Polarimetric Calibration of a Dual-Polarization Phased Array Weather Radar. *2019 IEEE International Symposium on Phased Array System & Technology (PAST)*, IEEE.

Nastrom, G. D., and F. D. Eaton, 1997: Turbulence Eddy Dissipation Rates from Radar Observations at 5-20km at White Sands Missile Range, New Mexico. *Journal of Geophysical Research*, **102**, 19 495–19 505.

Newman, J. F., and P. L. Heinselman, 2012: Evolution of a Quasi-Linear Convective System Sampled by Phased Array Radar. *Monthly Weather Review*, **140**, 3467–3486.

NSSL, 2022a: Research Tools: Advanced Technology Demonstrator. NOAA National Severe Storms Laboratory, URL https://www.nssl.noaa.gov/tools/radar/atd/.

NSSL, 2022b: Research Tools: Phased Array Radar. NOAA National Severe Storms Laboratory, URL https://www.nssl.noaa.gov/tools/radar/mpar/.

NWS Nashville, 2018: Twitter, URL https://twitter.com/NWSNashville/status/1008214282406891522.

Orfanidis, S. J., 2016: *Electromagnetic Waves and Antennas*. Sophocles J. Orfanidis, 1413 pp.

Palmer, R. D., C. J. Fulton, J. Salazar, H. Sigmarsson, and M. Yeary, 2019: The "Horus" Radar - An All-Digital Polarimetric Phased Array Radar for Multi-Mission Surveillance. *35th Conference on Environmental Information Processing Technologies*, American Meteorological Society, Phoenix, AZ.

Palmer, R. D., and Coauthors, 2022: Transportable Phased Array Radar: Meeting Weather Community Needs. *38th Conference on Environmental Information Processing Technologies*, American Meteorological Society, Houston, TX.

Pazmany, A. L., J. B. Mead, H. B. Bluestein, J. C. Snyder, and J. B. Houser, 2013: A Mobile Rapid-Scanning X-band Polarimetric (RaXPol) Doppler Radar System. *Journal of Atmospheric and Oceanic Technology*, **30**, 1398–1413.

Radar Operations Center, 2021a: NEXRAD Coverage Below 10,000 Feet AGL. Radar Operations Center, URL https://www.roc.noaa.gov/wsr88d/Images/USACoverageBoB10kFt.png.

Radar Operations Center, 2021b: WSR-88D Service Life Extension Program (SLEP). Radar Operations Center, URL https://www.roc.noaa.gov/WSR88D/SLEP/SLEP.aspx.

Roberts, R. D., and J. W. Wilson, 1989: A Proposed Microburst Nowcasting Procedure Using Single-Doppler Radar. *Journal of Applied Meteorology*, **28**, 285–303.

Rodi, A. R., K. L. Elmore, and W. P. Mahoney, 1983: Aircraft and Doppler Air Motion Comparisons in a JAWS Microburst. American Meteorological Society, 624-629 pp., Preprint, *21st Conference on Radar Meteorology*.

Sachidananda, M., and D. Zrnic, 1986: Differential Propagation Phase Shift and Rainfall Rate Estimation. *Radio Science*, **21**, 235–247.

Salazar, J. L., and Coauthors, 2019: An Ultra-Fast Scan C-band Polarimetric Atmospheric Imaging Radar (PAIR). *2019 IEEE International Symposium on Phased Array System Technology (PSAT)*, 1–5, doi:10.1109/PAST43306.2019.9021042.

Samenow, J., 2013: Ronald Reagan's near Brush with Weather-Induced Death: the August 1, 1983 Microburst. *Washington Post*.

Schuss, J., T. Sikina, J. Hilliard, P. Makridakis, J. Upton, J. Yeh, and S. Sparagna, 2016: Large Scale Phased Array Calibration. *2016 IEEE International Symposium on Phased Array Systems and Technology (PSAT)*, IEEE.

Schvartzman, D., 2020: Signal Processing Techniques and Concept of Operations for Polarimetric Rotating Phased Array Radar. Ph.D. thesis, University of Oklahoma.

Schvartzman, D., J. D. D. Diaz, J. L. Salazar-Cerreno, T. Yu, R. D. Palmer, and M. S. McCord, 2022a: A Hybrid Antenna Pattern Synthesis Method for the Polarimetric Atmospheric Imaging Radar (PAIR). *2022 IEEE Radar Conference*.

Schvartzman, D., R. Palmer, T. Yu, R. Reinke, and F. Nai, 2022b: A Pattern Synthesis Method for Polarimetric Weather Observations with the All-Digital Horus Phased Array Radar. *38th Conference on Environmental Information Processing Technologies*, American Meteorological Society.

Skolnik, M., 1981: *Introduction to Radar Systems*. McGraw-Hill, Auckland, New Zealand.

Smalley, D. J., M. F. Donovan, B. J. Bennett, K. T. Hood, E. Griffin, M. S. Veillette, and E. R. Williams, 2015: NEXRAD Dual Polarization Data for FAA Aviation Products. *37th International Radar Conference*, American Meteorological Society.

Smith, J., 2018: OU's Radar Team Developing Fastest, Most Advanced Radar in the Nation. University of Oklahoma, URL https://www.ou.edu/web/news_events/articles/news_2018/ou-radar-team-developing-fastest-most-advanced-radar-in-the-nation.

Smith, M., 2014: Defeating the Downburst: 20 years since the last U.S. Commercial Jet Accident from Wind Shear. *Washington Post*.

Srivastava, R., 1987: A Model of Intense Downdrafts Driven by Melting and Evaporation of Precipitation. *Journal of the Atmospheric Sciences*, **44**, 1752–1773.

Sun, J., and Coauthors, 2014: Use of NWP for Nowcasting Convective Precipitation: Recent Progress and Challenges. *Bulletin of the American Meteorological Society*, **95**, 409–426.

Supinie, T. A., N. Yussouf, Y. Jung, M. Xue, J. Cheng, and S. Wang, 2017: Comparison of the Analyses and Forecasts of a Tornadic Supercell Storm from Assimilating Phased-Array Radar and WSR-88D Observations. *Weather and Forecasting*, **32**, 1379–1401.

Torres, S., and Coauthors, 2014: A Demonstration of Adaptive Weather-Surveillance Capabilities on the National Weather Radar Testbed Phased-Array Radar. *2014 International Radar Conference*, IEEE.

Torres, S. M., and D. Schvartzman, 2020: A simulation framework to support the design and evaluation of adaptive scanning for phased-array weather radars. *Journal of Atmospheric and Oceanic Technology*, **37**.

Torres, S. M., and D. Wasielewski, 2022: The Advanced Technology Demonstrator at the National Severe Storms Laboratory: Challenges and Successes. *2022 IEEE Radar Conference*, IEEE.

University of Wyoming, 2021: University of Wyoming, College of Engineering, Department of Atmospheric Sciences, URL http://weather.uwyo.edu/upperair/sounding.html.

van der Voort, T., 2021: Memories of the attempted Reagan assassination. University of Virginia Miller Center, URL https://millercenter.org/issues-policy/the-first-year/the-attempted-reagan-assassination.

Vasiloff, S., and K. Howard, 2009: Investigation of a Severe Downburst Storm near Phoenix, Arizona, as seen by a mobile Doppler Radar and the KIWA WSR-88D. *Weather and Forecasting*, **24**, 856–867.

Visser, H. J., 2005: *Array and Phased Array Antenna Basics*. John Wiley & Sons, Ltd., West Sussex, England.

Wakimoto, R., and V. Bringi, 1988: Dual-Polarization Observations of Microbursts Associated with Intense Convection: The 20 July Storm during the MIST Project. *Monthly Weather Review*, **116**, 1521–1539.

Wakimoto, R. A., 1985: Forecasting Dry Microburst Activity over the High Plains. *Monthly Weather Review*.

Wakimoto, R. A., 2001: *Severe Convective Storms*, chap. Convectively Driven High Wind Events, 255–298. No. 50, Meteorological Monographs, American Meteorological Society.

Walter, J., 2007: A New Climatology of 25-Year, 50-Year, and 100-Year Microburst Winds. *22nd Conference on Weather Analysis and Forecasting/18th Conference on Numerical Weather Prediction*, American Meteorological Society.

Wang, S., 2013: Waveform and Transceiver Optimization for Multi-Functional Airborne Radar Through Adaptive Processing. Ph.D. thesis, University of Oklahoma.

Wang, Y., and V. Chandrasekar, 2010: Quantitative Precipitation Estimation in the CASA X-band Dual-Polarization Radar Network. *Journal of Atmospheric and Oceanic Technology*, **27**, 1665–1676.

Weber, M., K. Hondl, N. Yussouf, and et al., 2021: Towards the Next Generation Operational Meteorological Radar. *Bulletin of the American Meteorological Society*, **102**, E1357–E1382.

Weber, M., V. Melnikov, D. Zrnic, K. Hondl, R. R. Zellner, and B. Hudson, 2020: Experimental Validation of the Multibeam Technique for Rapid-Scan, Meteorological Phased-Array Radar. American Meteorological Society, *36th Conference on Environmental Information Processing Techniques*.

Weber, M. E., J. Pica, C. D. Curtis, I. R. Ivic, D. Conway, and J. Y. N. Cho, 2019: Panel Discussion: The Next-Generation Operational Weather Radar Network. American Meteorological Society, Phased Array Radar Symposium.

Wilson, J. W., R. D. Roberts, C. Kessinger, and J. McCarthy, 1984: Microburst Wind Structure and Evaluation of Doppler Radar for Airport Wind Shear Detection. *Journal of Applied Meteorology and Climatology*, **23 (6)**, 898–915.

Wilson, K. A., P. L. Heinselman, C. M. Kuster, D. M. Kingfield, and Z. Kang, 2017: Forecaster Performance and Workload: Does Radar Update Time Matter? *Weather and Forecasting*, **32**, 253–274.

Wolfson, M., 1983: Doppler Radar Observations of an Oklahoma Downburst. American Meteorological Society, 590-595 pp., Preprint, 21st Conference on Radar Meteorology.

Wolfson, M. M., and C. A. Meuse, 1993: Quantifying Airport Terminal Area Weather Surveillance Requirements. American Meteorological Society, 5-7 pp., Preprints, *26th International Conference on Radar Meteorology*.

Wurman, J., and M. Randall, 2001: An Inexpensive, Mobile, Rapid-scan Radar. 30th International Conference on Radar Meteorology, Americam Meteorological Society, Munich, Germany, URL https://ams.confex.com/ams/30radar/techprogram/paper_21577.htm.

Yu, T., M. B. Orescanin, C. D. Curtis, D. S. Zrnic, and D. E. Forsyth, 2007: Beam Multiplexing Using the Phased-Array Weather Radar. *Journal of Atmospheric and Oceanic Technology*, **24**, 616–626.

Zhang, G., R. Doviak, D. Zrnic, and J. Crain, 2008: Phased Array Radar Polarimetry for Weather Sensing: Challenges and Opportunities. *2008 IEEE International Geoscience and Remote Sensing Symposium*, IEEE.

Zrnic, D. S., V. M. Melnikov, R. J. Doviak, and R. Palmer, 2015: Scanning STrategy for the Multifunction Phased-Array Radar to Satisfy Aviation and Meteorological Needs. *IEEE Geoscience and Remote Sensing Letters*, **12**, 1204–1208.

Zrnic, D. S., and Coauthors, 2007: Agile-Beam Phased Array Radar for Weather Observations. *Bulletin of the American Meteorological Society*, **88**.

Appendix A

Comparisons of RSim Emulations with Model Domain Data

This appendix contains a more detailed analysis and comparison between the RSim emulations and the model domain data used to generate those emulations mentioned in Section 2.2.4. Below are two sections that focus on differences in observations at the two different ranges used within this study (30 km and 90 km). Each range comparison has a different VCP scanning strategy that was used for the true RHI and atmospheric imaging cases due to different scanning needs at different heights relative to model domain data limits. Namely, VCP Alpha is used for the 30 km comparisons which goes up to 20° in elevation ($\approx$ 10.3 km AGL), and VCP Beta is used for the 90 km comparisons which goes up to 15° as the model domain only reaches up to 20 km in height.

A.1 30km Comparisons

The first set of comparisons between the model domain and the RSim emulated data will be looking at the 30 km case. The emulated data for these comparisons was generated with a 60 s temporal resolution and the model domain will be compared at those 60 s intervals. Other information regarding the process of the emulations can be found in Chapter 2.

For the comparisons, a 10-minute interval of 60 second resolution data is analyzed. This range covers observations of the microburst reaching the surface and the evolution of some of the precursor signatures to showcase that the emulations are accurate representations of the model domain environment. These comparisons will all occur along azimuth angle 174 in RHI format to provide a baseline for comparing the three different variables: Z_h, V_r, and K_{DP}.

First looking at reflectivity factor, in Figure A.1, the $t = 2340$ s panels show the beginnings of an elevated reflectivity region around 4–6 km AGL that is observed by the emulator in the same location and general size as the model data. However, the emulator does have a smaller intensity (indicated by the absence of a purple pixel in the middle of the elevated reflectivity region). It is speculated to be due to the spatial sampling differences because the model domain is on a 0.5° resolution while the emulations at 30 km have 1° sampling above 2° in elevation. There is also a weak reflectivity region (circled in black) that is detected by the emulator, but this is not the magnitude seen in the model data; however, this region is associated with sharp reflectivity gradients with values ranging from $\approx$ 10 dBZ to $\approx$ 50 dBZ along radial across a 1 km in distance on either side of the weak reflectivity region. Furthermore, in range between 25 and 28 km, there is a region of very weak reflectivities (< -5 dBZ) that is not detected by the emulations (black arrow). This region is likely censured due to having too low SNR values.

The $t = 2400$ s panels are very similar throughout much of the domain, but the same comments made about the $t = 2340$ s panels can be made here. A small lower reflectivity region (circled in black) is not resolved well within the emulations. Furthermore, the weak Z_h values between 25 and 28 km are not detected by the emulations. This lack of weak reflectivity detection continues for most of the panels until the $t = 2580$ s panels when finally most of the weak reflectivites along the left edge of the storm are resolved.

When looking at the different panel sets between the emulations and model data from times $t = 2640$ s and $t = 2880$ s, there are not any major differences that appear within the data. The emulations (left column) appear coarser, from a spatial sampling perspective, compared to the model data, but that is because they are in fact coarser with a 1.0° sampling spacing as opposed to the 0.5° sampling spacing of the model data.

Now, considering K_{DP}, Figure A.2 is the same set up as Figure A.1 but shows K_{DP} instead of Z_h. Generally speaking, the vast majority of panels are very similar to one another. The main difference observed here is the upward formation of a small appendage of elevated K_{DP} values ($\geq 2^\circ$ km^{-1}) in the model data. The main difference is observed in the $t = 2460$ s panels where the appendage is rather thin, and the emulations are only able to pick up the very top and very bottom of the appendage. However, this lack of detection is mostly fixed by $t = 2520$ s, when the only difference occurs in a small gap in the appendage in the emulations, which is not seen in the model data (black arrows at $t = 2520$ s and $t = 2640$ s). This can be attributed to the spatial sampling grid used in the emulations.

When moving forward in time, the similarities between the K_{DP} images is still seen with only minor differences observed, which can be attributed to the sampling spacing of the emulation data (Figure A.2). There are no major noticeable differences between the K_{DP} images in the model and emulation data with the general size, shape, and intensity being fairly consistent between the two columns. The most notable thing that can be said is that the emulations typically have a lower maximum value compared to the model data, but this is to be expected given that the maximum values typically occur over a small area that is difficult for the emulations to properly resolve given the sampling differences.

The last set of comparisons for the 30 kilometer case involved radial velocity (V_r), and Figure A.3 has a similar setup to those previously presented. Figure A.3 showcases a similar story to those for Z_h and K_{DP} where the general size, shape, and intensity of the velocity signatures are consistent between the columns in each figure. When closely interrogating the images, some small differences can be observed; however, they are small features that do not impact the observations in a meaningful way and are again caused by the sampling differences.

Therefore, at 30 kilometers range, the emulations are representative of the model environment. There are some minor differences throughout each of the different variables; however, these can be attributed to the emulations sampling at 1° in elevation above the 2.0° elevation level while the model data has 0.5° sampling in elevation providing more detail. Furthermore, the truncated domain seen in the emulation data throughout Appendix A.1 is a result of the emulations not detecting data where there are weak reflectivity returns. This is not believed to be an issue and is not expected to impact the data or analysis. Thus, it has been shown that the use of RSim is representative of the model domain with corresponding radar sampling effects and can be used as a comparison method for different scanning strategies for the 30 kilometer cases.

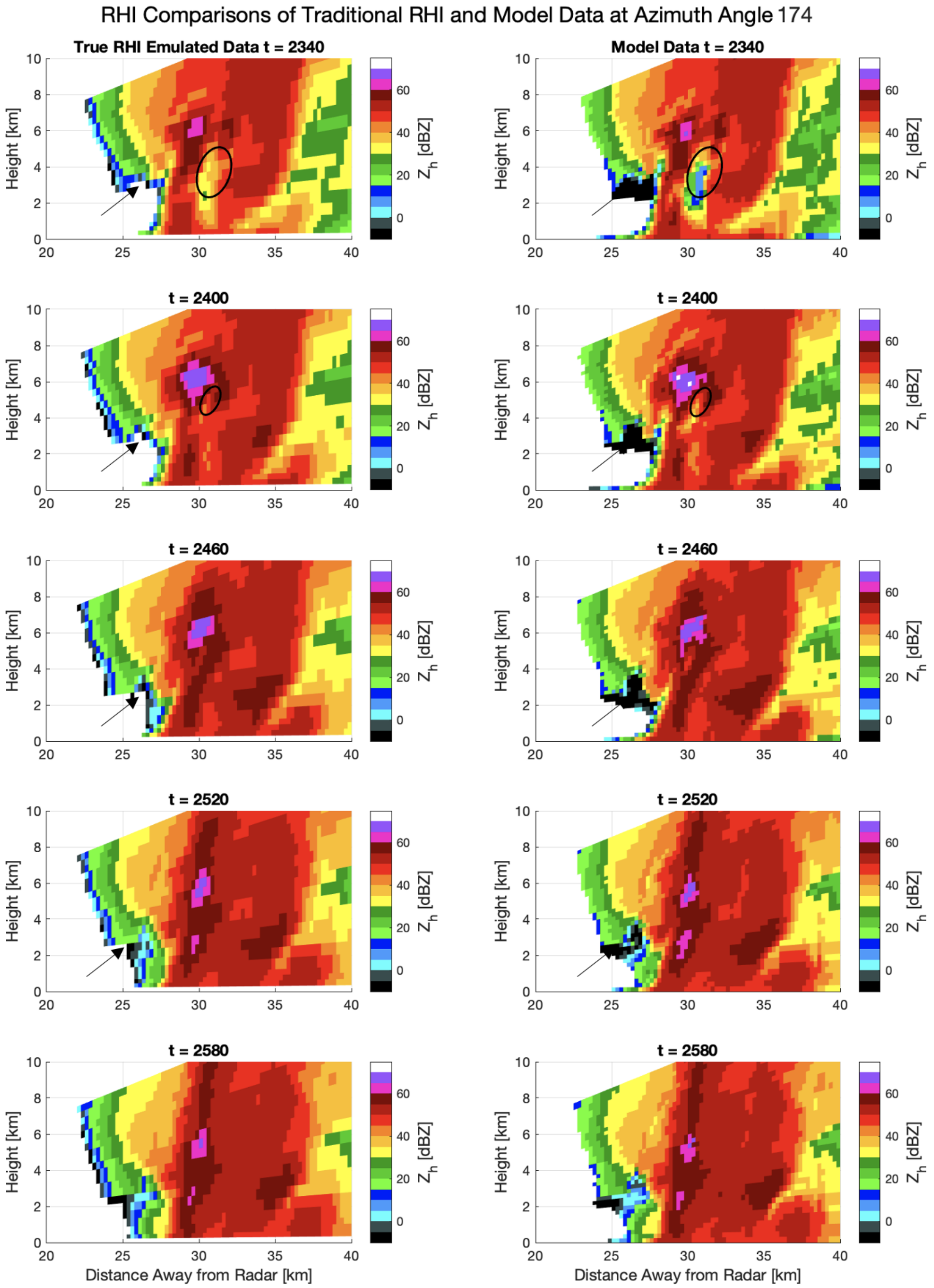

Figure A.1: RHI Images of Emulation (left column) and Model (right column) Z_h data along azimuth angle 174 at 60 s temporal resolution from $t = 2340$ s to 2880 s. Panels are labeled with their respective time and panels in the left column are emulated data while the right column contains the model data. All annotations highlight differences that were observed between the emulation and model data such as those in $t = 2340$ s.

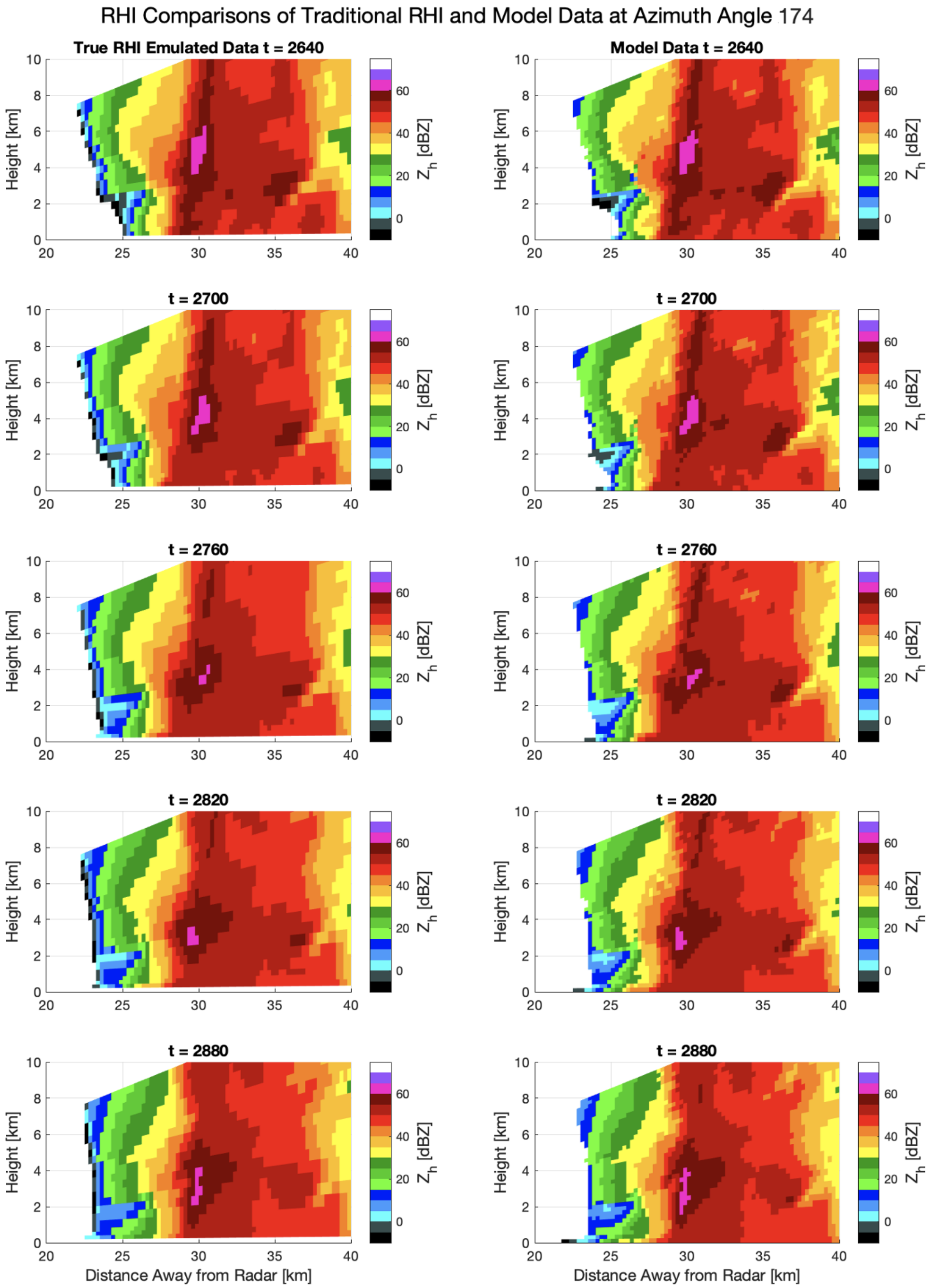

Figure A.1 (*Continued*)

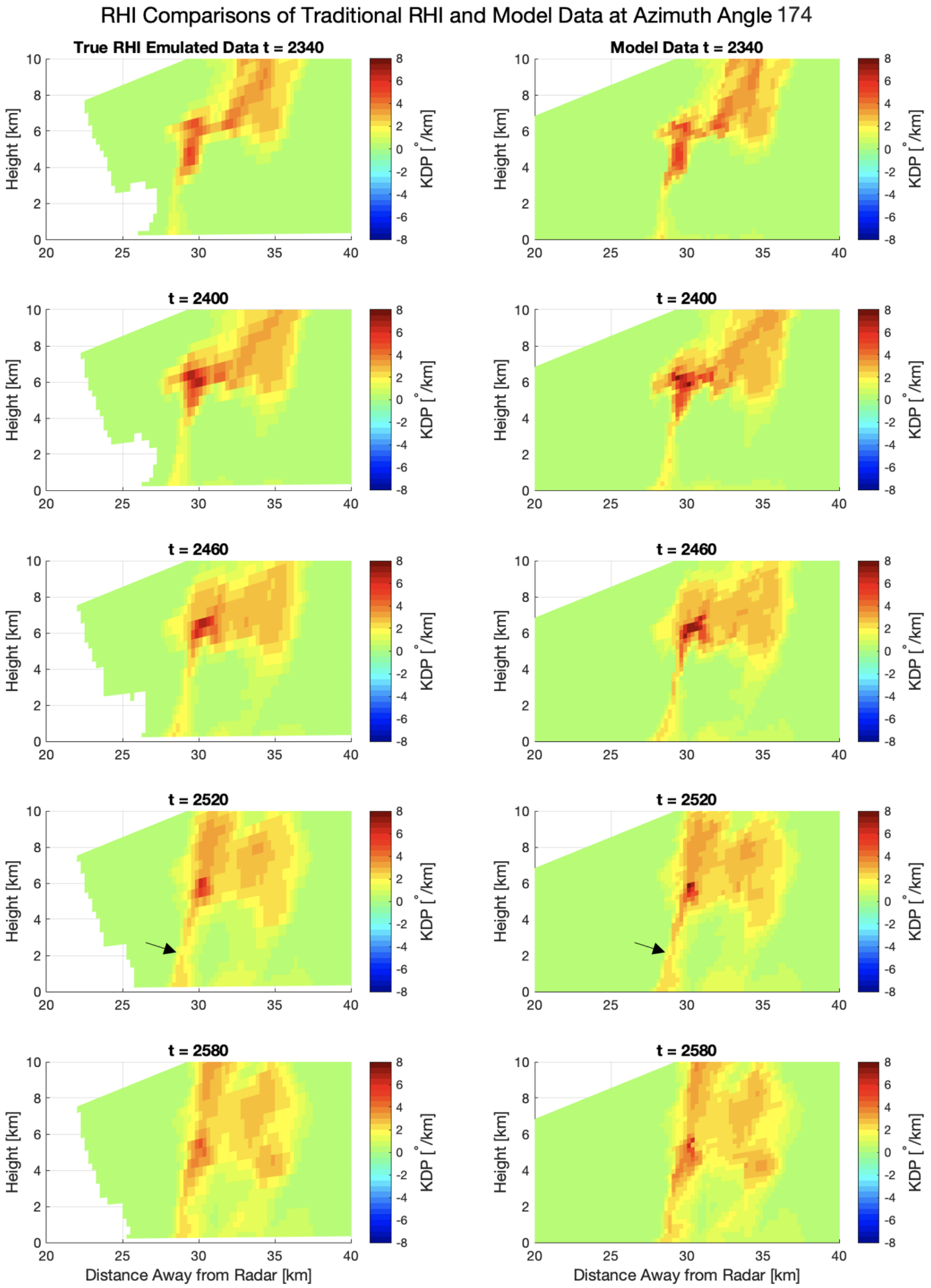

Figure A.2: RHI Images of Emulation (left column) and Model (right column) K_{DP} data along azimuth angle 174 at 60 s temporal resolution from $t = 2340$ s to 2880 s. Panels are labeled with their respective time and panels in the left column are emulated data while the right column contains the model data. All annotations highlight differences that were observed between the emulation and model data such as those in $t = 2520$ s.

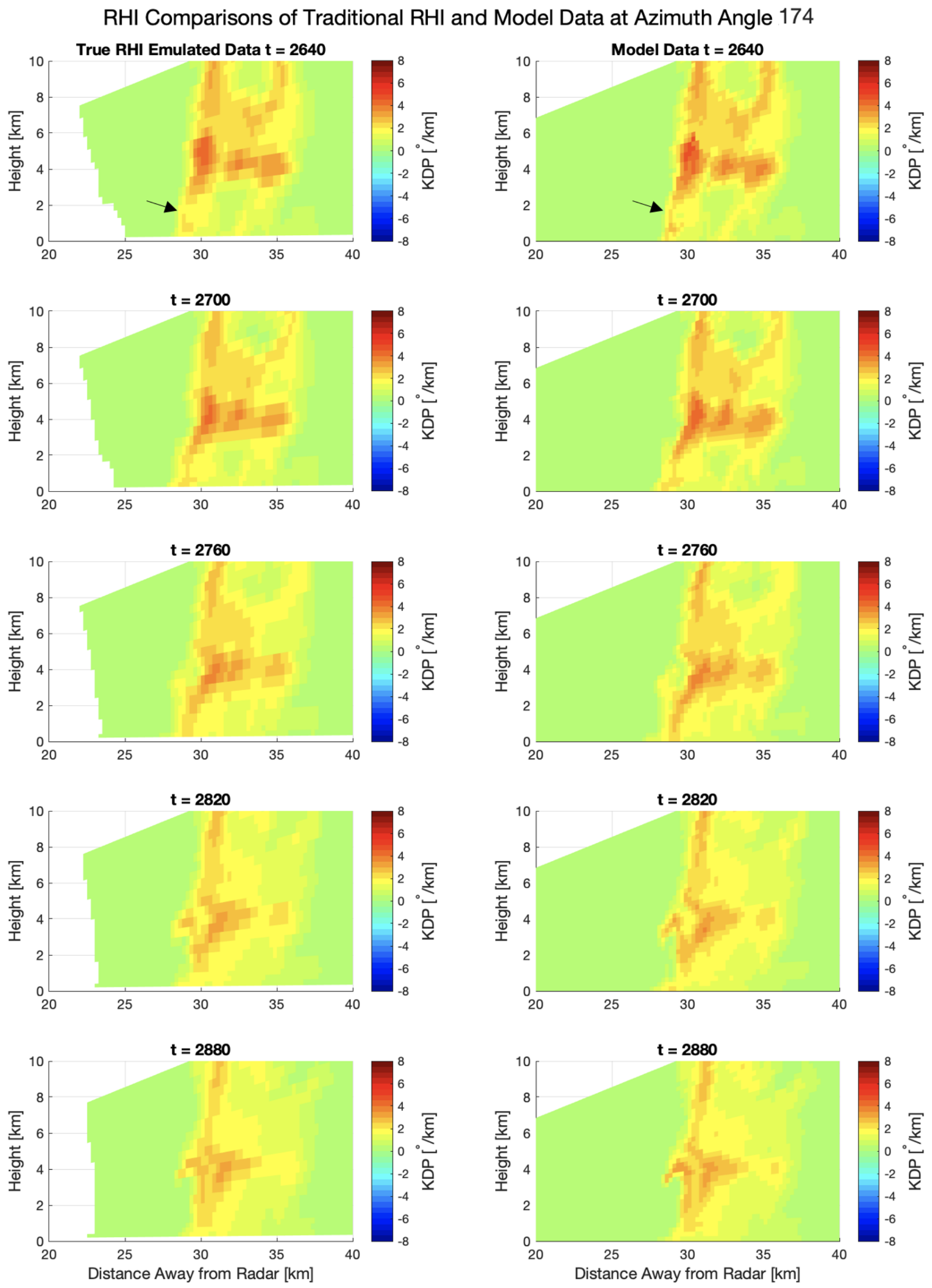

Figure A.2 (*Continued*)

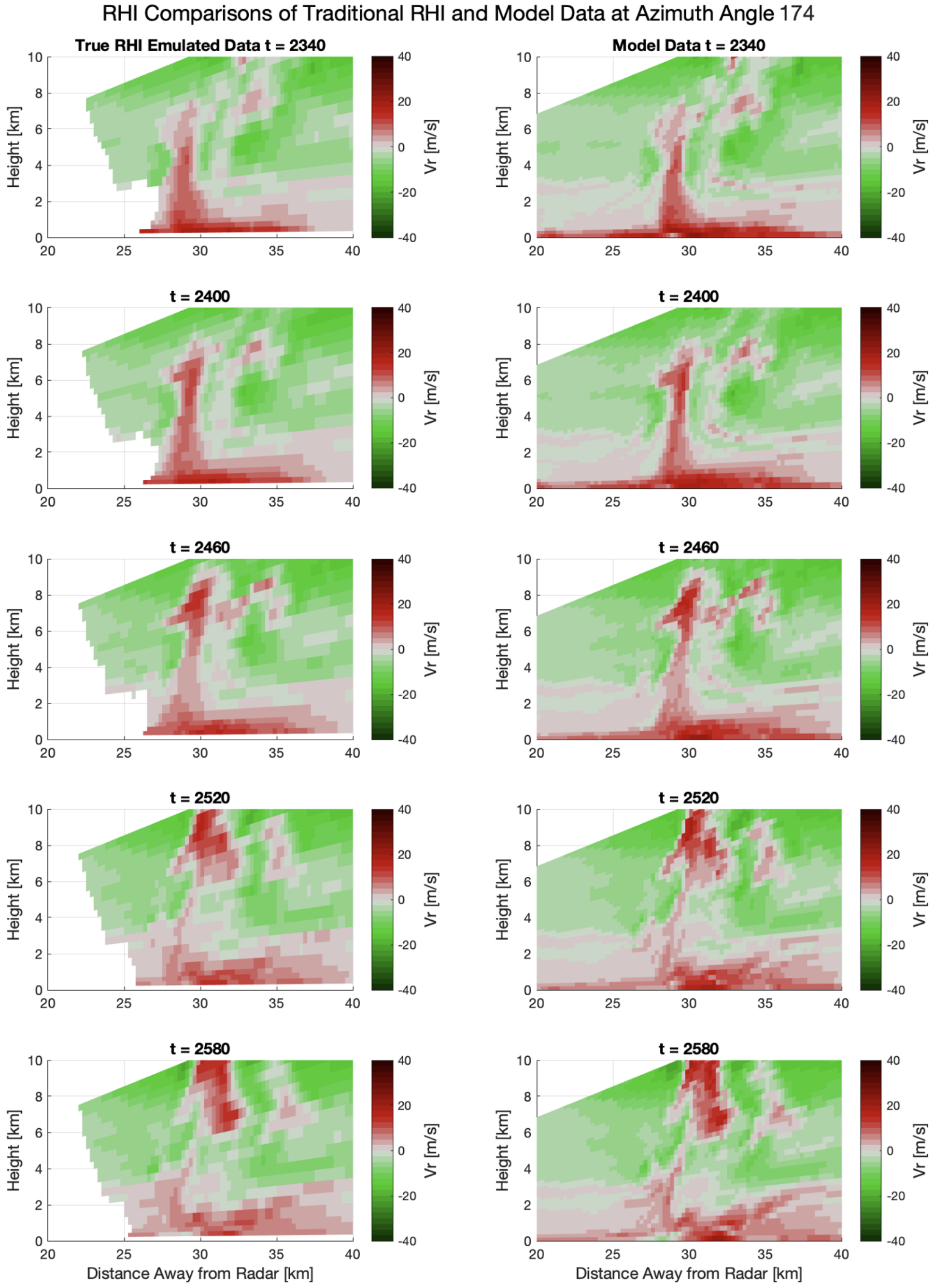

Figure A.3: RHI Images of Emulation (left column) and Model (right column) V_r data along azimuth angle 174 at 60 s temporal resolution from $t = 2340$ s to 2880 s. Panels are labeled with their respective time and panels in the left column are emulated data while the right column contains the model data.

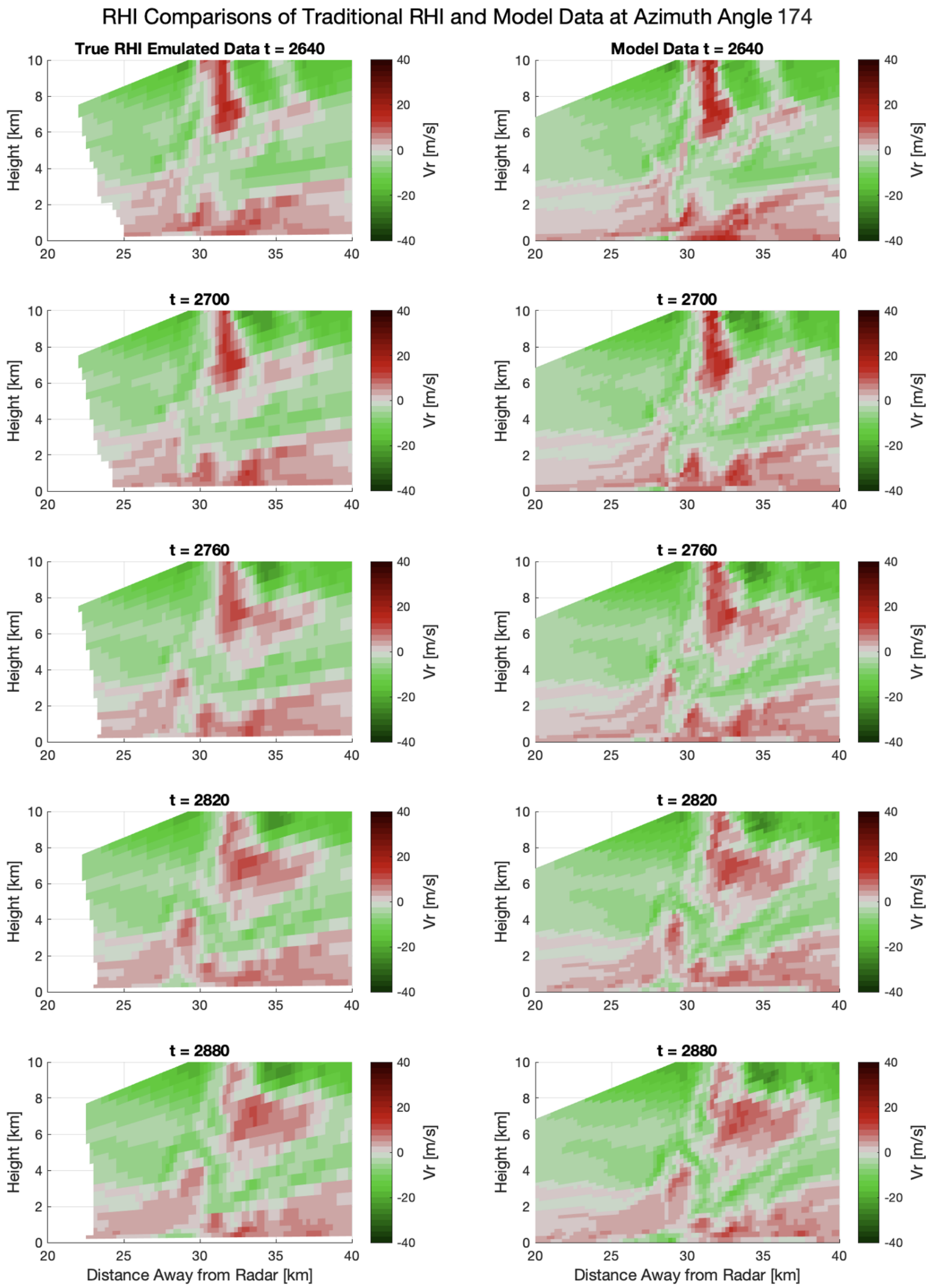

Figure A.3 (*Continued*)

A.2 90km Comparisons

The second set of comparisons between the model domain and the RSim emulated data will be looking at the 90 km case. As with the 30 km comparisons above in Appendix A.1, comparisons will be done at 60 s temporal sampling for the same variables: Z_h, K_{DP}, and V_r. These comparisons will cover the same 10-minute interval as those in Appendix A.1 but will have moved in range from the radar. This change in range from the radar also moved the observations from azimuth 174 to azimuth 178.

Looking at reflectivity factor, Figure A.4 the $t = 2340$ s panels show the early stages of an elevated reflectivity column around 89 km range and around 6 km AGL. As seen in the 30 km comparisons in Figure A.1, there is a small region of weak reflectivities between 90 and 91 km range and around 3 km AGL that is not detected by the emulations (black circle in $t = 2340$ s panels). However, this weak Z_h region is associated with sharp reflectivity gradients on nearly every side giving the emulation problems in proper detection. Furthermore, the azimuthal sampling of the emulations is 1° while the azimuthal sampling of the model data is 0.5°, so there could be influences not shown causing this feature to not be properly resolved. A similar low reflectivity level is seen in a similar spot in the $t = 2400$ s panels (black circle). The other major difference seen in the $t = 2460$ s and $t = 2520$ s panels and is indicated by the black square in each. In this region weaker reflectivities (20 dBZ) are smeared over in the emulations and are not properly resolved. This issue is likely cause by spatial sampling differences.

In the second time period from $t = 2640$ s to $t = 2880$ s, the general structure, evolution, and decay of the elevated reflectivity region remains fairly consistent between the two sets of panels. The one major difference is located in the $t = 2760$ s panel and indicated by the black arrow. This region shows a break in an elevated reflectivity region (≥ 55 dBZ) that is not properly resolved by the emulations. This corresponds to the region where the emulations move to 1.0° sampling spacing and is likely the reason for this discrepancy.

For specific differential phase, there is one minor difference that appears in both the $t = 2400$ s and $t = 2460$ s panel sets in Figure A.5. There is a small appendage of elevated K_{DP} (circled in black) that stretches to the surface in the model data that is not fully resolved by the emulation data until $t = 2520$ s. Outside of this difference, there are only minor differences and the general size, shape, evolution, and intensity of the elevated K_{DP} region are similar between the two sets of panels. The same can be said for the data between times $t = 2640$ s and $t = 2880$ s where the general structure, size, and decay of the elevated K_{DP} region is very similar between the two sets of panels.

Finally, looking at radial velocity, Figure A.6 has similar radial velocities between the emulation and model data. The panels in this figure were so similar that no annotations were provided to highlight obvious differences. It can again be said that the general structure and magnitudes of the radial velocity field is similar between the emulation and model data with the most major difference occurring because of the sampling spacing associated with the emulations.

Therefore, as was seen in Appendix A.1, the emulations are representative of the model domain with the main concerns being attributed to the sampling difference between the emulations and the model data. Furthermore, the truncated domain seen in the emulation

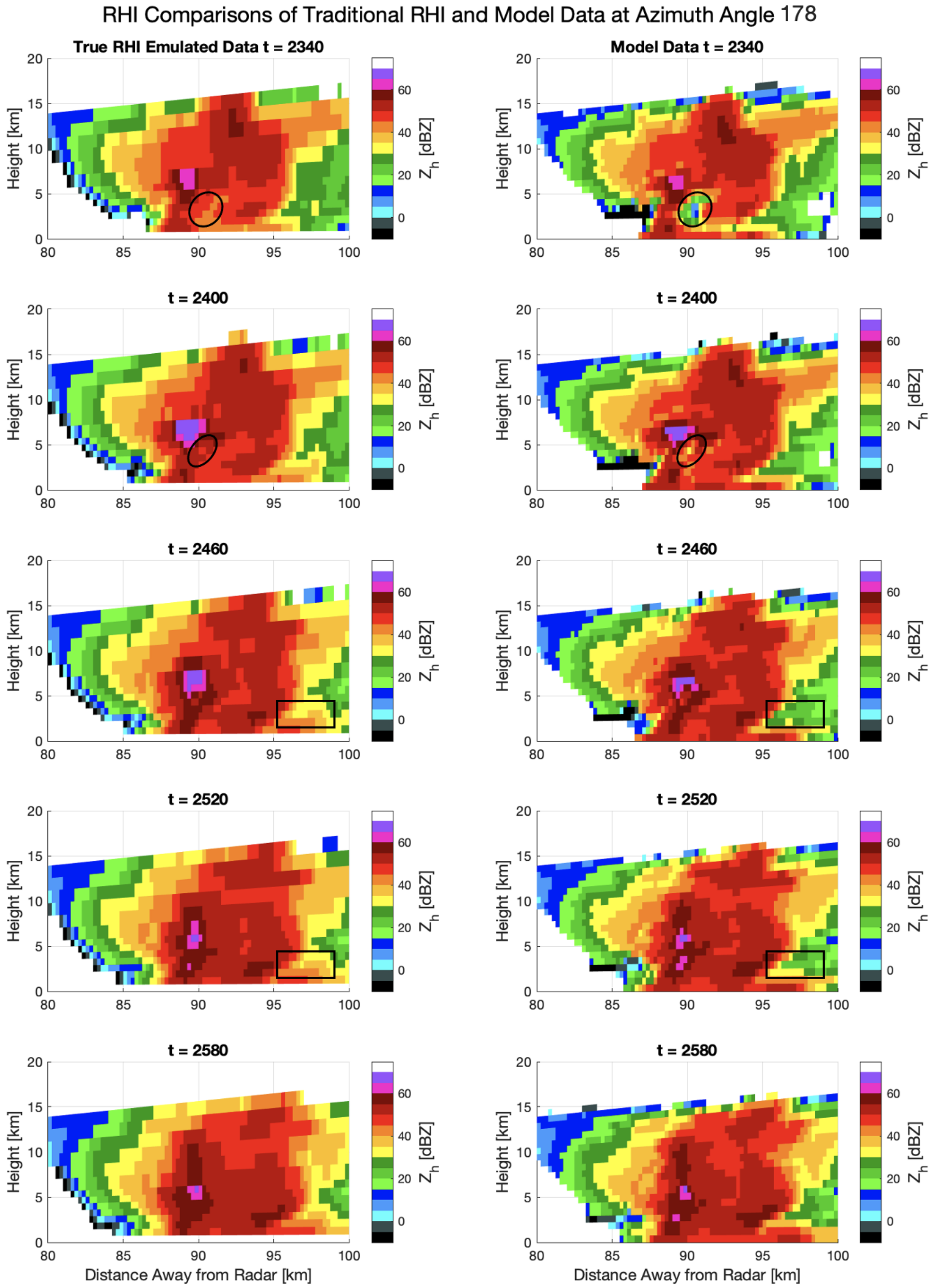

Figure A.4: RHI Images of Emulation (left column) and Model (right column) Z_h data along azimuth angle 178 at 60 s temporal resolution from $t = 2340$ s to 2880 s. Panels are labeled with their respective time and panels in the left column are emulated data while the right column contains the model data. All annotations highlight differences that were observed between the emulation and model data such as those in $t = 2340$ s.

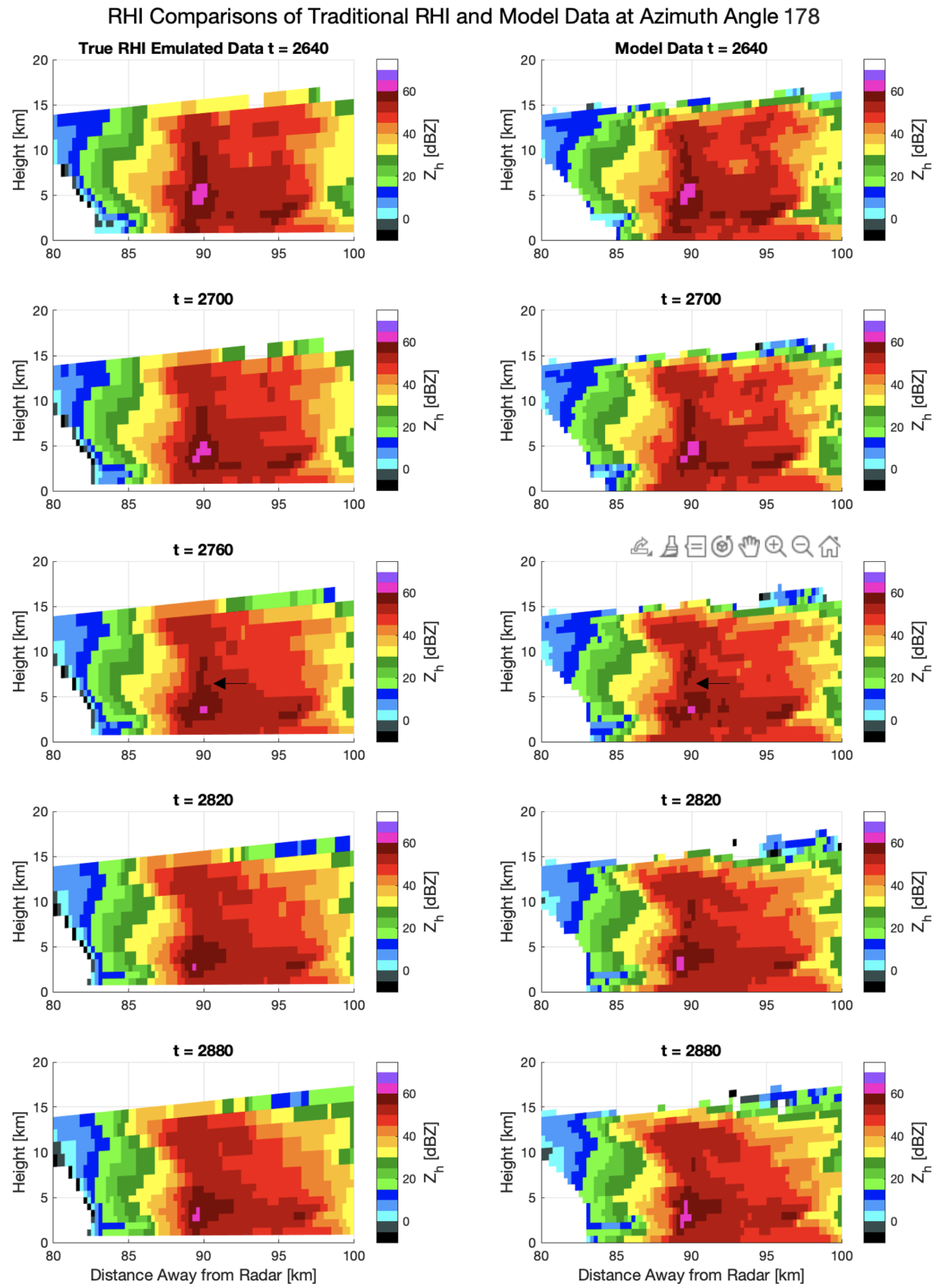

Figure A.4 (*Continued*)

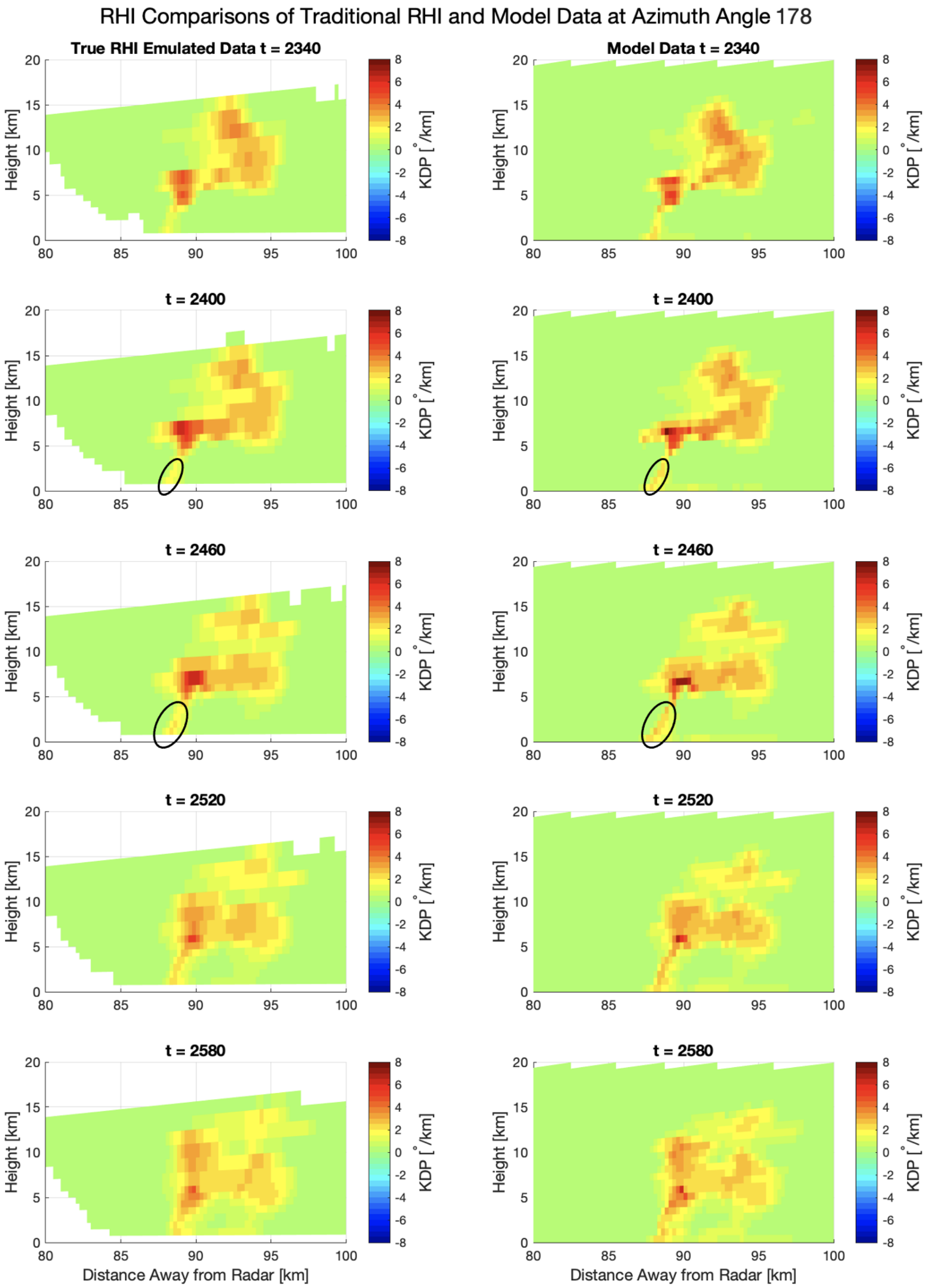

Figure A.5: RHI Images of Emulation (left column) and Model (right column) K_{DP} data along azimuth angle 178 at 60 s temporal resolution from $t = 2340$ s to 2880 s. Panels are labeled with their respective time and panels in the left column are emulated data while the right column contains the model data. All annotations highlight differences that were observed between the emulation and model data such as those in $t = 2400$ s.

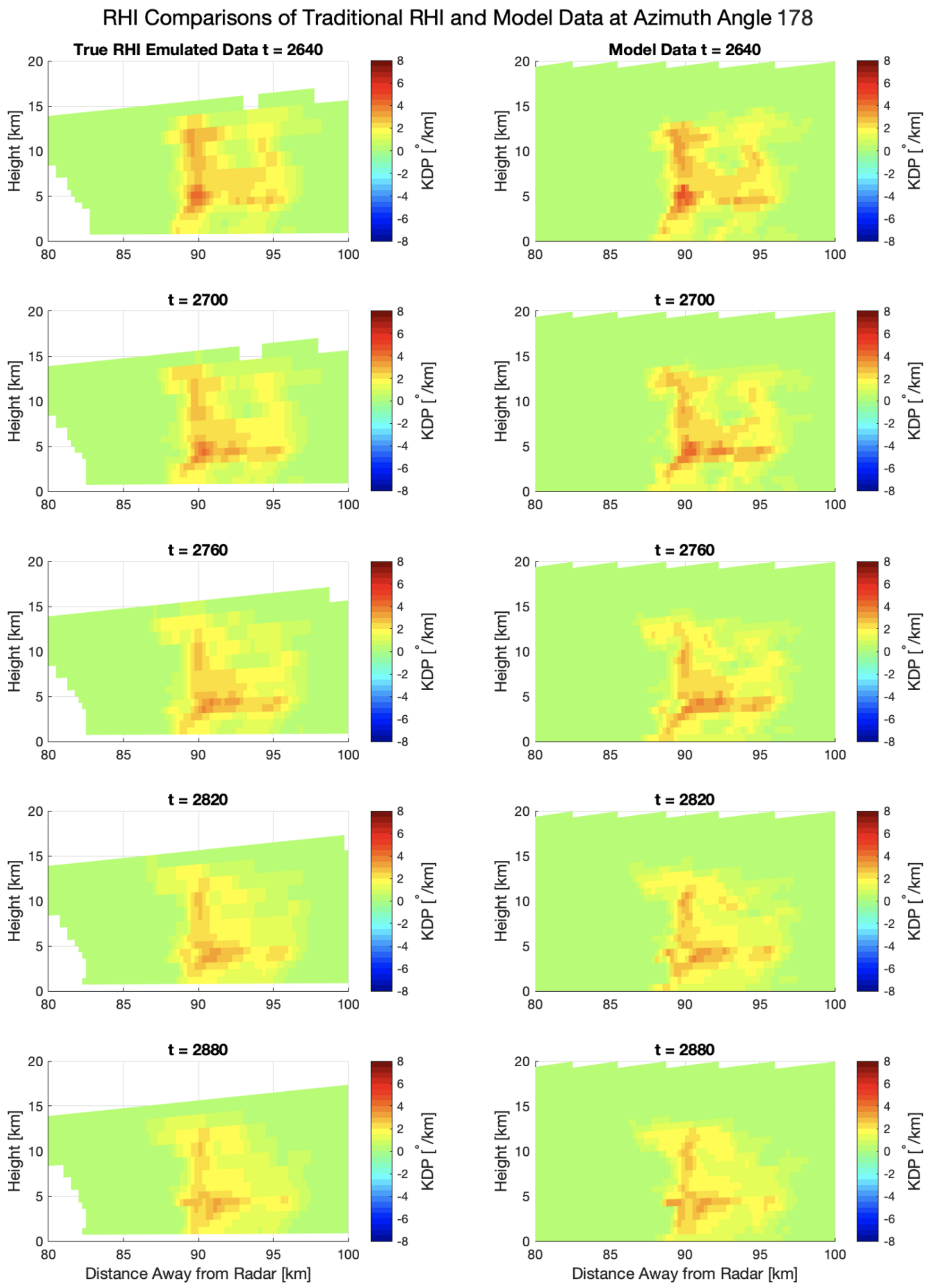

Figure A.5 (*Continued*)

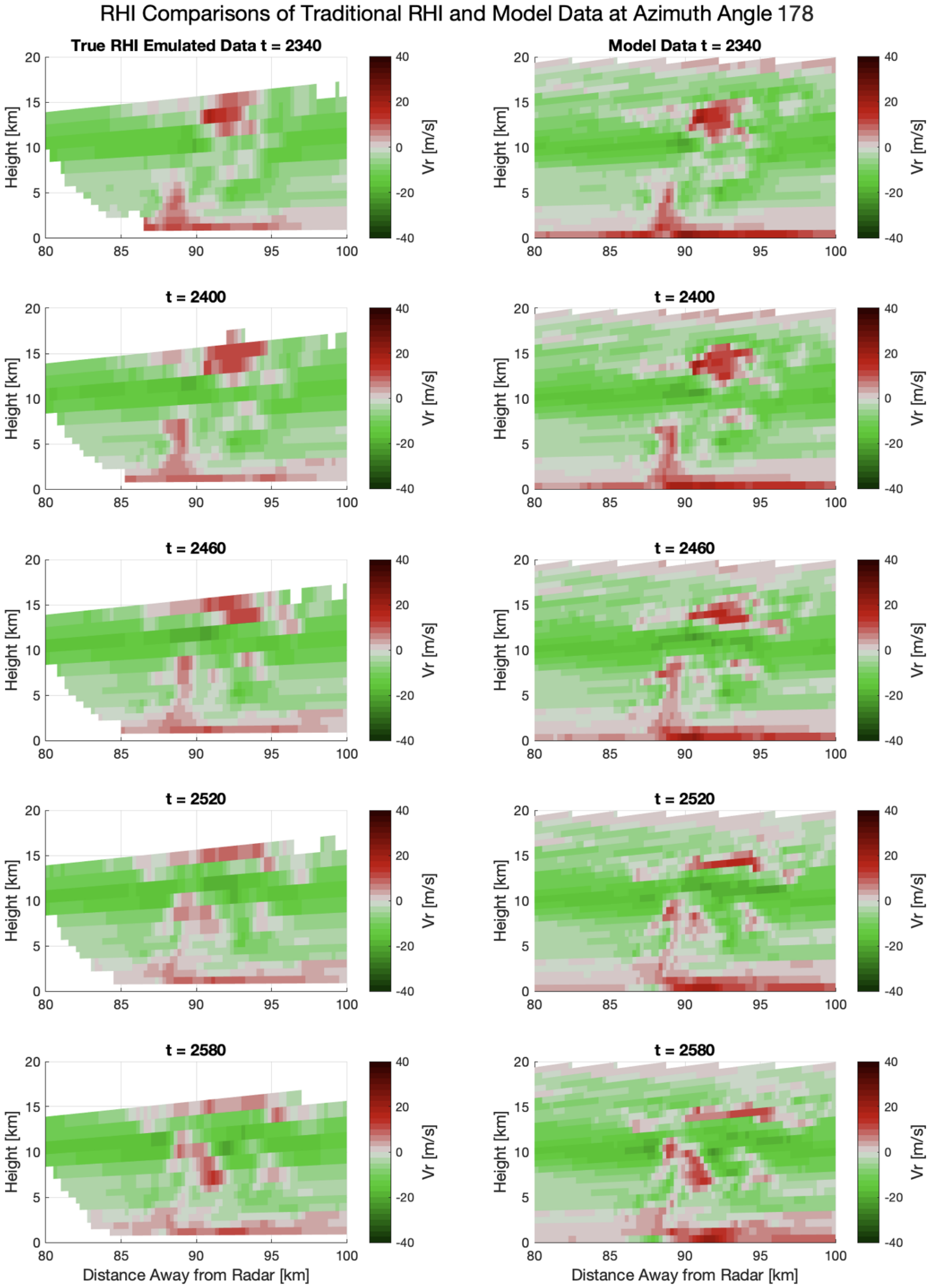

Figure A.6: RHI Images of Emulation (left column) and Model (right column) V_r data along azimuth angle 178 at 60 s temporal resolution from $t = 2340$ s to 2880 s. Panels are labeled with their respective time and panels in the left column are emulated data while the right column contains the model data.

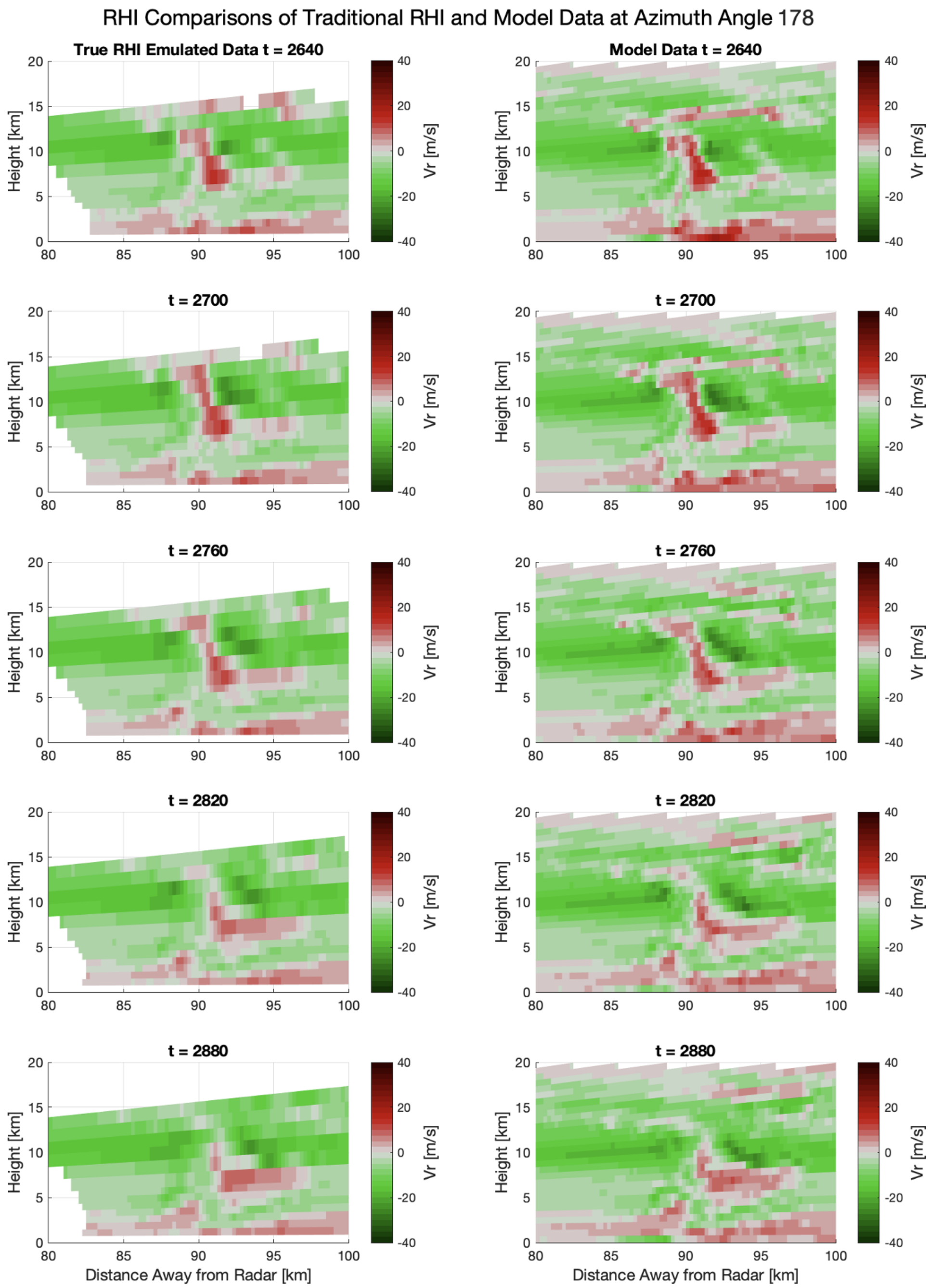

Figure A.6 (*Continued*)

data throughout Appendix A.2 is a result of the emulations not detecting data where there are weak reflectivity returns. Thus, it has been shown that the use of RSim is representative of the model domain and can be used as a comparison method for different scanning strategies for the 90 km cases.

Appendix B

Additional Supporting Error Analysis Results

The following appendix will contain additional error analysis figures not directly discussed in Sections 3.2.1 and Section 3.2.2. No further analysis is provided below, but figures similar to those found in Sections 3.2.1 and 3.2.2 are shown. These figures provide a more detailed background into the calculated MAEs found in both Tables 3.1 and 3.2.

Figures B.1 through B.6 are additional figures associated with Section 3.2.1, and figures B.7 through B.12 are additional figures associated with Section 3.2.2.

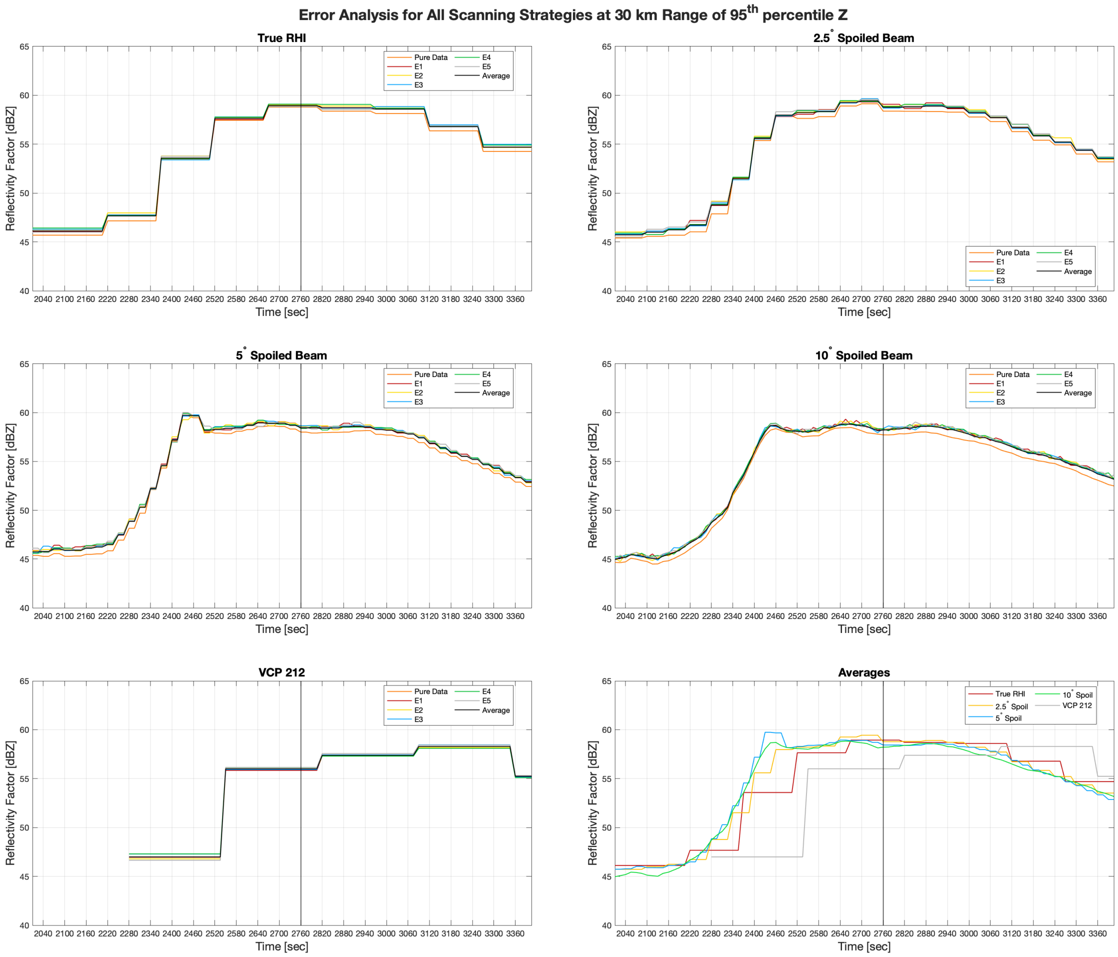
Error Analysis for All Scanning Strategies at 30 km Range of 95th percentile Z

Figure B.1: Same as Figure 3.37 but for 95^{th} percentile Z_h.

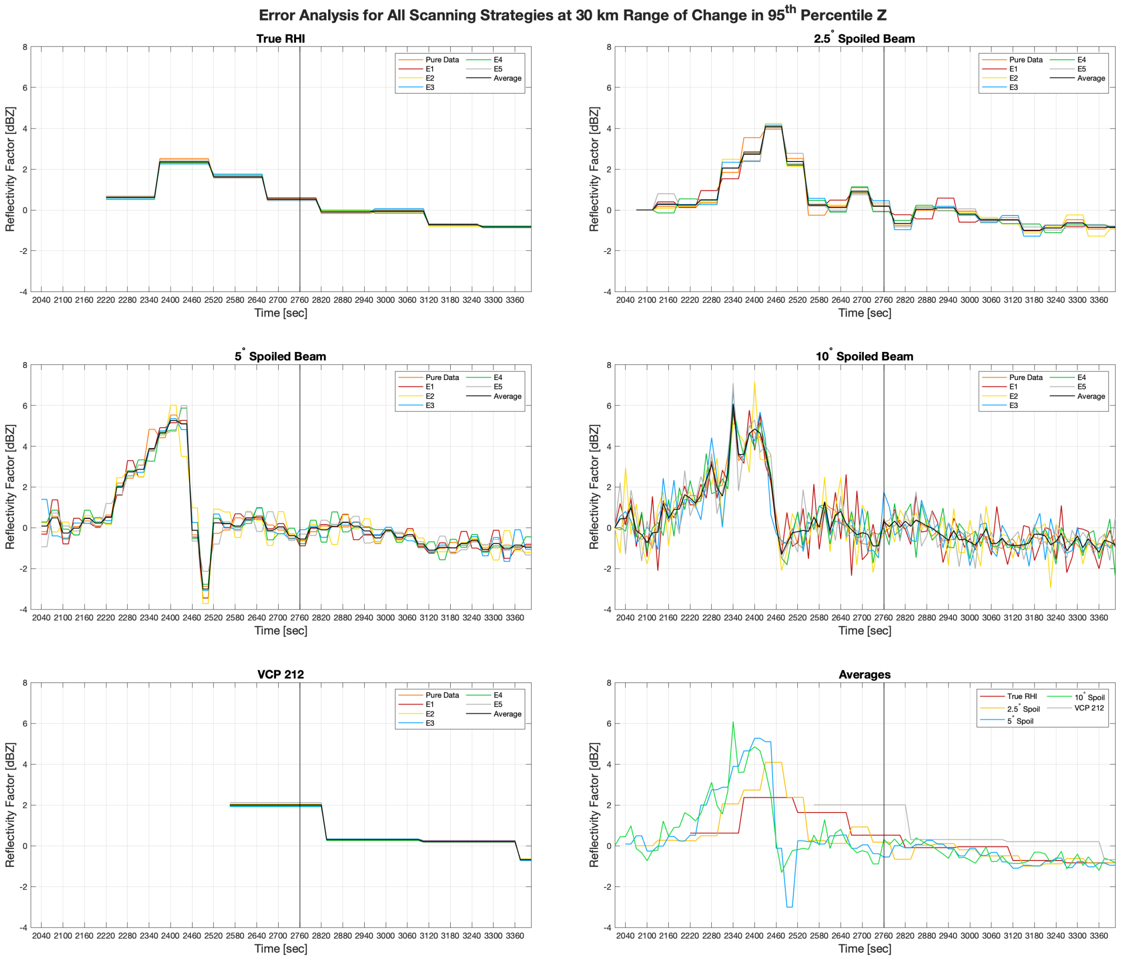

Figure B.2: Same as Figure 3.37 but for change in 95^{th} percentile Z_h per unit time.

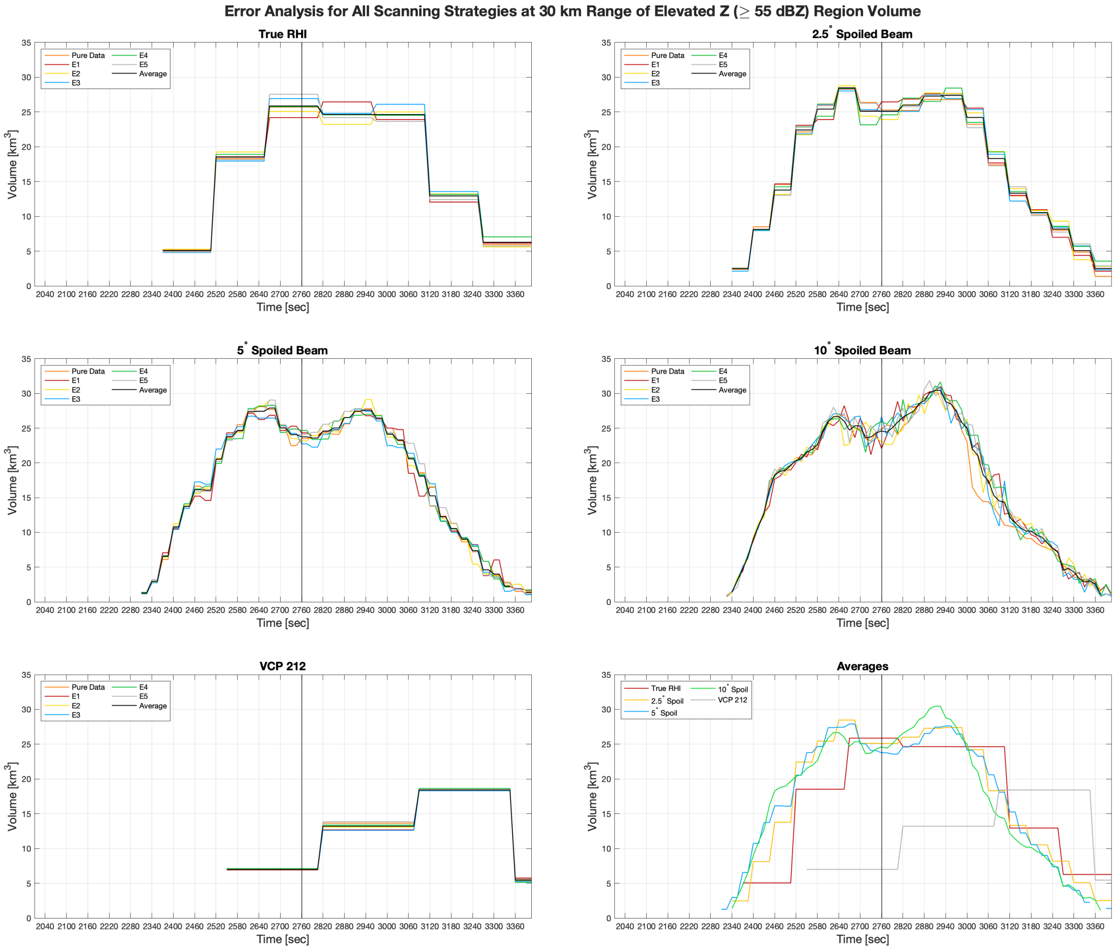

Figure B.3: Same as Figure 3.37 but for Z_h column total volume.

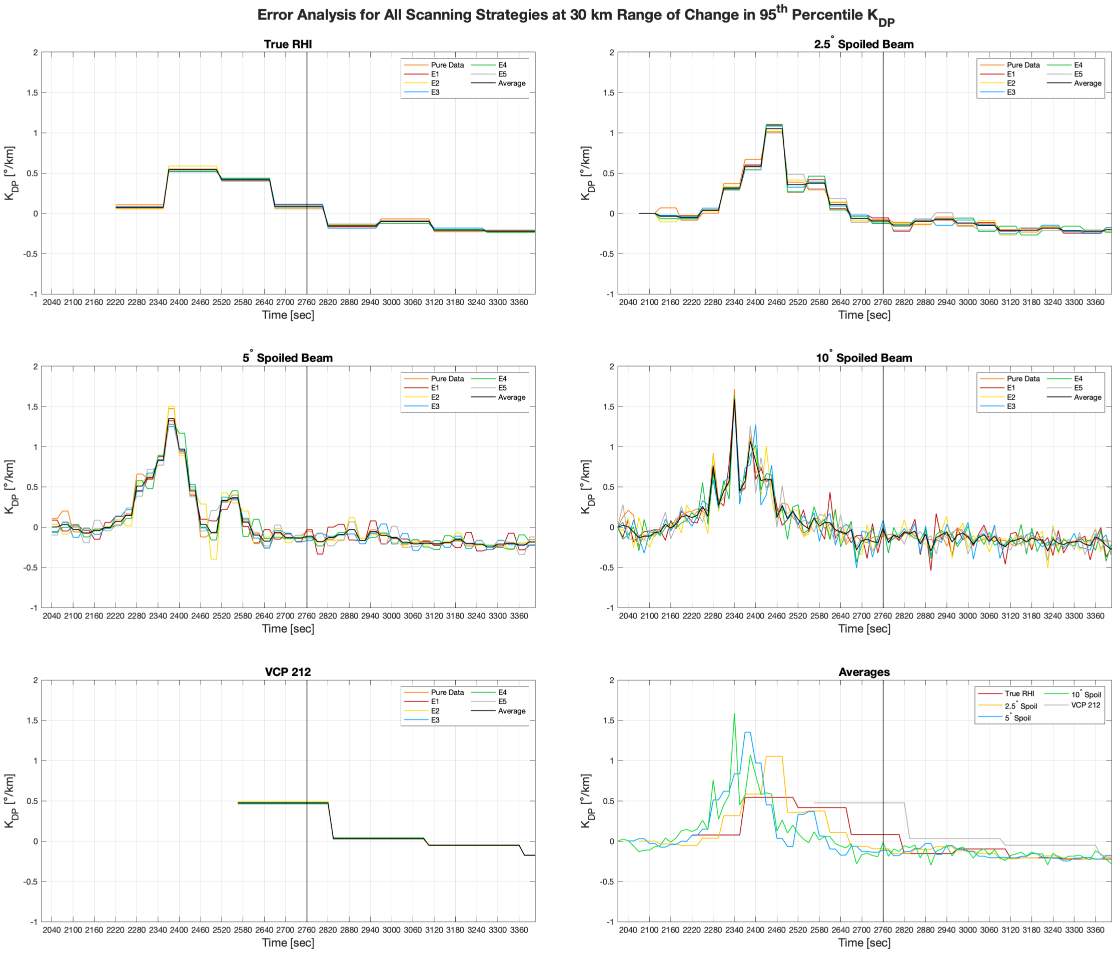

Figure B.4: Same as Figure 3.37 but for the change in 95^{th} percentile K_{DP} per unit time.

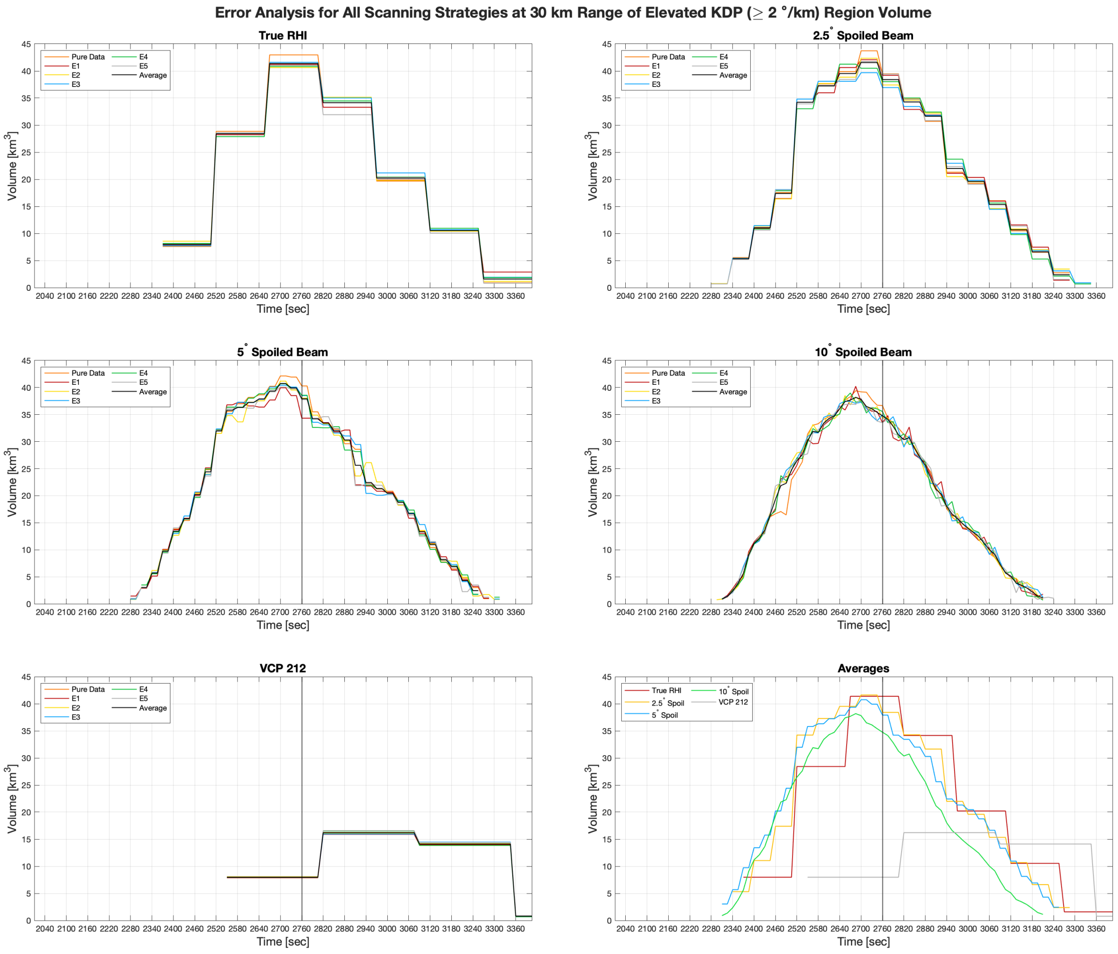

Figure B.5: Same as Figure 3.37 but for K_{DP} core total volume.

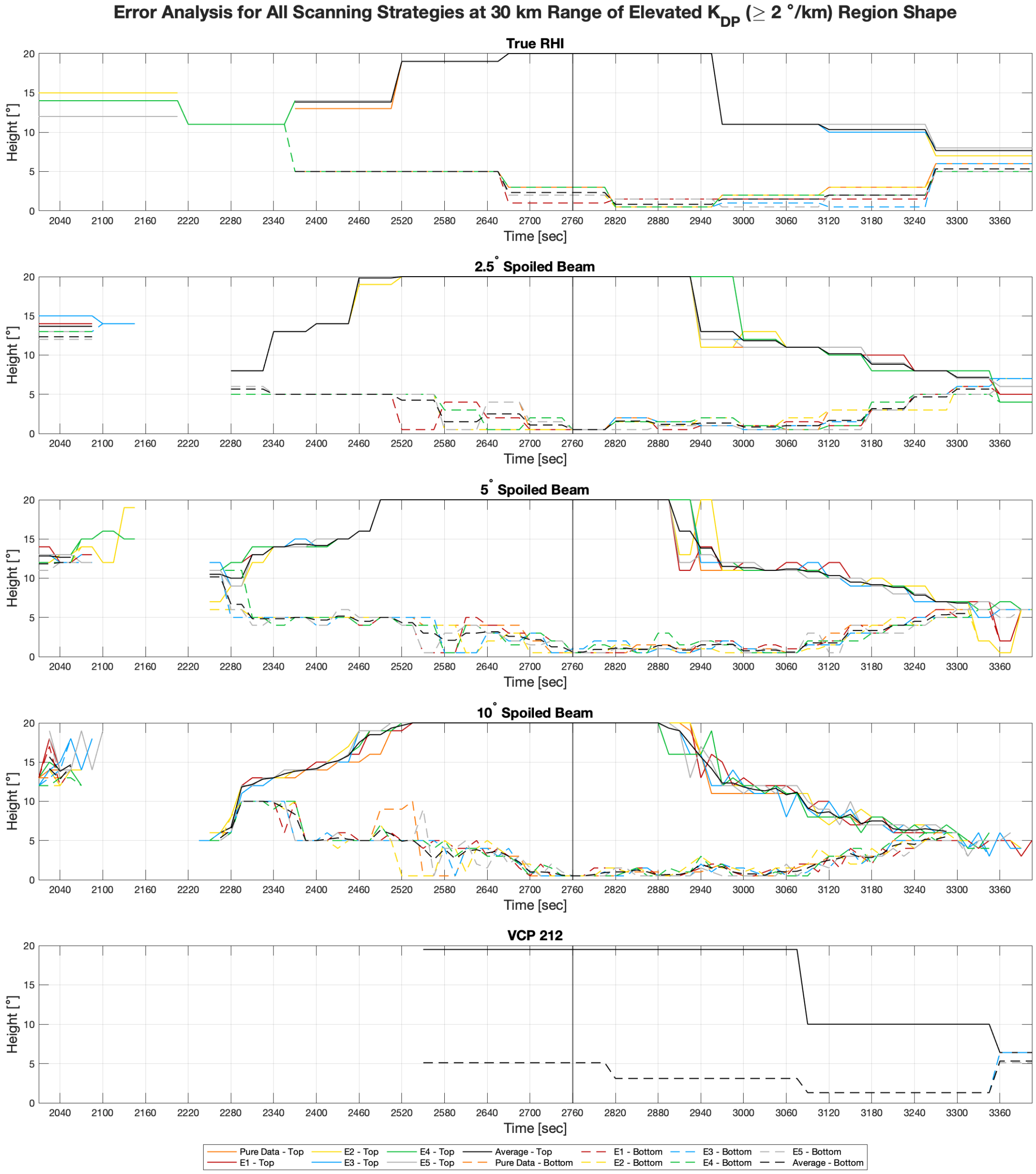

Figure B.6: Same as Figure 3.37 but for the shape of the K_{DP} core.

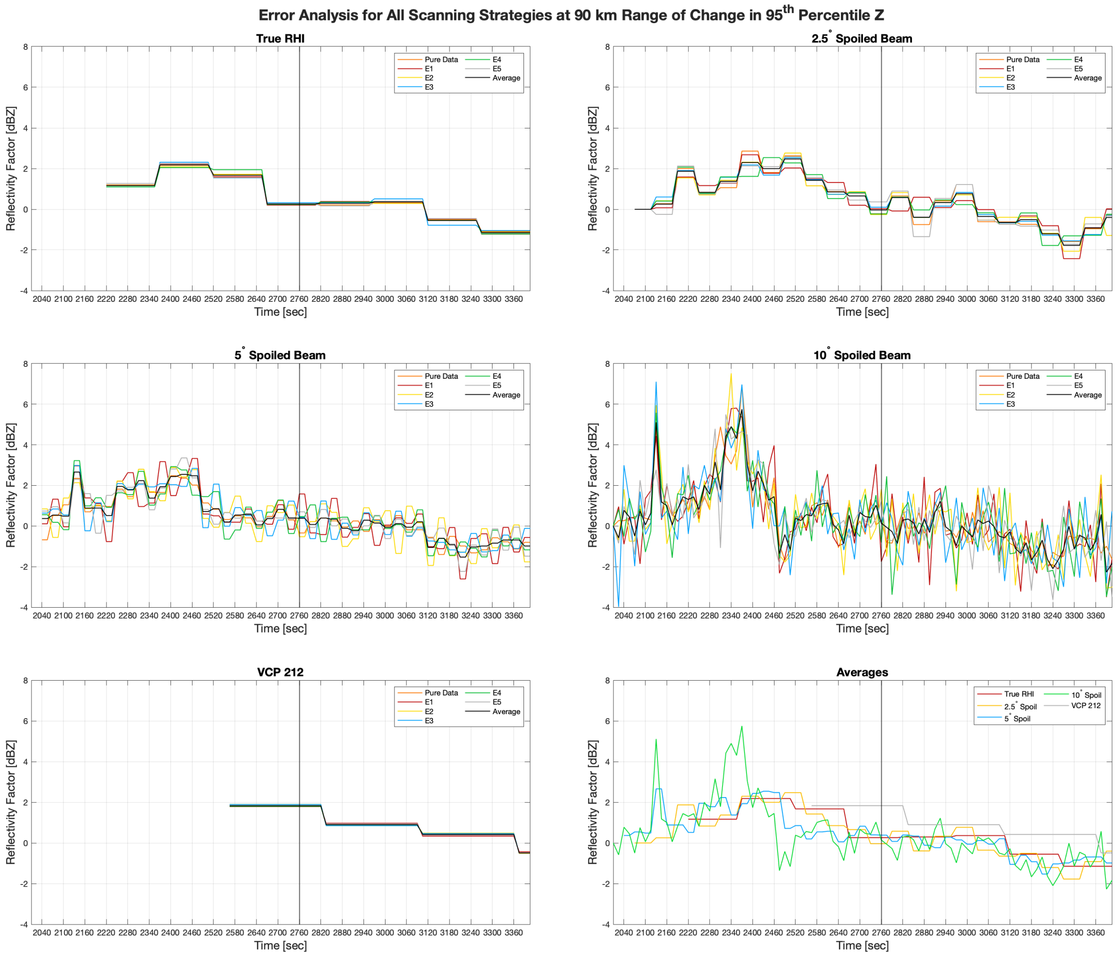

Figure B.7: Same as Figure 3.37 but for change in 95th percentile Z_h per unit time at 90 km.

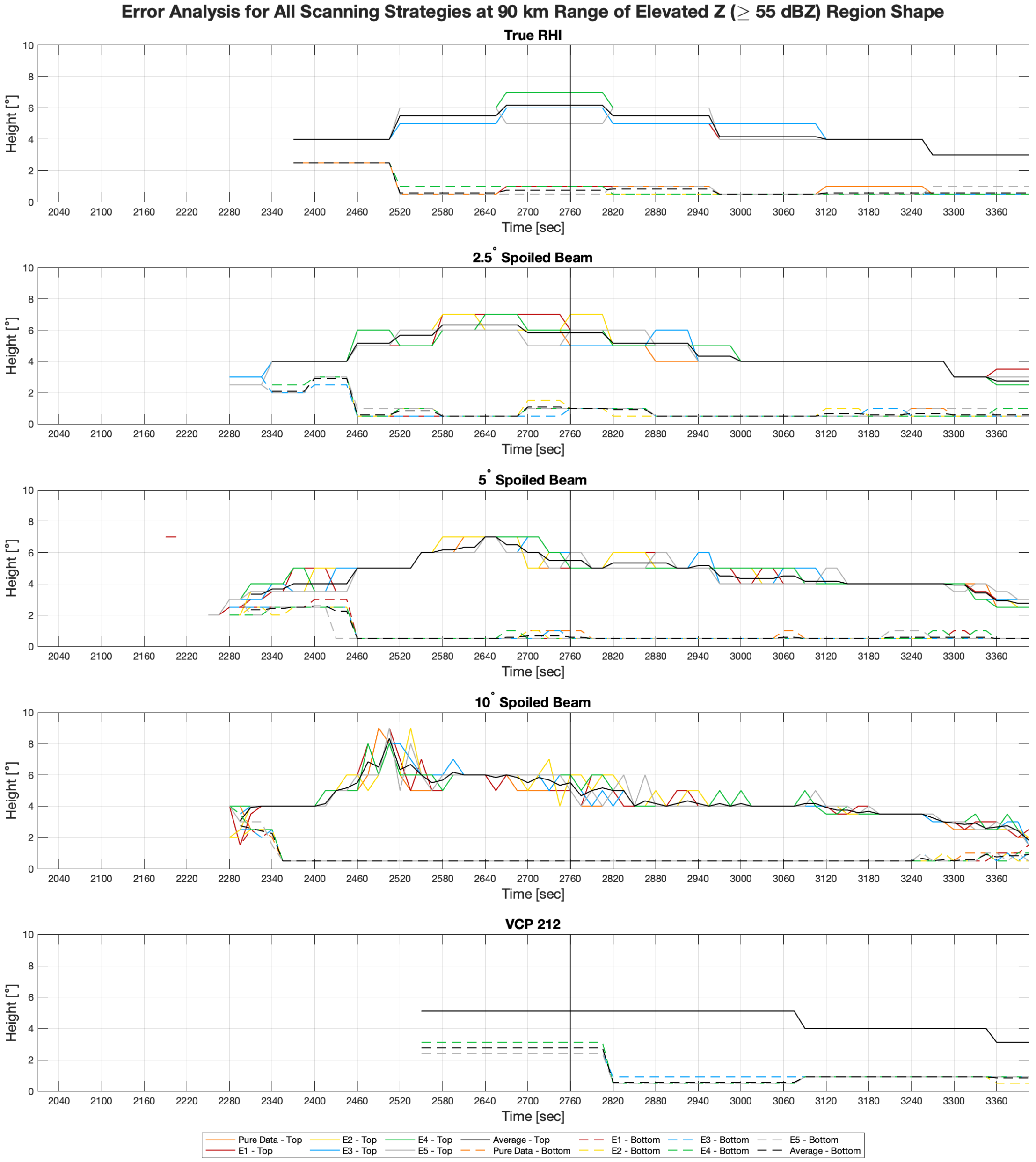

Figure B.8: Same as Figure 3.37 but for the shape of the Z_h column at 90 km range.

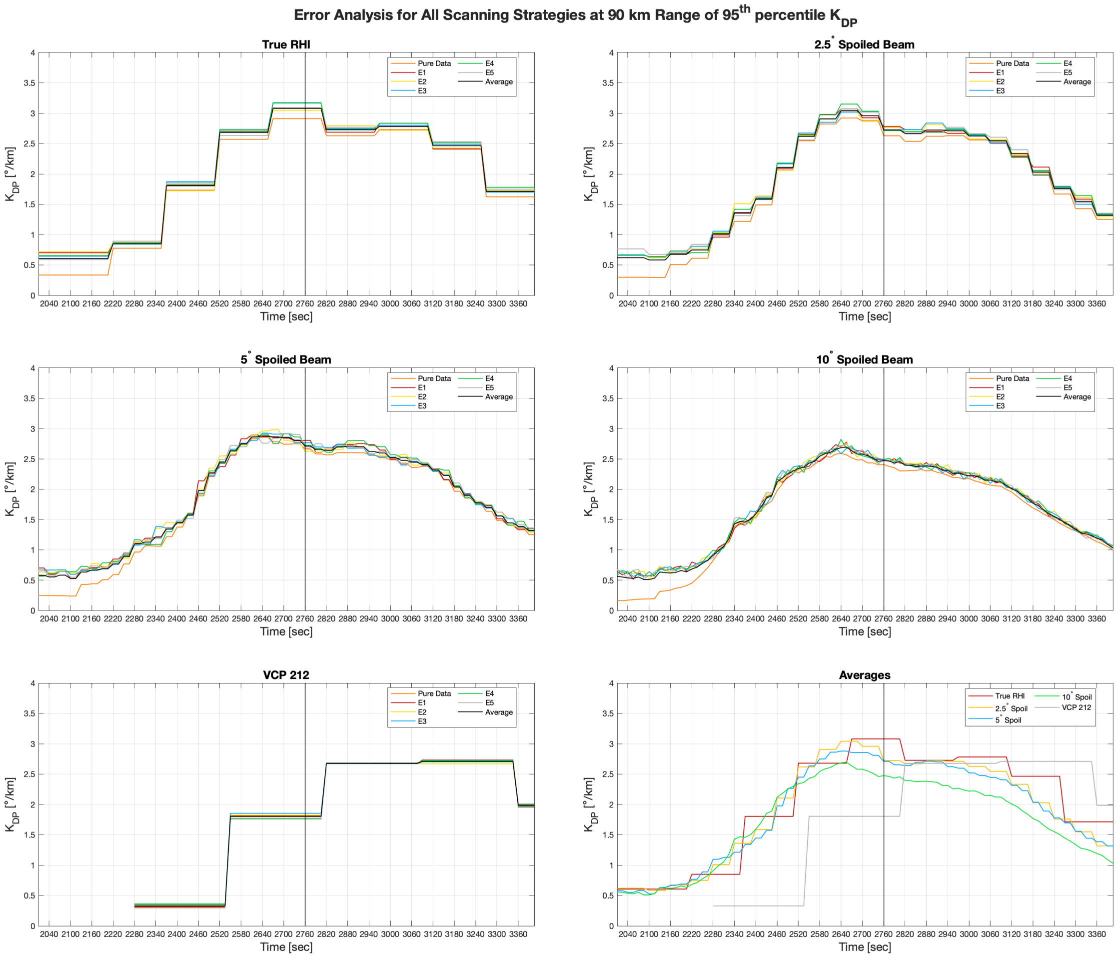

Figure B.9: Same as Figure 3.37 but for 95th percentile K_{DP} at 90 km range.

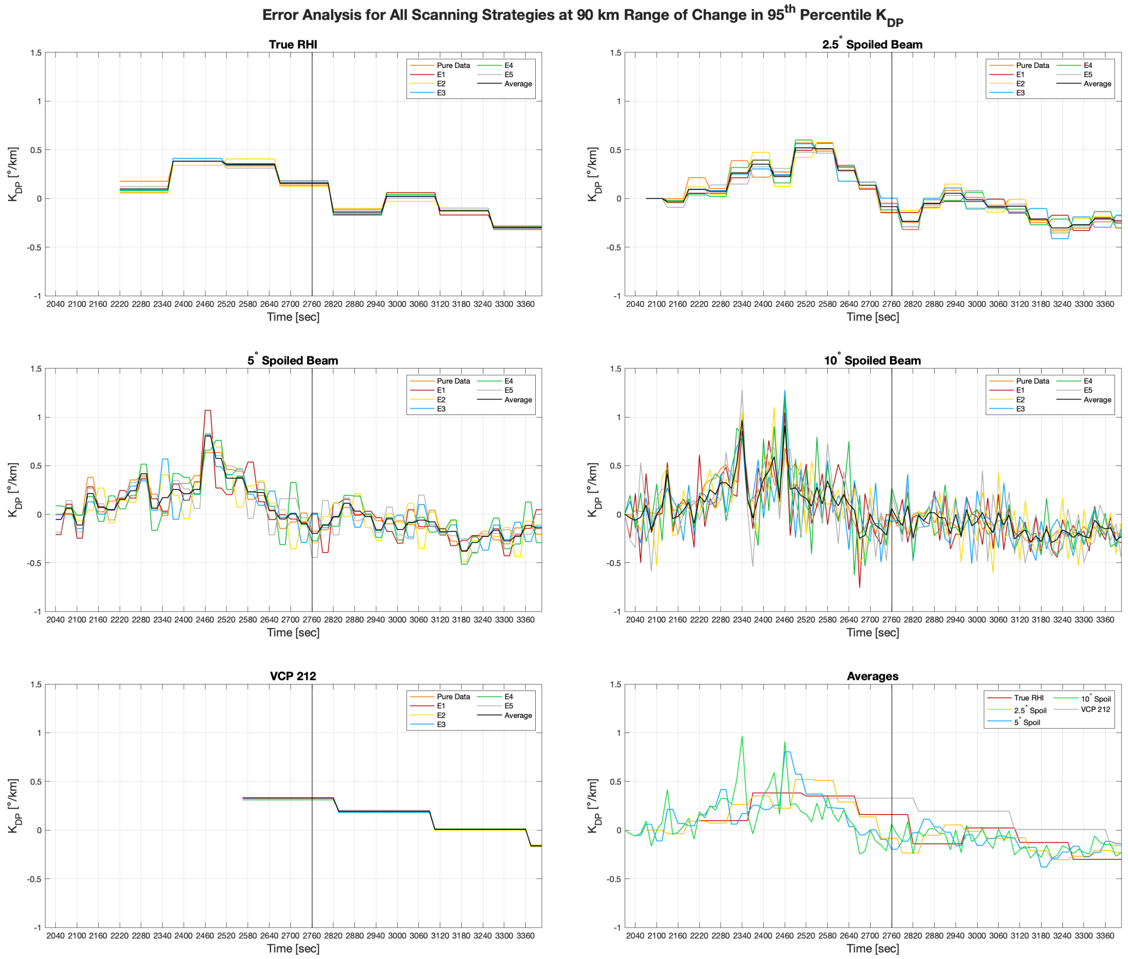

Figure B.10: Same as Figure 3.37 but for the change in 95^{th} percentile K_{DP} per unit time at 90 km range.

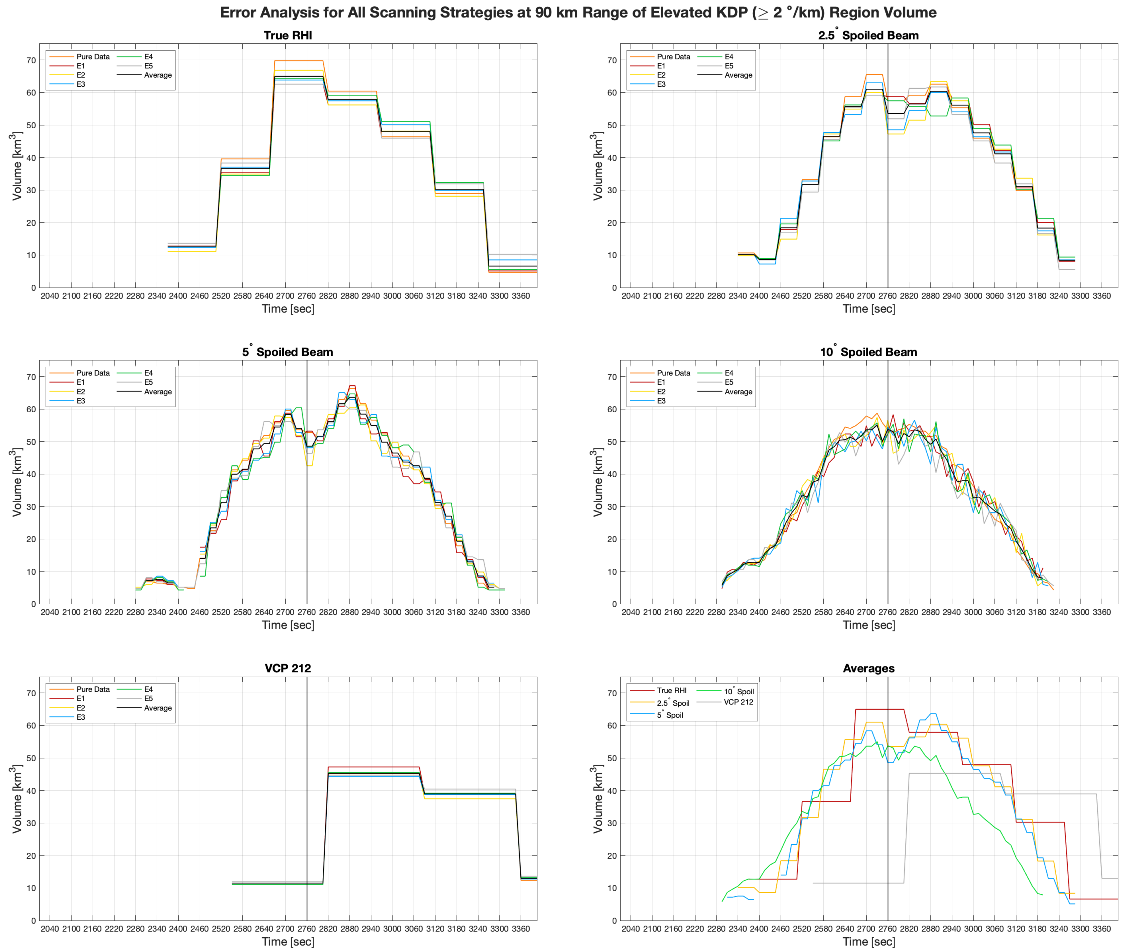

Figure B.11: Same as Figure 3.37 but for K_{DP} core total volume at 90 km range.

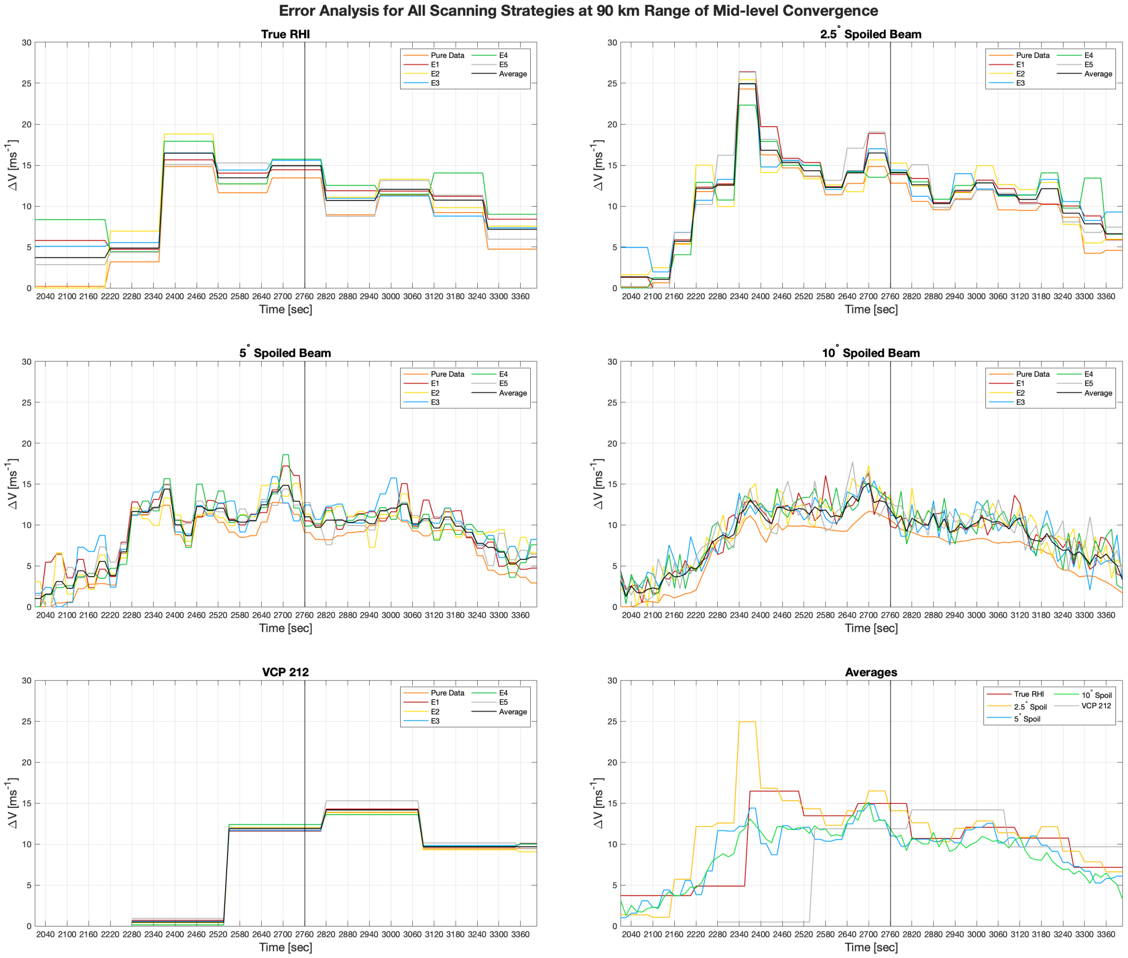

Figure B.12: Same as Figure 3.37 but for mid-level convergence at 90 km range.